Design and Synthesis of Porous Organic Polymers for Sensing and Visible Light Photocatalytic Applications

Harpreet Singh

A thesis submitted for the partial fulfilment of

the degree of Doctor of Philosophy

Department of Chemical Sciences

Indian Institute of Science Education and Research (IISER) Mohali

Knowledge City, Sector 81, SAS Nagar, Manauli PO, Mohali 140306, Punjab, India.

August 2020

DEDICATED TO

My family

Declaration

The work presented in this thesis has been carried out by me under the guidance of **Dr. Santanu Kumar Pal** in the Department of Chemical Sciences, Indian Institute of Science Education and Research (IISER) Mohali. This work has not been submitted in part or full for a degree, diploma, or a fellowship to any other university or institute. Whenever contributions of others are involved, every effort is made to indicate this clearly, with due acknowledgments of collaborative work and discussions. This thesis is a bonafide record of original work done by me and all sources listed within have been detailed in the bibliography.

Harpreet Singh

In my capacity as the supervisor of the candidate's thesis work, I certify that the above statements by the candidate are true to the best of my knowledge.

Dr. Santanu Kumar Pal

Acknowledgment

<div align="right">Harpreet Singh</div>

Contents

1

Chapter 1

Porous Organic Polymers: An Introduction
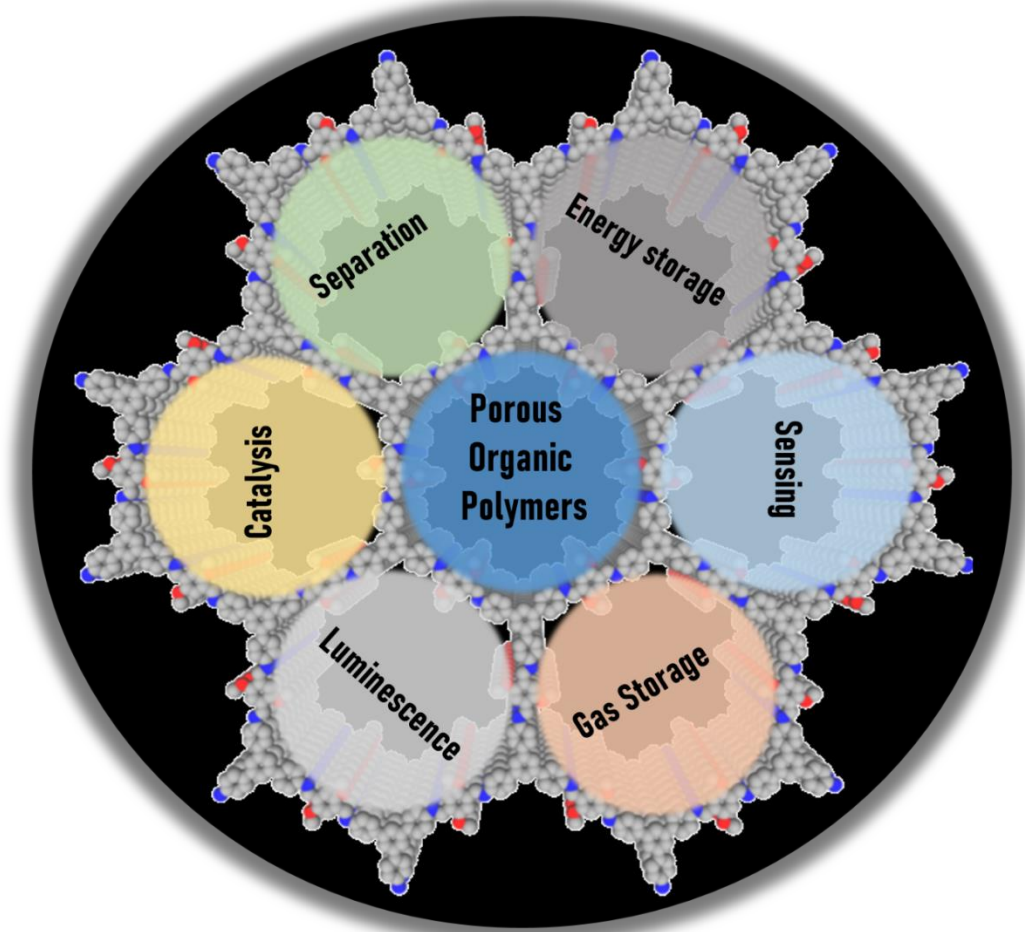
Mimicking porous structures found in nature has been an attractive area of science. Accumulating the knowledge in this direction, scientists have made a great progress in constructing various extended porous structures. Among all the porous materials, porous organic polymers (POPs) with well-defined pores and very high surface area received a great attention due to their easy synthesis and tailorable chemical structures. POPs are excellent performers in gas storage/separation, catalysis, environmental remediation, and sensing. This chapter summarizes the various types POPs, along with their design/synthesis and potential applications in various fields.

1.1 Outline:

The key objective of science is to study nature and reproduce it for the prosperity of living being. Porosity is an inherent phenomenon of nature used for various purposes such as storage, separation, and filtration by various living creatures. For example, the honeycomb is an excellent porous structure for the storage of honey and honey bee larvae (Figure 1.1a). Many aquatic animals such as sponges use pores on their body surfaces for filtering the food and oxygen from seawater as well as waste elimination necessary for their existence (Figure 1.1b). Furthermore, various human organs like alveoli in the lungs are specially designed porous structures to absorb the oxygen from the air that we breathe (Figure 1.1c). Mimicking porous structures found in nature, from macro to molecular level, has long been an attractive area of science. By accumulating the knowledge in this direction, researchers have made a great progress[1–13] in constructing numerous disordered[14] to regular[15] porous structures. The porous structures made of purely inorganic (e.g., Zeolites or porous silica) to purely organic (COFs or POPs) and hybrid (MOFs) components are 0D[16, 17] to 3D[10] extended chemical architectures.

Figure 1.1: Examples of porosity existing in nature materials: (a) honeycomb; (Adapted from www.shutterstock.com) (b) aquatic Sponges animals; (Image adapted from https://kknews.cc/science/remzvjr.html) (c) SEM image of alveolar tissue in mouse lung. (Image adapted from https://fineartamerica.com/featured/2-mouse-lung-sem-david-phillips.html)

Due to the porous nature, porous polymeric materials have been actively used for various applications such as adsorption of greenhouse gases,[18-23] gas separation,[24-30] catalysis,[31-36] energy storage,[37-45] proton conduction,[46, 47] semiconductor,[48-54] photocatalysis, photoluminescence,[55-68] solar cells,[69] enantiomeric separation,[70-71] drug delivery,[72] iodine intake[73, 74] and so on. The above applications and constant exploration led the research field of porous polymeric materials having a huge impact on industry and academics.

Among all porous polymeric materials, porous organic polymers (POPs) having combined advantages of porosity and processability, received great attention due to their easily designed well-defined pores and very high surface area.[75-77] POPs can be easily processed to produce molded monolith[78-80] or thin films.[81, 82] Further, solvent processability of these materials provides an advantage to cast the large flexible membranes without hampering the intrinsic porosity of the porous polymer[83-85] which is nearly impossible in the case of other inorganic/hybrid porous structures. The chemical and physical properties of POPs can easily be fine-tuned *via* rich organic synthetic tools.[75, 86-88] For example, functionalization of the porous polymer can produce a stimuli-responsive characteristic, thus altering the pore structure reversibly[89-92] or opening and closing of the pore with external changes.[93, 94] These characteristics are hard to find in other porous polymeric materials. These advantages of POPs mark them as unique, where they should be recognized among different segments of porous polymeric materials and will be discussed in detail in the following sections.

1.2 Classification of Pores:

The porous polymers are polyhydrocarbons having voids or pores. These voids can be of two types according to the IUPAC recommendations,[95] namely open and close pores. Open pores are that which connect its opening to the outer surface at both ends and closed

pores are isolated voids in polymeric structure not connected to other pores. For example, in Figure 1.2a pore 1 and 2 are open pores, and pore 3 and 4, show close pores. As far as practical applications are concerned, researchers are interested in open pores as they provide a dynamic medium for the interaction between the external environment and the internal surface area of porous materials (PMs). Figure 1.2b provides an example of a synthetic porous material having open pores.
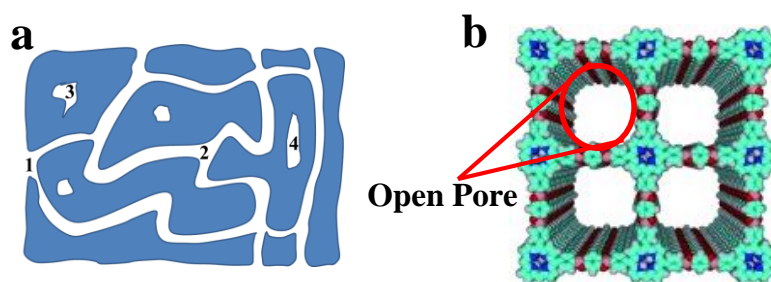
Figure 1.2: (a) Schematic representation of the cross-section area of PMs showing open and closed pores; (b) Illustration of a synthetic PMs having open pores. Reproduced (adapted)/Reprinted with permission from reference [100]. Copyright © 2007 John Wiley & Sons, Inc.

1.3 Classification of Porous Organic Polymers:

Based on the size of these open voids, POPs divided into three categories namely, microporous <2 nm, 2 nm <mesoporous <50 nm, and 50 nm < macroporous.[95, 96] Apart from the pore size, there are many unique structural features of porous polymers like the pore structure, functionality, composition, and topology,[97-99] which play a crucial role for the specific applications. Pore geometry includes sphere shape, tube shape, and complex network-types that can be ordered or disordered depending upon the choice of monomer and the synthetic procedure. Further, the specific surface area of the PMs is closely related to the pore size as it was seen that smaller pores are known to produce the PMs with the high surface area. Along with physical topology, the chemical composition also

plays an important role.[101] Chemical composition of the pore walls can be easily tailored either *via* a selection of monomers with desired functionality or through the post-synthetic functionalization of pores.[102-106] The ability to control the pore size and functionality through well-developed organic synthetic procedures has made POPs take the spotlight in the world of porous materials.

In general, POPs can be classified into two major categories: crystalline and amorphous POPs. The next sections discuss these two categories in detail.

1.3.1 Amorphous Porous Organic Polymers:

The polymers having pores in a disordered manner are known as amorphous porous polymers. Due to the flexibility of using nearly all the chemical reactions and no specific requirement of the organic building units, they are the major stockholders among all the POPs. Tremendous efforts have been made to design and synthesize the amorphous POPs for various applications, especially on gas adsorption/separation and heterogeneous catalysis. Based on the frameworks and topology amorphous POPs can be subdivided into hyper cross-linked polymers (HCPs),[107] polymers with intrinsic microporosity (PIMs),[108, 109] conjugated microporous polymers (CMPs)[110] and porous aromatic frameworks (PAFs).[76]

1.3.1.1 Hyper-Cross-Linked Polymers (HCPs):

HCPs, an important class of amorphous POPs awarded with high surface areas, microporosity, and low-density were the first synthetic POPs among all POPs.[111-113] The various synthetic advantages of HCPs such as very mild conditions and low-cost reagents[79, 114] provides an easy scale-up opportunity for practical applications. Further, the properties like apparent swelling, high chemical and thermal stability reasoned with a high degree of the cross-linked structure made them a potential candidate for gas
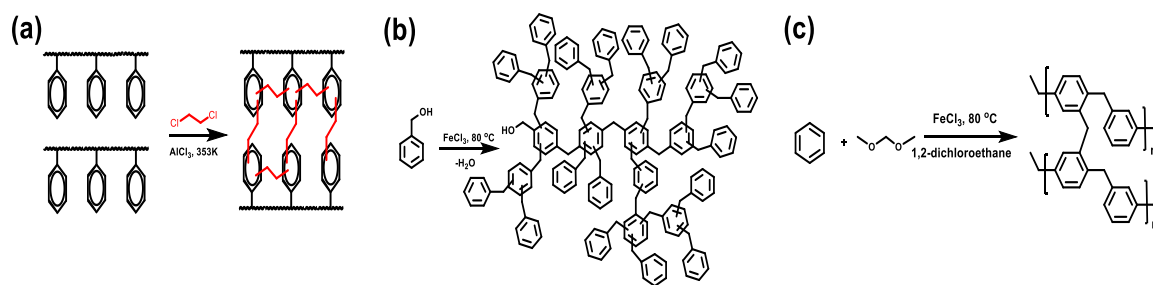
Figure 1.3: Schematic representation of the HCPs synthesis process *via* (a) post-cross-linking of polymers. Redrawn from Ref. 119; (b) One-step polycondensation. Redrawn from Ref. 120; (c) Cross-linking using an external cross-linker. Redrawn from Ref. 121.

storage/adsorption, catalysis, selective in-take of aromatic molecules from water, etc. There are three main synthetic routes available for the construction of HCPs namely: (1) post-cross-linking of organic polymer chains (Figure 1.3a); (2) one-step polycondensation of functional monomer (Figure 1.3b), (3) cross-linking *via* external cross-linkers (Figure 1.3c).[114] In the post-cross-linking method, a polymer that could cross-link was dissolved in a solvent to produce a solvent polymers matrix where solvent occupies a space produced between the untangled polymer chains. Now, this polymer-solvent matrix was subjected to the cross-linking process. Cross-linking helps to hold the polymers matrix upon the removal of the solvent to provide an interlinked porous polymer with voids.[115] Davankov et al. in the late 1960s reported the first HPC using the polystyrene as the precursor polymer and made a substantial contribution to this area of research.[107] On the contrary, post-cross-linking technique, the second method, doesn't require any precursor cross-linkable polymer and is synthesized *via* direct condensation of a small monomer. The direct one-step polycondensation technique provides an opportunity to use a large variety of diverse organic molecules available for condensation chemistry to produce different HCPs with various properties.[116] The Cooper group first demonstrated the successful synthesis of HCPs as a monolithic block *via* this technique and showed its

application in enhancing the volumetric storage of methane.[79] The third method provides the advantage of being comfortable with nearly all the aromatic monomers without any prior modification. Its controlled micromorphology involves knitting of small monomeric organic aromatic motifs with external cross-linkers. Tan et al. synthesized the first HPCs through this method in 2011.[117] Further, the Cooper group have used this method for the synthesis of HCPs with excellent CO_2 adsorption capacities under dry conditions.[118]

1.3.1.2 Polymers with Intrinsic Microporosity (PIMs):

The porosity in PIMs is a direct consequence of the inefficient packing of polymer chains due to "awkward" rigid macromolecular geometry.[122-125] PIMs were first reported by McKeown et al. in 2002. PIMs are generally prepared by reacting specially designed building blocks like A (Figure 1.4a) and B (Figure 1.4b). These can further combine efficiently through double-aromatic nucleophilic substitution (Figure 1.4c) to produce a rigid structure like dibenzodioxin linkage shown in Figure 1.4d.[126-130] A series of PIMs were prepared to have intrinsic microporous character and conjugation through a polymer backbone.[131] PIMs differs greatly from other POPs in the sense of having microporosity without cross-linking. However, they share a brotherhood with the CMPs because of its extended conjugation. In addition to the conjugation and porous nature, lack of cross-linking makes them soluble/dispersible in organic solvents. Due to this soluble/dispersible nature, PIMs can be cast into membranes, which justifying their high demand in the industry. Besides processability, scalability is another issue that should be addressed for the industrialization of any product. In this respect, recent developments in the synthetic procedures, where PIMs can be synthesized *via* solvent-free mechanical grinding offers a benefit of the quick synthesis.[132, 133] Their vast applications as pervaporation membranes,[134, 135] organic solvent nanofiltrates,[136, 137] gas separation membranes[138-142] and

sensors,[143-145] drives their research area to focus on developing more applications along with enriching current properties.[146-148]
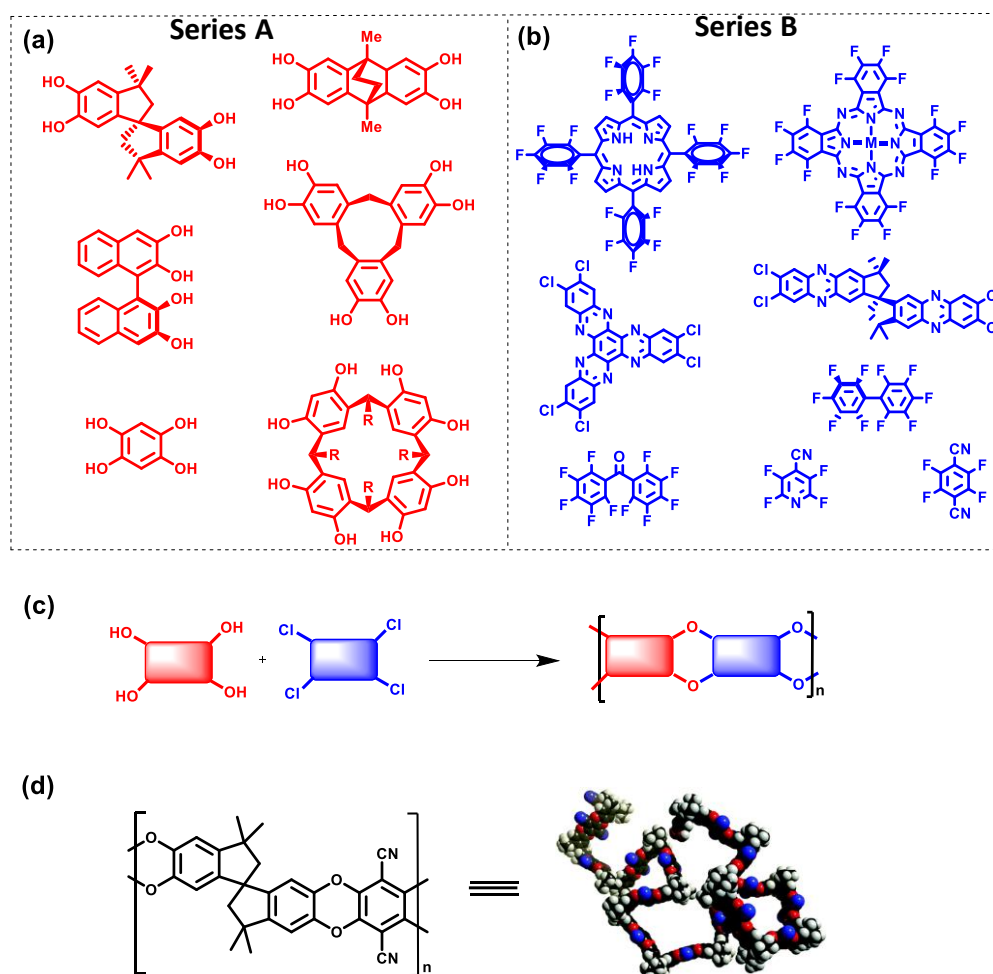
Figure 1.4: (a) Type of A-type building units of PIMs; (b) Type of B-type building units of PIMs; (c) Schematic representation of double-aromatic nucleophilic substitution of A and B; (d) Chemical structure and modeling of PIM-1. Reproduced/Adapted from Ref. 149 with permission from The Royal Society of Chemistry.

1.3.1.3 Porous Aromatic Frameworks (PAFs):

This category of POPs came into the limelight with the report published by Qiu et al. in 2009. Qiu et al. demonstrate the synthesis of PAF-1 with an exceptional surface area of 5600 m^2g^{-1} and with good thermal and chemical stability (Figure1.5a, b).[76, 171]
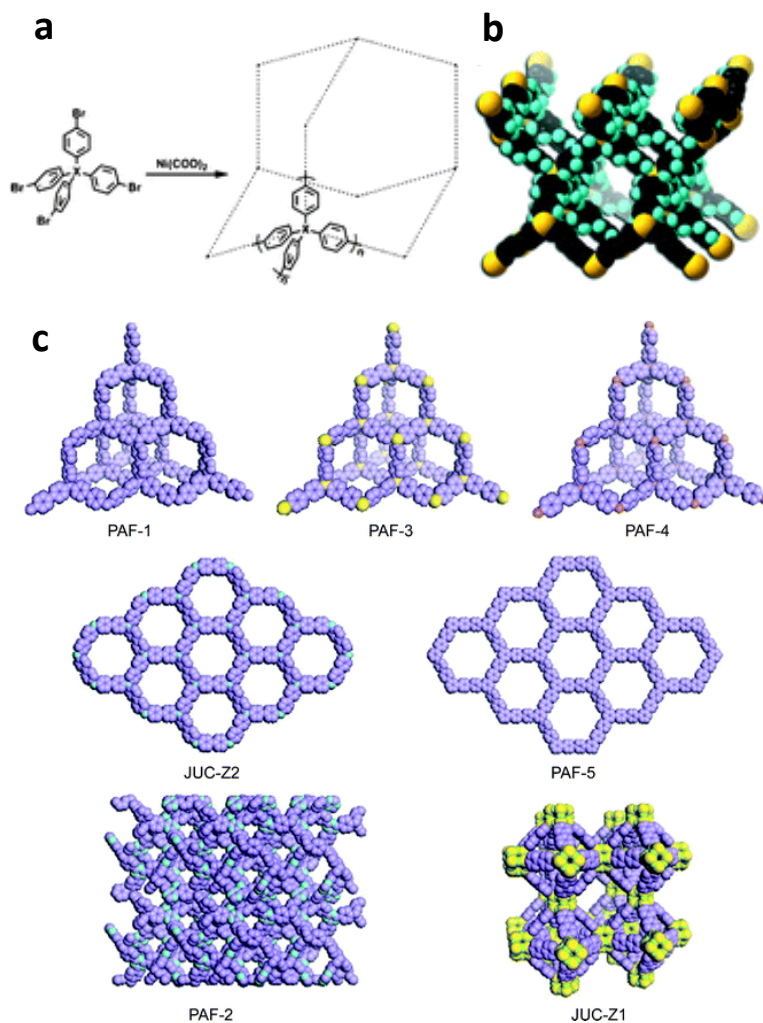
Figure 1.5: (a) Synthetic route for PPN-3 (X: Adamantane), PPN-4 (X: Si), PPN-5 (X: Ge), and PAF-1 (X: C). b) The default non-interpenetrated diamond-like network of PPN-4 (black, C; pale grey, H; grey, Si). (a and b are Reprinted with permission from reference [171]. Copyright © 2010 John Wiley & Sons, Inc. (C) Structure model of synthesized and simulated PAF. (C, purple; N, blue; Si, yellow; O, green; Ge, brown). Reproduced/Adapted from Ref. 172 with permission from The Royal Society of Chemistry.

In general, PAFs are open aromatic frameworks with a very high surface area due to the unique molecular structure of its building units along with the synthetic reaction condition used for synthesizing them. These monomers are linked together through the carbon-carbon bond to produce a thermally and chemically stable rigid phenyl framework. PAF-1

has a framework similar to diamond, where carbon-carbon bonds in the diamond structure were replaced by the rigid aromatic ring, which was connected *via* covalent bonds through nickel (II) catalyzed Yamamoto-Ullman cross-coupling reaction. Compared to other C–C coupling reactions such as Sonogashira–Hagihara cross-coupling,[150-159] Suzuki cross-coupling,[160-169] and Yamamoto coupling efficiently remove the terminal halogen group. This unique feature of Yamamoto coupling results in ultra-high porous solids, as the unreacted halogen atom reduces the surface area to some extent. Further, Yamamoto coupling typically is an aryl-aryl coupling of haloarenes, which requires a halogen-functionalized building unit, thus offers a simple method for synthesis of CMPs, PAFs, etc. Considering the simplicity of the functionality of the monomer unit, a variety of PAFs have been synthesized using different building blocks. Figure 1.5c shows few representative examples of PAFs.[59, 170, 172] The PAFs differ from CMPs in the sense of conjugation, as PAFs lose conjugation due to the tetrahedral central atom of the monomers, whereas CMPs possess conjugation throughout the framework. The ease of post-synthetic functionalization of pores extends their scope of various applications. Recently, a large number of PAFs have been reported for the application in gas storage, heterogeneous catalysis, and selective adsorption such as CO_2, CH_4 etc.[23]

1.3.1.4 Conjugated Microporous Polymers (CMPs):

Conjugated microporous polymers (CMPs) are POPs having conjugation throughout the polymer backbone with the advantages of microporosity as well as mesoporosity which makes them a versatile tool for light-harvesting,[61, 173] heterogeneous photocatalysis[58, 59, 174] gas storage,[173, 188-190] chemical entrapping[170, 191-194] and chemo-sensing.[66, 68, 195]

The word conjugation came from the Latin word *conjugatus*, which means to join. Conjugated polymers (CPs) are carbon-based macromolecules having alternative single and π-bonds along the polymer's backbone. Due to the resonance, the π-electrons are

delocalized, hence, generating an electron current along the polymer chain. Some examples of linear CPs have given in Figure 1.6.
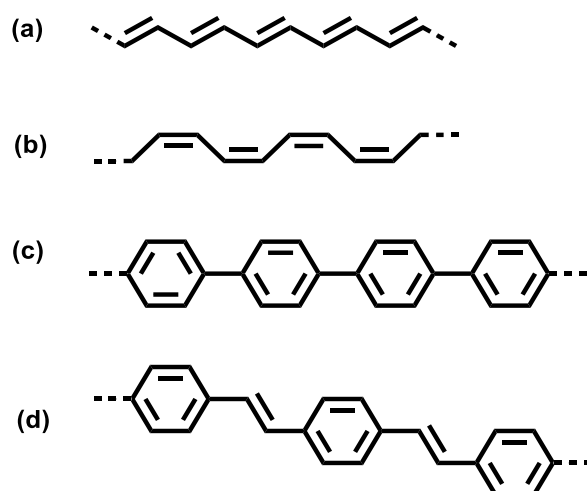
Figure 1.6: Chemical structure of (a) Cis-polyacetylene; (b) trans-polyacetylene; (c) poly(para-phenylene); (d) poly(para-phenylene vinylene).

Shirakawa, Heeger, and MacDiarmid were awarded the Nobel Prize in 2000 for their work on Conjugated Polymers in 1977. They saw that polyacetylene films when doped with iodine vapor showed a tremendous increase in conductance covering the range of 10^{-14} Siemens, exactly between the semiconductor to the metal conductance range (Figure 1.7). Since then owing to their high conductivity and optoelectronic properties (combined with their mechanical properties and intrinsic processing advantages) they paved the way for their various applications like light-emitting devices,[196-198] nonlinear optical devices,[199, 200] photovoltaic devices,[201, 202] plastic field-effect transistors[203, 204] and electromagnetic shielding.[205] The bandgaps of CPs range from 1.5 eV to 3 eV, allowing these polymers to absorb photons from visible light and near-infrared.[206] This property makes them the best organic candidate for light-harvesting materials as the majority of sunlight consist of visible and near-infrared light.
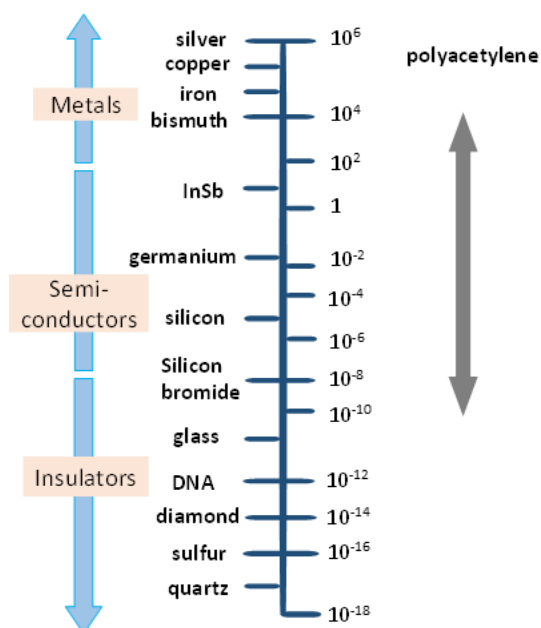
Figure 1.7: Conductivity (Siemens) Range covered by doped polyacetylene in comparison with other materials. Redrawn from Ref. 206.

Like most of the CPs, CMPs are generally synthesized from rigid aromatic monomers. However, CMPs are cross-linked conjugation polymers to produce porous structures. Due to the rigidity of the monomer and cross-linking, CMPs are insoluble amorphous polymer networks.[110] However, their solubility can be improved *via* introducing the bulky side groups which give an advantage of solvent processability. [189, 207] Depending on the targeted applications, the chemical and physical properties of CMPs can be tailored by various methods. The pore size and surface area of CMPs can be easily tailored by choosing the linkers with the appropriate length. [208] Other methods like varying the reaction solvent[171, 209] or using templating methods[187] can also be used to change the pore volume[75, 110, 190, 187, 209, 210-212] and the surface area[75, 110, 171, 187, 190, 209, 211, 213, 214] while keeping the bandgap as such. The specific energy levels (HOMO-LUMO) and bandgap (energy difference between HOMO-LUMO) are the crucial parameters when CMPs are used as photoactive materials for specific applications. Mostly homopolymers have a fixed bandgap. The CMP with the desired bandgap with band position can also be

17

designed *via* choosing different electron donor-acceptor combinations.[215] In this case, the donor means an electron-rich molecule, while an acceptor is an electron-deficient one. It must be noted that donor moiety will affect the HOMO level and the acceptor moiety will affect the LUMO level of the CMP.[215] In Figure 1.8, this designing concept for CMPs along with bandgap position is displayed**.** Further, as reported by using the statistical copolymerization scheme, three-component CMPs can also be prepared with good control of porosity and bandgap. Several recent reviews on CMPs provide an excellent overview of the synthesis and property-control techniques of these unique materials.[216, 217]
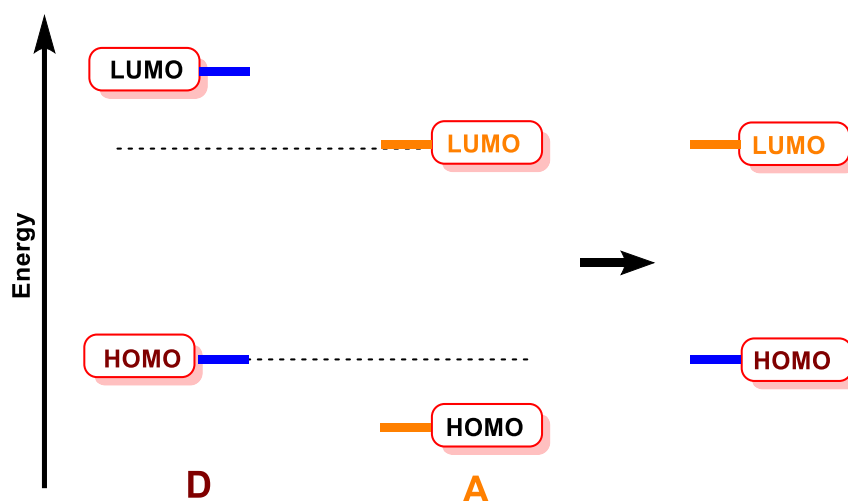
Figure 1.8: HOMO and LUMO levels in a donor-acceptor based system.

1.3.1.4.1 Synthesis of CMPs:

The conductivity and unique electrochemical properties of CMPs,[218-221] highly depend on the mode of conjugation, effective conjugation length, stereo-regio regularity and characteristics of the substituents in the polymers. The synthesis of CMPs has been mainly done *via* the oxidative coupling of heteroatom-containing aromatic rings.[222] However, these methods are not very useful in the presence of monomers having bulky substituents because they generate highly irregular frameworks. On the other hand, the transition-metal-catalyzed cross-coupling methods generally known to produce well-

defined polymers with good regioregularity.[223-225] Some common cross-coupling reactions include Migita-Kosugi-Stille, Kumada-Tamao-Corriu, Suzuki-Miyaura, Negishi, Sonogashira-Hagihara coupling, etc. The focus will be placed on the Suzuki-Miyaura coupling and Sonogashira-Hagihara oxidative coupling are mainly used in this thesis for CMP synthesis which are discussed below.

1.3.1.4.1.1 Suzuki-Miyaura Coupling:

Suzuki and Miyaura reaction was developed in 1979[226, 227] and well adopted by the chemist because of the advantages it brings, i.e., the stability of starting reactant toward

$$Ar_1\!\!-\!\!X \quad + \quad Ar_2\!\!-\!\!B(OH)_2 \quad \xrightarrow[\textbf{Base}]{\textbf{Pd cat.}} \quad Ar_1\!\!-\!\!Ar_2$$
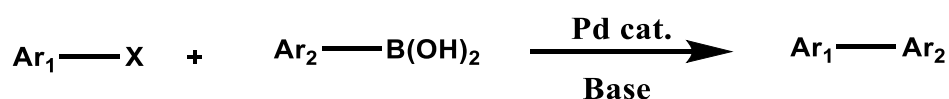
Figure 1.9: Reaction scheme of Suzuki-Miyaura coupling.
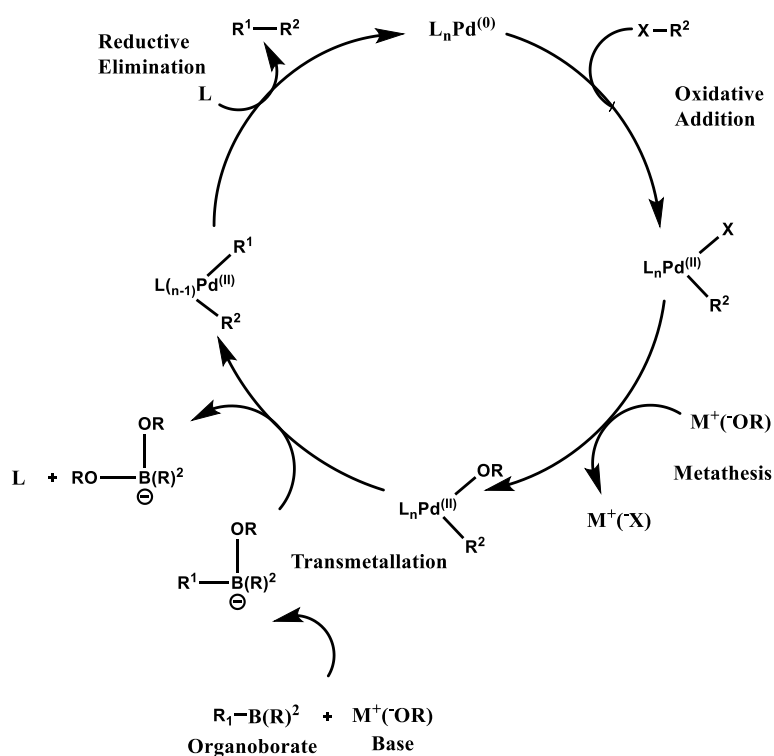
Figure 1.10: The mechanism of the Suzuki cross-coupling reaction. (Redrawn from Ref. 228).

19

moisture and high temperature; high tolerance towards various functional groups; low toxicity of the by-products. Figure 1.9 shows the general reaction scheme of Suzuki-Miyaura coupling.

In general, most metal catalysed cross-coupling reactions are known to go through mainly three steps; (1) step oxidative addition, (2) transmetalation and (3) reductive elimination. The mechanism of the Suzuki-Miyaura coupling is similar to the catalytic cycle for other cross-coupling reactions as given in Figure 1.10. However, the role of the base and the exact mechanism is still debatable.

1.3.1.4.1.2 Sonogashira-Hagihara Coupling:

Sonogashira and Hagihara have first reported the protocol for this coupling in 1975.[151] In a typical method terminal alkynes and aryl/alkyl halides are cooked together in the presence of palladium catalysts and cuprous iodide (CuI) to produce the C-C bond. Several advantages like very mild reaction conditions, retention of stereospecificity, stereochemical information of the substrates and no requirement of the moisture-free environment made this reaction all-time favorite for researchers and industry. The general reaction scheme for Sonogashira-Hagihara Coupling is presented in Figure 1.11.

$$R^1 \!\!-\!\! X \;\; + \;\; H \!\!=\!\! R^2 \quad \xrightarrow[\text{Cu(I)-salt/base/solvent}]{\text{Pd-Catalyst}} \quad R^1 \!\!=\!\! R^2$$
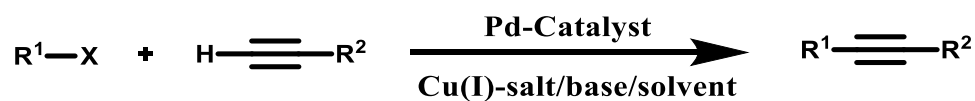
Figure 1.11: Reaction scheme of Sonogashira-Hagihara coupling.

Similar to Suzuki cross-coupling reaction, the mechanism of Sonogashira cross-coupling (Figure 1.12) follows the general oxidative addition-reductive elimination pathway.[229-231] However, the structure of the catalytically active species and the exact role of the copper (I) catalyst is still not clear.
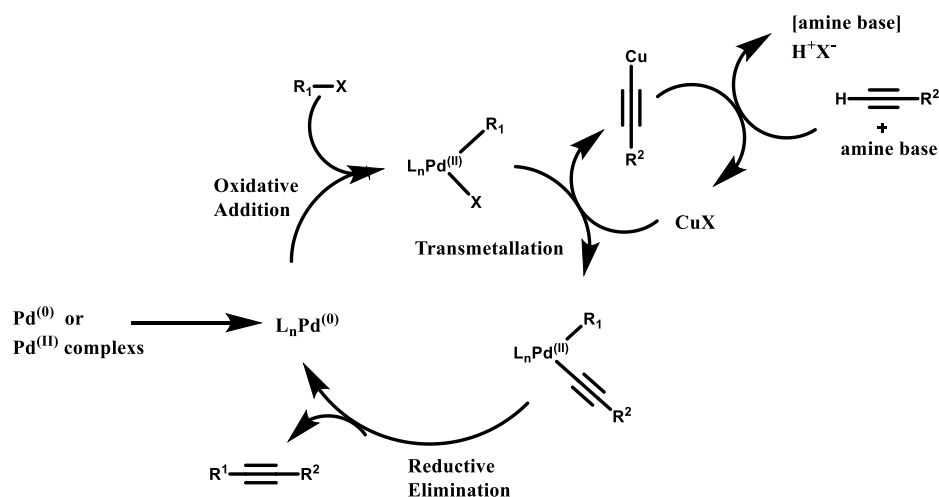
Figure 1.12: Reaction mechanism of Sonogashira-Hagihara coupling. (Redrawn from Ref. 228).

1.3.1.4.2 CMPs as Visible-light Photocatalysts:

It is a well-known fact that nearly 44% of solar energy fall in the visible region of the solar spectrum. Thus, the photocatalysts harvesting the visible light are highly desirable to trigger the chemical transformations. Recently, visible-light-induced photo-redox catalysis using iridium or ruthenium complexes and dyes have shown successful results in a variety of chemical transformations.[232-241] However, their intrinsic drawbacks like high cost due to the scarcity of rare metals, environmental concern due to potential toxicity are the major issues yet to be addressed. These shortcomings of metal-based photocatalysts are the main driving forces to the development of visible-light-driven metal-free photocatalysts. A variety of organic chromophores and dyes were successfully employed as photo-redox catalyst. Although these chromophores and dyes are easily available and commercially viable, the recyclability due to photo-bleaching in addition to the cost of post-reaction removal of the catalyst makes them non-feasible for large scale industrial applications. To address these drawbacks, it is necessary to design and develop metal-free insoluble visible light absorbing photocatalysts with high stability.

In this respect, along with the various applications mentioned in section 1.3.1.4, CMPs with permanent high porosity, photoactive structure, high thermal stability, and high flexibility are the centre of attraction to explore them as photocatalysts. The scope of CMPs as photocatalysts are much wider because their optoelectronic properties can be easily engineered at the molecular level with the help of rich organic chemistry tools.

There are multiple strategies to design the CMPs photocatalyst: First, CMPs with defined energetic levels can be used as heterogeneous photocatalyst whose bandgap can be easily tuned by smartly choosing the building blocks.[174, 184, 185, 187] In the second approach, an already established photocatalyst can be used as a precursor to synthesize the CMPs. The second strategy not only helps in stabilizing the homogeneous catalysts form photobleaching but also provide an advantage of the easy post-reaction separation of photocatalyst.[59, 175-177, 180] Considering these advantages, a series of CMP based photocatalyst were reported to carry out various chemical reactions such as molecular oxygen activation, oxidation of organic sulfides, dehalogenation, carbon-carbon bond formation, oxidative hydroxylation aryl boronic acids, cationic polymerization, and hydrogen evolution.

1.3.1.4.2.1 Photocatalytic Mechanisms:

To play the role of a photocatalyst (PC) the catalytic material should be photoactive i.e. it should achieve a photo-excited state (PC*) on absorbing a photon with energy equal to its bandgap. This photon energy stored in the PC* can be transferred to a reagent R_1, converting it into an active species R_A and deactivate the photocatalyst (PC_D).[242] This active reagent attack on another reagent R_2 to form a reaction intermediate (R_B). This intermediate R_B finally reacts with the PC_D to result in the product and regenerate the

photocatalyst in its original ground state.[242] Figure 1.13 represents the general process of photocatalysis.
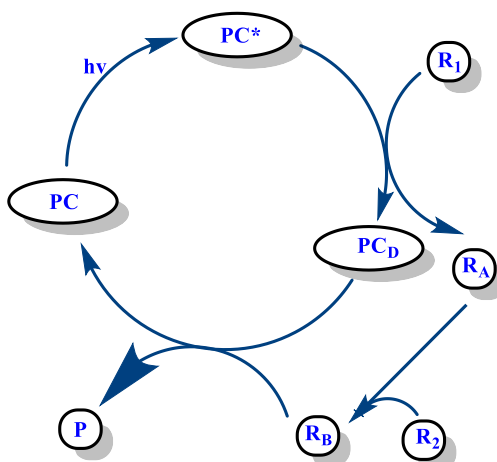
Figure 1.13: General process of photocatalytic process. Redrawn from Ref. 242.

An ideal visible light photocatalyst should fulfil two criteria to drive a chemical conversion efficiently: (1) it should have a bandgap low enough to promote the electron from HOMO to LUMO by absorbing in visible spectrum (Figure 1.14) and (2) the oxidation potential (E_{ox}) or reduction potential (E_{red}) of the reagent should be aligned in accordance to facilitate the oxidation or reduction process. The E_{ox} of the reagent should be slightly higher than the HOMO level of the PC to use the PC materials for oxidation
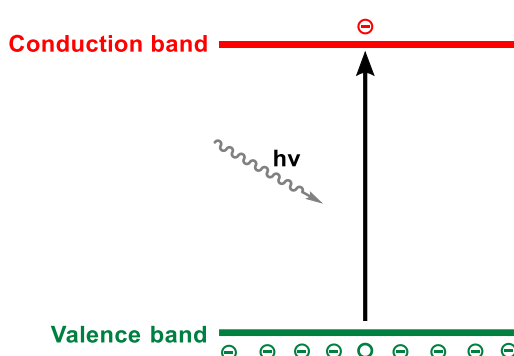
Figure 1.14: Light-induced excitation in a semiconducting material.

reaction, however, in the case of the reductive process, E_{red} should be lower than LUMO in respect to the standard/ Nernst hydrogen electrode scale. In this respect, CMPs can be

the best candidate for photocatalyst as their bandgap as well as the position of HOMO-LUMO can be finely tuned by choosing the appropriate Donor-Acceptor and the extent of conjugation for any particular chemical conversion.

1.3.2 Crystalline Porous Organic Polymers:

As compared to the amorphous POPs, crystalline POPs are very limited. There are two main reasons for this: one is the requirement of monomers with high symmetry and rigidity, which is limited due to the less availability of such monomeric units. Next to link these building blocks together kinetic-reversible-reactions are must produce crystalline framework, which again narrowed the options as a few reversible chemical reactions (i.e., imine condensation/metathesis, boronic acid self-condensation, boronic acid-diol condensation, etc.) qualify on this scale. These specific reactions would allow "error-correction" during the reaction, which helps in the formation of more ordered and thermodynamically stable frameworks. Recently crystalline POPs gained great attention due to their long-range order with regular and uniform pore structures and broadly divided into two categories namely covalent triazine frameworks (CTFs) and covalent organic frameworks (COF), which are discussed below in detail.

1.3.2.1 Covalent Triazine Frameworks (CTFs):

Thomas and group reported the first CTF in 2008 *via* trimerization of cyano group-containing organic molecules in molten zinc chloride ($ZnCl_2$) at high temperature (400-700 °C) as shown in Figure 1.15.[243-245] At this high-temperature, $ZnCl_2$ melts and act as a solvent as well as the catalyst. Thomas et al.[245] synthesized a series of CTFs by using di- or tri-cyano functionalized small organic molecules with good crystallinity and permanent porosity. The reaction conditions like temperature, reaction time and amount of $ZnCl_2$

catalyst along with the structure of monomer are the crucial factors, which are responsible for the properties and framework structure of CTFs.[246]
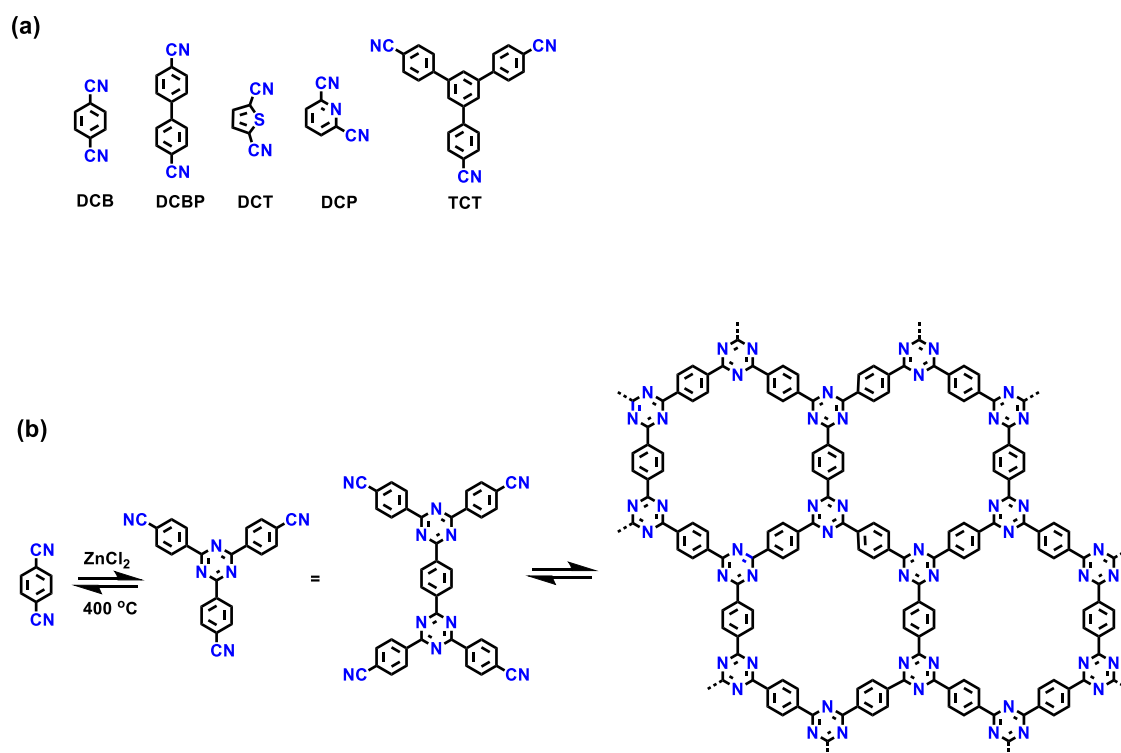
Figure 1.15: (a) Cyano based building blocks, (b) Synthesis of triazine frameworks. Redrawn from Ref. 245.

The above synthesis doesn't require any precious metal catalysts and thus can be easily scalable. However, it suffers from some serious drawbacks like long reaction time, high temperature and complete post-reaction separation of $ZnCl_2$.[247] To remove these obstacles, Cooper and the group put effort to perform the trimerization reaction at room temperature and in microwave heating condition by replacing the $ZnCl_2$ with trifluoromethanesulfonic acid (catalyst). Very low order crystallinity was obtained using microwave heating conditions, whereas polymer obtained at room temperature was amorphous. Later, Martinez-Alvarez and group have used trifluoromethanesulfonic anhydride for trimerization of nitrile group and showed significant mild reaction conditions for the CTFs synthesis.[248] CTFs are connected through strong triazine moieties,

which make them physiochemically stable and can be efficiently used for gas adsorption and separation. More recently, they are also explored as heterogeneous catalysts[249] and fluorescent materials, etc.[247]

1.3.2.2 Covalent Organic Frameworks (COFs):

COFs are crystalline porous organic frameworks devised through the reticular chemistry using kinetically reversible reactions. The very first COF was reported by Yaghi *et al.* in 2005. Since then, due to their controlled predefined structures and pores, COFs became the center of attraction among all the POPs.[9] Unlike other POPs, chemical and physical

(a)   **(b)**

COF-5   Pc-PBBA COF

(c)   **(d)**

$D_1 = 26.9$ Å
$D_2 = 7.1$ Å

COF-108   Dual-Pore COF
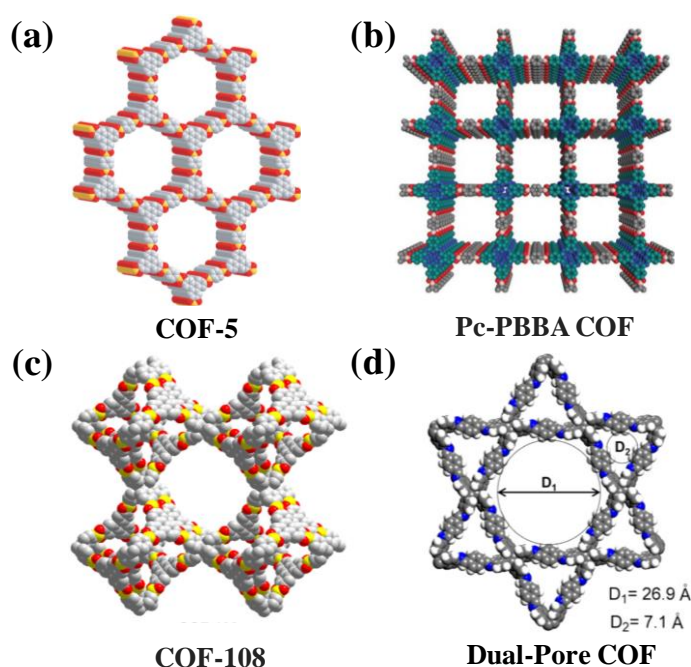
Figure 1.16: (a) COF-5, Reprinted with permission from Ref. 9. American Association for the Advancement of science; (b) Pc-PBBA COF, Reproduced (adapted)/Reprinted with permission from reference [293]. Copyright © 2016 John Wiley & Sons, Inc.; (c) COF-108, (d) Dual –Pore COF. Reprinted with permission from Ref. 77. American Association for the Advancement of science.

properties of COFs can be easily tuned *via* synthesis offered positional control over their building blocks resulting in the porous structures with high regularity. The defined nano-channels and open voids in COF are an excellent environment for storage, separation, sensing and catalysis applications. Further, to well-connected and well-arranged organic units make the COFs potential candidates for the verity of applications depending on charge carrier mobility, which includes electrochemical energy storage and optoelectronics. Figure 1.16 provides the example of a few representative COFs.[9, 77, 293, 294]

1.3.2.2.1 Synthesis of COFs:

To design a crystalline COF mainly two conditions should be followed strictly; one is the selection of the monomer and synthetic procedure. First, the building blocks should possess high symmetry with good rigidity. In a COF synthesis, the structure of the framework is highly related to the symmetry of rigid building blocks. Figure 1.17 shows the structure of the resulted COF corresponding to the combination of the linker with different symmetry.
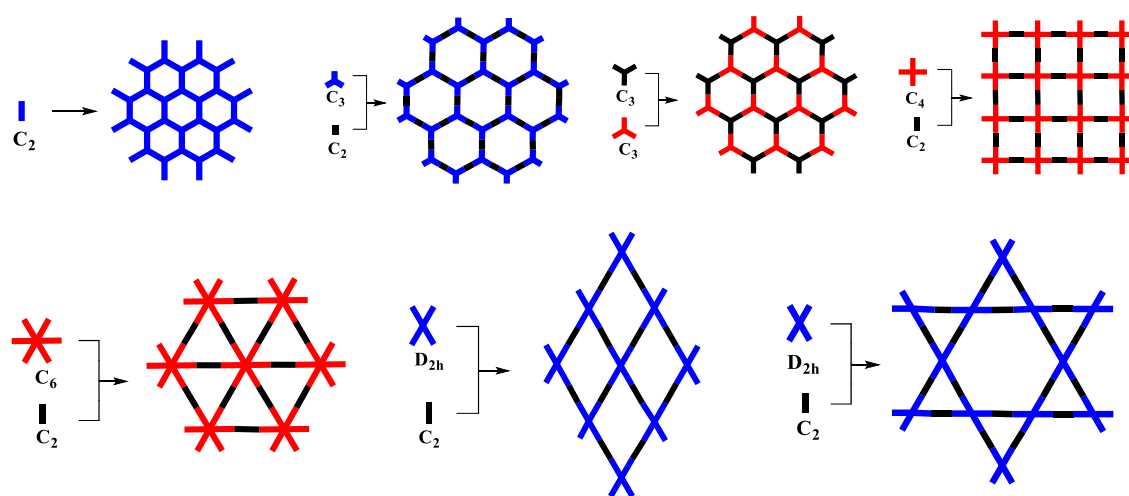
Figure 1.17: COF framework structure resulted from the combination of different linkers with different geometries. Redrawn from Ref. 245.

As shown in Figure 1.17, the combination of trigonal planar linkers will produce the hexagonal pores and condensation of tetragonal linkers with linear linkers result in tetragonal pores and so on. Further, these 2D sheets stack on each other *via* π-π stacking to generate a layered structure with nanochannels, named as 2D COFs. However, 3D COFs are formed *via* condensation of the linkers having functionality in three dimensions, resulting in 3D network.
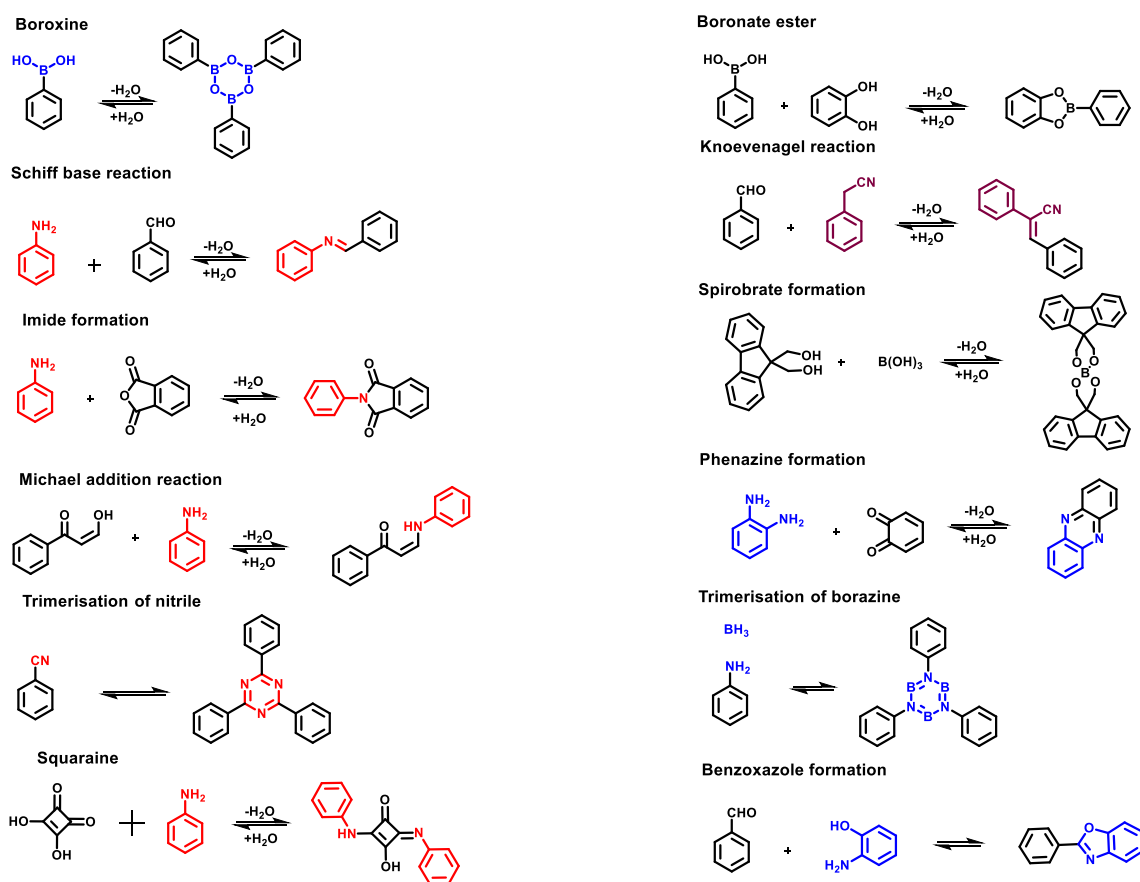
Figure 1.18: Various reversible organic reactions to produce different linkages-based COFs.

The second requirement demands the reversible coupling reaction to link these symmetric building blocks covalently to form an ordered framework. The reversible nature provides an advantage of error correction *via* backward and forward reaction mechanism to produce the thermodynamically stable product rather than kinetically driven amorphous

polymer. Yagi et al. produced the first crystalline COF *via* co-condensation of boronic acids with catechols through reversible boronic ester-linkage.[9] The drawbacks of these boronic ester-based COFs are sensitivity toward moisture and very less chemical stability led to the discovery of alternative coupling reaction which can produce the ordered framework. A pool of various reactions has been successfully used to synthesize the COF which is given in Figure 1.18. Besides, the boronic ester linkages, imine linkages resultedfrom the condensation of aldehydes and primary amines are vastly used in the synthesis of COFs due to their relatively increased tolerance toward moisture as compared to the boronic ester linkages. Further, to produce the chemically stable COFs, various strategies like increasing the hydrophobicity,[250-254] decreasing the nucleophilicity of the imine bonds,[41 255-260] improvement of the interlayer stacking,[33, 261-267] and post-synthetic modification,[266] were applied successfully *via* smartly choosing the building blocks.

1.3.2.2.2 COF as Sensors:

In spite of their type, porous materials have always been explored for sensing applications due to their unique host matrices containing various functional species. The composition of the porous material, crystalline structure, surface area, functionalization, stability, and morphology are crucial parameters that affect the crucial sensing attributes, including sensitivity, selectivity, and response/recovery times.[51] In this respect, COFs possessing the above-mentioned attributes are the potential candidates for sensing applications.

1.3.2.2.2.1 COF as Electrochemical Sensor:

Electrochemical sensors produce the signals in the form of an electric parameter such as capacitance, resistance and conductance with the change in a chemical environment and are very important for agriculture, pharmaceutical and semiconductor industries,

climatology and geographic information system (GIS), and also for human comfort.[268-278] The schematic diagrams in Figure 1.19 show the device setup of a general electrochemical sensor. In general, an interdigitated electrode coated with a thin layer of the sensing substrate was connected to the electric interface to produce the electric signal, which was further connected to a display to convert this electric signal to visual signal or audio signal. In our group, for the first time we used COF as a substrate for the electrochemical sensing of humidity. Chapter 1 of this thesis deal with the Truxene based COFs and its application for humidity sensing application.
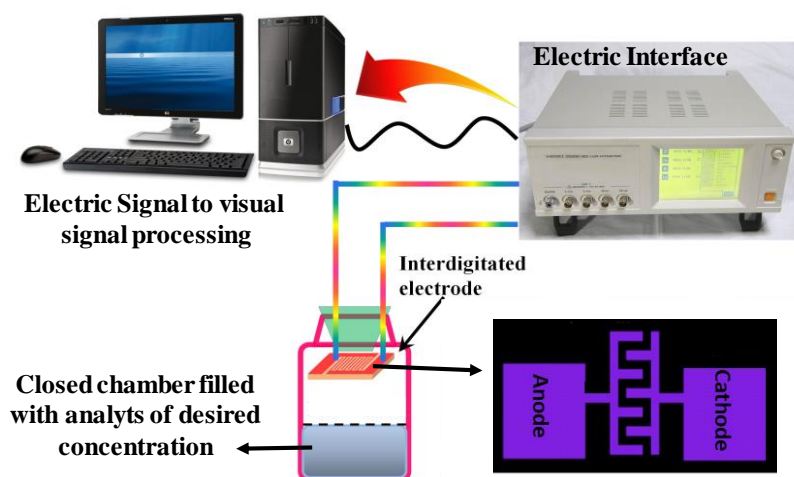
Figure 1.19: Schematic diagram represents a general electrochemical sensor set up.

1.3.2.2.2.2 COF as Chemosensors:

Chemosensors show changes in color or fluorescence intensity as a signal, when exposed to the targeted analyte. The efficiency of a chemosensor is judged by its response time and its detection limits. Many groups have reported the luminescent COFs for the detection of the nitroaromatic compounds via fluorescence turn-off mechanism.[279-283] Dalapati and group synthesized an azine linked COF, highly sensitive for potentially explosive picric acid in solution as well as in solid-phase.[67] Similarly, another group reported an imine linked pyrene-based 3D-COF and detection of picric acid by

fluorescence quenching up to 70% at a very low concentration of 20 ppm of picric acid (Figure 1.20).[279] In another work, imine linked azatruxene based luminescent COF was also reported which efficiently sensed the nitrobenzene, 2-nitrotoluene, and phenol *via* fluorescent turn-off mechanism and show the variation in luminescent intensity with
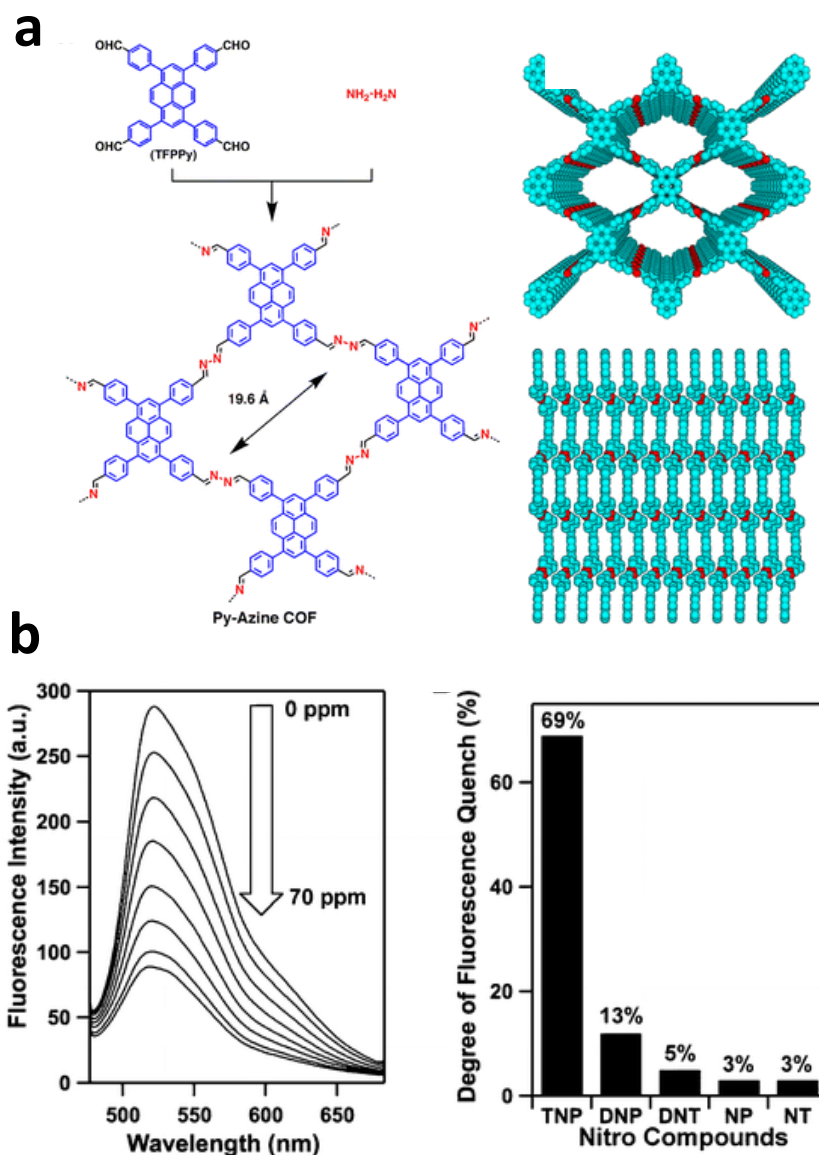
Figure 1.20: (a) Synthetic scheme of azine-linked COF; (b) Fluorescence quenching of the Py-Azine COF upon addition of TNP (0−70 ppm) in acetonitrile and % fluorescence quenching concerning different nitro compounds (70 ppm). Reproduced

(adapted)/Reprinted with permission from Ref. [67]. Copyright © 2013 American Chemical Society.

many other organic molecules.[280] The ketoenamine COFs produced *via* Michael addition-elimination reaction are also shown the sensitivity toward the peroxide- and nitro- based explosives with a detection limit of $\approx 1 \times 10^{-6}$ M for triacetone triperoxide due to the oxidation-reduction reaction between the of the enamine units of COF and analytes.[281] By exploiting the Lewis acid-base interaction between lone pair of ammonia and boronic ester bond, a boronic ester-linked COF was shown to efficiently sense the ammonia content down to 1 ppm (measured in toluene) *via* reducing its fluorescence intensity by 30%.[63] Beside sensing the organic molecules, COFs are also designed for metal sensing application. The hydrazine linked COF having the thio functionalized pendant chains in the pores was reported to sense the highly toxic Hg^{2+} ions in water *via* fluorescence turn-off mechanism (Figure 1.21). Due to the specific interactions between thiol group and Hg^{2+} ions, the reported COF can sense Hg^{2+} ions down to the concentration of 33×10^{-6} M in solution with 83% quenching efficiency. Further, this material can be reversibly used after removing the Hg^{2+} showing the recyclable nature of the material.[282] Another, azine-linked COF having its pore decorated with the chelating site was used for the detection of Cu^{2+} *via* fluorescence turn-off mechanism. This COF can also be easily recycled *via* removing the Cu^{2+} ions and can be reused again as a fluorescent Cu^{2+} detecting unit. Along with the strongest quenching effect with Cu^{2+}, COF also shows the smaller response toward Co^{2+}, Fe^{3+}, and Ni^{2+}.[283]

In comparison to the exponential growth of various COFs, only limited numbers of COFs are reported to date as chemosensors. The main reason behind this is that in spite of highly conjugated structures most of the 2D COFs are weakly fluorescent because of

"aggregation-caused quenching (ACQ)". This arises due to π-π stacked layers of 2D COFs, furthermore, due to poor electron mobility and ineffective interaction of inner active sites with analytes in aggregated p-stacked layers, bulk COFs exhibit only moderate chemical sensing ability.[298] This problem can be easily tackled out *via* exfoliation of the COF layers into the single sheet or up to a few sheets which are discussed below in the next section.
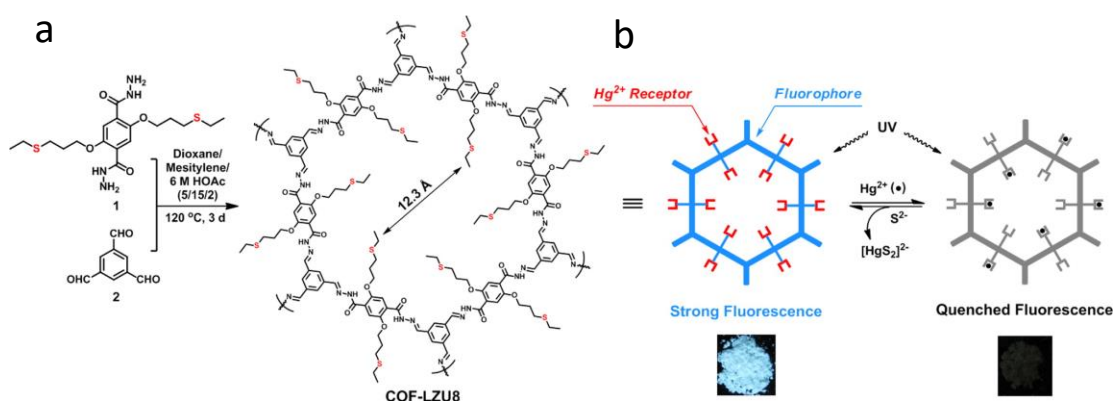
Figure 1.21: (a) Synthesis scheme of COF-LZU8 having the π-conjugated framework as the fluorophore and the thioether groups as the Hg^{2+} receptor. (b) Fluorescence emission of COF-LZU8 before (left) and after (right) the adsorption of Hg^{2+}. Reproduced (adapted)/Reprinted with permission from Ref. [282]. Copyright © 2016 American Chemical Society.

1.3.2.2.2 Exfoliation of COFs:

Impressed by blossoming technological impact of graphene exfoliation, exfoliated two-dimensional (2D) materials have been widely explored for their unique chemical and physical properties associated with their quantum sized effect at nanosized thickness.[284] Among all 2D materials, Covalent organic frameworks (COFs) are widely explored after Graphene, due to their tailorable structures and affordable functionalization at the molecular level.[285-290] Exfoliation of COFs is mainly dependent on the interlayer forces holding them like interlayer π–π interactions or in some cases additional hydrogen

bonding.[291, 292] Though, these forces are responsible for producing highly porous, crystalline, chemically and thermally stable structures for various applications.[293-295] However, there are some disadvantages associated with them like "aggregation-caused quenching (ACQ)" which arises due to π–π stacked layers, poor electron mobility and poor accessibility of interior active sites deeply buried inside the 1D resulting in channels cause the moderate performance of bulk COFs. The exfoliation of 2D COFs not only helps to reduce fluorescence turn-off phenomena, but also provides the well-exposed active sites for fast response and recovery for various applications as proved by recent reports.[296, 297] Many groups have adopted this approach to develop the COF based chemosensor and shown that the exfoliated COF show more efficient sensing as compared to the bulk COF.[298, 299] In literature, it was shown that exfoliation of imide linked porphyrin and 3,4,9,10-perylenetetracarboxylic dianhydride COF into nanosheets show a higher sensitivity with a quenching constant 1×10^{-7} M^{-1} for 2,4,6-trinitrophenol as compare to the bulk COF.[298] Similar results were also observed with exfoliated sheets of the COF TfpBDH (from pyromellitic N,N′-bisaminoimide, and 1,3,5- tris(4-formylphenyl)benzene) for the sensing of nitroaromatic compounds when compared with bulk COF (Figure 1.22).[299]

The exfoliation of COFs has been demonstrated in literature via various techniques like mechanical demolition,[257] chemical modification,[300, 301] ultra-sonification,[297, 302] and so on. One of the very innovative methodologies involves the choice of the ionic building blocks to construct the COF. These ionic moieties create an ionic repulsion between COF layers and favor the self-exfoliation of COF into single or few layers commonly called ionic covalent organic Nanosheets (iCONs).[303, 304] Due to their highly fluorescent property and well exposed active sites, iCONs can be efficiently used as a chemosensor for molecular recognition via fluorescence intensity variation or via color change and

provide a simple, sensitive and selective method for naked-eye detection of molecular entities.
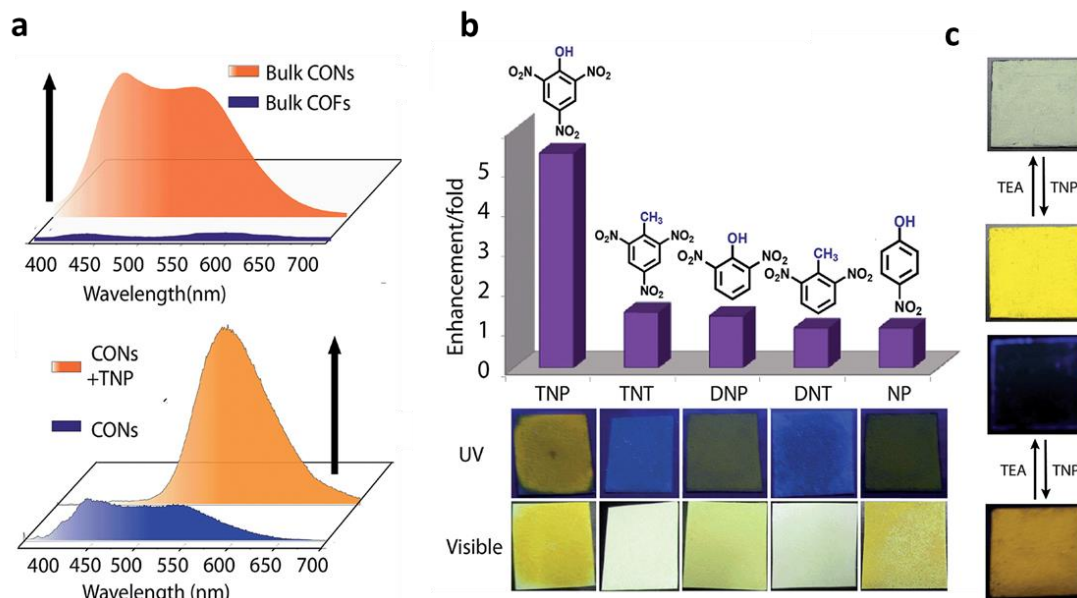
Figure 1.22: (a) Fluorescence spectra of bulk TfpBDH and exfoliated TfpBDH; (b) Fluorescence enhancement of CONs when exposed to different nitro compound (d and e) solid-state sensing (turn on) of TNP by CONs under visible and UV light (365 nm) with reversible color change from blue to yellow and *vice versa* upon TEA treatment. Reproduced/Adapted from Ref. 285 with permission from The Royal Society of Chemistry.

The research of this thesis work mainly focuses to explore the sensing and photocatalytic applications of newly designed crystalline and amorphous porous frameworks. **Chapter 2** of the thesis describes the design and synthesis of the first truxene-based covalent organic framework and its application in humidity sensing via electrochemical sensing methods. **Chapter 3** demonstrates the design and synthetic strategy to develop the luminescent covalent organic nanosheets (iCONs) along with its application for selective chemical sensing. **Chapter 4** presents the design and synthesis of truxene-based conjugated microporous polymer for harvesting the natural sunlight to drive the chemical

transformation. **Chapter 5** describes a strategy to tune the band gap and aligning the energy levels of the CMP to drive a specific visible-light-driven photocatalytic conversion via choosing a donor-acceptor combination. **Chapter 6** provides a brief summary of the thesis work.

References:

1. Whitesides, G. M.; Simanek, E. E.; Mathias, J. P.; Seto, C. T.; Chin, D.; Mammen M.; Gordon, D. M. *Acc. Chem. Res.* **1995**, 28, 37.

2. Wuest, J. D. *Chem. Commun.* **2005**, 0, 5830.

3. Palmer L. C.; Stupp S. I. *Acc. Chem. Res.* **2008**, 41, 1674.

4. Zang, L.; Che Y.; Moore, J. S. *Acc. Chem. Res*. **2008**, 41, 1596.

5. De Greef, T. F. A.; Smulders, M. M. J.; Wolffs, M.; Schenning, A. P. H. J.; Sijbesma R. P.; Meijer, E. W. *Chem. Rev*. **2009**, 109, 5687.

6. Zayed, J. M.; Nouvel, N.; Rauwald, U.; Scherman, O. A. *Chem. Soc. Rev*. **2010**, 39, 2806.

7. Corey E. J.; Cheng, X.-M. *Wiley-Interscience, New York* **1989**.

8. Thomas, A. *Angew. Chem., Int. Ed*. **2010**, 49, 8328.

9. Cote, A. P.; Benin, A. I.; Ockwig, N. W.; O'Keeffe, M.; Matzger A. J.; Yaghi, O. M. *Science* **2005**, 310, 1166.

10. Zhou, H. C.; Long, J. R.; Yaghi O. M. *Chem. Rev*. **2012**, 112, 673.

11. Wang, N.; Cai Y.; Zhang, R. Q. *Mater. Sci. Eng*. **2008**, 60, 1.

12. Wang, Z. L. Nanowires and Nanobelts, Kluwer Academic Publishers, **2003**, 2, 1062.

13. Rowan, S. J.; Cantrill, S. J.; Cousins, G. R. L.; Sanders J. K. M.; Stoddart, J. F. *Angew. Chem., Int. Ed*. **2002**, 41, 898.

14. McCrum, N. G.; Buckley C. P.; Bucknall, C. B. Principles of polymer engineering, *Oxford University Press, New York* **1997**.

15. Davis, M. E. *Nature* **2002**, 417, 813.

16. Buzea, C.; Pacheco, I. I.; Robbie, K. *Biointerphases* **2007**, 2, 17.

17. Hyeon, T.; Lee, S. S.; Park, J.; Chung Y.; Na. H. B. *J. Am.Chem. Soc*. **2001**, 123, 12798.

18. Li, Z.; Feng, X.; Zou, Y.; Zhang, Y.; Xia, H.; Liu X.; Mu, *Y. A. Chem. Commun*. **2014**, 50, 13825.

19. Li, Z.; Zhi, Y.; Feng, X.; Ding, X.; Zou, Y.; Liu X.; Mu, Y. *Chem. Eur. J*. **2015**, 21, 12079.

20. Stegbauer, L.; Hahn, M. W.; Jentys, A.; Savasci, G.; Ochsenfeld,C.; Lercher, J. A.; Lotsch, B. V. *Chem. Mater*. **2015**, 27, 7874.

21. Huang, N.; Chen, X.; Krishna, R.; Jiang, D. *Angew. Chem., Int. Ed*. **2015**, 54, 2986.

22. Wang, K.; Huang, H.; Liu, D.; Wang, C.; Li, J.; Zhong, C. *Environ. Sci. Technol*. **2016**, 50, 4869.

23. Ben, T.; Pei, C.; Zhang, D.; Xu, J.; Deng, F.; Jing, X.; Qiu, S. *Energy Environ. Sci*. **2011**, 4, 3991.

24. Zhao, Y.; Yao, K. X.; Teng, B.; Zhang, T.; Han, Y. *Energy Environ. Sci*. **2013**, 6, 3684.

25. Li, B.; Zhang, Y.; Krishna, R.; Yao, K.; Han, Y.; Wu, Z.; Ma, D.; Shi, Z.; Pham, T.; Space, B. *J. Am. Chem. Soc*. **2014**, 136, 8654.

26. Hasell, T.; Miklitz, M.; Stephenson, A.; Little, M. A.; Chong, S. Y.; Clowes, R.; Chen, L.; Holden, D.; Tribello, G. A.; Jelfs, K. E. *J. Am. Chem. Soc*. **2016**, 138, 1653.

27. Fu, J.; Das, S.; Xing, G.; Ben, T.; Valtchev, V.; Qiu, S. *J. Am. Chem. Soc.* **2016**, 138, 7673.

28. Budd, P. M.; Msayib, K. J.; Tattershall, C. E.; Ghanem, B. S.; Reynolds, K. J.; McKeown, N. B.; Fritsch, D. *J. Membr. Sci.* **2005**, 251, 263.

29. Qiao, Z.-A.; Chai, S.-H.; Nelson, K.; Bi, Z.; Chen, J.; Mahurin, S. M.; Zhu, X.; Dai, S. *Nat. Commun.* **2014**, 5, 3705.

30. Song, Q.; Jiang, S.; Hasell, T.; Liu, M.; Sun, S.; Cheetham, A. K.; Sivaniah, E.; Cooper, A. *Adv. Mater.* **2016**, 28, 2629.

31. Ding, S.-Y.; Gao, J.; Wang, Q.; Zhang, Y.; Song, W.-G.; Su, C.-Y.; Wang, W. *J. Am. Chem. Soc*. **2011**, 133, 19816.

32. Fang, Q.; Gu, S.; Zheng, J.; Zhuang, Z.; Qiu, S.; Yan, Y. *Angew. Chem., Int. Ed*. **2014**, 53, 2878.

33. Xu, H.; Gao, J.; Jiang, D. *Nat. Chem*. **2015**, 7, 905.

34. Kamiya, K.; Kamai, R.; Hashimoto, K.; Nakanishi, S. *Nat. Commun*. **2014**, 5, 5040.

35. Iwase, K.; Yoshioka, T.; Nakanishi, S.; Hashimoto, K.; Kamiya, K. *Angew. Chem., Int. Ed.* **2015**, 54, 11068.

36. Thomas, P.; Pei, C.; Roy, B.; Ghosh, S.; Das, S.; Banerjee, A.; Ben, T.; Qiu, S.; Roy, S. *J. Mater. Chem. A* **2015**, 3, 1431.

37. Xu, F.; Chen, X.; Tang, Z.; Wu, D.; Fu, R.; Jiang, D. *Chem. Commun*. **2014**, 50, 4788.

38. Kou, Y.; Xu, Y.; Guo, Z.; Jiang, D. *Angew. Chem., Int. Ed*. **2011**, 50, 8753.

39. Lee, J.-S. M.; Wu, T.-H.; Alston, B. M.; Briggs, M. E.; Hasell, T.; Hu, C.-C.; Cooper, A. I. *J. Mater. Chem. A* **2016**, 4, 7665.

40. Xu, F.; Xu, H.; Chen, X.; Wu, D.; Wu, Y.; Liu, H.; Gu, C.; Fu, R.; Jiang, D. *Angew. Chem., Int. Ed*. **2015**, 54, 6814.

41. DeBlase, C. R.; Silberstein, K. E.; Truong, T.-T.; Abruña, H. D.; Dichtel, W. R. *J. Am. Chem. Soc*. **2013**, 135, 16821.

42. Mulzer, C. R.; Shen, L.; Bisbey, R. P.; McKone, J. R.; Zhang, N.; Abruña, H. D.; Dichtel, W. R. *ACS Cent. Sci*. **2016**, 2, 667.

43. Xu, F.; Jin, S.; Zhong, H.; Wu, D.; Yang, X.; Chen, X.; Wei, H.; Fu, R.; Jiang, D. *Sci. Rep*. **2015**, 5, 8225.

44. Guo, B.; Ben, T.; Bi, Z.; Veith, G. M.; Sun, X.-G.; Qiu, S.; Dai, S. *Chem. Commun*. **2013**, 49, 4905.

45. Li, Y.; Roy, S.; Ben, T.; Xu, S.; Qiu, S. *Phys. Chem. Chem. Phys*. **2014**, 16, 12909.

46. Xu, H.; Tao, S.; Jiang, D. *Nat. Mater*. **2016**, 15, 722.

47. Ma, H.; Liu, B.; Li, B.; Zhang, L.; Li, Y.-G.; Tan, H.-Q.; Zang, H.-Y.; Zhu, G. *J. Am. Chem. Soc*. **2016**, 138, 5897.

48. Wan, S.; Guo, J.; Kim, J.; Ihee, H.; Jiang, D. *Angew. Chem., Int. Ed*. **2008**, 47, 8826.

49. Wan, S.; Guo, J.; Kim, J.; Ihee, H.; Jiang, D. *Angew. Chem., Int. Ed*. **2009**, 48, 5439.

50. Ding, X.; Guo, J.; Feng, X.; Honsho, Y.; Guo, J.; Seki, S.; Maitarad, P.; Saeki, A.; Nagase, S.; Jiang, D. *Angew. Chem., Int. Ed*. **2011**, 50, 1289.

51. Ding, X.; Feng, X.; Saeki, A.; Seki, S.; Nagai, A.; Jiang, D. *Chem. Commun*. **2012**, 48, 8952.

52. Ding, X.; Chen, L.; Honsho, Y.; Feng, X.; Saengsawang, O.; Guo, J.; Saeki, A.; Seki, S.; Irle, S.; Nagase, S.; Parasuk V.; Jiang D. *J. Am. Chem. Soc.* **2011**, 133, 14510.

53. Wan, S.; Gándara, F.; Asano, A.; Furukawa, H.; Saeki, A.; Dey, S. K.; Liao, L.; Ambrogio, M. W.; Botros, Y. Y.; Duan, X. *Chem. Mater.* **2011**, 23, 4094.

54. Feng, X.; Liu, L.; Honsho, Y.; Saeki, A.; Seki, S.; Irle, S.; Dong,Y.; Nagai, A.; Jiang, D. *Angew. Chem., Int. Ed.* **2012**, 51, 2618.

55. Sprick, R. S.; Jiang, J.-X.; Bonillo, B.; Ren, S.; Ratvijitvech, T.; Guiglion, P.; Zwijnenburg, M. A.; Adams, D. J.; Cooper, A. I. *J. Am. Chem. Soc.* **2015**, 137, 3265.

56. Vyas, V. S.; Haase, F.; Stegbauer, L.; Savasci, G.; Podjaski, F.; Ochsenfeld, C.; Lotsch, B. V. *Nat. Commun.* **2015**, 6, 8508.

57. Liras, M.; Iglesias, M.; Sánchez, F. *Macromolecules* **2016**, 49, 1666.

58. Xie, Z.; Wang, C.; Krafft, K. E.; Lin, W. *J. Am. Chem. Soc.* **2011**, 133, 2056.

59. Jiang, J.-X.; Li, Y.; Wu, X.; Xiao, J.; Adams, D. J.; Cooper, A. I. *Macromolecules* **2013**, 46, 8779.

60. Pan, L.; Xu, M.-Y.; Feng, L.-J.; Chen, Q.; He, Y.-J.; Han, B.-H. *Polym. Chem.* **2016**, 7, 2299.

61. Chen, L.; Honsho, Y.; Seki, S.; Jiang, D. *J. Am. Chem. Soc.* **2010**, 132, 6742.

62. Venkata Rao, K.; Haldar, R.; Maji, T. K.; George, S. J. *Phys. Chem. Chem. Phys.* **2016**, 18, 156.

63. Dalapati, S.; Jin, E.; Addicoat, M.; Heine, T.; Jiang, D. *J. Am. Chem. Soc.* **2016**, 138, 5797.

64. Hong, Y.; Lam, J. W. Y.; Tang, B. Z. *Chem. Commun.* **2009**, 4332.

65. Vyas, V. S.; Rathore, R. *Chem. Commun.* **2010**, 46, 1065.

66. Liu, X.; Xu, Y.; Jiang, D. *J. Am. Chem. Soc*. **2012**, 134, 8738.

67. Dalapati, S.; Jin, S.; Gao, J.; Xu, Y.; Nagai, A.; Jiang, D. *J. Am. Chem. Soc*. **2013**, 135, 17310.

68. Xiang, Z.; Cao, D. *Macromol. Rapid Commun*. **2012**, 33, 1184.

69. Gu, C.; Huang, N.; Chen, Y.; Qin, L.; Xu, H.; Zhang, S.; Li, F.; Ma, Y.; Jiang, D. *Angew. Chem., Int. Ed*. **2015**, 54, 13594.

70. Zhang, J.-H.; Xie, S.-M.; Chen, L.; Wang, B.-J.; He, P.-G.; Yuan, L.-M. *Anal. Chem*. **2015**, 87, 7817.

71. Xie, S.-M.; Zhang, J.-H.; Fu, N.; Wang, B.-J.; Chen, L.; Yuan, L.-M. *Anal. Chim. Acta* **2016**, 903, 156.

72. Fang, Q.; Wang, J.; Gu, S.; Kaspar, R. B.; Zhuang, Z.; Zheng, J.; Guo, H.; Qiu, S.; Yan, Y. *J. Am. Chem. Soc*. **2015**, 137, 8352.

73. Pei, C.; Ben, T.; Xu, S.; Qiu, S. *J. Mater. Chem. A* **2014**, 2, 7179.

74. Yan, Z.; Yuan, Y.; Liu, J.; Li, Q.; Nguyen, N.-T.; Zhang, D.; Tian, Y.; Zhu, G. *Huaxue Xuebao* **2016**, 74, 67.

75. Jiang, J. X.; Trewin, A.; Su, F.; Wood, C. D.; Niu, H.; Jones, J. T.A.; Khimyak, Y. Z.; Cooper, A. I. *Macromolecules* **2009**, 42, 2658.

76. Ben, T.; Ren, H.; Ma, S.; Cao, D.; Lan, J.; Jing, X.; Wang, W.; Xu, J.; Deng, F.; Simmons, J. M.; Qiu, S.; Zhu, G. *Angew. Chem., Int. Ed*. **2009**, 48, 9457.

77. El-Kaderi, H. M.; Hunt, J. R.; Mendoza-Cortés, J. L.; Côté, A. P.; Taylor, R. E.; O'Keeffe, M.; Yaghi, O. M. *Science* **2007**, 316, 268.

78. Beiler, B.; Vincze, Á.; Svec, F.; Sáfrány, Á. *Polymer* **2007**, 48, 3033.

79. Wood, C. D.; Tan, B.; Trewin, A.; Su, F.; Rosseinsky, M. J.;Bradshaw, D.; Sun, Y.; Zhou, L.; Cooper, A. I. *Adv. Mater*. **2008**, 20, 1916.

80. Rose, M.; Klein, N.; Senkovska, I.; Schrage, C.; Wollmann, P.; Böhlmann, W.; Böhringer, B.; Fichtner, S.; Kaskel, S. *J. Mater. Chem.* **2011**, 21, 711.

81. Olson, D. A.; Chen, L.; Hillmyer, M. A. *Chem. Mater.* **2008**, 20, 869.

82. Kim, J. K.; Yang, S. Y.; Lee, Y.; Kim, Y. *Prog. Polym. Sci.* **2010**, 35, 1325.

83. Budd, P. M.; Ghanem, B. S.; Makhseed, S.; McKeown, N. B.; Msayib, K. J.; Tattershall, C. E. *Chem. Commun.* **2004**, 230.

84. Ghanem, B. S.; McKeown, N. B.; Budd, P. M.; Fritsch, D. *Macromolecules* **2008**, 41, 1640.

85. Weber, J.; Su, Q.; Antonietti, M.; Thomas, A. *Macromol. Rapid Commun.* **2007**, 28, 1871.

86. Du, N.; Robertson, G. P.; Song, J.; Pinnau, I.; Thomas, S.; Guiver, M. D. *Macromolecules* **2008**, 41, 9656.

87. Hu, X.; An, Q.; Li, G.; Tao, S.; Liu, J. *Angew. Chem., Int. Ed.* **2006**, 45, 8145.

88. Rzayev, J.; Hillmyer, M. A. *Macromolecules* **2005**, 38, 3.

89. Li, G.; Liu, G.; Kang, E.; Neoh, K.; Yang, X. *Langmuir* **2008**, 24, 9050.

90. Zhang, Y.; Jiang, M.; Zhao, J.; Ren, X.; Chen, D.; Zhang, G. *Adv. Funct. Mater.* **2005**, 15, 695.

91. Schacher, F.; Ulbricht, M.; Müller, A. H. E. *Adv. Funct. Mater.* **2009**, 19, 1040.

92. Du, J.; Armes, S. P. *J. Am. Chem. Soc.* **2005**, 127, 12800.

93. Chen, Z.; He, C.; Li, F.; Tong, L.; Liao, X.; Wang, Y. *Langmuir* **2010**, 26, 8869.

94. Hyuk, Im, S.; Jeong, U.; Xia, Y. *Nat. Mater.* **2005**, 4, 671.

95. Rouquerol, J.; Avnir, D.; Fairbridge, C. W.; Everett, D. H.; Haynes, J. H.; Pernicone, N.; Ramsay, J. D. F.; Sing, K. S. W.; Unger, K. K. *Pure Appl. Chem.* **1994**, 66, 1739.

96. Sing, K. S. W.; Everett, D. H.; Haul, R. A. W.; Moscou, L.; Pierotti, R. A.; Rouquerol, J.; Siemieniewska, T. *Pure Appl. Chem*. **1985**, 57, 603.

97. Matyjaszewski, K. *Science* **2011**, 333, 1104.

98. Gao, H.; Matyjaszewski, K. *Prog. Polym. Sci*. **2009**, 34, 317.

99. Gao, H.; Matyjaszewski, K. *J. Am. Chem. Soc*. **2007**, 129, 11828.

100. Feng, X.; Liu, L; Honsho Y.; Saeki A.; Seki S.; Irle S.; Dong Y.; Nagai A.; Jiang D. *Angew. Chem., Int. Ed.* **2012**, 51, 2618.

101. Doonan, C. J.; Tranchemontagne, D. J.; Glover, T. G.; Hunt, J. R.; Yaghi, O. M. *Nat. Chem.* **2010**, 2, 235.

102. Pernites, R. B.; Foster, E. L.; Felipe, M. J. L.; Robinson, M.; Advincula, R. C. *Adv. Mater*. **2011**, 23, 1287.

103. Liu, X.; Basu, A. *J. Am. Chem. Soc*. **2009**, 131, 5718.

104. Rzayev, J.; Hillmyer, M. A. *J. Am. Chem. Soc*. **2005**, 127, 13373.

105. Yang, X.; Jin, Y.; Zhu, Y.; Tang, L.; Li, C. J. *Electrochem. Soc*. **2008**, 155, 23.

106. Nagai, A.; Guo, Z.; Feng, X.; Jin, S.; Chen, X.; Ding, X.; Jiang, D. *Nat. Commun*. **2011**, 2, 536.

107. Rogozhin, S. V.; Davankov, V. A.; Tsyurupa, M. P. Patent USSR 299165, **1969**.

108. McKeown, N. B.; Makhseed, S.; Budd, P. M. *Chem. Commun*. **2002**, 2780.

109. McKeown, N. B.; Hanif, S.; Msayib, K.; Tattershall, C. E.; Budd, P. M. *Chem. Commun*. **2002**, 2782.

110. Jiang, J.-X.; Su, F.; Trewin, A.; Wood, C. D.; Campbell, N. L.; Niu, H.; Dickinson, C.; Ganin, A. Y.; Rosseinsky, M. J.; Khimyak, Y. Z. *Angew. Chem., Int. Ed*. **2007**, 46, 8574.

111. Urban, C.; McCord, E. F.; Webster, O. W.; Abrams, L.; Long, H. W.; Gaede, H.; Tang, P.; Pines, A. *Chem. Mater.* **1995**, 7, 1325.

112. Webster, O. W.; Gentry, F. P.; Farlee, R. D.; Smart, B. E. *Polym. Prepr. (Am. Chem. Soc., Div. Polym. Chem.)* **1991**, 32, 412.

113. Davankov, V. A.; Tsyurupa, M. P. *React. Polym.* **1990**, 13, 27.

114. Xu, S.; Luo, Y.; Tan, B. *Macromol. Rapid Commun*. **2013**, 34, 471.

115. Germain, J.; Fréchet, J. M. J.; Svec, F. *J. Mater. Chem*. **2007**, 17, 4989.

116. Wood, C. D.; Tan, B.; Trewin, A.; Niu, H.; Bradshaw, D.; Rosseinsky, M. J.; Khimyak, Y. Z.; Campbell, N. L.; Kirk, R.; Stöckel, E.; Cooper, A. I. *Chem. Mater*. **2007**, 19, 2034.

117. Li, B.; Gong, R.; Wang, W.; Huang, X.; Zhang, W.; Li, H.; Hu, C.; Tan, B. *Macromolecules* **2011**, 44, 2410.

118. Dawson, R.; Stevens, L. A.; Drage, T. C.; Snape, C. E.; Smith, M. W.; Adams, D. J.; Cooper, A. I. *J. Am. Chem. Soc*. **2012**, 134, 10741.

119. Fu, Z.; Jia, J.; Li, J.; Liu C. *Chem. Eng. J*. **2017**, 323, 557.

120. Luo, Y.; Zhang, S.; Ma, Y.; Wang, W.; Tan, B. *Polym. Chem*. **2013**, 4, 1126.

121. Li, B.; Gong, R.; Wang, W.; Huang, X.; Zhang, W.; Li, H.; Hu, C.; Tan, B. *Macromolecules* **2011**, 44, 2410.

122. Ilinitch, O. M.; Fenelonov, V. B.; Lapkin, A. A.; Okkel, L. G.; Terskikh, V. V.; Zamaraev, K. I. *Micropor. Mesopor. Mat*. **1999**, 31, 97.

123. McKeown N. B.; Budd, P. M. "Polymers of intrinsic microporosity," in *Encyclopedia of Polymer Science and Technology*, John Wiley & Sons, New York, NY, USA, **2009**.

124. McKeown, N. B.; Li, H.; Makhseed, S.; Sherrington, D. C., Kybett, A. P., Eds. RSC Publishing: Cambridge, UK, **2001**, 214.

125. McKeown, N. B. Polymers of Intrinsic Microporosity. *ISRN Materials Science* **2012**, 2012, 1.

126. Bailey, W. F.; "Ladder polymers," in The Encyclopaedia of Polymer Science and Engineering, Mark, H. F.; Ed., 158, John Wiley & Sons, New York, NY, USA **1993**.

127. Scherf, U.; *J. Mater. Chem.* **1999**, 9, 1853.

128. Eastmond, G. C.; Paprotny, J.; Steiner, A.; Swanson, L. *New J. Chem.* **2001**, 25, 379.

129. Makhseed, S.; McKeown, N. B.; Msayib, K.; Bumajdad, A. *J. Mater. Chem.* **2005**, 15, 1865.

130. Msayib, K.; Makhseed, S.; McKeown, N. B. *J. Mater. Chem.* **2001**, 11, 2784.

131. Cheng, G.; Bonillo, B.; Sprick, R. S.; Adams, D. J.; Hasell, T.; Cooper, A. I. *Adv. Funct. Mater*. **2014**, 24, 5219.

132. Zhang, P.; Jiang, X.; Wan, S.; Dai, S. *J. Mater. Chem. A* **2015**, 3, 6739.

133. Zhang, P.; Jiang, X.; Wan, S.; Dai, S. *Chem-Eur. J.* **2015**, 21, 12866.

134. Budd, P. M.; Elabas, E. S.; Ghanem B. S.; Makhseed, S.; McKeown, N. B.; Msayib, K. J.; Tattershall, C. E.; Wang, D. *Adv. Mater.* **2004**, 16, 456.

135. Adymkanov, S. V.; Yampol'skii Yu. P.; Polyakov, A. M.; Budd, P. M.; Reynolds, K. J.; McKeown, N. B.; Msayib, K. *J. Polymer Science A* **2008**, 50, 444.

136. Vandezande, P.; Gevers, L. E. M.; Vankelecom, I. F. J. *Chem. Soc. Rev.* **2008**, 37, 365.

137. Fritsch, D.; Merten, P.; Heinrich, K.; Lazar, M.; Priske M. *J. Membr. Sci.* **2012**, 401, 222.

138. Fritsch, D.; Bengtson, G.; Carta, M.; McKeown, N. B. *Macromol. Chem. Phys.* **2011**, 212, 1137.

139. Park, H. B.; Jung, C. H.; Moo Lee, Y.; Hill, A. J.; Pas, S. J.; Mudie, S. T.; Wagner, E. V.; Freeman, B. D.; Cookson D. J. *Science* **2007**, 318, 254.

140. Han, S. H.; Misdan, N.; Kim, S.; Doherty, C. M.; Hill, A. J.; Lee, Y. M. *Macromolecules* **2010**, 43, 7657.

141. Han, S. H.; Lee, J. E.; Lee, K. J.; Park, H. B.; Lee, Y. M. *J. Membr. Sci.* **2010**, 357, 143.

142. Park, H. B.; Han, S. H.; Jung, C. H.; Lee, Y. M.; Hill, A. J. *J. Membr. Sci.* **2010**, 359, 11.

143. Wang, Y.; McKeown, N. B.; Msayib, K. J.; Turnbull, G. A.; Samuel, I. D. W. *Sensors* **2011**, 11, 2478.

144. Thomas, J. C.; Trend, J. E.; Rakow, N. A.; Wendland, M. S.; Poirier, R. J.; Paolucci, D. M. *Sensors* **2011**,11, 3267.

145. Rakow, N. A.; Wendland, M. S.; Trend, J.E.; Poirier, R. J.; Paolucci, D. M.; Maki, S. P.; Lyons, C. S.; Swierczek, M. J. *Langmuir* **2010**, 26, 3767.

146. Zhang, C.; Li, P.; Cao, B. *J. Appl. Polym. Sci*. **2016**, 13310.

147. Zhao, H.; Xie, Q.; Ding, X.; Chen, J.; Hua, M.; Tan, X.; Zhang, Y. *J. Membr. Sci*. **2016**, 514, 305.

148. Shin, Y.; Prestat, E.; Zhou, K.-G.; Gorgojo, P.; Althumayri, K.; Harrison, W.; Budd, P. M.; Haigh, S. J.; Casiraghi, C. *Carbon* **2016**, 102, 357.

149. McKeown, N. B.; Budd, P. M. *Chem. Soc. Rev.* **2006**, 35, 675.

150. Bunz, U. H. F. *Chem. Rev*. **2000**, 100, 1605.

151. Sonogashira, K.; TohdaY.; Hagihara, N. *Tetrahedron Lett*. **1975**, 16, 4467.

152. Trumbo D. L.; Marvel, C. S. *J. Polym. Sci*. **1986**, 24, 2311.

153. Hettinger, E.; Kokil, A.; Weder, C. *Angew. Chem*., **2004**, 116, 1844; *Angew. Chem., Int. Ed*. **2004**, 43, 1808.

154. Mendez, J. D.; Schroeter, M.; Weder, C. *Macromol. Chem. Phys*. **2007**, 208, 1625.

155. Donhauser, Z. J.; Mantooth, B. A.; Kelly, K. F.; Bumm, L. A.; Monnell, J. D.; Stapleton, J. J.; Price, D. W.; Rawlett, A. M.; Allara, D. L.; Tour, J. M.; Weiss, P. S. *Science* **2001**, 292, 2303.

156. Zhou, Q.; Swager, T. M. *J. Am. Chem. Soc*. **1995** 117, 12593.

157. Venkataraman, D.; Lee, S.; Zhang, J. S.; Moore, J. S. *Nature* **1994**, 371, 591.

158. Zhang, W.; Moore, J. S. *Angew. Chem*. **2006**, 118, 4524.

159. Kiang, Y. H.; Gardner, G. B.; Lee, S.; Xu, Z. T.; Lobkovsky, E. B. *J. Am. Chem. Soc*. **1999**, 121, 8204.

160. Miyaura, N.; Yamada, K.; Suzuki, A. *Tetrahedron Lett*. **1979**, 36, 343.

161. Miyaura, N.; Yanagi, T.; Suzuki, A. *Synth. Commun*. **1981**, 11, 513.

162. Zhang, H.; Xue, F.; Mak, T. C. W.; Chan, K. S. *J. Org. Chem*. **1996**, 61, 8002.

163. Zhang, H.; Chan, K. S. *Tetrahedron Lett*. **1996**, 37, 1043.

164. Badone, D.; Baroni, M.; Cardamone, R.; Ielmini, A.; Guzzi, U. *J. Org. Chem*. **1997**, 62, 7170.

165. Casalnuovo, A. L.; Calabrese, J. C. *J. Am. Chem. Soc*. **1990**, 112, 4324.

166. Yamada, Y. M. A.; Takeda, K.; Takahashi, H.; Ikegami, S. *Org. Lett*. **2002**, 4, 3371.

167. Frenette, R.; Friesen, R. W. *Tetrahedron Lett*. **1994**, 35, 9177.

168. Ishiyama, T.; Murata, M.; Miyaura, N. *J. Org. Chem*. **1995**, 60, 7508.

169. Ishiyama, T.; Itoh, Y.; Kitano, T.; Miyaura, N. *Tetrahedron Lett*. **1997**, 38, 3447.

170. Trewin, A.; Cooper, A. I. *Angew. Chem., Int. Ed*. **2010**, 49, 1533.

171. Yuan, D.; Lu, W.; Zhao, D.; Zhou, H. *Adv. Mater*. **2011**, 23, 3723.

172. Ben, T.; Qiu, S. *CrystEngComm* **2013**, 15, **17**.

173. Suresh, V. M.; Bonakala, S.; Roy, S.; Balasubramanian, S.; Maji, T. K. *J. Phys. Chem. C* **2014**, 118, 24369.

174. Kang, N.; Park, J. H.; Ko, K. C.; Chun, J.; Kim, E.; Shin, H. W.; Lee, S. M.; Kim, H. J.; Ahn, T. K.; Lee, J. Y.; Son, S. U. *Angew. Chem., Int. Ed.* **2013**, 52, 6228.

175. Cho, H. C.; Lee, H. S.; Chun, J.; Lee, S. M.; Kim, H. J.; Son, S. U. *Chem. Commun.* **2011**, 47, 917.

176. Du, X.; Sun, Y.; Tan, B.; Teng, Q.; Yao, X.; Su, C.; Wang, W. *Chem. Commun.* **2010**, 46, 970.

177. Kiskan, B.; Antonietti, M.; Weber, J. *Macromolecules* **2012**, 45, 1356.

178. Chan-Thaw, C. E.; Villa, A.; Katekomol, P.; Su, D.; Thomas, A.; Prati, L. *Nano Lett.* **2010**, 10, 537.

179. Chen, L.; Yang, Y.; Guo, Z.-Q.; Jiang, D.-L. *Adv. Mater.* **2011**, 23, 3149.

180. Zhang, Y.; Zhang, Y.; Sun, Y. L.; Du, X.; Shi, J. Y.; Wang, W. D.; Wang, W. *Chem-Eur. J.* **2012**, 18, 6328.

181. Chen, L.; Yang, Y.; Jiang, D. *J. Am. Chem. Soc.* **2010**, 132, 9138.

182. Ma, L.; Wanderley, M. M.; Lin, W. *ACS Catal.* **2011**, 1, 691.

183. Palkovits, R.; Antonietti, M.; Kuhn, P.; Thomas, A.; Schueth, F. *Angew. Chem., Int. Ed.* **2009**, 48, 6909.

184. Urakami, H.; Zhang, K.; Vilela, F. *Chem. Commun.* **2013**, 49, 2353.

185. Wang, Z. J.; Ghasimi, S.; Landfester, K.; Zhang, K. A. *Chem. Commun.* **2014**, 50, 8177.

186. Wang, Z. J.; Ghasimi, S.; Landfester, K.; Zhang, K. A. I. *J. Mater. Chem. A* **2014**, 2, 18720.

187. Zhang, K.; Kopetzki, D.; Seeberger, P. H.; Antonietti, M.; Vilela, F. *Angew. Chem., Int. Ed.* **2013**, 52, 1432.

188. Li, A.; Lu, R.-F.; Wang, Y.; Wang, X.; Han, K.-L.; Deng, W. Q. *Angew. Chem., Int. Ed.* **2010**, 49, 3330.

189. Cheng, G.; Hasell, T.; Trewin, A.; Adams, D. J.; Cooper, A. I. *Angew. Chem., Int. Ed.* **2012**, 51, 12727.

190. Ren, S.; Dawson, R.; Laybourn, A.; Jiang, J.-x.; Khimyak, Y.; Adams, D. J.; Cooper, A. I. *Polym. Chem.* **2012**, 3, 928.

191. Dawson, R.; Laybourn, A.; Clowes, R.; Khimyak, Y. Z.; Adams, D. J.; Cooper, A. I. *Macromolecules* **2009**, 42, 8809.

192. Liu, X.; Xu, Y.; Guo, Z.; Nagai, A.; Jiang, D. *Chem. Commun.* **2013**, 49, 3233.

193. Tan, D.; Fan, W.; Xiong, W.; Sun, H.; Cheng, Y.; Liu, X.; Meng, C.; Li, A.; Deng, W. Q. *Macromol. Chem. Phys.* **2012**, 213, 1435.

194. Li, A.; Sun, H.-X.; Tan, D.-Z.; Fan, W.-J.; Wen, S.-H.; Qing, X.-J.; Li, G.-X.; Li, S.-Y.; Deng, W.-Q. *Energy Environ. Sci.* **2011**, 4, 2062.

195. Gu, C.; Huang, N.; Gao, J.; Xu, F.; Xu, Y.; Jiang, D. *Angew. Chem. Int. Ed. Engl.* **2014**, 53, 4850.

196. Reineke, S.; Lindner, F.; Schwartz, G.; Seidler, N.; Walzer, K.; Lussem, B.; Leo, K. *Nature* **2009**, 459, 234.

197. Burroughes, J. H.; Bradley, D. D. C.; Brown, A. R.; Marks, R. N.; Mackay, K.; Friend, R. H.; Burn, P. L.; Holmes, A. B. *Nature* **1990**, 347, 539.

198. Sekitani, T.; Nakajima, H.; Maeda, H.; Fukushima, T.; Aida, T.; Hata, K.; Someya, T. *Nat. Mater.* **2009**, 8, 494.

199. Katz, H. E.; Singer, K. D.; Sohn, J. E.; Dirk, C. W.; King, L. A.; Gordon, H. M. *J. Am. Chem. Soc.* **1987**, 109, 6561.

200. Kajzar, F.; Lee, K. S.; Jen, A. K. Y. *Adv. Polym. Sci.* **2003**, 161, 1.

201. Li, G.; Shrotriya, V.; Huang, J. S.; Yao, Y.; Moriarty, T.; Emery, K.; Yang, Y. *Nat. Mater.* **2005**, 4, 864.

202. Bronstein, H.; Chen, Z. Y.; Ashraf, R. S.; Zhang, W. M.; Du, J. P.; Durrant, J. R.; Tuladhar, P. S.; Song, K.; Watkins, S. E.; Geerts, Y.; Wienk, M. M.; Janssen, R. A. J.; Anthopoulos, T.; Sirringhaus, H.; Heeney, M.; McCulloch, I. *J. Am. Chem. Soc.* **2011**, 133, 3272.

203. Sirringhaus, H. *Adv. Mater.* **2005**, 17, 2411.

204. Muccini, M. *Nat. Mater.* **2006**, 5, 605.

205. Wang, Y. Y.; Jing, X. L. *Polym. Advan. Technol.* **2005**, 16, 344.

206. Strobl, G. R. *The Physics of Polymers*; *Springer,* **2007**.

207. Deng, S.; Zhi, J.; Zhang, X.; Wu, Q.; Ding, Y.; Hu, A. *Angew. Chem., Int. Ed. Engl.* **2014**, 53, 14144.

208. Jiang, J. X.; Su, F.; Trewin, A.; Wood, C. D.; Niu, H.; Jones, J. T. A.; Khimyak, Y. Z.; Cooper, A. I. *J. Am. Chem. Soc.* **2008**, 130, 7710.

209. Dawson, R.; Laybourn, A.; Khimyak, Y. Z.; Adams, D. J.; Cooper, A. I. *Macromolecules* **2010**, 43, 8524.

210. Germain, J.; Svec, F.; Frechet, J. M. J. *Chem. Mater.* **2008**, *20*, 7069.

211. Weder, C. *Angew. Chem., Int. Ed.* **2008**, 47, 448.

212. Xu, Y.-H.; Chen, L.; Guo, Z.-Q.; Nagai, A.; Jiang, D.-L. *J. Am. Chem. Soc.* **2011**, 133, 17622.

213. Chen, Q.; Wang, J.-X.; Yang, F.; Zhou, D.; Bian, N.; Zhang, X.-J.; Yan, C.-G.; Han, B.-H. *J. Mater. Chem.* **2011**, 21, 13554.

214. Stoeckel, E.; Wu, X.; Trewin, A.; Wood, C. D.; Clowes, R.; Campbell, N. L.; Jones, J. T. A.; Khimyak, Y. Z.; Adams, D. J.; Cooper, A. I. *Chem. Commun.* **2009**, 212.

215. Müllen, K.; Reynolds, J. R.; Masuda, T. *Conjugated Polymers*; RSC: Cambridge, UK, **2014**.

216. Xu, Y. H.; Jin, S. B.; Xu, H.; Nagai, A.; Jiang, D. L. *Chem. Soc. Rev.* **2013**, 42, 8012.

217. Vilela, F.; Zhang, K.; Antonietti, M. *Energ. Environ. Sci.* **2012**, 5, 7819.

218. Zhan, X. W.; Zhu, D. B. *Polym. Chem.* **2010**, 1, 409.

219. Park, D. H.; Kim, M. S.; Joo, J. *Chem. Soc. Rev.* **2010**, 39, 2439.

220. Tuncel, D. *Nanoscale* **2011**, 3, 3545.

221. He, M.; Qiu, F.; Lin, Z. Q. *J. Mater. Chem.* **2011**, 21, 17039.

222. Waltman, R. J.; Bargon, J. *Can. J. Chem.* **1986**, 64, 76.

223. Yamamoto, T. *J. Organomet. Chem.* **2002**, 653, 195.

224. Cheng, Y. J.; Luh, T. Y. *J. Organomet. Chem.* **2004**, 689, 4137.

225. Osaka, I.; McCullough, R. D. *Acc. Chem. Res.* **2008**, 41, 1202.

226. Miyaura, N.; Suzuki, A. *J. Chem. Soc., Chem. Comm.* **1979**, 866.

227. Miyaura, N.; Yamada, K.; Suzuki, A. *Tetrahedron Lett.* **1979**, 20, 3437.

228. Choi, J. H.; Choi, K. M.; Jeon, H. J.; Choi, Y. J.; Lee, Y.; Kang, J. K. *Macromolecules* **2010**, 43, 5508.

229. Pirguliyev, N. S.; Brel, V. K.; Zefirov, N. S.; Stang, P. J. *Tetrahedron* **1999**, 55, 12377.

230. Bohm, V. P. W.; Herrmann, W. A. *Eur. J. Org. Chem.* **2000**, 3679.

231. Osakada, K.; Yamamoto, T. *Coord. Chem. Rev.* **2000**, 198, 379.

232. Prier, C. K.; Rankic, D. A.; MacMillan, D. W. C. *Chem. Rev*. **2013**, 113, 5322.

233. Pham, P. V.; Nagib, D. A.; MacMillan, D. W. C. *Angew. Chem., Int. Ed*. **2011**, 50, 6119.

234. Nguyen, J. D.; Tucker, J. W.; Konieczynska, M. D.; Stephenson, C. R. J. *J. Am. Chem. Soc*. **2011**, 133, 4160.

235. Nagib, D. A.; MacMillan, D. W. C *Nature* **2011**, 480, 224.

236. Furst, L.; Narayanam, J. M. R.; Stephenson, C. R. *Angew. Chem., Int. Ed*. **2011**, 50, 9655.

237. Yoon, T. P.; Ischay, M. A.; Du, J. *Nat. Chem.* **2010**, 2, 527.

238. Tucker, J. W.; Nguyen, J. D.; Narayanam, J. M. R.; Krabbe, S. W.; Stephenson, C. R. J. *Chem. Commun*. **2010**, 46, 4985.

239. Du, J.; Yoon, T. P. *J. Am. Chem. Soc*. **2009**, 131, 14604.

240. Marin, M. L.; Santos-Juanes, L.; Arques, A.; Amat, A. M.; Miranda, M. A. *Chem. Rev*. **2012**, 112, 1710.

241. Romero, N. A.; Nicewicz, D. A. *Chem. Rev*. **2016**, 116, 10075.

242. Ravelli, D.; Fagnoni, M.; Albini, A. *Chem. Soc. Rev.* **2013**, *42*, 97.

243. Mooibroek, T. J.; Gamez, P. *Inorg. Chim. Acta* **2007**, 360, 381.

244. Katekomol, P.; Roeser, J.; Bojdys, M.; Weber, J.; Thomas, A. *Chem. Mater*. **2013**, 25, 1542.

245. Kuhn, P.; Antonietti, M.; Thomas, A. *Angew. Chem., Int. Ed*. **2008**, 47, 3450.

246. Kuhn, P.; Forget, A.; Su, D.; Thomas, A.; Antonietti, M. *J. Am. Chem. Soc*. **2008**, 130, 13333.

247. Ren, S.; Bojdys, M. J.; Dawson, R.; Laybourn, A.; Khimyak, Y. Z.; Adams, D. J.; Cooper, A. I. *Adv. Mater*. **2012**, 24, 2357.

248. Herrera, A.; Riaño, A.; Moreno, R.; Caso, B.; Pardo, Z. D.; Fernández, I.; Sáez, E.; Molero, D.; Sánchez-Vázquez, A.; Martínez-Alvarez, R. *J. Org. Chem.* **2014**, 79, 7012.

249. Roeser, J.; Kailasam, K.; Thomas, A. *Chemsuschem* **2012**, 5, 1793.

250. Lanni, L. M.; Tilford, R. W.; Bharathy, M.; Lavigne, J. J. *J. Am. Chem. Soc.* **2011**, 133, 13975.

251. Natural gas 1998: Issues and trends; DOE/EIA-0560-98; Energy Information Administration, Office of Oil and Gas: Washington, DC, **1999**.

252. Beychok, M. R. Fundamentals of Stack Gas Dispersion; Milton R. Beychok: Irvine, CA, **1994.**

253. Peighambardoust, S. J.; Rowshanzamir, S.; Amjadi, M. *Int. J. Hydrogen Energy* **2010**, 35, 9349.

254. Du, Y.; Mao, K.; Kamakoti, P.; Ravikovitch, P.; Paur, C.;Cundy, S.; Li, Q.; Calabro, D. *Chem. Commun.* **2012**, 48, 4606.

255. Kandambeth, S.; Mallick, A.; Lukose, B.; Mane, M. V.; Heine, T.; Banerjee, R. *J. Am. Chem. Soc.* **2012**,134, 19524.

256. Biswal, B. P.; Chandra, S.; Kandambeth, S.; Lukose, B.; Heine, T.; Banerjee, R. *J. Am. Chem. Soc.* **2013**, 135, 5328.

257. Chandra, S.; Kandambeth, S.; Biswal, B. P.; Lukose, B.; Kunjir, S. M.; Chaudhary, M.; Babarao, R.; Heine, T.; Banerjee, R. *J. Am. Chem. Soc.* **2013**, 135, 17853.

258. Shinde, D. B.; Aiyappa, H. B.; Bhadra, M.; Biswal, B. P.; Wadge, P.; Kandambeth, S.; Garai, B.; Kundu, T.; Kurungot, S.; Banerjee, R. *J. Mater. Chem. A* **2016**, 4, 2682.

259. Chandra, S.; Kundu, T.; Dey, K.; Addicoat, M.; Heine, T.;Banerjee, R. *Chem. Mater.* **2016**, 28, 1489.

260. Thote, J.; Aiyappa, H. B.; Kumar, R. R.; Kandambeth, S.;Biswal, B. P.; Shinde, D. B.; Roy, N. C.; Banerjee, R. *IUCrJ* **2016**, 3, 402.

261. Kandambeth, S.; Shinde, D. B.; Panda, M. K.; Lukose, B.; Heine, T.; Banerjee, R. *Angew. Chem., Int. Ed.* **2013**, 52, 13052.

262. Ascherl, L.; Sick, T.; Margraf, J. T.; Lapidus, S. H.; Calik, M.; Hettstedt, C.; Karaghiosoff, K.; Döblinger, M.; Clark, T.; Chapman, K. W.; Auras, F.; Bein, T. *Nat. Chem.* **2016**, 8, 310.

263. Halder, A.; Karak, S.; Addicoat, M.; Bera, S.; Chakraborty, A.; Kunjattu, S. H.; Pachfule, P.; Heine, T.; Banerjee, R. *Angew. Chem., Int. Ed.* **2018**, 57, 5797.

264. Desiraju, G. R. *Acc. Chem. Res.* **2002**, 35, 565.

265. Desiraju, G. R.; Steiner, T. *Oxford University Press: Oxford*, **1999**.

266. Waller, P. J.; Lyle, S.; Osborn Popp, T.; Diercks, C. S.; Reimer, J. A.; Yaghi, O. M. *J. Am. Chem. Soc.* **2016**, 138, 15519.

267. Campbell, N. L.; Clowes, R.; Ritchie, L. K.; Cooper, A. I. *Chem. Mater.* **2009**, 21, 204.

268. Rittersma, Z. M. *Sens. Actuators A* **2002**, 96, 196.

269. Chen, Z.; Lu, C. *Sensor Lett.* **2005**, 3, 274.

270. Yamazoe, N.; Shimizu, Y. *Sens. Actuators* **1986**, 10, 379.

271. Traversa, E.; Gnappi, G.; Montenero, A.; Gusmano, G. *Sens. Actuators B* **1996**, 31, 59

272. Wang, K.; Qian, X.; Zhang, L.; Li, Y.; Liu, H. *ACS Appl. Mater. Interfaces*, **2013**, 5, 5825.

273. Yuan, Q.; Li, N.; Tu, J.; Li, X.; Wang, R.; Zhang, T.; Shao, C. *Sens. Actuators B* **2010**, 149, 413.

274. Imran, Z.; Batool, S. S.; Jamil, H.; Usman, M.; Israr-Qadir, M.; Shah, S. H.; Jamil-Rana, S.; Rafiq, M. A.; Hasan, M. M.; Willander, M. *Ceram. Int*. **2013**, 39, 457.

275. Chen, Y. S.; Li, Y.; Yang, M. *J. Appl. Polym. Sci*. **2007**, 105, 3470

276. Khanna, V. K.; Nahar, R. K. *J. Phys. D: Appl. Phys*. **1986**, 19, 141.

277. Sakai, Y.; Sadaoka, Y.; Matsuguchi, M.; Rao, V. L.; Kamigaki, M. *Polymer* **1989**, 30, 1068.

278. Kuroiwa, T.; Hayashi, T.; Ito, A.; Matsuguchi, M.; Sadaoka, Y.; Sakai, Y. *Sens. Actuators B* **1993**, 13, 89.

279. Lin, G.; Ding, H.; Yuan, D.; Wang, B.; Wang, C. *J. Am. Chem. Soc.* **2016**, 138, 3302.

280. Xie, Y.-F.; Ding, S.-Y.; Liu, J.-M.; Wang, W.; Zheng, Q.-Y. *J. Mater. Chem. C* **2015**, 3, 10066.

281. Rao, M. R.; Fang, Y.; Feyter, S. De; Perepichka, D. F. *J. Am. Chem. Soc.* **2017**, 139, 2421.

282. Ding, S.-Y.; Dong, M.; Wang, Y.-W.; Chen, Y.-T.; Wang, H.-Z.; Su, C.-Y.; Wang, W. *J. Am. Chem. Soc.* **2016**, 138, 3031.

283. Li, Z.; Zhang, Y.; Xia, H.; Mu, Y.; Liu, X. *Chem. Commun.* **2016**, 52, 6613.

284. Zeng, M.; Xiao, Y.; Liu, J.; Yang, K.; Fu L. *Chem. Rev.* **2018**, 118, 6236.

285. Thomas, A. *Angew. Chem.* **2010**, 122, 8506.

286. Colson, J. W.; Dichtel, W. R. *Nat. Chem.* **2013**, 5, 453.

287. Ding, S. Y.; Wang, W. *Chem. Soc. Rev.* **2013**, 42, 548.

288. Dogru, M.; Bein, T. *Chem. Commun.* **2014**, 50, 5531.

289. Parvez, K.; Wu, Z.-S.; Li, R.; Liu, X.; Graf, R.; Feng, X.; Mgllen, K. *Adv. Mater.* **2015**, 27, 6083.

290. Huang, N.; Wang, P.; Jiang, D. *Nat. Rev. Mater.* **2016**, 1, 16068.

291. Chen, X.; Addicoat, M.; Jin, E.; Zhai, L.; Xu, H.; Huang, N.; Guo, Z.; Liu, L.; Irle, S.; Jiang, D. *J. Am. Chem. Soc.* **2015**, *137*, 3241.

292. Mo, Y.-P.; Liu, X.-H.; Sun, B.; Yan, H.-J.; Wang, D.; Wan, L.-J. *Phys. Chem. Chem. Phys.* **2017**, *19*, 539.

293. Qian, C.; Xu, S.-Q.; Jiang, G.-F.; Zhan, T.-G.; Zhao, X. *Chem. Eur. J.* **2016**, 22, 17784.

294. Halder, A.; Kandambeth, S.; Biswal, B. P.; Kaur, G.; Roy, N. C.; Addicoat, M.; Salunke, J. K.; Banerjee, S.; Vanka, K.; Heine, T.; Verma, S.; Banerjee, R. *Angew. Chem.* **2016**, 128, 7937.

295. Gole, B.; Stepanenko, V.; Rager, S.; Grgne, M.; Medina, D. D.; Bein, T.; Wgrthner, F.; Beuerle, F. *Angew. Chem.* **2018**, 130, 856.

296. Berlanga, I.; Ruiz-Gonzalez, M. L.; Gonzalez-Calbet, J.; Fierro, J. L. G.; Mas-Balleste, R.; Zamora, F. *Small* **2011**, 7, 1207–1211

297. Wang, S.; Wang, Q.; Shao, P.; Han, Y.; Gao, X.; Ma, L.; Yuan, S.; Ma, X.; Zhou, J.; Feng, X.; Wang, B. *J. Am. Chem. Soc.* **2017**, 139, 4258.

298. Zhang, C.; Zhang, S.; Yan, Y.; Xia, F.; Huang, A.; Xian, Y. *ACS Appl. Mater. Interfaces* **2017**, 9, 13415.

299. Das, G.; Biswal, B. P.; Kandambeth, S.; Venkatesh, V.; Kaur, G.; Addicoat, M.; Heine, T.; Verma, S.; Banerjee, R. *Chem. Sci.* **2015**, 6, 3931.

300. Khayum, M. A.; Kandambeth, S.; Mitra, S.; Nair, S. B.; Das, A.; Nagane, S. S.; Mukherjee, R.; Banerjee, R. *Angew. Chem.* **2016**, 128, 15833.

301. Kong, W.; Wan, J.; Namuangruk, S.; Guo, J.; Wang, C. *Sci. Rep.* **2018** 8, 5529.

302. Liu, X.-H.; Guan, C.-Z.; Wang, D.; Wan, L. J. *Adv. Mater*. **2014**, 26, 6912.

303. Mitra, S.; Kandambeth, S.; Biswal, B. P.; Khayum, A.; Choudhury, M. C. K.; Mehta, M.; Kaur, G.; Banerjee, S.; Prabhune, A.; Verma, S.; Roy, S.; Kharul, U. K.; Banerjee, R. *J. Am.Chem. Soc*. **2016**, 138, 2823.

304. Chen, H.; Tu, H.; Hu, C.; Liu, Y.; Dong, D.; Sun, Y.; Dai, Y.; Wang, S.; Qian, H.; Lin, Z. *J. Am. Chem. Soc*. **2018**, 140, 896.

Chapter 2

Truxene based Porous, Crystalline Covalent Organic Frameworks and its Applications in Humidity Sensing
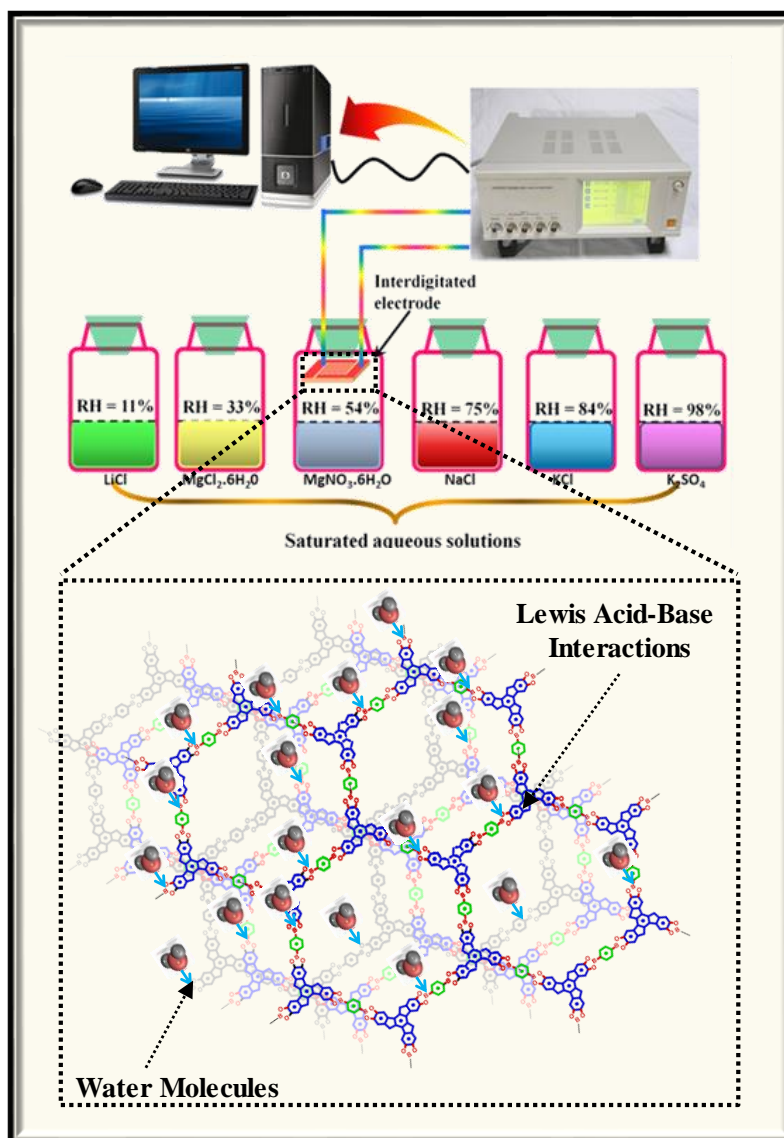
This chapter demonstrates the design and synthesis of boronic ester linked Truxene based highly porous crystalline COF and its application in humidity sensing. The COF shows change in impedance with varying relative humidity in very short response and recovery times due to boronic ester linkage decorated nanochannels generated by periodic layers.

2.1 Aim:

The physical and chemical properties of COFs exclusively depend upon the building blocks of COF and the covalent linkages between them. Generally, synthesis of COFs requires rigid building blocks with a specific geometry to perform reticular chemistry with very few available kinetically reversible chemical reactions. These specific requirements limit their scope to explore them for various applications. To overcome these challenges, the continuous design of new building blocks to accelerate this research field is of utmost requirement. Addressing the mentioned challenges, this chapter introduces Truxene (Tx) as the building block of COFs, for the first time.

Tx, (10,15-dihydro-5H-diindeno[1,2-a;1',2'-c]fluorene), is a C_3 symmetric, star-shaped π-conjugated polyarene obtained by trimerization of indan-1-one. It can also be formally considered as 1,3,5-triphenylbenzene (a very common building block for the synthesis of various COFs) derivative with three methylene clips, responsible for keeping the four benzene rings coplanar and π-conjugated. These methylene clips make Tx, a strong electron-donor with strong π-π stacking ability, which hints that Tx can be a potential candidate to built the advanced functional materials for various applications. Tx molecular derivatives have been widely investigated in supramolecular chemistry, especially in organic electronics. Tx based dendrimer, oligomers, and polymers were known to show very interesting properties as photosensitizers, photoresistors, organic lasers, OLEDs, OFETs, and OPVs.[1] Further, octupolar character combined with polyaromatic and rigid planar structure makes its derivatives a good candidate for more efficient non-linear optical (NLO) properties than the conventional dipolar molecules.[2, 3] These interesting features of Tx molecular identity was the main motivation to design the Tx based COF.

Among all the interesting properties shown by COFs due to confined pores and easily controllable pore environment, COFs can also be potential candidates for the sensing applications. In this context, various groups have designed the COF-based chemosensors for the detection of explosives[4, 5] and toxic metal ions.[6, 7] However, as compared to the chemosensors, electrochemical sensor based on COFs has not explored before this report. The research work in this chapter aims to develop a methodology to use COFs as a substrate for an electrochemical sensor for real-time application.

Exploiting the inherent crystallinity, enhanced surface area and electron-rich linker groups, the precise detection of relative humidity (%RH) using COFs is a paradigm shift from conventional metal-oxide-semiconductor,[8] silica,[9] polymer,[10] carbon nitrides,[11] and relatively new MOFs[12] or inorganic/organic hybrid[13] based %RH sensors.

Considering the affinity of boron ester linkage towards water molecule and facilitated interaction between them, due to the enhanced diffusion effect of nanochannels, we explored the newly synthesized Tx-based COF for the detection of %RH at room temperature for the first time.

2.2 Experimental Section:

2.2.1 Chemicals and Instruments:

All chemicals and solvents were of analytical grade quality and used without further purification. 3,4-Dihydroxyhydrocinnamic acid, polyphosphoric acid (PPA), 1,4-phenylenediboronic acid, Boron tribromide (BBr$_3$), potassium carbonate and dimethylsulphate were purchased from Sigma-Aldrich (Bangalore, India). Thin-layer chromatography was performed on aluminium sheets pre-coated with silica gel (Merck, kiesel gel 60, F254). Column chromatographic separations were performed on silica gel (60–120 mesh). Structural characterization of the compounds were carried out by ^{1}H

NMR and ^{13}C NMR (Bruker Biospin, Switzerland, Avance-iii 400 and 100 MHz spectrometers, respectively), infrared spectroscopy (Perkin Elmer Spectrum AX3), UV-vis spectrophotometer 3000+, Photoluminescence (excitation wavelength 404 nm) and HRMS (Water g-2 synapt gases). Nuclear magnetic resonance (NMR) spectra of monomer were recorded using deuterated chloroform (CDCl$_3$) & deuterated dimethylsulfoxide (DMSO-d$_6$) and tetramethylsilane as an internal standard. The humidity sensing measurements were performed on Interdigitated electrodes (13.4mm x 7mm x 0.5mm) having 5 tracks of Ag-Pd electrodes. Prior to the measurements, a dilute paste of the sample in ethanol was dropped onto the electrodes and dried at 60 °C. The controlled environments for % relative humidity (%RH) were prepared by using air-tight chambers containing saturated aqueous salts solution of lithium chloride (LiCl), magnesium chloride, hexahydrate (MgCl$_2$•6H$_2$O), magnesium nitrate tetahydrate (MgNO$_3$•4H$_2$O), sodium chloride (NaCl), potassium chloride (KCl) and potassium sulfate (K$_2$SO$_4$) generating 11%, 33%, 54%, 75%, 84% and 98% relative humidity, respectively, at 25 ºC. The electric impedance was measured using a two-probe Keithley source meter. The measurements were carried out at 1V AC voltage with frequency varying from 100 Hz.

2.2.2 Synthesis:

Scheme 2.1 describes the various steps followed in the synthesis of Tx monomer. Detailed synthesis procedures are given below. All the ^{1}H and ^{13}C NMR of the monomers are given in Appendix 2, Figure A2.1-2.6 at the end of this chapter.

3-(3,4-dimethoxyphenyl) propanoic acid (a): To obtain compound (**a**), 3,4-dihydroxyhydrocinnamic acid was refluxed with dimethyl sulfate (Me$_2$SO$_4$) and dry potassium carbonate (K$_2$CO$_3$) in acetone under N$_2$ atmosphere. After 12 h, the reaction

was stopped and cooled to room temperature. Solid K$_2$CO$_3$ was removed by filtration and acetone was removed by vacuum distillation. After distillation, the residue was dissolved in ethyl acetate. The organic layer was washed with water, brine and dried over anhydrous sodium sulphate. A brown colored organic residue left after vacuum distillation was further refluxed in 50% (v/v) methanol and 10% NaOH solution till TLC showed a single spot. The reaction mixture was cooled and acidified with conc. HCl. A white colour solid was precipitated, which was filtered and dried. Further purification was done by recrystallization in hexane/ethyl acetate solvent mixture. Yield 85.5%; ^{1}H-NMR (400 MHz, CDCl$_3$) δ: 6.82 (d, 1H), 6.77 (d, 2H), 3.89 (s, 3H), 3.88 (s, 3H), 2.93 (t, 2H), 2.69 (t, 2H). ^{13}C NMR (100 MHz, CDCl$_3$): δ179.03, 148.86, 147.52, 132.74, 120.08, 111.57, 111.25, 55.90, 55.81, 35.90, 30.24.
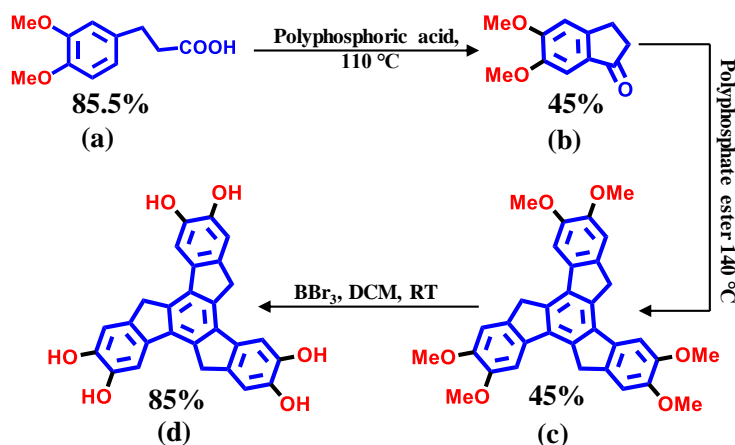
Scheme 2.1: Synthetic scheme of truxene monomer.

5,6-dimethoxy-1H-inden-1-one (b): Polyphosphoric acid (PPA) (86.8 g) was heated at 110 °C in a 100 ml round bottom flask closed with anhydrous CaCl$_2$ filled guard tube. Compound **(a)** (3.0 g) was added to this hot PPA and mixed with a glass rod and heated at 110 ºC for 45 min. The reaction mixture was cooled and poured into cold water, which was extracted with ethyl acetate. After removing the solvent by vacuum distillation, the

crude compound was further purified by column chromatography using hexane and ethyl acetate solvent mixture. After purification, compound **(b)** was obtained as a yellow solid. Yield 45 %; ^{1}H NMR (400 MHz, CDCl$_3$) δ: 7.19 (s,1H), 6.90 (s, 1H), 3.97 (s, 3H), 3.91 (s, 3H), 3.06 (t, 2H), 2.68 (t, 2H). ^{13}C NMR (100 MHz, CDCl$_3$) δ: 205.84, 155.37, 150.47, 149.34, 129.88, 107.51, 107.42, 104.16, 104.08, 56.31, 56.17, 56.03, 36.53, 25.58.

2,3,7,8,12,13-hexamethoxy-10,15-dihydro-5H-diindeno[1,2-a:1',2'-c] fluorine (c): Polyphosphoric ester (PPE) (10.4 g) was taken in a 25 mL round-bottom flask which was placed in a preheated oil bath at 140 ℃. To this preheated PPE compound (b) (3.0 g) was added and stirred for 5 min maintaining the temperature at 140 ℃. The temperature was subsequently increased to 160 ℃ and the reaction mixture was stirred for 25 min. During this reaction condition, excessive foaming occurred. The reaction mixture was then poured in acetone and stirred well. A bright pink colored solid was settled at the bottom, which was collected after repeated centrifugation by washing with DCM until DCM layer couldn't become clear. Pink-colored solid was dried in vacuum and was subjected to the next reaction without purification. The pink-colored solid obtained was insoluble in nearly all the solvents available in the lab, so with an assumption that ~99% of this pink solid is compound **(c)** we subjected the crude product for the next reaction. Yield 45%.

Hexahydroxy truxene [Tx(OH)$_6$)] (d): The pink-colored solid obtained in the previous step was insoluble in nearly all the solvents available in lab, so with an assumption that ~99% of this pink solid is compound (c), we subjected the crude product for demethylation and got demethylated product hexahydroxy truxene (d). Yield 85 %; ^{1}H NMR (400 MHz, DMSO-d$_6$) δ: 9.04 (s, 6H), 7.35 (s, 3H), 7.13 (s, 3H), 3.90 (s, 3H), 3.55 (s, H$_2$O), 4.04 (s, 6H). ^{13}C NMR (100 MHz, CDCl$_3$) δ: 145.11, 137.28, 135.17, 132.04, 112.94, 109.47, 35.61.

Synthesis of COF-TXDBA: Compound **(d)** (150 mg, 1 equiv.) was dissolved in 30 ml dioxane. To this solution 1.5 equivalents of 1,4-phenylenediboronic acid (DBA) were added and sonicated, in order to obtained the homogeneous mixture. After that 6 ml of mesitylene was added to the resulting mixture and again sonicated followed by the addition of 0.2 ml methanol.
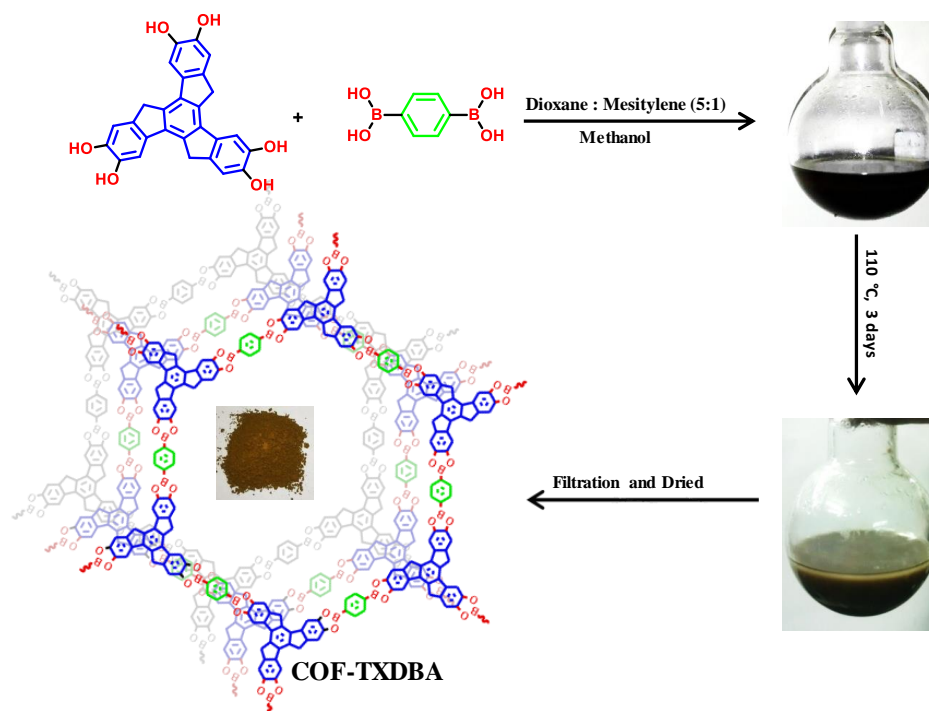

Figure 2.1: Synthetic scheme of Truxene based COF, COF-TXDBA diagram shows the color change of reaction mixture due to COF formation.

Finally, the reaction mixture was refluxed at 110 ℃ under Nitrogen atmosphere. After three days, the precipitate was filtrated and washed with dry dioxane followed by THF several times. The obtained light brown colored COFs was dried under vacuum oven at 150 ℃. The synthesis scheme of COF-TXDBA is shown in Figure 2.1.

2.3 Result and Discussion:

2.3.1 Structural Analysis and Thermal Stability:

The as-synthesized COF-TXDBA was subjected to Fourier-transform infrared spectroscopy (FTIR) and ^{13}C{^{1}H} CP/MAS NMR characterization to obtain the structural bonding information. FTIR showed the strong bands at 1398, 1354 and 1295 cm^{-1} which is attributed to the asymmetric B−O stretches, confirming the formation of boronate ester links. Furthermore, for a boronic–based COF, the characteristic band corresponding to C−B stretching vibration in the boronate esters and C−O stretching vibration in the catechol moieties were observed at approximately 1080 and 1241 cm^{-1}, respectively, as shown in Figure 2.2. These FTIR results confirm the formation of COF.
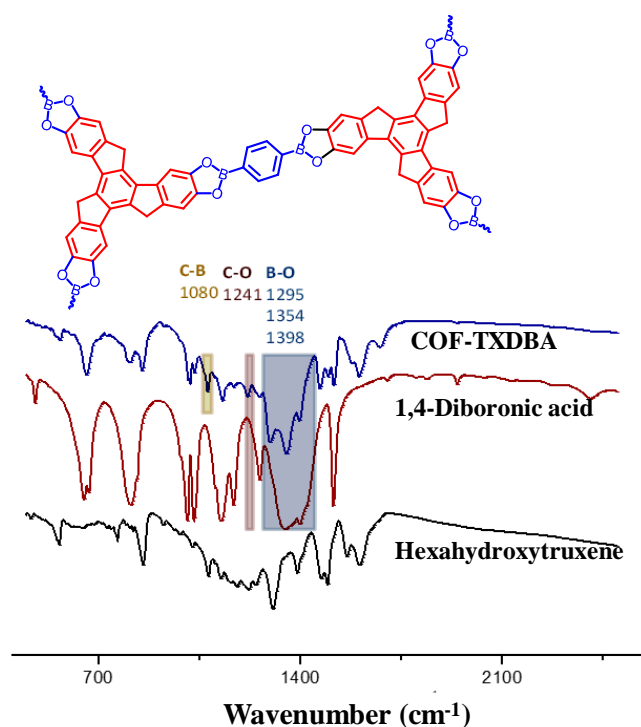
Figure 2.2: The IR spectrum of COF-TXDBA (Blue); Compound (d) (Black); 1,4 phenylenediboronic acid (Red).

Further, COF-TXDBA was characterized by solid-state ^{13}C{^{1}H} CP/MAS NMR spectroscopy. The spectra displayed a dominant aliphatic carbon signal centered at 36

ppm that originates from the methylene bridging units. In the aromatic region, it displays four broad signals at 148, 135, 126 and 106 ppm indicating the ten non-equivalent carbons of the COF structure in Figure 2.3a. Thermogravimetric analyses (TGA) of as-synthesized COF-TXDBA shows minimal weight loss up to 410 ℃. The weight loss at lower temperatures < 200 ℃ is attributed to the evaporation of solvent molecules present in the nano-channels of COF-TXDBA (Figure 2.3b).
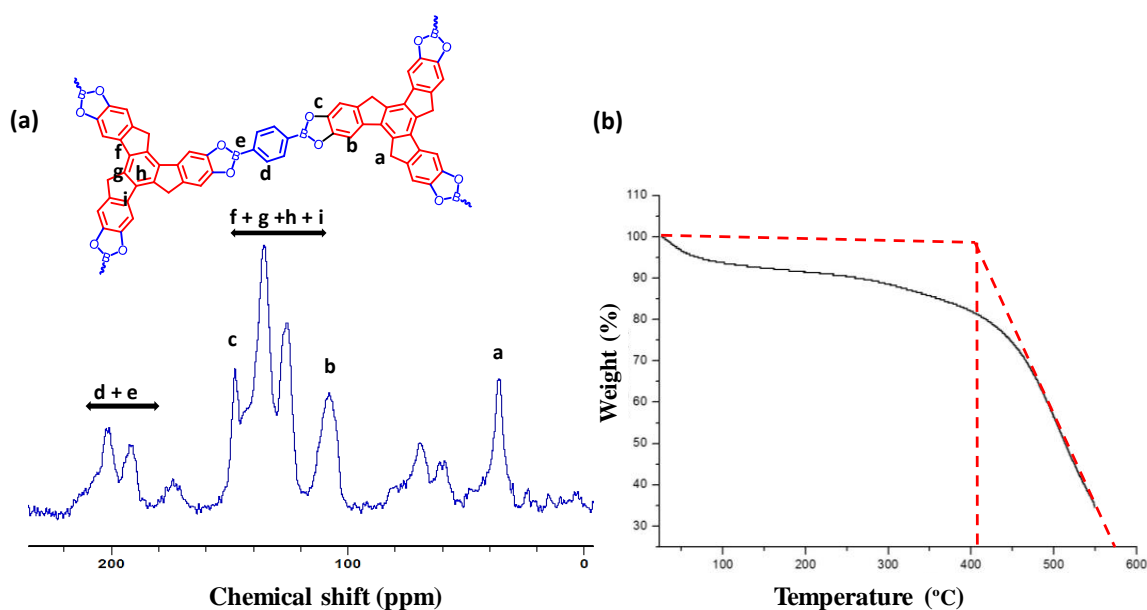
Figure 2.3: (a) Solid-state $^{13}C\{^1H\}$ CPMAS NMR of COF-TXDBA; (b) Thermogravimetric analysis (TGA) of as-synthesized COF-TXDBA.

The structure and crystallinity of COF-TXDBA have been analyzed using the density functional theory (DFT) approach. Two possible structural arrangement, in which two truxene units can link to a diboronic acid unit (Figure 2.4a, 2.4c), has been considered to build the periodic crystal lattices, symmetric-COF-TXDBA (s-COF-TXDBA) with symmetric honeycomb-like pore and asymmetric-COF-TXDBA (a-COF-TXDBA) with asymmetric pore shape (Figure 2.4b, 2.4d). The periodic crystal lattices with an interlayer spacing of 3.74 Å have been built upon the optimized geometries of s-COF-TXDBA and

Symmetric-COF-TXDBA (s-COF-TXDBA)

(a)

Anticlockwise

Anticlockwise

(b)

Asymmetric-COF-TXDBA (s-COF-TXDBA)

(c)

clockwise

Anticlockwise

(d)
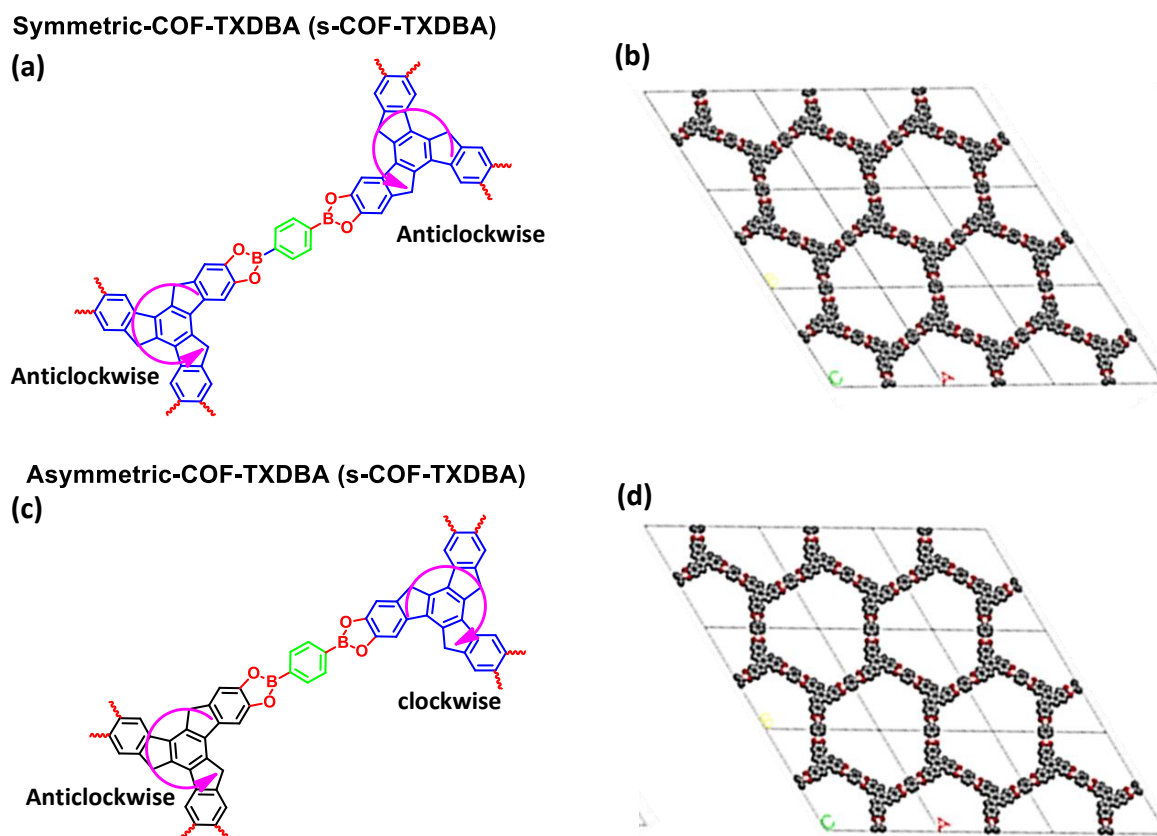
Figure 2.4: (a, c) Two possible structural arrangement of the precursors to build the periodic crystal lattices, Symmetric-COF-TXDBA (s-COF-TXDBA) and Asymmetric-COF-TXDBA (a-COF-TXDBA); (b) Symmetric-COF-TXDBA (s-COF-TXDBA) with symmetric honeycomb like pore produced by symmetric building block; (d) Asymmetric-COF-TXDBA (a-COF-TXDBA) with asymmetric pore shape produced by asymmetric building blocks.

a-COF-TXDBA using 6-311G basis set with B3LYP exchange-correlation functions, as implemented in Gaussian 09 package.[14] These layers were stacked with 12 Å interlayer offset to match the pore size obtained from physisorption measurements. The simulated PXRD of s-COF-TXDBA in its near eclipsed geometry with an interlayer offset of 12 Å resembles more likely the experimental PXRD patterns at low angle regime with a sharp peak at $2\Theta = 3.2°$, reflection arising from (100) plane which infers good crystallinity and long-range molecular ordering structure of COF-TXDBA with subsequent peaks from

69

(110), (200) and (210) plane. However, the deviation at a higher angle has been observed moving from eclipsed packing to staggered packing arrangement. This infers the geometry of COF-TXDBA is more likely towards the eclipsed form of s-COF-TXDBA. PXRD of both s-COF-TXDBA and a-COF-TXDBA in their eclipsed and staggered geometries have also been analyzed (Fig. 2.5a-d).
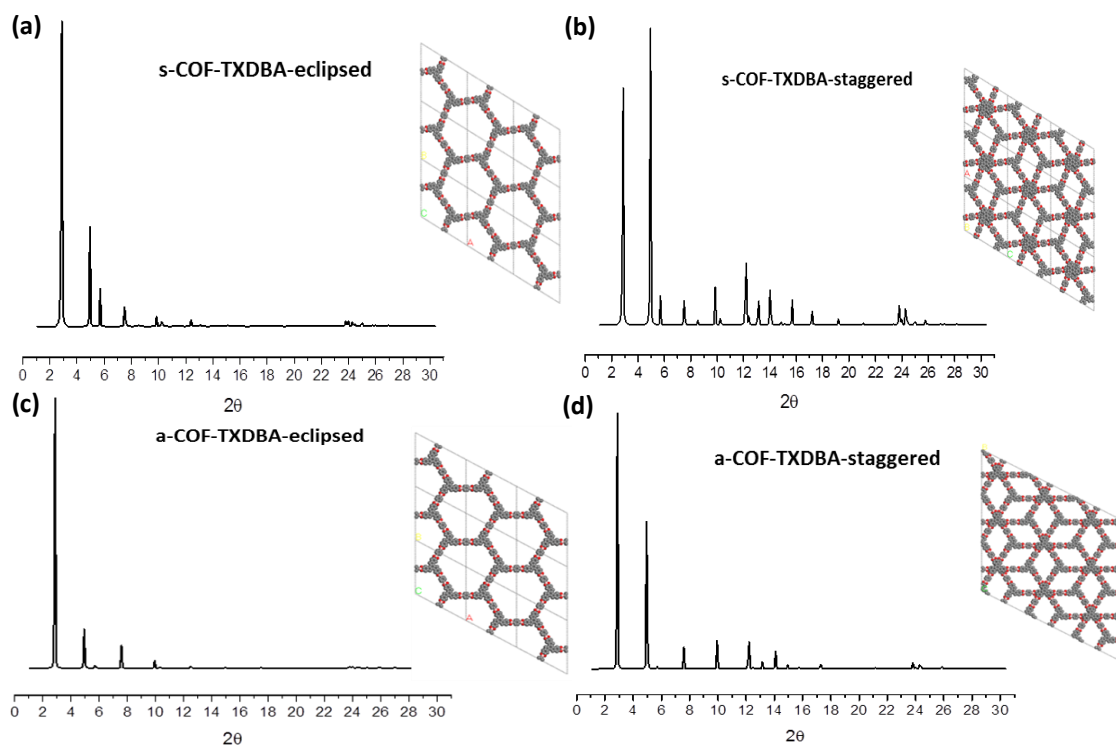

Figure 2.5: Simulated PXRD of (a) Symmetric-COF-TXDBA in eclipsed geometry (symmetric hexagonal pore); (b) Symmetric-COF-TXDBA in staggered geometry; (c) Asymmetric-COF-TXDBA in eclipsed geometry (asymmetric hexagonal pore) (d) Asymmetric-COF-TXDBA in staggered geometry.

Finally, s-COF-TXDBA with interlayer upset of 12 Å have been considered for Pawley refinement with experimental PXRD result using Reflex module of Accelrys's Materials Studio 7.0 package[15] to determine the lattice parameters, which results the unit-cell parameters as, a = b = 35.88 Å, c = 3.74 Å, $\alpha = \beta = 90°$, and $\gamma = 120°$. Pseudo-Voigt

function for peak broadening and Berrar-Baldinozzi function for asymmetry correction have been considered simultaneously to improve profile fitting and the refinement converged with residuals; $R_{wp} = 4.11\%$ and $R_p = 2.66\%$, resulting in hexagonal space group of P6/M as shown in Figure 2.6a and 2.6b.

2.3.2 Morphology:

Scanning electron microscopy images at different magnifications reveals a uniform spongy morphology of COF-TXDBA sample (Figure 2.6c and 2.6d). However, as shown in Figure 2.6e and 2.6f, the formation of a few hollow nanorods was also observed. Attempts were made to enrich these nanorods phase by changing the dioxane and mesitylene ratio.
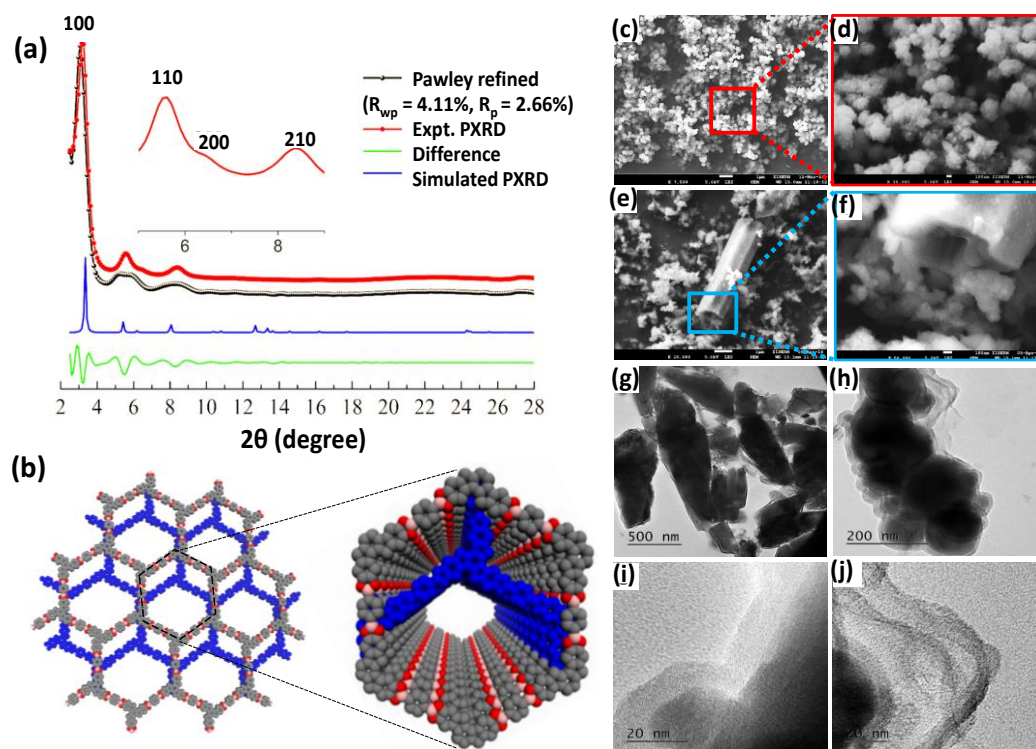
Figure 2.6: Simulated PXRD of upset geometry of COF-TXDBA with Pawley refinement; (a) Simulated PXRD patterns, Experimental PXRD diffraction and PXRD patterns after Pawley refinement; (b) Top view of eclipsed geometry of COF-TXDBA

offset by 12Å in order to account for the experimental pore size distribution. SEM image of the COF-TXDBA (c); A higher magnification image of a square portion (yellow highlight) of the Figure 2.6a (d); Nanorods structures of the same COF at lower (X 10000); (e) and higher magnification (X 50000) (f), respectively. TEM images of COF-TXDBA at different magnifications (g-j).
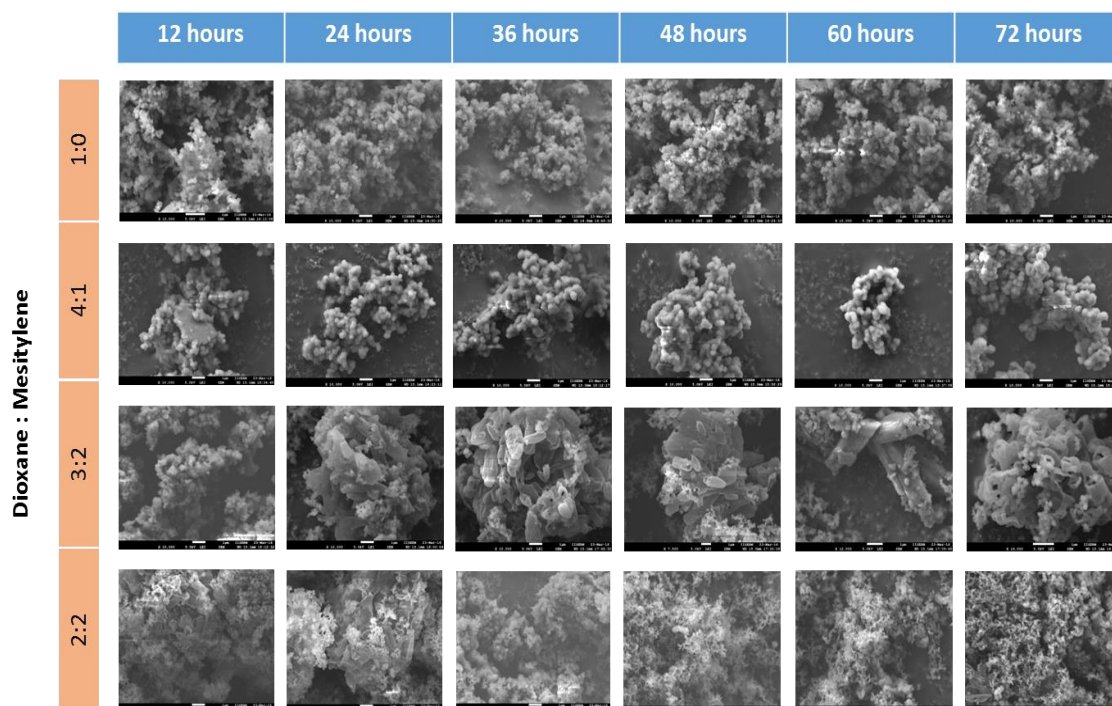
Figure 2.7: SEM images of Truxene COF at different Mesitylene and dioxane ratio at different times shows the formation of capsules at Dioxane: Mesitylene ratio 3:2.

It was observed that the systematic increase in the mesitylene ratio from 0 to 50% initially increases the crystallite size and promotes the formation of vesicles of random size and shape along with the nanorods (Figure 2.7). Further work is going on to optimize the conditions to enrich the nanorod phases, as these hollow nanorods show similarity to Fullerene C_{60} crystallized from 2 mM solution in xylene solvent.[16] It should be noted that Tx can also be formally considered as a building block of Fullerene C_{60}, because of its alternative six- and a five-member ring containing a skeleton. The TEM images at

different magnifications (Figure 2.6g-h) show the scrambled sheet-like structural morphology especially at edges (Figure 2.6i-j), which agrees with the XRD data and in-line with DFT calculation results.

2.3.3 Surface Area and Porosity:

N_2 adsorption-desorption isotherms were measured on Nova Quantachrome at 77 K to determine the porous nature of the COF. Before measurements, the samples were degassed overnight under vacuum at 120 °C. The specific surface area was calculated in the pressure range of $0.01 < p/p_0 < 0.25$ using the BET micropore assistant surface area method. The density functional theory (DFT) method was employed to approximate the pore size distributions of COF-TXDBA sample. Total pore volume was obtained by the amount of N_2 adsorbed at $p/p_0 \sim 0.9$ and 0.95, assuming that adsorption on the external surface was negligible compared to adsorption in pores. The studies revealed reversible adsorption and desorption curves typical of type-IV isotherms with a Sharp uptake below $p/p_0 = 0.01$ as shown in Figure 2.8. The significant adsorption at $p/p_0 < 0.01$ shows the presence of micropores with a narrow distribution. Further the step observed between $0.01 < p/p_0 < 0.25$ indicates condensation in the mesopores. The absence of hysteresis in adsorption-desorption curves is a common nature of hexagonally aligned 1D mesopores materials, as shown by the COF-TXDBA. It exhibits the surface area of around 1526 m^2/g calculated in the pressure range of $0.01 < p/p_0 < 0.25$ using the BET micropore assistant surface area calculations. Density functional theory (DFT) method was employed to approximate the pore size distributions of COF-TXDBA employing a cylindrical pore-oxide surface model, which yielded average pore size of 23 Å. Deviation of pore size from theoretical value (ideal pore size of 31 Å is predicted for the eclipsed form) can be taken into account due to the significant offsets between the stacking layers.[17, 18] There is

a steep increase of the adsorbed nitrogen at high relative pressures ($p/p_0 < 0.95$), which is often assigned to outer surface area or interparticle voids of smaller COF-TXDBA particles, which was confirmed by DFT pore size distribution analysis. The total pore volume calculated at $p/p_0 = 0.95$ is about 0.35 cm^3 g^{-1} and at $p/p_0 = 0.99$ is about 0.45 cm^3 g^{-1}. These crystalline features of the COF-TXDBA samples and high surface area attributes were utilized for humidity sensing application. Up to best of our knowledge, this is the first report to use a COF for humidity sensing applications so far.
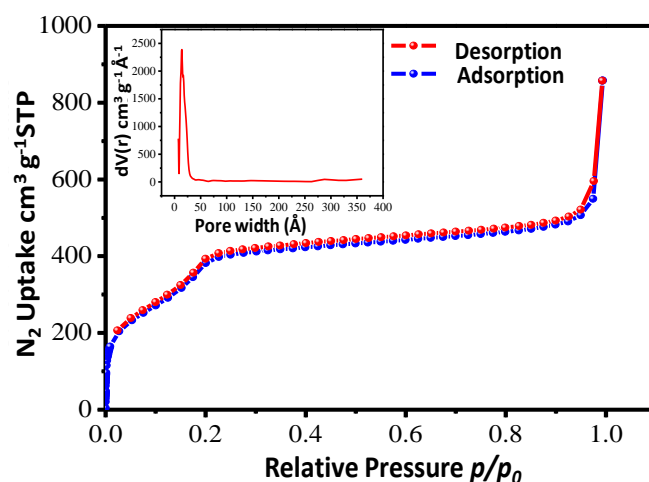
Figure 2.8: Nitrogen isotherms at 77 K for COF-TXDBA and NLDFT pore size distributions of COF-TXDBA (Inset).

2.4 Humidity Sensing:

The %RH dependent impedance response of the prepared COF-TXDBA in the 11-98 %RH range is shown in Figure 2.9a. As can be seen, at low %RH, the sample exhibit very high impedance, however, as the %RH increases, a dramatic decrease in impedance was observed. The COF-TXDBA exhibits ~3 orders of magnitude change in impedance in 11-98% RH range. Hysteresis is another important attribute to estimate the reliability of the sensor and is defined as the maximum difference between the processes of adsorption and desorption. Generally, a sensing material undergoes hysteresis effect at increasing and

decreasing %RH. The hysteresis was measured by switching the sensor between the closed chambers (11 – 98 %RH and 98 – 11 %RH). The hysteresis curves for COF-TXDBA based humidity sensor are shown in Figure 2.9b, where solid circle line represents the process of adsorption (11-98 %RH) and hollow circle line represents the process of desorption (98-11 %RH). The maximum humidity hysteresis error was ~2.5% for COF-TXDBA in the range of 11–98 %RH.
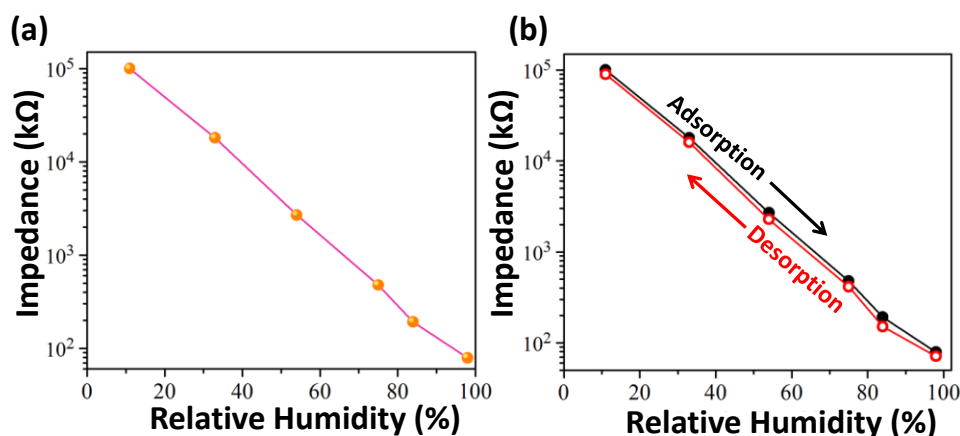

Figure 2.9: (a) Humidity sensing curves showing decrease in impedance with increase in %RH; (b) The hysteresis curve showing adsorption-desorption responses measured in the 11-98 %RH range.

The response and recovery time are other important parameters to evaluate the performance of humidity sensor and defined as the time taken by a sensor to achieve ~90% of total impedance change in case of the process of adsorption and desorption, respectively.[8, 9] Figure 2.10a shows the response and recovery curve of COF-TXDBA measured continuously in the lowest and highest humidity environment. The response time (humidification from 11-98 %RH) was about 37 s and the recovery time (desiccation from 98-11 %RH) was around 42 s. The response transients of COF-TXDBA based %RH sensor were measured by switching back and forth the sensor in 4 loops of 11 %RH and 98 %RH, respectively (Figure 2.10b). It was observed that the impedance of the sensor

retains its original value when humidity is restored to the initial state, which indicates the excellent reversibility of the sensor. The standard deviation in the process of switching sensor response was 2.3%. A comparison of humidity sensing performance with those of published literature in Appendix Table A2.1 shows that our material exhibits satisfactory %RH sensing attributes as compared to conventional %RH sensors under similar test conditions.

Thus, the high surface area and ordered micropores/ mesopores in COF-TXDBA are effectively utilized for addressing any target-oriented, herein, effective humidity sensing which further opens up the broad role the COFs can play in different applications. These functional designed COFs will be good candidates for being explored in the sensing of different other analytes like volatile organic compounds (VOCs).
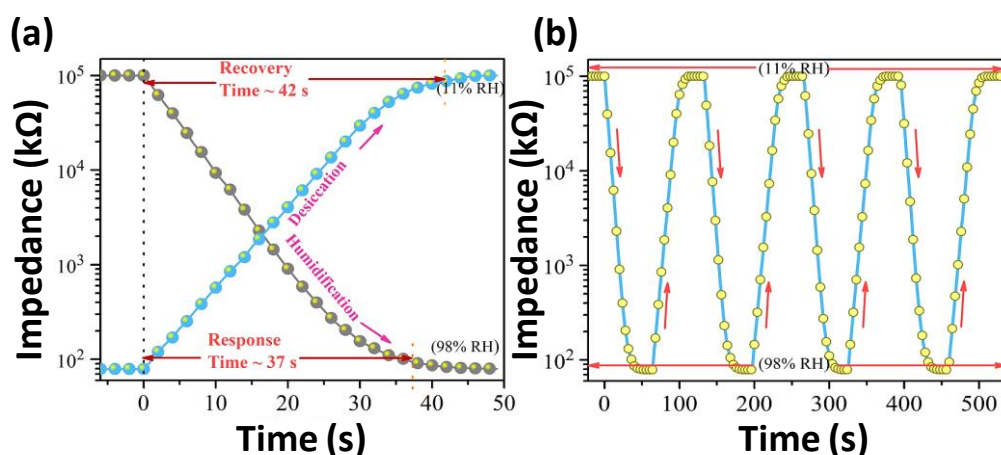
Figure 2.10: (a) Response and recovery curves of COF-TXDBA; (b) Repeated response and recovery characteristics of COF-TXDBA measured at consecutive intervals of time in four loops.

2.5 Stability and Recyclability:

To study the effect of humidity on the stability of COF-TXDBA, PXRD patterns were recorded for 5 loops after every cycle (11 $\rightarrow$ 98 $\rightarrow$ 11 %RH) of measurement. The

sample was scratched out from the sensing substrate and dried at 100 °C for 10 min. As can be seen in Figure 2.11a, the crystallinity of the COF remains intact during the test experiments as can be seen from the characteristic sharp peak at 3.2° in PXRD.
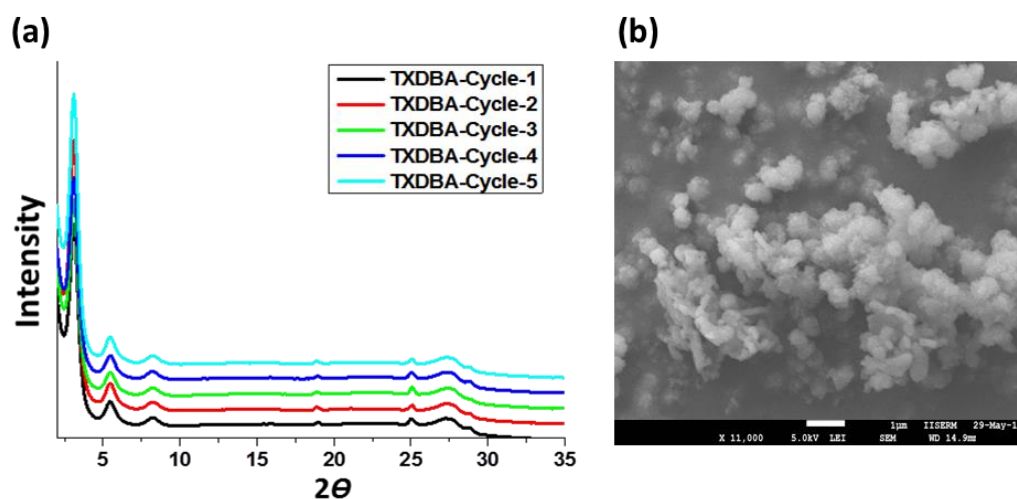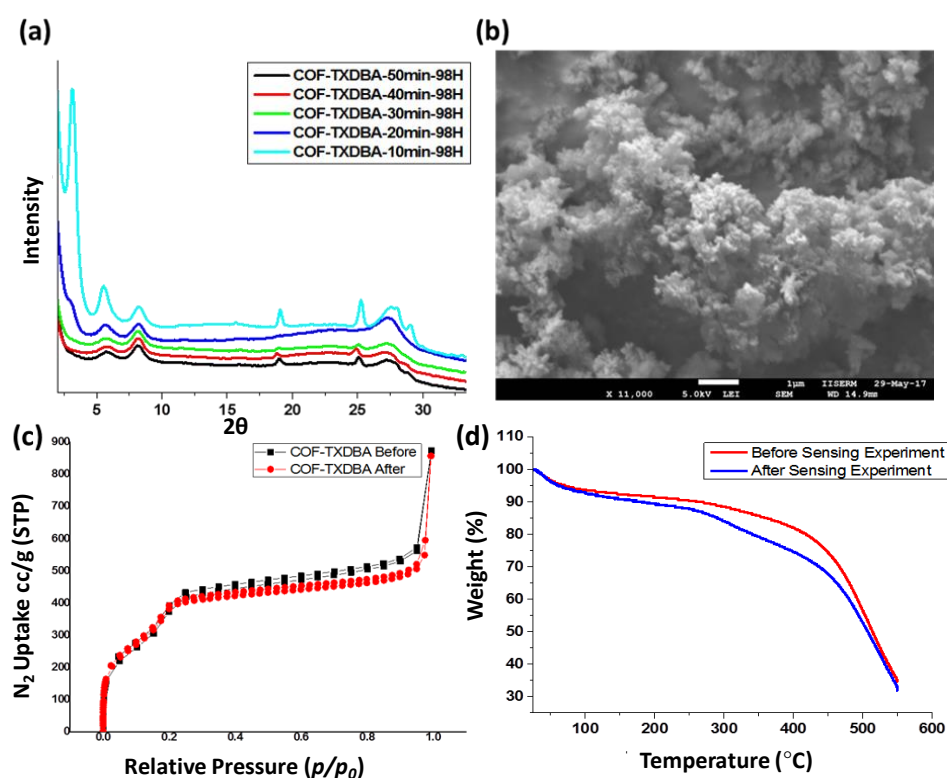

Figure 2.11: (a) %RH dependent stability test of COF-TXDBA is performed by checking its PXRD after each cycle of an experiment from 11-98 %RH. The sample was dried at 100 °C after each cycle. PXRD of COF shows that the crystallinity of COF-TXDBA remains intact after five cycles of measurements; (b) SEM images of COF-TXDBA after the fifth cycle of humidity sensing experiments.

However, very low-intensity extra peaks also appeared near $2\Theta = 18°$ and $25°$, which shows very few boronic ester bonds are dissociating during the experiment. The SEM image of COF-TXDBA (Figure 2.11b) after the fifth cycle of the humidity sensing experiment also confirms that the morphology of the COF was retained and confirms the excellent stability of the material.

The PXRD patterns as a result of time-dependent stability test for COF-TXDBA were recorded by placing the sample in a chamber containing 98 %RH for 10 min, 20 min, 30 min and 50 min time interval. PXRD was recorded after drying the sample at 100 °C for 10 min. The PXRD patterns of COF-TXDBA measured as a result of the time-dependent

stability test in Figure 2.12a shows that the sample can sustain its long-range order and structural morphology in high humidity conditions (98 %RH) as well. The SEM image of COF-TXDBA (Figure 2.12b) after 50 min time interval also confirms that the morphology of the COF was retained and confirms the excellent stability of the material (Figure 2.12c) .

Figure 2.12: (a) Time-dependent stability test of COF-TXDBA by keeping the sample in 98 %RH humidity chamber for 50 min. PXRD was measured after each 10 min intervals show that the long-range order of COF-TXDBA has reduced with time; (b) SEM images of COF-TXDBA after keeping the sample in 98 %RH for long 50 min; (c) Nitrogen isotherm at 77 K for COF-TXDBA before and after 98 %RH for 50 min followed by overnight vacuum drying at 120 °C; (d) Thermogravimetric analysis (TGA) of as-synthesized COF-TXDBA and analysis of the sample after the sensing experiment.

The BET measurement study for COF-TXDBA after exposing the sample to 98 %RH and thereafter drying overnight (120 °C) shows that the porous feature of the COF remains intact after this treatment. However, a decrease in the surface area was observed for the treated COF (1048 m²/g) as compared to the as-synthesized COF (1526 m²/g). Thermogravimetric analyses (TGA) of COF-TXDBA after the sensing experiment shows nearly 10% weight loss after 250 °C as compare to as-synthesized COF-TXDBA, which can be attributed to the formation of the small number of oligomers during interaction of water molecule and COF-TXDBA (Figure 2.12d). This also confirms that the condition used during the sensing experiment is not too harsh to affect the nature of the COF. The long-term stability response of the COF-TXDBA sensor was measured by recording the sensor impedance at each %RH for 70 days (Figure 2.13). A standard deviation of just 2.3%, which is calculated as the average value of impedance at each %RH level accounts for the excellent stability of the COF-TXDBA material.
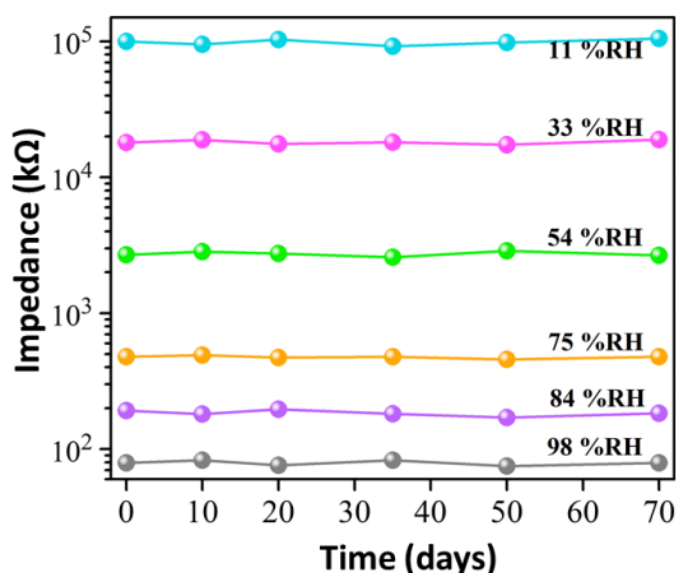
Figure 2.13: The response of COF-TXDBA monitored at different humidity conditions for 70 days.

2.6 Mechanism:

The reason for the good response towards humidity sensing is due to the presence of boronic ester linkages, which interacts with the water molecules in the planar sheets of COF backbone. Due to the high surface area and ordered micropores/ mesopores in this COF-TXDBA, a large number of boronic ester active site is exposed for the interaction of water molecules. Under the low %RH conditions, little amount of water molecules are adsorbed on the surface of sensor and form first chemisorbed layer through Lewis acid-base interaction, where empty orbitals of boron atom interact with the electron lone pair of oxygen atom of water molecule. A few water molecules forms a discontinuous layer and causes hinder in the free movement of water molecules, as a result, high impedance was observed under low %RH conditions. However, high %RH pushes the system for multilayer adsorption of water molecules and helps in the formation of continues array of water molecules in nanoporous channels. This continues array of water molecules provides a favorable condition for the process of charge transportation following the Grotthuss chain reaction ($H_2O + H_3O^+ \rightarrow H_3O^+ + H_2O$) and an abrupt increase in conductivity of the sensor was observed.[19] Under high %RH conditions, the electric field ionizes the water molecules to produce hydronium ions (H_3O^+) as charge carriers, which upon hydration produces protons ($H_3O^+ \rightarrow H_2O + H^+$) and hopping of these protons between adjacent water molecules become easier at high %RH.

2.7 Photophysical Properties:

In addition to the sensing attributes, we tried to explore the optical properties of COF-TXDBA samples for their application in the related areas. The diffuse reflectance spectra show the sample has wide absorbance in the visible region centered at around 450 nm with the significance tail absorption from 800 nm onwards, see Figure 2.15a. The

emission spectra of the photoluminescence spectra with a peak at around 565 nm shows the applicability of these frameworks in optical sensing applications (Figure 2.15b). The bandgap is estimated using Kubelka-Munk function to be around 2.3 eV, (Appendix, Figure A2.7).
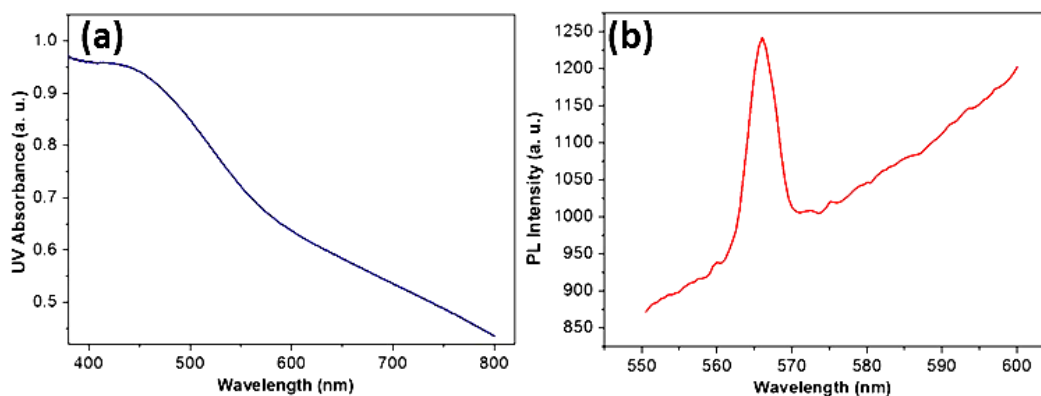
Figure 2.15: Diffuse-reflectance UV‑Vis spectra (a) and Photoluminescence spectra; (b) of the COF-TXDBA sample.

2.8 Summary:

In this report, we have demonstrated the first example in which Tx was used as a building block for the COF-TXDBA synthesis. DFT calculation shows a good agreement with experimental PXRD and the pore size distribution of this framework. The interaction of boronic ester linkage with the water molecules in the nanoporous channels of COF-TXDBA helps in humidity sensing. The COF-TXDBA based %RH sensor shows efficient sensing capabilities with 3 orders magnitude change of impedance in 11-98 %RH range with response time and recovery time of 37 s and 42 s, respectively. They show excellent reversibility with a deviation of 2.3% in the process of switching back and forth in the process of adsorption and desorption. The quick recoverability ad stability of the COF-TXDBA is shown through repeated humidity exposure, sensing measurements followed

by PXRD analysis. These features unfold the additional role that the COFs can play in emerging applications.

References:

1. Goubard, F.; and Dumur, F. *RSC Adv.* **2015**, 5, 3521.

2. Sanguinet, L.; Williams, J. C.; Yang, Z.; Twieg, R. J.; Mao, G.; Singer, K. D.; Wiggers, G.; Petschek, R. G. *Chem. Mater.* **2006**, 18, 4259.

3. Lambert, C.; Noell, G.; Schmaelzlin, E.; Meerholz, K.; Braeuchle, C. *Chem.–Eur. J.* **1998**, 4, 2129.

4. Das, G.; Biswal, B. P.; Kandambeth, S.; Venkatesh, V.; Kaur, G.; Addicoat, M.; Heine, T.; Verma, S.; Banerjee, R. *Chem. Sci.* **2015**, 6, 3931.

5. Xie, Y. F.; Ding, S. Y.; Liu, J. M.; Wang, W.; Zheng, Q. Y. *J. Mater. Chem. C* **2015**, 3, 10066.

6. Li, Z.; Zhang, Y.; Xia, H.; Mu, Y.; Liu, X. *Chem. Commun.* **2016**, 52, 6613.

7. Ding, S. Y.; Dong, M.; Wang, Y. W.; Chen, Y. T.; Wang, H. Z.; Su, C. Y.; Wang, W. *J. Am. Chem. Soc.* **2016**, 138, 3031.

8. Tomer, V. K.; Duhan, S. *Sens. Actuators B* **2016**, 223, 750.

9. Tomer, V. K.; Duhan, S.; Malik, R.; Nehra, S. P.; Devi, S. *J. Am. Ceram. Soc.* **2015**, 98, 3719.

10. Jiang, K.; Zhao, H.; Dai, J.; Kuang, D.; Fei, T.; Zhang, T. *ACS Appl. Mater. Interfaces* **2016**, 8, 25529.

11. Tomer, V. K.; Thangaraj, N.; Gahlot, S.; Kailasam, K. *Nanoscale* **2016**, 8, 19794.

12. Robinson, A. L.; Stavila, V.; Zeitler, T. R.; White, M. I.; Thornberg, S. M.; Greathouse, J. A.; Allendorf, M. D. *Anal. Chem.* **2012**, 84, 7043.

13. Wang, K.; Qian, X.; Zhang, L.; Liand, Y.; Liu, H. *ACS Appl. Mater. Interfaces* **2013**, 5, 5825.

14. Frisch, M. J. E. A.; Trucks, G. W.; Schlegel, H. B.; Scuseria, G. E.; Robb, M. A.; Cheeseman, J. R.; Scalmani, G.; Barone, V.; Mennucci, B.; Petersson, G.; Nakatsuji, H. *Gaussian 09, Revision A. 02*, Gaussian. Inc., **2009**.

15. *Materials Studio, version 7.0*, Accelrys Software Inc., San Diego, CA, **2009**.

16. Masuhara, A.; Tan, Z.; Kasai, H.; Nakanishi, H.; Oikawa, H. *Jpn. J. Appl. Phys.* **2009**, 48, 050206.

17. Fang, Q.; Zhuang, Z.; Gu, S.; Kaspar, R. B.; Zheng, J.; Wang, J.; Qiu, S.; Yan, Y. *Nat. Commun.* **2014**, 5, 4503.

18. Koo, B. T.; Dichtel, W. R.; Clancy, P. A. *J. Mater. Chem.* **2012**, 22, 17460.

19. Grotthuss, D. *Ann. Chim.* **1806**, 58, 54.

20. Wang, R.; Zhang, T.; He, Y.; Li, X.; Geng, W.; Tu J.; Yuan, Q.; *J. Appl. Polym. Sci.* **2010**, 115, 3474.

21. Tomer, V. K.; Duhan, S. *Sens. Actuators B* **2015**, 212, 517.

22. Qi, Q.; Zhang, T.; Zheng X.; Wan, L. *Sens. Actuators B* **2008**, 135, 255.

23. Geng, W.; Wang, R.; Li, X.; Zou, Y.; Zhang, T.; Tu, J.; He, Y.; Li, N.; *Sens. Actuators B* **2007**, 127, 323.

24. Tsai F. S.; Wang, S. J. *Sens. Actuators B* **2014**, 193, 280.

25. Zhang, N.; Yu, K.; Zhu Z.; Jiang, D. *Sens. Actuators A* **2008**, 143, 245.

26. Wang, L. L.; Wang, H. Y.; Wang, W. C.; Li, K.; Wang X. C.; Li, X. J. *Sens. Actuators B* **2013**, 177, 740.

27. Qiu Y.; Yang, S. *Adv. Funct. Mater.* **2007**, 17, 1345.

28. Zhang, T.; Wang, R.; Geng, W.; Li, X.; Qi, Q.; He Y.; Wang, S. *Sens. Actuators B* **2008**, 128, 482.

29. Anbia M.; Fard, S. E. M. *Sens. Actuators B* **2011**, 160, 215.

30. Sundaram, R. *Sens. Actuators B* **2007**, 124, 429.

31. Hu, S.; Chen, H.; Fu G.; Meng, F. *Sens. Actuators B* **2008**, 134, 769.

32. Pandey, N. K.; Roy, A.; Tiwari, K.; Mishra, A.; Rai, A.; Jayaswal, S.; Rashmi M.; Govindan, A. *1st International Symposium on Physics and Technology of Sensors (ISPTS-1), Pune, India,* **2012**, 1, 129.

33. He, X.; Geng, W.; Zhang, B.; Jia, L.; Duan L.; Zhang, Q. *RSC Adv.* **2016**, 6, 38391.

34. Xia, Y.; Zhao, H.; Liu S.; Zhang, T. *RSC Adv.* **2014**, 4, 2807.

35. Zhen, Y.; Sun, F.–H.; Zhang, M.; Jia, K.; Li L.; Xue, Q. *RSC Adv.* **2016**, 6, 27008.

36. Fei, T.; Zhao, H.; Jiang K.; Zhang, T. *Sens. Actuators B* **2015**, 208, 277.

37. Lin, W.–D.; Liao, C.–T.; Chang, T.–C.; Chen, S.–H.; Wu, R.–J. *Sens. Actuators B* **2015**, 209, 555.

38. Liang, S.; He, X.; Wang, F.; Geng, W.; Fu, X.; Ren J.; Jiang, X.; *Sens. Actuators B* **2015**, 208, 363.

39. Khadse, V.R.; Thakur, S.; Patil K. R.; Patil, P. *Sens. Actuators B* **2014**, 203, 229.

Appendix 2

1H.005.esp
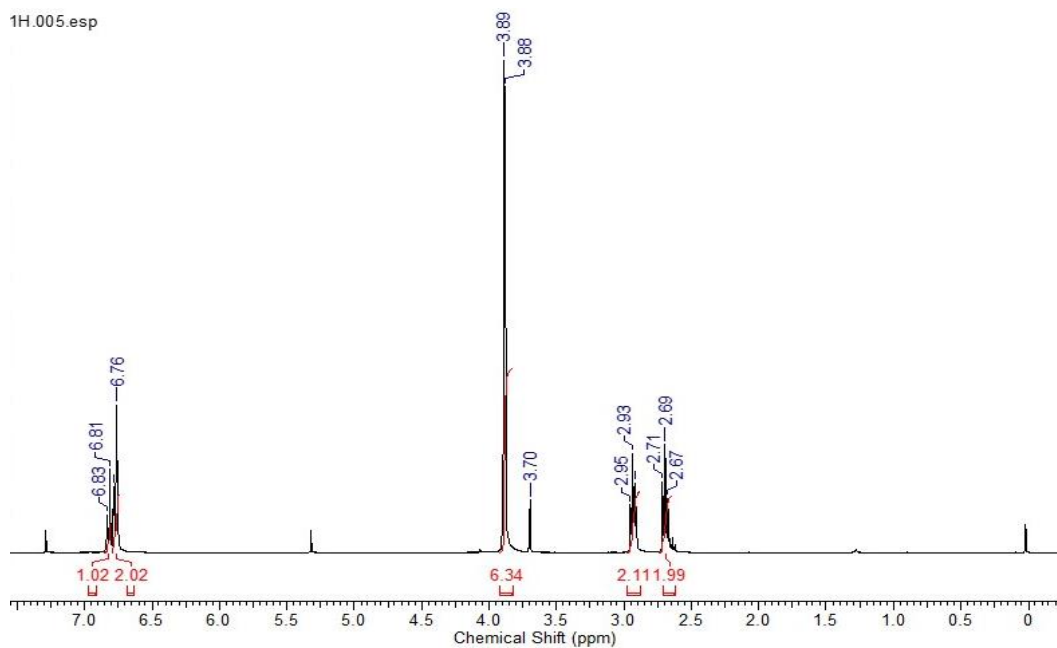
Figure A2.1: ^{1}H NMR spectra of compound (a).

13C.010.esp
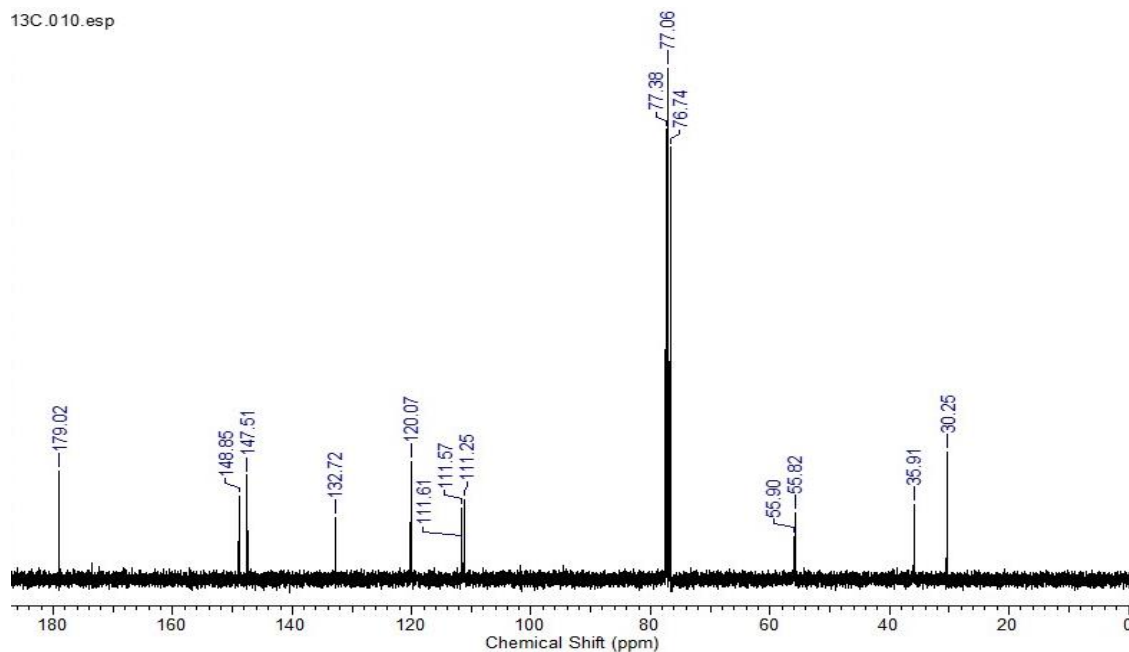
Figure A2.2: ^{13}C NMR spectra of compound (a).

1H.006.esp
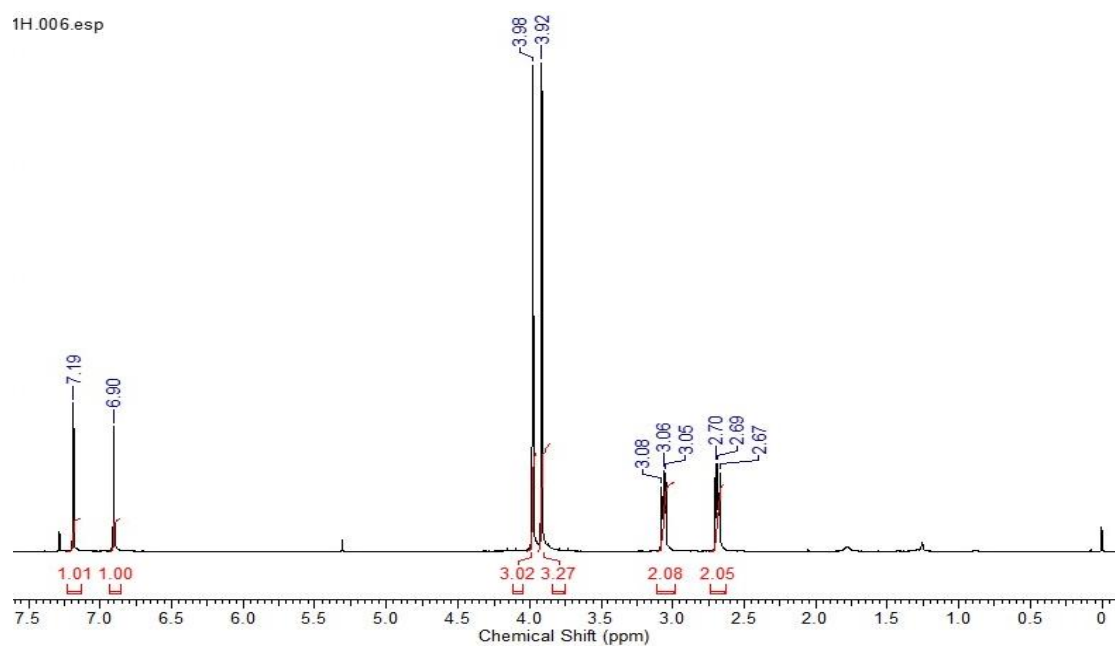
Figure A2.3: ^{1}H NMR spectra of compound (b).

13C.020.esp
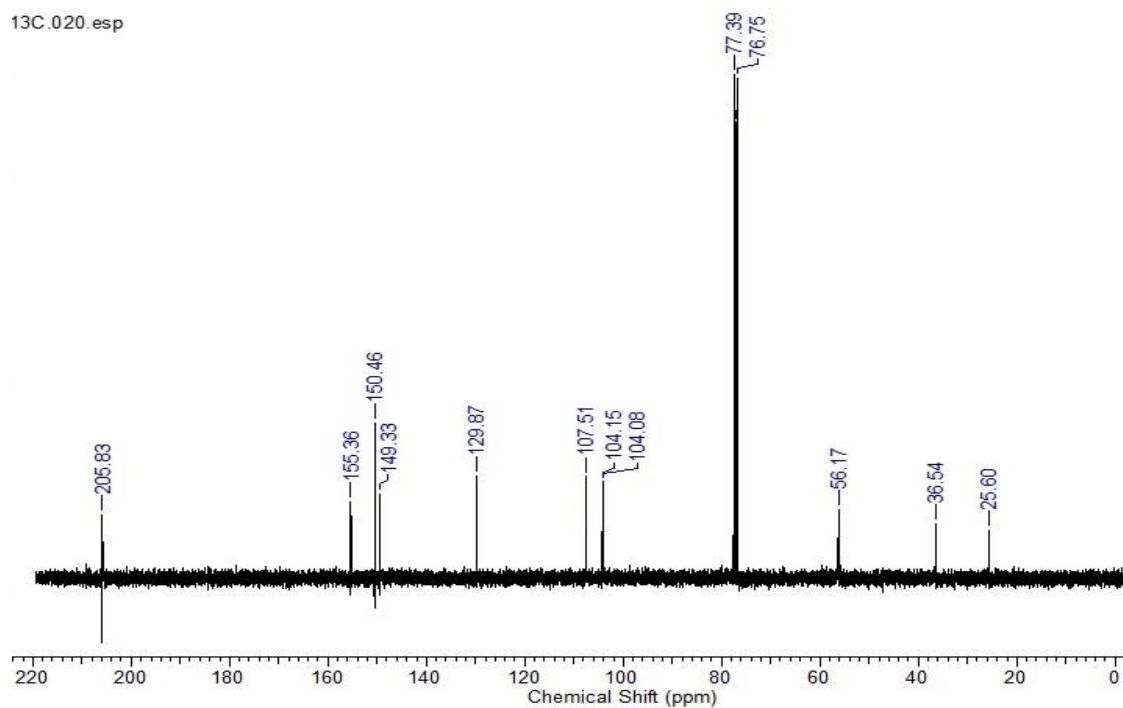
Figure A2.4: ^{13}C NMR spectra of compound (b).
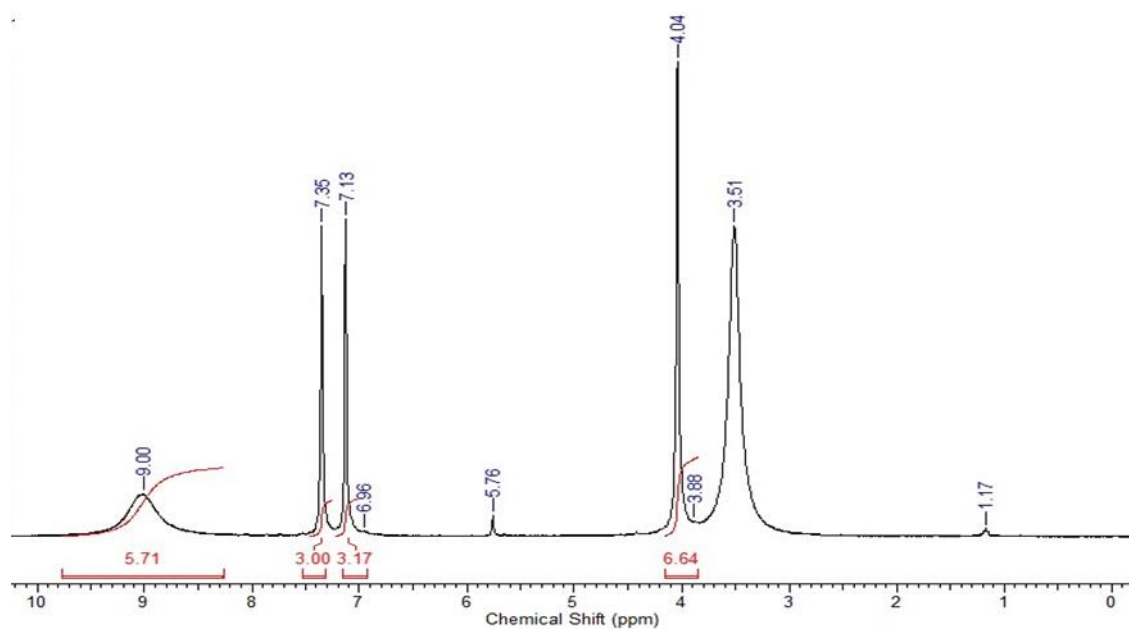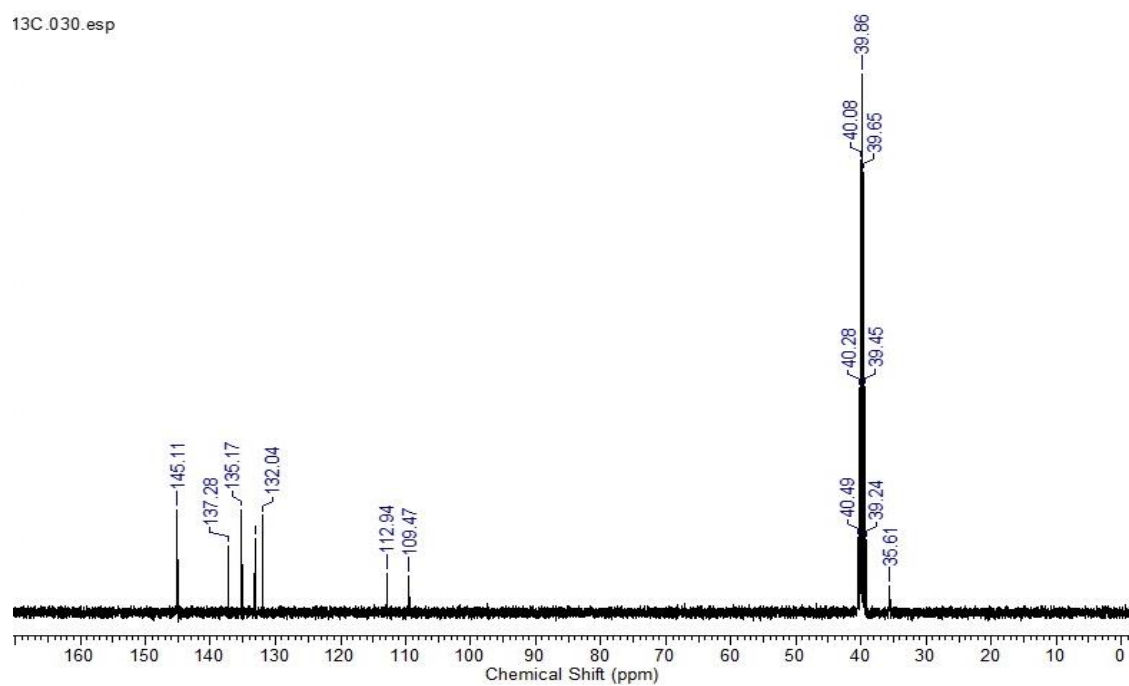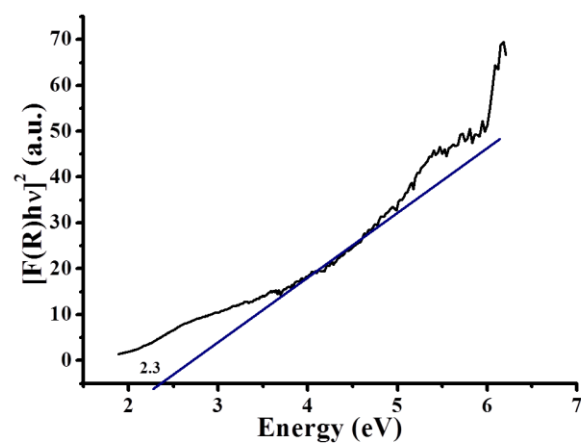
Figure A2.5: ^{1}H NMR spectra of compound (d).

Figure A2.6: ^{13}C NMR spectra of compound (d).

Table A2.1: A comparison of humidity sensing performance of previously published works.

Sr. No.	Material	Order of magnitude change in impedance in complete %RH range	Response time (s)	Recovery time (s)	Hysteresis (%)	Ref
1	NiO-PPY/SBA-15	3.5	45	90	--	20
2	SnO_2/SBA-15	4.5	33	50	2.9	21
3	Fe/SiO_2	3.5	20	50	--	22
4	Li doped mesoporous silica	3	21	51	6	23
5	ZnO nanosheets	2	600	3	5	24
6	Feather like ZnO	2	40	80	--	25
7	ZnO cauliflowers	--	20	3	4.16	26
8	ZnO nanotetrapods	--	36	17	--	27
9	La^{3+} and K^+ doped TiO_2–10 mol% SnO_2	5	11	18	--	28
10	$SnWO_4$-SnO_2	3	30	100	--	29
11	K^+-doped SnO_2–$LiZnVO_4$	3	80	100	--	30
12	MgO-KCl/SiO_2	4	6	26	4	31
13	WO_3-SnO_2	3	117	411	3	32
14	NaCl-KIT-6	5	47	150	--	33
15	MCM-48 fibre	2	15	18	5	34
16	Fe/SnO_2	4	1	4	--	35
17	Nanoporous polymers based on 1,4-divinylbenzene	3	3	75	4	36
18	Graphene/TiO_2	3	128	68	0.39	37
19	LiCl-PEBAX nanofiber	4	30	80	negligible	38
20	CeO_2	3	2-3	9-10	<1	39
21	COF-TXDBA	3	37	42	2.5	This work

Figure A2.7: Bandgap estimated of COF-TXDBA using Kubelka-Munk function.

Chapter 3

Proton Triggered Fluorescence Switching in Self-Exfoliated Ionic Covalent Organic Nanosheets for Applications in Selective Detection of Anions
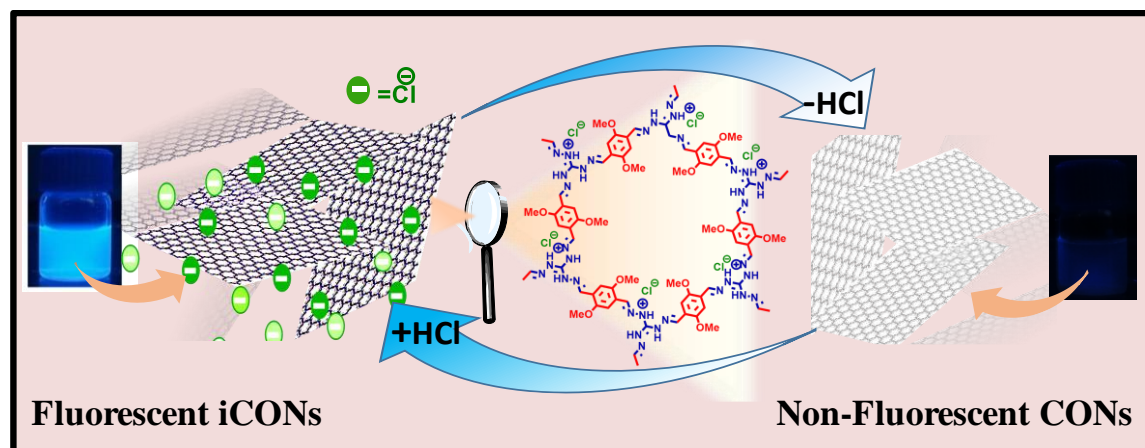
The exfoliation of covalent organic frameworks (COFs) into covalent organic nanosheets (CONs) not only helps to reduce fluorescence turn-off phenomena but also provides well-exposed active sites for fast response and recovery for various applications. The present work is an example of the rational designing of highly fluorescent self-exfoliable ionic CONs. These fluorescent iCONs are able to sense fluoride ions selectively down to ppb level via fluorescence turn-off mechanism. A closer look at the quenching mechanism reveals unique proton triggered fluorescence switching behavior of newly synthesized DATG$_{Cl}$-iCONs.

3.1 Aim:

As mentioned in chapter 2, secondary forces (π-π interactions, H-bonding, etc.) play a crucial role to produce highly crystalline, stable COFs with 1D nano-channels for various applications.[1-3] However, some adverse effects of these layered structures like aggregation-caused quenching (ACQ), poor electron mobility and poor accessibility of deeply buried active sites in the nano-channels lead to the moderate performance of 2D COFs, especially for applications where photoluminescence properties and fast response-recovery are concerned.[4] To counter these negative effects, exfoliation of COFs has been carried out using mechanical delamination,[5] chemical modification,[6-7] ultrasonication[8-9] to obtain the nanosheets of single layer or a few layers.[4-11] But, these techniques have some own disadvantages like small-scale processing, alteration of the original chemical structure and high energy consumption, etc., which limits their widespread use in large-scale commercial applications. These issues, however, can be addressed through the development of self-exfoliate 2D COFs[12-15] to produce smart materials with tunable photoluminescence properties and well-exposed active sites for desired applications.

In this chapter, the bottom-up synthesis of highly fluorescent self-exfoliable covalent organic nanosheets (CONs) via condensation of the fluorophore with an ionic linker is demonstrated. This unique design not only provides an opportunity to tune the photophysical properties of CONs *via* choosing an appropriate fluorophore but also promote the exfoliation due to intrinsic ionic repulsions between the layers. Moreover, if the ionic linker itself has a molecular sensing ability then these ionic CONs (iCONs) can be potential candidates to transduce molecular recognition into fluorescence signals that are visible to the naked eye.

In pursuit of this, we have chosen guanidinium chloride, a well-known anion receptor[16-24] for the construction of the CONs to the realization of a new class of sensors for anion

detection. Anion sensing has attracted significant attention in supramolecular chemistry as anions play a crucial role in various chemical and biological processes.[25]Among various anions, fluoride (F⁻) ion is of great interest because of its adverse effects. It is useful in dental care, in the treatment of osteoporosis, water treatment, and in many other applications. Excess presence of F⁻ causes fluorosis and the fluorination of drinking water supplies. Hence, the development of precise methods for the detection of fluoride ions are in acute demand for fluoride hazard assessment and fluoride pollution management.[24-28] These important aspects of fluoride (F⁻) sensing make this work important, as newly synthesized CONs have shown ppb level sensitivity and high selectivity towards fluoride (F⁻).

3.2 Experimental Section:

All chemicals and solvents were of analytical grade and used as it is received for the synthesis and spectroscopic studies. The synthesized materials and iCONs were characterized by various spectroscopic techniques as reported in Chapter 2.

3.2.1 Synthesis:
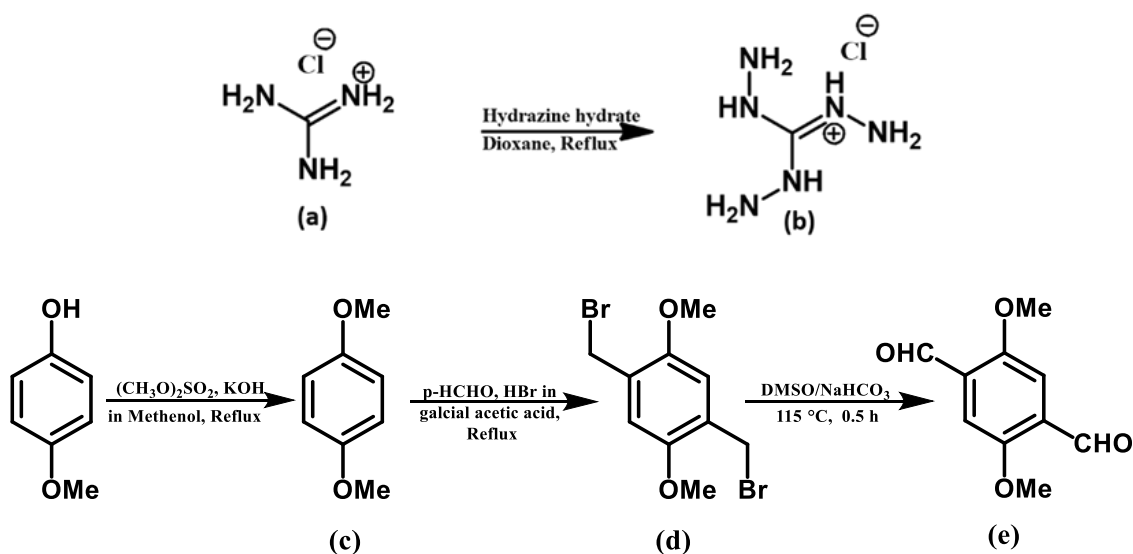
Scheme 3.1: Synthesis of monomer used to build the iCONs.

94

The monomers used to build the iCONs were synthesized according to the literature with slight modifications (Scheme 3.1).[14, 29] In addition to the iCONs, model compound (ATG$_{Cl}$) was also synthesized as a reference to characterize the bulk iCONs (Scheme 3.2).

Synthesis of Triaminoguanidinium Chloride (TG$_{Cl}$) (b): Triaminoguanidinium chloride **(b)** was synthesized according to reported procedure.[14] Guanidine hydrochloride (1.9 g, 19.9 mmol) **(a)** and hydrazine hydrate (3.4 g, 68 mmol) were refluxed in 10 mL of 1,4-dioxane for 4 h under N$_2$ environment. After cooling the reaction mixture to room temperature, a white precipitate was filtered and washed with plenty of 1,4-dioxane to remove excess hydrazine hydrate and finally drying the crude in vacuum at 60 ˚C results **(b)** (Yield: 98%). The formation of **(b)** was confirmed via comparing FT-IR spectrum with previously reported data.[14]

Synthesis of 1,4-Dimethoxybenzene (c)[29]: Compound **(c)** was synthesized as per reported procedure.[29] 4-methoxyphenol (10.0 g, 80.60 mmol) and KOH (6.7 g, 120.9 mmol) was dissolved in 40 mL methanol in ice-cold solution under N$_2$ atmosphere. Dimethylsulfate (17.5 mL) was added slowly to the reaction mixture was refluxed at 60 °C for 6 h. After cooling to room temperature, the reaction mixture was poured into a large amount of water and extracted by ethyl acetate. After solvent evaporation, the product was obtained as a white solid which was purified by column chromatography. Formation of **(c)** was confirmed by comparing ^{1}H and ^{13}C NMR spectra with previously reported data.[29]

Synthesis of 1,4-Bis(bromomethyl)-2,5-dimethoxybenzene (d)[29]: Compound **(d)** was synthesized as per reported procedure.[29] Compound **(c)** (10.0 g, 72.40 mmol) and *p*-HCHO (8.70 g, 289.80 mmol) were dissolved in acetic acid (50 mL). Using a pressure-

equalizing funnel 36.23 mL of HBr in acetic acid (30–33 wt%) was added dropwise to the above reaction mixture and refluxed for 8 h. After cooling to room temperature, the reaction mixture was poured into water. The crude material obtained as white precipitate was washed with an excess of cold water until the filtrate became neutral. Formation of **(d)** was confirmed by comparing ¹H and ¹³C NMR spectra with previously reported data.[29]
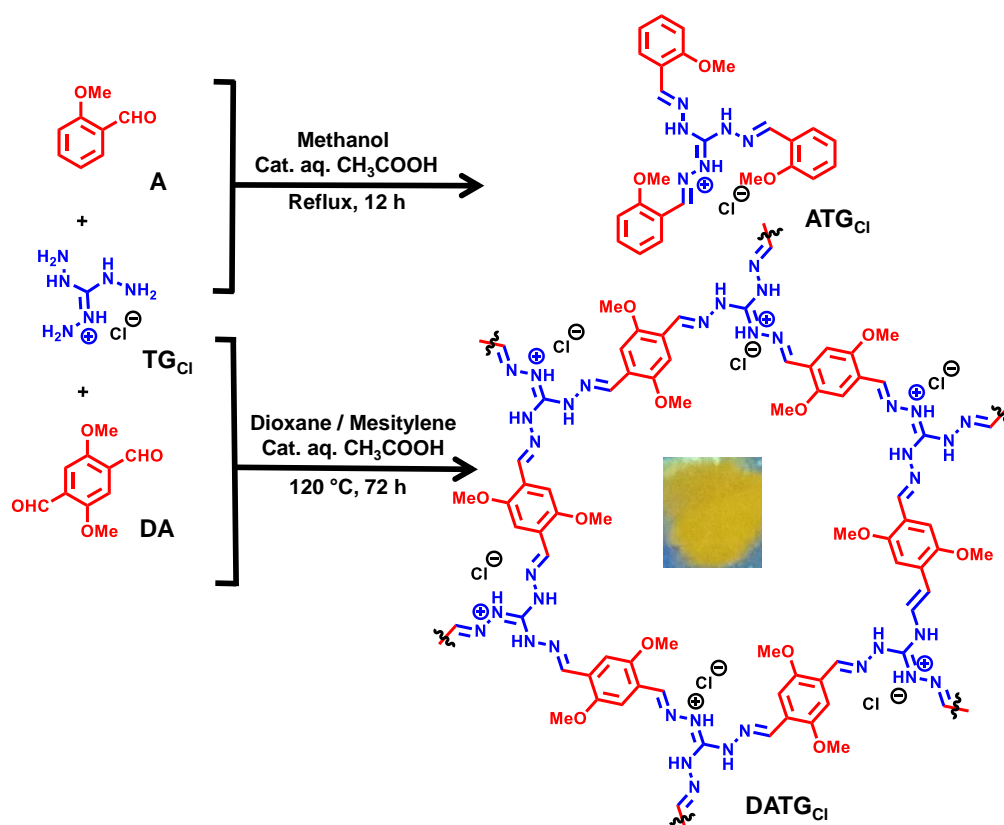
Scheme 3.2. Synthesis of monomeric unit ATG$_{Cl}$ and the bulk DATG$_{Cl}$-iCONs.

Synthesis of 2,5-dimethoxyterephthalaldehyde (DA) (e): Compound **(d)** (1.6 g, 5 mmol) and sodium bicarbonate (6.3 g, 75 mmol) were stirred in 80 mL DMSO at 115 °C for 0.5 h. And then the reaction mixture was poured into water (200 mL). The precipitate was filtered and dried. Crude product was further recrystallized in DCM/hexane mixture

to get the pure compound (**e**) in 69% isolated yield.[14] ^1H NMR (CDCl$_3$, 400 MHz) δ ppm: 10.50 (s, 2H, Ar-C**HO**), 7.45 (s, 2H, Ar–**H**), 3.94 (s, 6H, Ar–OC**H₃**).

Synthesis of Model Compound (ATG$_{Cl}$): Model compound (ATG$_{Cl}$) was synthesized according to the previously reported procedure.[14] Triaminoguanidinium chloride (TG$_{Cl}$) (2.34 g, 0.017 mol) and was dissolved in 81 ml hot mixture of MeOH and H$_2$O (2:1 v/v). 2-methoxybenzaldehyde (A) (0.05 mol) in MeOH was added dropwise to the above mixture and refluxed for overnight. The precipitate of ATG$_{Cl}$ monomer was obtained as yellow solid. The crude product was washed with acetone and dried under high vacuum. Hot saturated ethanol solution of crude ATG$_{Cl}$ was slowly cooled to room temperature and kept it overnight to obtain the needle like transparent crystals of pure ATG$_{Cl}$. (Appendix, Figure A3.1).

Synthesis of DATG$_{Cl}$: In a typical procedure, amine TG$_{Cl}$ (28 mg) and 58 mg aldehyde DA (2, 5-dimethoxyterephthalaldehyde) were taken in 1:1 ml solvent mixture of dioxane/mesitylene (1:1v/v) in one neck round bottom flask.. This mixture was then sealed, purged with nitrogen for 15 min followed by sonication for 5 min. To this mixture, 0.1 ml CH$_3$COOH (6 M) was added and kept for heating at 120 °C for 3 days. Finally, yellow colour precipitate was collected at room temperature *via* centrifuge which was washed thoroughly with THF and dried at 90 °C in vacuum oven. Yield: 83%.

3.2.2 Preparation of DATG$_{Cl}$-iCON:

Self-exfoliation: DATG$_{Cl}$-iCON was prepared via suspending 10 mg bulk DATG$_{Cl}$ in 100 ml methanol for 24 h to get a transparent solution. The solvent was removed via centrifugation (5 min at 3000 rpm) and solid was dried in a vacuum oven for 2 h at 90 °C prior to further characterization via different techniques like PXRD, BET, SEM, TEM, and AFM.

Exfoliation by Sonication: Bulk $DATG_{Cl}$ (1mg) was suspended in 15ml of methanol and sonicated using a simple bath sonicator for about 1 to 2 min to achieve the transparent solution. This method provides quick exfoliation of Bulk $DATG_{Cl}$ and reduces the sample preparation time.

It should be mentioned that the rational design strategy of having intrinsic cationic charge in the $DATG_{Cl}$ allows the material to self-exfoliate into nanosheets within 24 h without any external stimuli to prepare the $DATG_{Cl}$-iCONs. The drawback of this method is that it's a time-consuming process. However, the exfoliation can also be achieved by sonication of bulk $DATG_{Cl}$ in methanol for 2 min in a bath sonicator. We believe that this quick exfoliation is the result of the intrinsic cationic charge already present in the $DATG_{Cl}$.

3.2.3 Anion Sensing Studies:

A stock solution of iCONs was prepared by taking 1 mg $DATG_{Cl}$-iCONs in 15 ml MeOH which was sonicated for 2 min to obtain a nearly transparent dispersion. For sensing studies, 0.1 M aqueous solution of corresponding potassium salts of different anions (F^-, Br^-, I^-, NO_3^-, HPO_4^-, HSO_4^- and SCN^-) were diluted 100 times with methanol to get required 10^{-3} M solution. After each incremental addition of anions, the fluorescent spectra of iCONs were recorded at an excitation wavelength of 337 nm. The selectivity of iCONs towards F^- ions was tested by recording fluorescence spectra on adding F^- in the presence of other anions under similar conditions.

### 3.3 Results and Discussion:

3.3.1 Characterization:

Constructed from robust building blocks, $DATG_{Cl}$ is insoluble in common organic solvents such as THF, DCM, methanol, acetone, acetonitrile, trichloromethane, and *o-*

Dichlorobenzene. Because of the insolubility of DATG$_{Cl}$-iCONs, model compound (ATG$_{Cl}$) was also synthesized as a reference to characterize the bulk iCONs (Scheme 3.2).
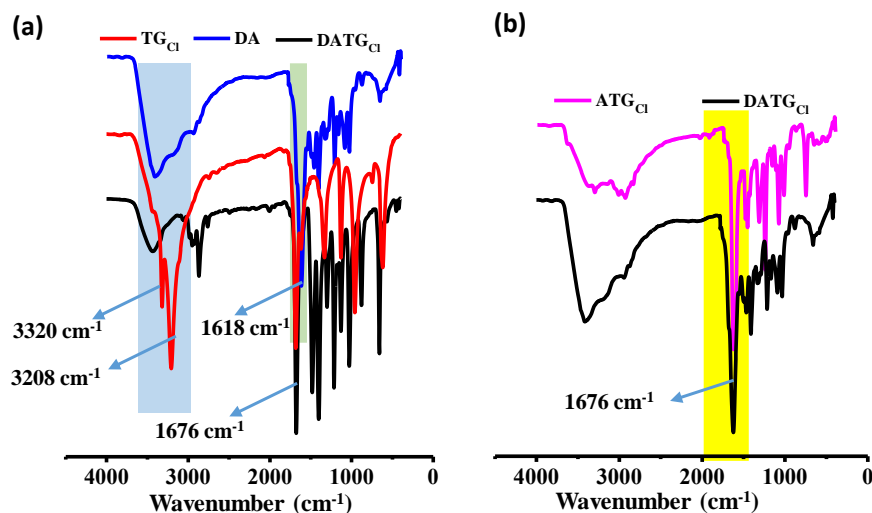

Figure 3.1: (a) Comparison between FT-IR spectra of triaminoguanidinium chloride (TG$_{Cl}$), 2,5-dimethoxyterephthalaldehyde (DA) and DATG$_{Cl}$; (b) Comparison between FT-IR spectra of Model compound, ATG$_{Cl}$, and DATG$_{Cl}$.

The newly developed iCONs were further characterized using various spectroscopy and microscopy techniques (vide infra). FTIR spectrum of iCONs and the precursors were recorded to analyze the formation of Schiff base bond (-C=N-). The comparison shows that the stretching peak of C=O bonds at 1618 cm^{-1} of aldehyde group and N-H vibration bands at 3320 cm^{-1} and 3208 cm^{-1} of TG$_{Cl}$ disappear from the DATG$_{Cl}$ spectrum. However, intense characteristic peaks for C=N bond stretching at 1676 cm^{-1} appeared, which clearly indicates the successful condensation of the monomers (Figure 3.1a). The spectral pattern was satisfactorily matched with the model compound, with a small shift due to the extended conjugation, confirming the formation of iCONs (Figure 3.1b). To ensure the construction of iCONs, the ^{13}C CP-MAS solid-state NMR spectroscopic measurement was carried out. A sharp peak at 56 ppm corresponding to –
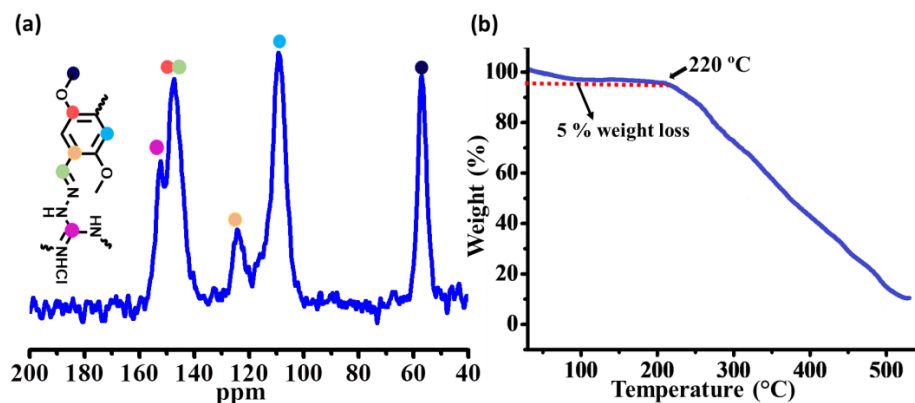
**Figure 3.2:** (a) ^{13}C CP-MAS solid-state NMR spectroscopy of DATG$_{Cl}$; (b) TGA profiles of activated DATG$_{Cl}$.

OCH$_3$ carbon and peaks at 152 ppm carbon from guanidinum unit along with a peak at 147 ppm (from - C=N and benzene carbon attached to -OCH$_3$ group) confirmed the formation of DATG$_{Cl}$ (Figure 3.2a). Thermogravimetric analysis shows that iCONs are stable upto ∼220 °C (Figure 3.2b).
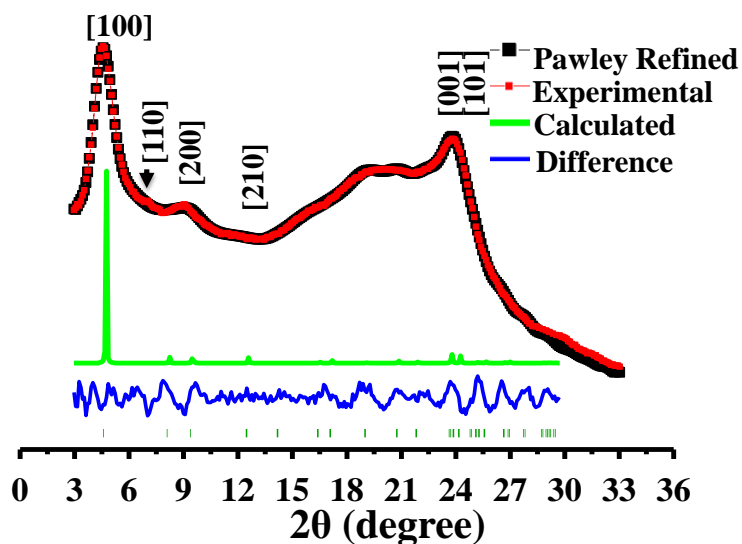
Figure 3.3: Simulated (green) and experimental (black) PXRD of DATG$_{Cl}$-iCONs with Pawley refinement (red) and difference between experimental and simulated PXRD (Blue).

The crystalline structure of iCONs was determined by powder X-ray diffraction (PXRD) analysis with CuK$_\alpha$ radiation. PXRD of iCONs showed the first broad peak at 2θ = ~4.7° corresponding to [100] refection plane. The subsequent minor peaks occurring at an angle 7.2° and 9.5° in the PXRD pattern are attributed to the reflections from [110] and [200] planes, respectively (Figure 3.3, Appendix, Figure A3.2). The broad peak at 2θ = ~ 24.7°signifies poor aromatic π−π stacking and is justifiable by the ionic repulsion between the layers arising from the intrinsic positive charge.
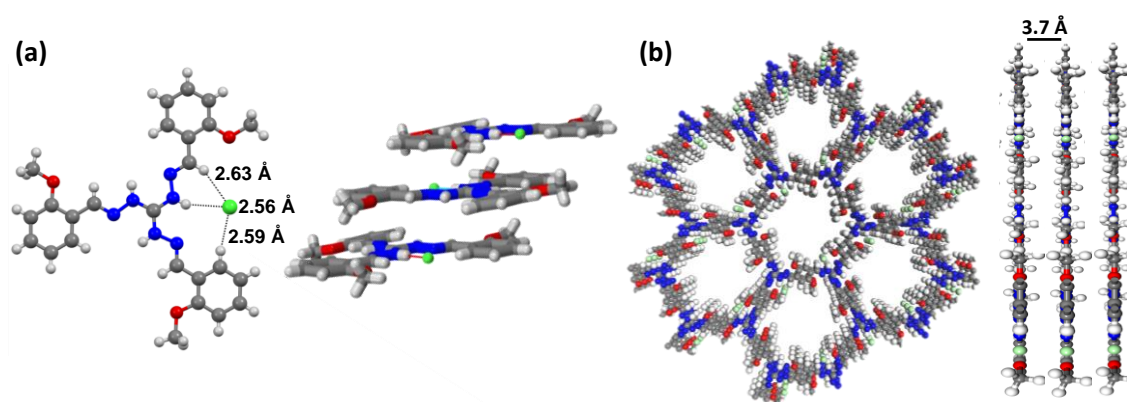
Figure 3.4: (a) Model compound ATG$_{Cl}$ at 50% ellipsoid probability level at 100 K. Moiety formula $C_{25}H_{27}N_6O_3Cl$, space group $P\bar{1}$, a=10.6172(14) Å, b=12.2394(16) Å, c= 12.8906(17) Å; α=97.354(4), β=90.322(5), γ=94.404(4); cell volume 1656.22; (CCDC: **1913917**); (b) Eclipsed geometry of DATG$_{Cl}$-iCONs, top (left) and side (right) view.

In order to obtain precise information of the structure, the single-crystal structure of the model compound was analyzed, which revealed that monomeric units are planar and stacked on each other with inter layer distance ~3.7 Å. The Cl⁻ anion is present in the plane and remains hydrogen bonded with the guanidinium nitrogen (N-H•••• Cl⁻, d = 2.56 Å) (Figure 3.4a). Based on these data, possible 2D eclipsed structure was modeled for DATG$_{Cl}$ (Appendix, Figure A3.2-3.5). The lattice modeling and Pawley refinement with the residual R-weighted-profile factor, Rwp = 0.63% and R-pattern factor, Rp = 0.48% (Accelry's Materials Studio v7.0 package)[30] have furnished optimized parameters of a = b

= 21.37 Å and c = 3.73 Å, α = β = 90°, and γ = 120° for the unit cell with the space group of *P*1. Upon geometrical energy minimization using Gaussian 09,[31] the refined PXRD pattern matches well with that of the experimental one. Comparison of the observed and the simulated PXRD patterns suggest the favorable structure to have the eclipsed arrangement (Figure 3.4b).

3.3.2 Morphology:

To investigate the morphology of iCONs at the nanoscale, various microscopic techniques have been used. The SEM data reveals that the bulk material comprised of overlapping thin sheets having lateral dimensions from micron to sub-micron scale. These structures appear quite transparent in certain regions, even at the low energy (5 keV) beam (Figure 3.5a-b, Appendix, Figure A3.6).[32] The sheet-like morphology was also supported by TEM images, which show crumbled thin sheets laying on each other (Figures 3.5c-d, Appendix, Figure A3.7). To measure the height of nanosheets AFM was
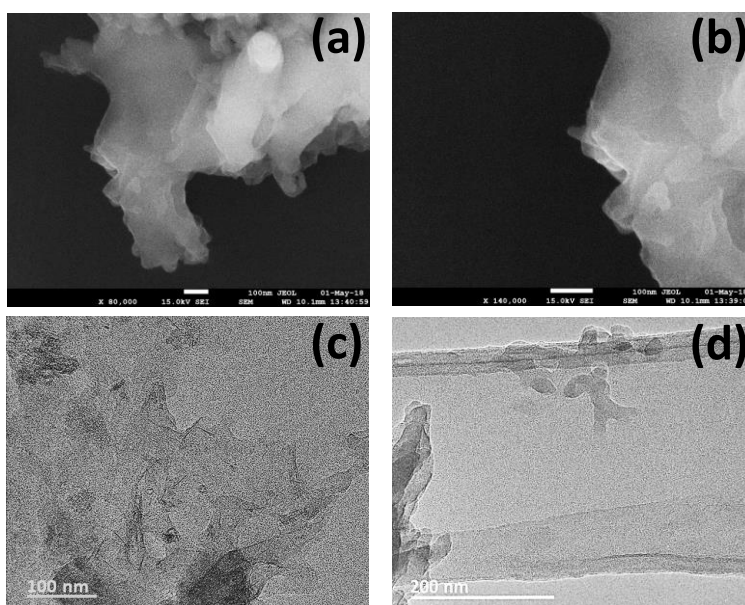
Figure 3.5 (a, b) SEM (scale bar = 100 nm) and (c, d) TEM images of DAG$_{Cl}$-iCONs at different magnifications.

carried out in the tapping mode. The height of the iCONs sheets was in the range 5-7 nm, indicating that iCONs could be exfoliated into 13-18 layers (Figure 3.6a-d).
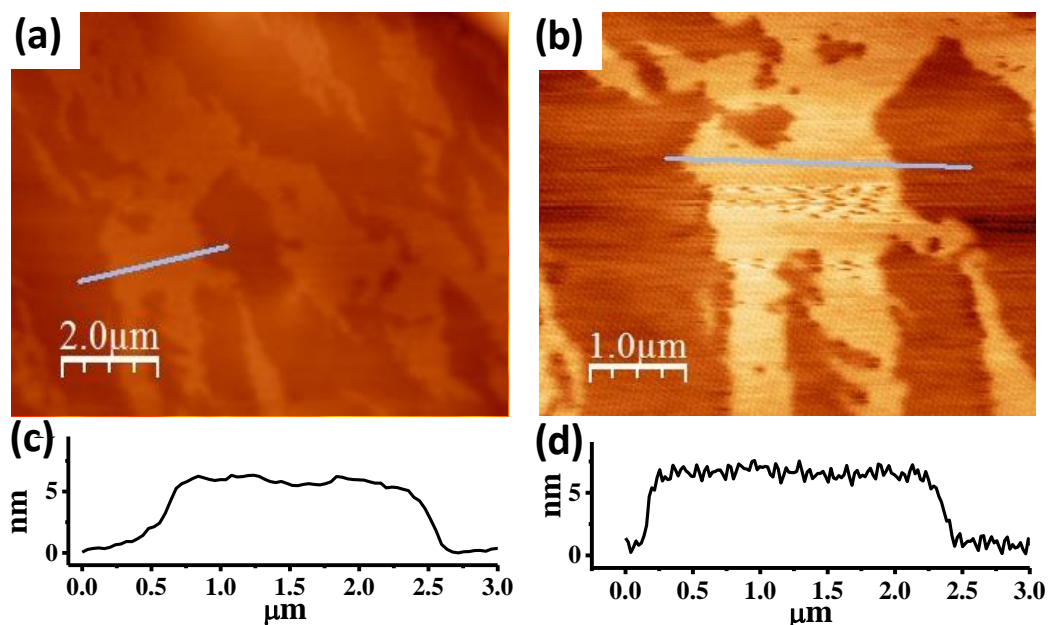
Figure 3.6 (a, b) AFM images and their corresponding height profile (c, d) of DATG$_{Cl}$-iCONs.

3.3.3 Surface Area and Porosity:
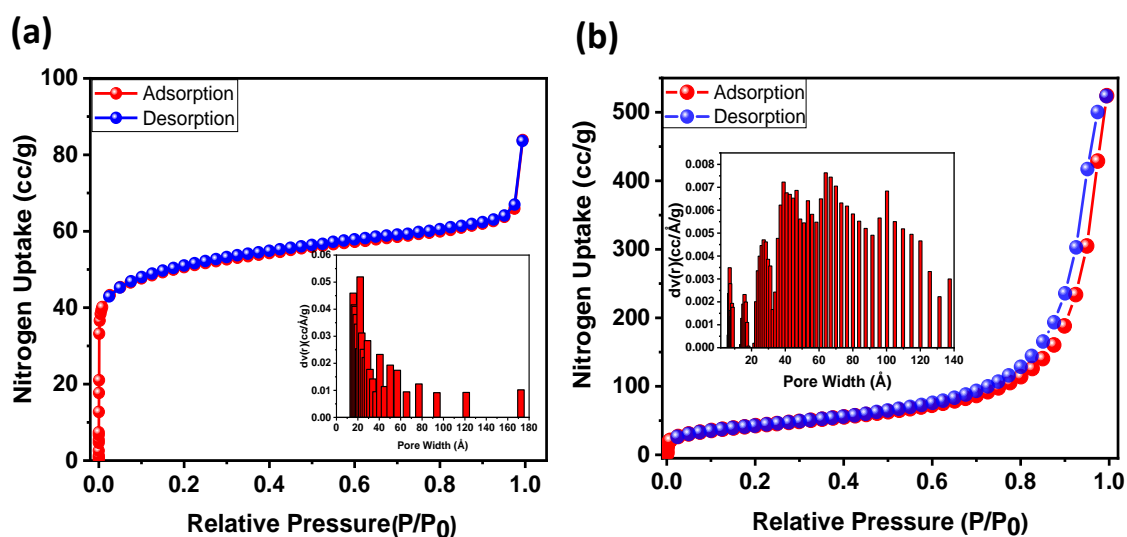
Figure 3.7: Nitrogen adsorption (red) and desorption (blue) isotherm curves and Pore size distribution profile of bulk DATG$_{Cl}$ (inset) of: (a) as synthesized DATG$_{Cl}$; (b) DATG$_{Cl}$-iCONs.

The Brunauer-Emmett-Teller (BET) surface area of $DATG_{Cl}$-iCONs was found to be 155 $m^2\ g^{-1}$, which is found a little lesser than the as-synthesized bulk $DATG_{Cl}$ (189 $m^2\ g^{-1}$)(Figure 3.7). The lesser surface area is probably caused by the self-exfoliation of the as-synthesized $DATG_{Cl}$ in methanol solvent. This low surface area and broad pore size distribution is probably due to the poor stacking and pore blocking by chloride anions. These results were consistent with the previous reports based on CONs.[2, 6, 14]

3.3.4 Photophysical Behaviour:

To investigate the photophysical behavior of the nanosheets absorbance spectra of monomer and iCONs were recorded. In the solid state, DA and ATG_{Cl} exhibited an electronic absorption band at 405 and 364 nm, respectively. However, in case of nanosheets, the absorption band shifted to higher wavelength (441 nm) which is likely due to extended conjugation in their structure (Figure 3.8a). Similarly, we have recorded absorbance spectra of ATG_{Cl} and iCONs in methanol. ATG_{Cl} exhibit an electronic absorption band at 337 nm while iCONs exhibits electronic absorption bands at 302 nm, 340 nm and 390 nm (Figure
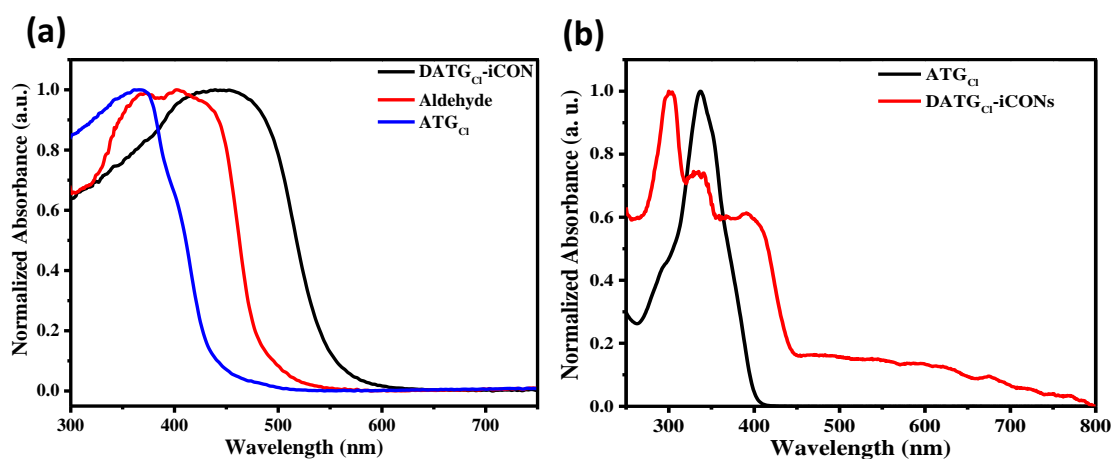
Figure 3.8: (a) Solid state electronic absorption spectra of iCON (black curve), aldehyde (red curve) and monomer (blue curve); (b) Solution state Absorption spectra of $DATG_{Cl}$-iCONs (red) and the corresponding model compound (black).
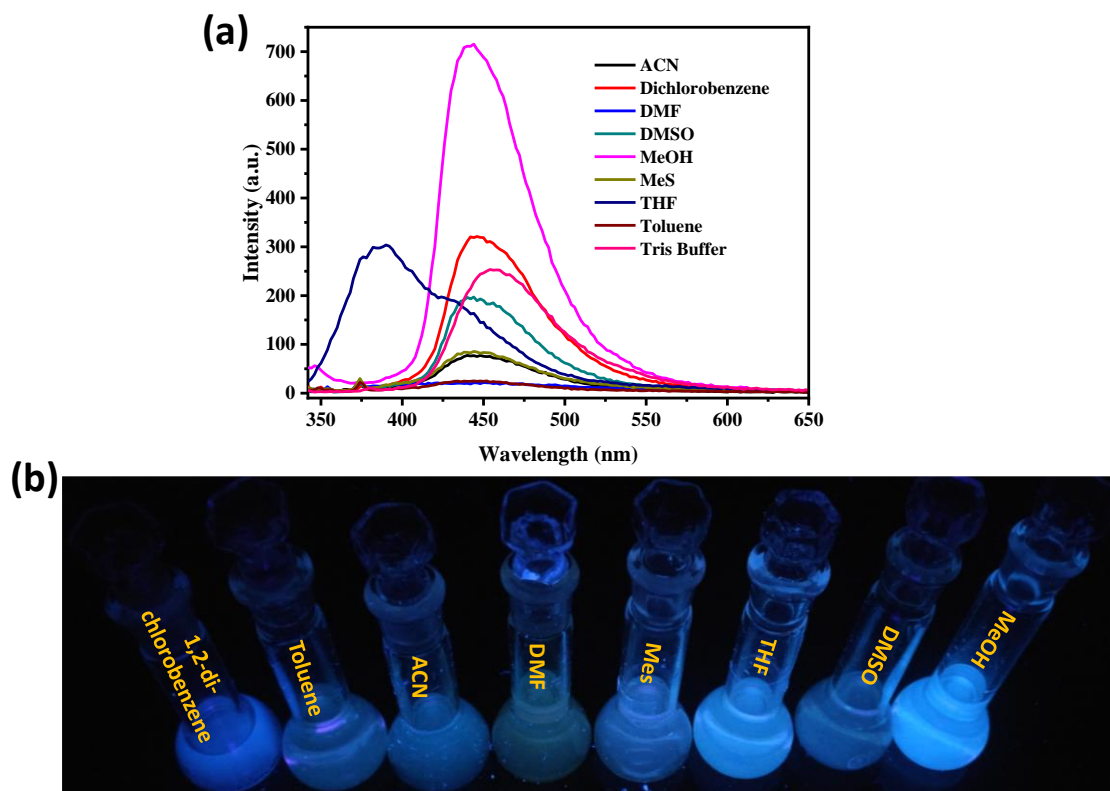
Figure 3.9: (a) Fluorescence spectra of DATG$_{Cl}$ in different solvents, λ_{ex} = 337 nm; (b) DATG$_{Cl}$ in different solvents under UV lamp, λ_{ex} = 365 nm.
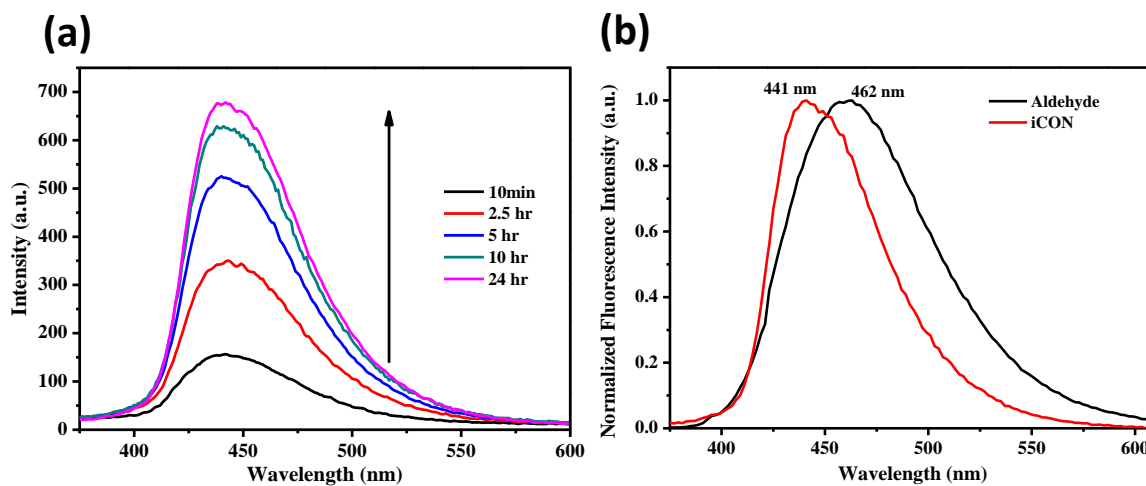
Figure 3.10: (a) Time-dependent changes in emission of DATG$_{Cl}$ in MeOH (λ_{ex} = 337 nm); (b) Fluorescence spectra of monomer aldehyde (DA) and iCONs in methanol.

3.8b). Further, we explored the behavior of fluorescence properties of iCONs in various solvents. It was observed that methanol dispersed iCONs show highest fluorescence intensity among others (Figure 3.9).

(a)   **(b)**

ζ-potential = +32±1.37
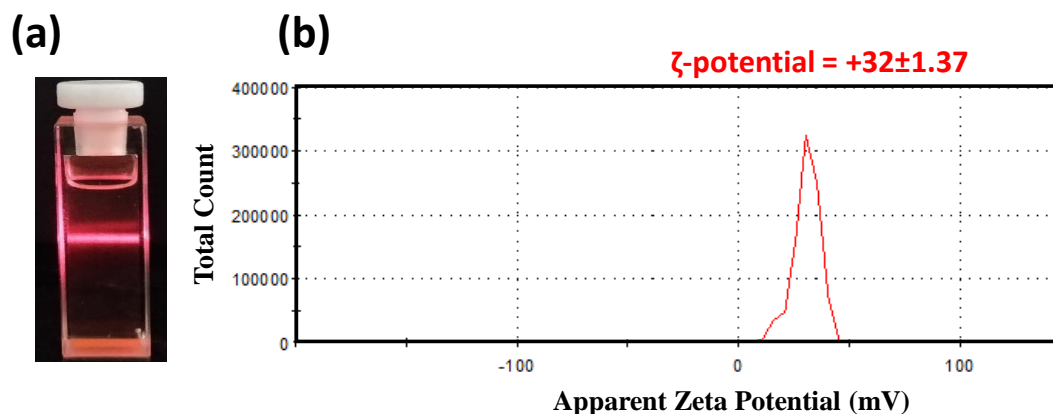
Figure 3.11: (a) Tyndall effect and (b) Zeta potential analysis of DATG$_{Cl}$.

To support the self-exfoliation process, 1 mg of DATG$_{Cl}$-iCONS was suspended in 15 ml of methanol without any external mixing and the emission spectra were recorded with increasing time. A consistent increment in the fluorescence intensity was observed with increasing time and gets saturated within 24 h with a small deviation. We believe that with increasing time, more numbers of sheets of iCONs get detached from the bulk material which minimizes the ACQ and results in the fluorescence enhancement (Figure 3.10a).It might be possible that the fluorescence enhancement could also be the result of the iCONs decomposition or the residual monomer exfiltration. To verify this, we have compared the emission spectra of both iCONs and the monomer aldehyde (DA) in methanol (Figure 3.10b). We have not observed any peak corresponding to DA (λ_{em}= 462 nm) in the emission spectra of the iCONs (λ_{em}= 441 nm). This ruled out the possibility of increased fluorescent intensity of iCONs via COF decomposition or the presence of residual monomer exfiltration. In addition, methanol dispersed iCONs exhibit Tyndall effect (Figure 3.11a) and positive surface zeta potential value (ζ) of +32±1.37 mV (Figure

3.11b). The methanol dispersed iCONs (λ_{max} = 337 nm) show strong blue luminescence at 441 nm with very high quantum yield ($\emptyset_f$ = 0.94).

3.3.5 Anion Sensing Studies:

Further, with the advantage of high fluorescence nature and as a labile counter anion, these iCONs are subjected to anion sensing studies. A stock solution of 1 mg iCONs is dispersed in 15 ml methanol and fluorescence spectra were recorded by adding 10^{-3} M methanol solution of the potassium salt of different anions like F^-, Br^-, I^-, NO_3^-, HPO_4^-, HSO_4^- and SCN^- to this solution. Surprisingly, upon adding the KF, the fluorescence of iCONs was drastically quenched by 67.3 fold leading to an absolute quantum yield 0.17.
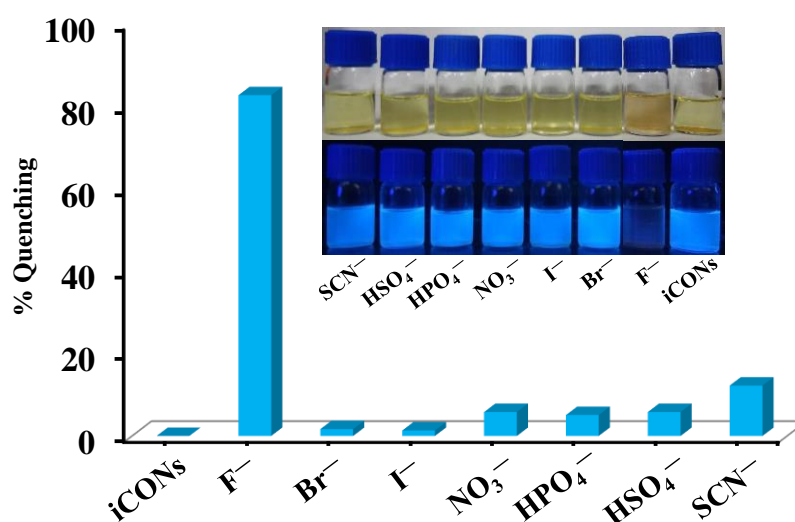
Figure 3.12: % Fluorescence quenching of DATG$_{Cl}$-iCONs on the addition of various anions.

However, no such effect on fluorescence intensity had been observed on the addition of other anions under similar conditions (Figure 3.12, Appendix A3.8). Thus, these systematic studies show that fluorescence intensity decreased with increasing concentration of F^- ion up to 0.5 µM and after that, it becomes saturated (Figure 3.13a). These experimental results showed that the concentration (Figure 3.13b), which is ranked

the best among F⁻ sensors.[25] Further, to check the necessity of DATG$_{Cl}$-iCONs for selective sensing, same experiment was performed with the fluorescent aldehyde building block. The corresponding results show that fluorescent DATG$_{Cl}$-iCONs are highly
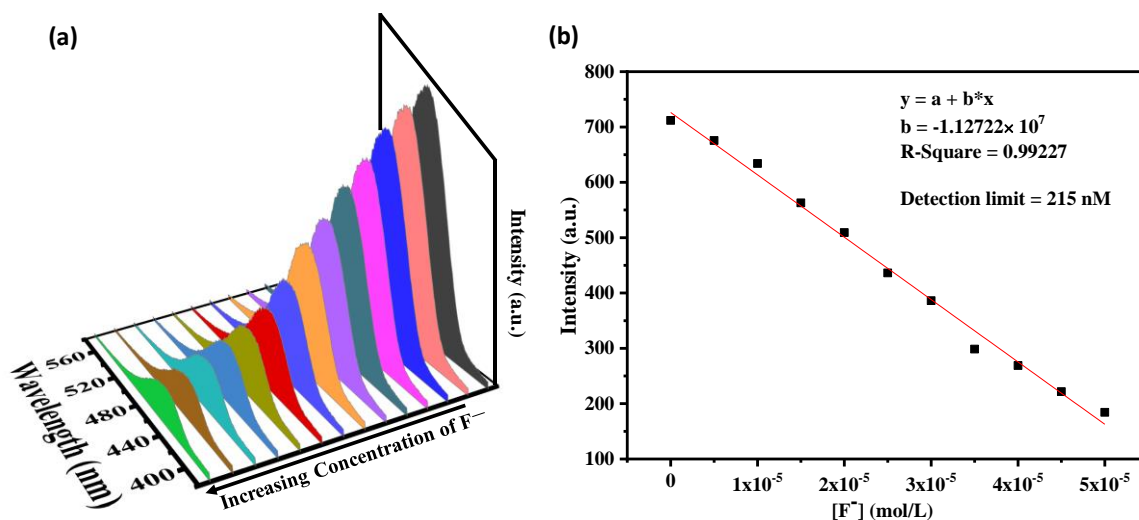
Figure 3.13: (a) Fluorescence spectra of DATG$_{Cl}$-iCONs at different concentrations of fluoride ion and (b) Detection limit of iCONs towards the detection of F⁻.
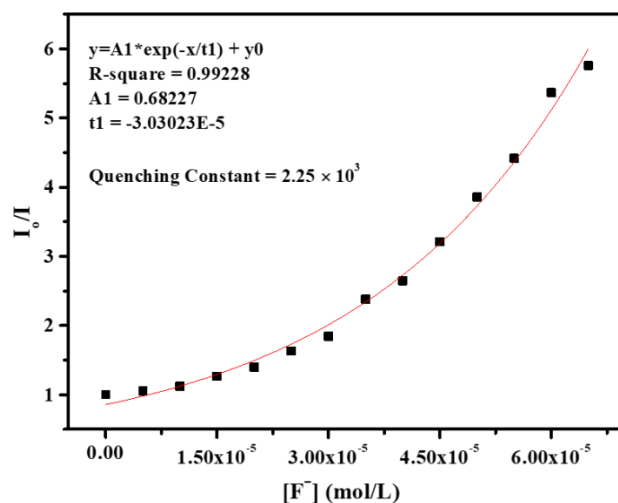
sensitive to F⁻ with a detection limit down to 5 ppb (215 nM) aldehyde has not shown any sensitivity toward F⁻ ion which clearly shows the necessity of unique structural feature of DATG$_{Cl}$-iCONs for selective sensitivity towards the fluoride anions (Figure 3.14).
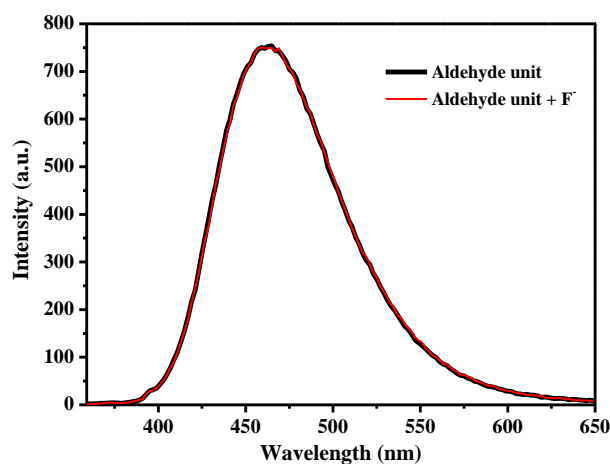
Figure 3.14: Fluorescence spectra of aldehyde in the presence or absence of F⁻.

3.3.6 Quenching Constant:

Figure 3.15: Quenching constant of iCONs towards F⁻.

The quenching constant of iCONs for F⁻ ion was determined from the non-linear Stern-Volmer curve. Quenching constant was calculated as 2.25×10^3 M⁻¹ using Stern-Volmer plot (Figure 3.15).

3.3.7 Interference Studies:

To check the real-time applicability of iCONs for selective F⁻ ion detection, a sensing experiment was performed by introducing F⁻ ion in the presence of other anions. There is no interference from other anions for the detection of F⁻ ion under similar conditions (Figure 3.16).
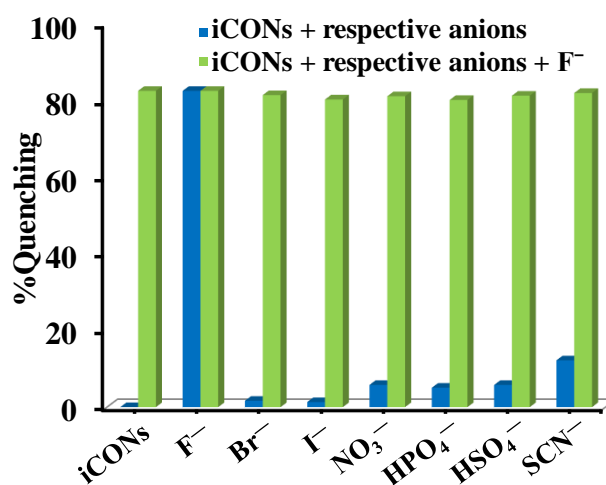
Figure 3.16: % Fluorescence quenching of DATG$_{Cl}$-iCONs by fluoride ions in the presence of other anions.

3.4 Mechanism:

To understand the possible interaction between iCONs and F⁻ ions, several experiments have been performed for understanding the fluorescence quenching process. ^{1}H NMR studies of model compound shows that peak corresponding to N-H protons (11.34 ppm) of guanidine moiety and it's becomes broaden in the presence of F⁻. Further, the comparison of integral area under this peak in both cases shows the abstraction of one N-H proton from the guanidine moiety (Figure 3.17, Appendix, Figure A3.9a). We also performed ^{1}H NMR experiments of ATG$_{Cl}$ and ATG$_{Cl}$ in presence of F⁻ ions in D$_4$-methanol solvent to create the similar environment as used in the sensing studies. The observed upfield shift of ^{1}H NMR peaks of ATG$_{Cl}$ upon adding the F⁻ ions also indicates the possibility of proton abstraction (Appendix, Figure A3.9b).
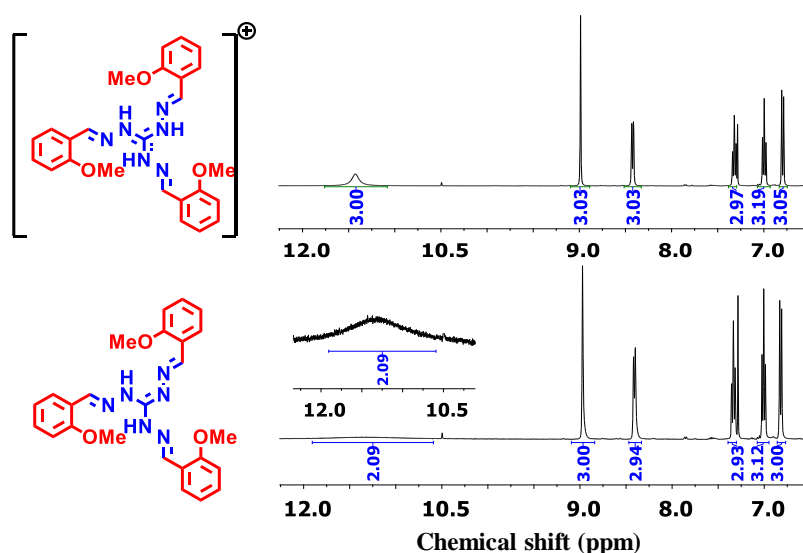
Figure 3.17: ^{1}H NMR spectra of ATG$_{Cl}$ (top) and ATG$_{Cl}$+ F⁻ (bottom).

The decrease in positive surface zeta potential on addition of F⁻ ion also supports proton abstraction from iCONs (Figure 3.18a). With an assumption that this proton abstraction is

responsible for the fluorescence quenching, an equivalent amount of proton have been supplied by adding HCl to the already quenched sample of iCONs. The revival of the fluorescence intensity to the same extent supports our assumption of the proton abstraction. The sequential subtraction and addition of a proton show reversible fluorescence turn-off and turn-on phenomenon at least up to 5 cycles, which reveals the proton triggered fluorescence switching behavior of $DATG_{Cl}$-iCONs (Figure 3.18b).
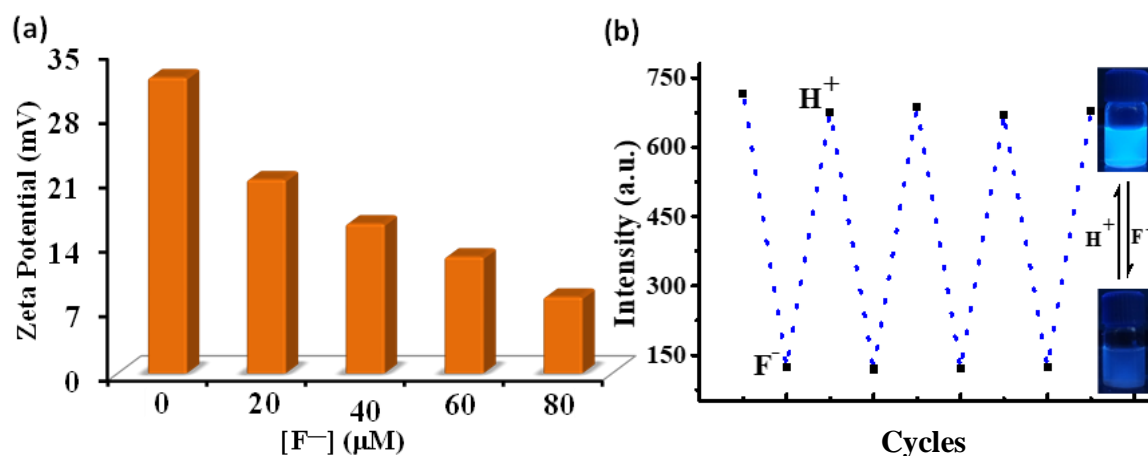
Figure 3.18: (a) Surface zeta potential values of $DATG_{Cl}$-iCONs at different concentrations of fluoride ion and (b) Fluorescence turn-off and turn-on phenomena of $DATG_{Cl}$-iCONs on subtraction and addition of a proton.

Thus, the selective sensing of F^- ion suggests that F^- ion is basic enough to abstract the acidic proton from the guanidinium ion leaving behind a neutral guanidine, which can transfer the electron to photo excited aldehyde fluorophore, commonly shown by nitrogen linkers.[33] To some extent, similar results were also observed, when F^- ion is replaced with other strong basic anions like OH^-, SO_4^{2-}, CO_3^{2-} (Appendix, Figure A3.10). Further, to understand the electron transfer phenomena, Density functional theory (DFT) calculations were carried out using Gaussian 09 program[R] B3LYP method employing 6-311++G(2d, 2p) as basis sets for HOMO-LUMO energies of DA, TG_{Cl} and triaminoguanidine (Figure 3.19).

The DFT calculation shows deprotonation of guanidinium increases the HOMO-LUMO

energy (Figure 3.19, Table 3.1) such that it can easily transfer an electron to excited
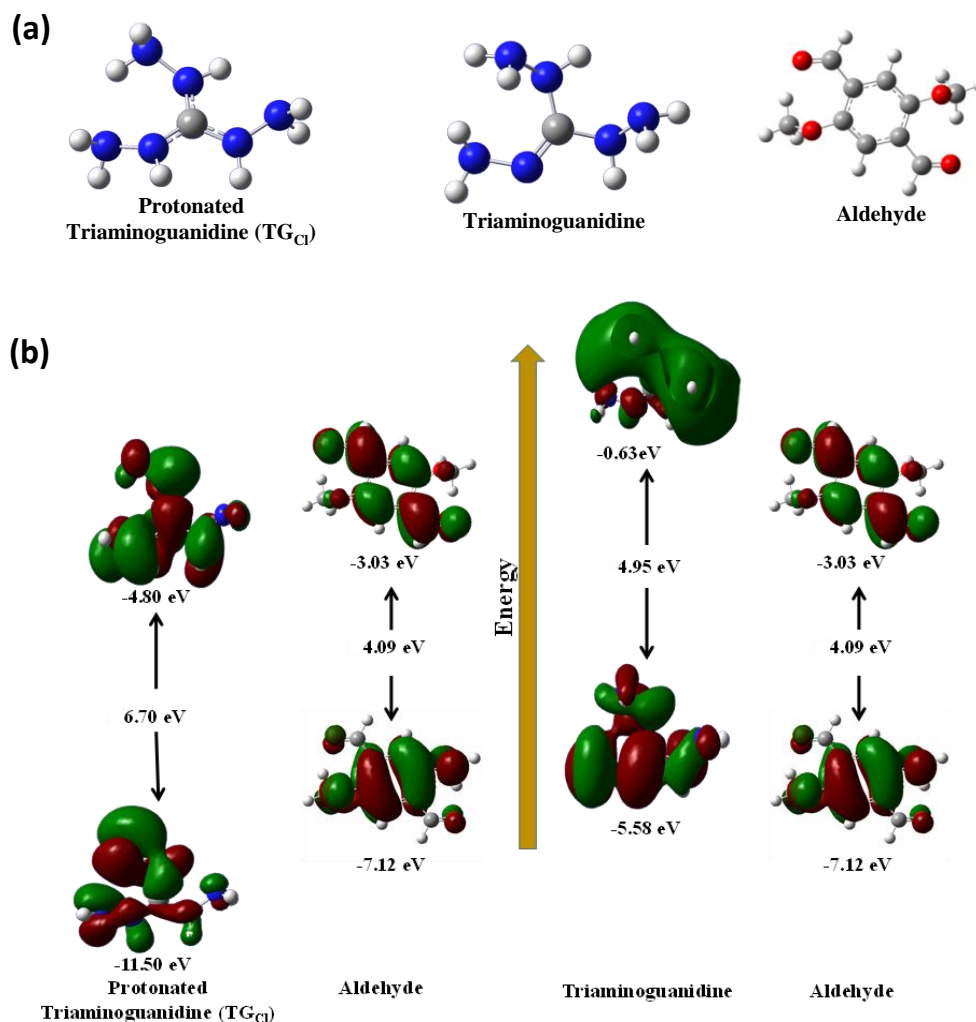
Figure 3.19: (a) Optimized Structure of protonated triaminoguanidine, triaminoguanidine

and aldehyde; (b) HOMO-LUMO orbitals of protonated triaminoguanidine,

triaminoguanidine and aldehyde.

Table 3.1: HOMO-LUMO energy of manomers calculated by using Density Functional

Theory (DFT).

Optimised Energy (a.u.)	E_{HOMO}	E_{LUMO}	E_{HOMO}- $E_{LUMO}^{(eV)}$

Protonated	-371.85182637	-11.50	-4.80	-6.70
Triaminoguanadine				
Triaminoguanadine	-371.45364607	-5.58	-0.63	-4.95
Aldehyde	-688.14102045	-7.12	-3.03	-4.09
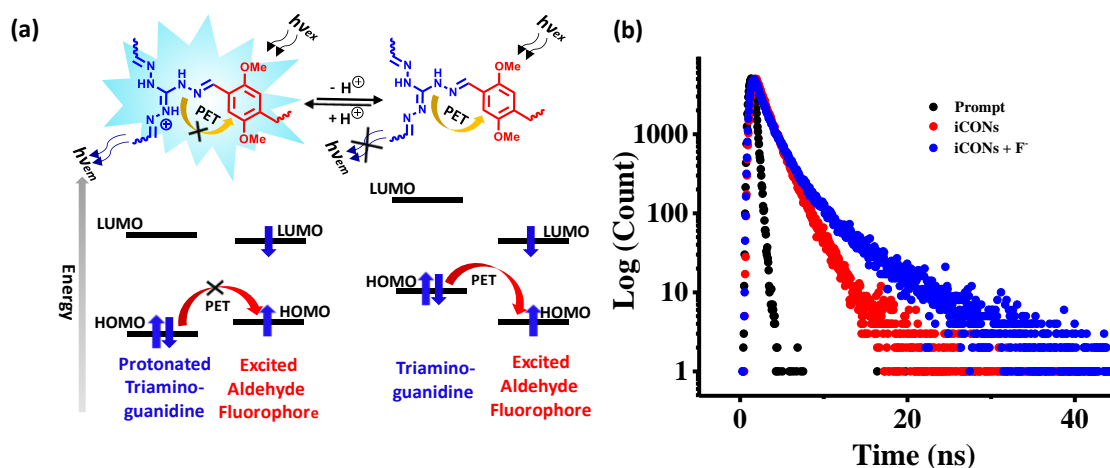
Figure 3.20: (a) Qualitative representation of HOMO-LUMO positions monomers calculated from DFT explaining the possible PET mechanism; (b) Time-resolved fluorescence spectroscopy of methanol dispersed iCONs (red), iCONs+ F⁻ ion (blue) and standard (black).

aldehyde fluorophore and quench the fluorescence via photon-induced electron transfer (PET) mechanism (Figure 3.20a). Furthermore, the DFT calculations for ATG$_{Cl}$ as the model compound (protonated and deprotonated) were also performed to understand the charge transfer process in DATG$_{Cl}$ (Appendix, Figure A3.11). The DFT calculations reveal that HOMOs of the protonated ATG$_{Cl}$ are localized to the aldehyde moiety, whereas LUMOs are diffused over the entire molecule. On the other hand, after deprotonation of ATG$_{Cl}$, the HOMO is concentrated over the guanidine moiety. The change in electron delocalization in HOMOs after deprotonation suggests the possibility

of electron transfer as after deprotonation, the guanidine molecule can behave as an electron donor. Again, prior to deprotonation, the HOMO orbital was destabilized by an energy of 3.49 eV. These results show that the guanidine molecule can easily transfer the electron to the photo-excited aldehyde fluorophore and quench the fluorescence via the electron transfer mechanism. To support the PET phenomena, time-resolved fluorescence spectroscopy of methanol dispersed iCONs was performed. Upon addition of F^-, the lifetime of iCONs decreased from 1.11 ns to 0.58 ns which indicates that deprotonation of iCONs enhances the electron transfer from amine linker to photo-excited aldehyde fluorophore, resulting in non-emissive iCONs (Figure 3.20b).

3.5 Summary:

In summary, we have demonstrated an example of the rational designing of highly fluorescent self-exfoliable ionic Covalent Organic Nanosheets and the first example of iCONs for anion sensing. These guanidinium chloride based fluorescent iCONs, due to their cationic nature and well exposed active sites, can sense F^- ion via fluorescence turn-off mechanism while other anions Br^-, I^-, NO_3^-, HPO_4^-, HSO_4^-, and SCN^- remain inactive. A very low level detection limit down to 5 ppb makes this material best among the F^- sensors. Extensive studies show the observed fluorescence quenching shows very unique proton triggered fluorescence switching behavior of iCONs with absolute reversibility at least up to 5 Cycles. These results provide a fundamental approach to develop photo-luminescent molecular sensors based on 2D organic nanosheets for the development of futuristic sensors.

References:

1. Qian, C.; Xu, S.-Q.; Jiang, G.-F.; Zhan, T.-G.; Zhao, X. *Chem. Eur. J.* **2016**, 22, 17784.

2. Halder, A.; Kandambeth, S.; Biswal, B. P.; Kaur, G.; Roy, N. C.; Addicoat, M.; Salunke, J. K.; Banerjee, S.; Vanka, K.; Heine, T.; Verma, S. *Angew. Chem., Int. Ed.* **2016**, 55, 7806.

3. Gole, B.; Stepanenko, V.; Rager, S.; Grgne, M.; Medina, D.; Bein, T.; Wgrthner, F.; Beuerle, F. *Angew. Chem. Int. Ed.* **2018**, 57, 846.

4. Wang, S.; Wang, Q.; Shao, P.; Han, Y.; Gao, X.; Ma, L.; Yuan, S.; Ma, X.; Zhou, J.; Feng, X.; Wang, B. *J. Am. Chem. Soc.* **2017**, 139, 4258.

5. Chandra, S.; Kandambeth, S.; Biswal, B. P.; Lukose, B.; Kunjir, S.M.; Chaudhary, M.; Babarao, R.; Heine, T.; Banerjee R. *J. Am. Chem. Soc.* **2013**, 135, 17853.

6. Khayum, M. A.; Kandambeth, S.; Mitra, S. ; Nair, S. B.; Das, A.; Nagane, S. S.; Mukherjee, R.; Banerjee, R. *Angew. Chem.* **2016**, 128, 15833.

7. Kong, W.; Wan, J.; Namuangruk, S.; Guo J.; Wang C. *Sci. Rep.***2018**, 8, 5529.

8. Berlanga, I.; Mas-Balleste, R.; Zamora, F. *Chem. Commun.* **2012**, 48, 7976.

9. Bunck, D. N.; Dichtel, W. R. *J. Am. Chem. Soc.* **2013**, 135, 14952.

10. Liu, X.-H.; Guan, C.-Z.; Wang, D.; Wan, L. J. *Adv. Mater.* **2014**, 26, 6912.

11. Berlanga, I.; Ruiz-Gonzalez, M. L.; Gonzalez-Calbet, J.; Fierro, J. L. G.; Mas-Balleste, R.; Zamora, F. *Small* **2011**, 7, 1207.

12. Haldar, S.; Roy, K.; Nandi, S.; Chakraborty, D.; Puthusseri, D.; Gawli, Y.; Ogale, S.; Vaidhyanathan, R. *J. Am. Chem. Soc.*, **2018**, 140, 896.

13. Mal, A; Mishra R. K.; Praveen, V. K.; Khayum, M. A.; Banerjee, R.; Ajayaghosh A. *Angew .Chem.* **2018**, 130, 8579.

14. Mitra, S.; Kandambeth, S.; Biswal, B. P.; Khayum, A.; Choudhury, M. C. K.; Mehta, M.; Kaur, G.; S. Banerjee, Prabhune, A.; Verma, S.; Roy, S.; Kharul, U. K., Banerjee, R. *J. Am. Chem. Soc.* **2016**, 138, 2823.

15. Chen, H.; Tu, H.; Hu, C.; Liu, Y.; Dong, D.; Sun, Y.; Dai, Y.; Wang, S.; Qian, H.; Lin, Z.; Chen L. *J. Am. Chem. Soc.* **2018**, 140, 896.

16. Onda, M.; Yoshihara, K.; Koyano, H.; Ariga K.; Kunitake, T. *J. Am. Chem. Soc.* **1996**, 118, 8524.

17. Schmidtchen, F. P.; Berger, M. *Chem. Rev.*, **1997**, 97, 1609.

18. Tobey S. L.; Anslyn, E. V. *J. Am. Chem. Soc.* **2003**, 125, 14807.

19. Schmuck C.; Geiger, L. *J. Am. Chem. Soc.* **2004**, 126, 8898.

20. Schmuck C.; Schwegmann, M. *J. Am. Chem. Soc.* **2005**, 127, 3373.

21. Blondeau, P.; Segura, M.; Fernandez R. P.; Mendoza, J. *Chem. Soc. Rev*. **2007**, 36, 198.

22. Schmuck C.; Bickert, V. *J. Org. Chem.* **2007**, 72, 6832.

23. Jadhav V. D.; Schmidtchen, F. P. *J. Org. Chem.* **2008**, 73, 1077.

24. Coles, M. P.*Chem. Commun.* **2009**, 0, 3659.

25. Zhou, Y.; Zhang, J. F.; Yoon J. *Chem. Rev.* **2014**, 114, 5511.

26. Kirk, L. K. Biochemistry of the Halogens and Inorganic Halides; Plenum Press: New York, **1991**.

27. Kleerekoper, M. *Endocrinol. Metab. Clin. North Am.* **1998**, 27, 441.

28. Briancon, D. Fluoride and osteoporosis: an overview.*Rev. Rhum.* **1997**, 64, 78.

29. Singh, H.; Balamurugan, A.; Jayakannan. M. *ACS Applied Materials & Interfaces***2013**, 5, 5578.

30. Accelrys Software Inc., Material Studio Modeling Environment, Release v7.0, SanDiego: Accelrys Software Inc., **2013**.

31. Gaussian 09, Revision A.02, Frisch, M. J.; Trucks, G. W.; Schlegel, H. B.; Scuseria, G. E.; Robb, M. A.; Cheeseman, J. R. ; Scalmani, G.; Barone, V.; Petersson, G. A.; Nakatsuji, H.; Li, X.; Caricato, M.; Marenich, A.; Bloino, J.;

Janesko, B. G.; Gomperts, R.; Mennucci, B.; Hratchian, H. P.; Ortiz, J. V.;Izmaylov, A. F.; Sonnenberg, J. L.; Williams-Young, D.; Ding, F. ; Lipparini, F.; Egidi, F.; Goings, J.; Peng, B.; Petrone, A.; Henderson, T.; Ranasinghe, D.; Zakrzewski, V. G.; Gao, J.; Rega, N.; Zheng, G.; Liang, W.; Hada, M.; Ehara, M.; Toyota, K.; Fukuda, R.; Hasegawa, J.; Ishida, M.; Nakajima, T.; Honda, Y.; Kitao, O.; Nakai, H.; Vreven, T.; Throssell, Jr.K.; Montgomery, J. A.;. Peralta, J. E; Ogliaro, F.; Bearpark, M.; Heyd, J. J.; Brothers, E.; Kudin, K. N;. Staroverov, V. N.; Keith, T.; Kobayashi, R.; Normand, J.; Raghavachari, K.; Rendell, A.; Burant, J. C.; Iyengar, S. S.;Tomasi, J.;Cossi, M.;Millam, J. M.; Klene, M.; Adamo, C.; Cammi, R.; Ochterski, J. W.; Martin, R. L.; Morokuma, K.;Farkas, O. ; Foresman, J. B.; D. Fox, J.; Gaussian, Inc., Wallingford CT, **2016**.

32. Vempati, S.; Mitra, J.; Dawson, P. *Nanoscale Research Letters***2012**, 7, 470.

33. Li Z.; Huang N.; Lee K. H.; Feng Y.; Tao S.; Jiang Q.; Nagao Y.; Irle S.; Jiang D. *J. Am. Chem. Soc.* **2018**, 39, 12374.
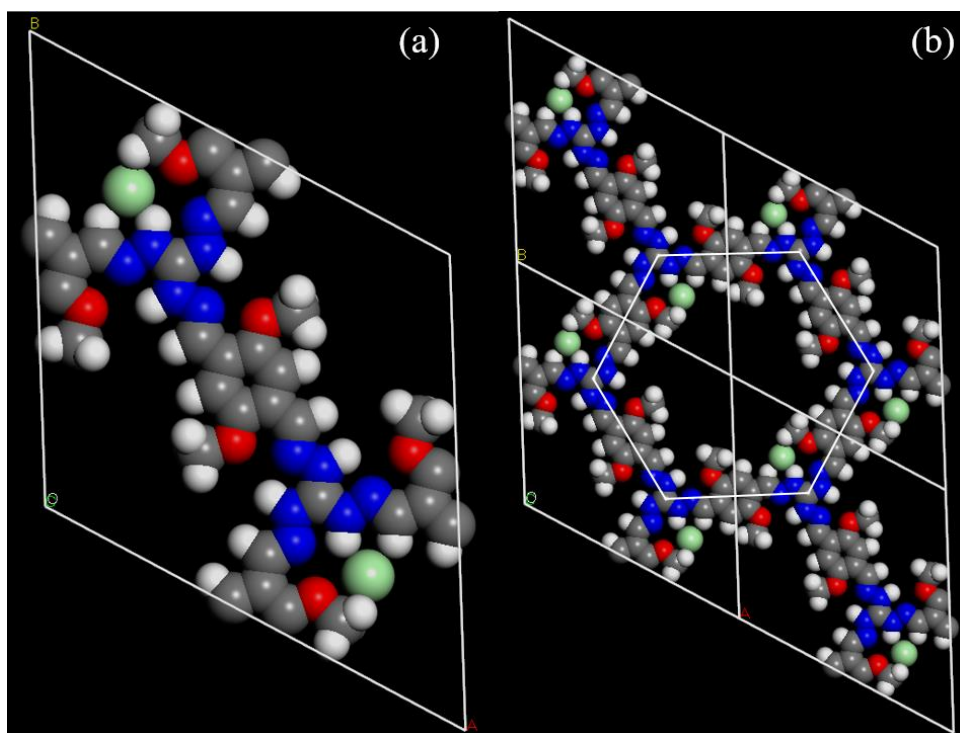
Appendix 3:
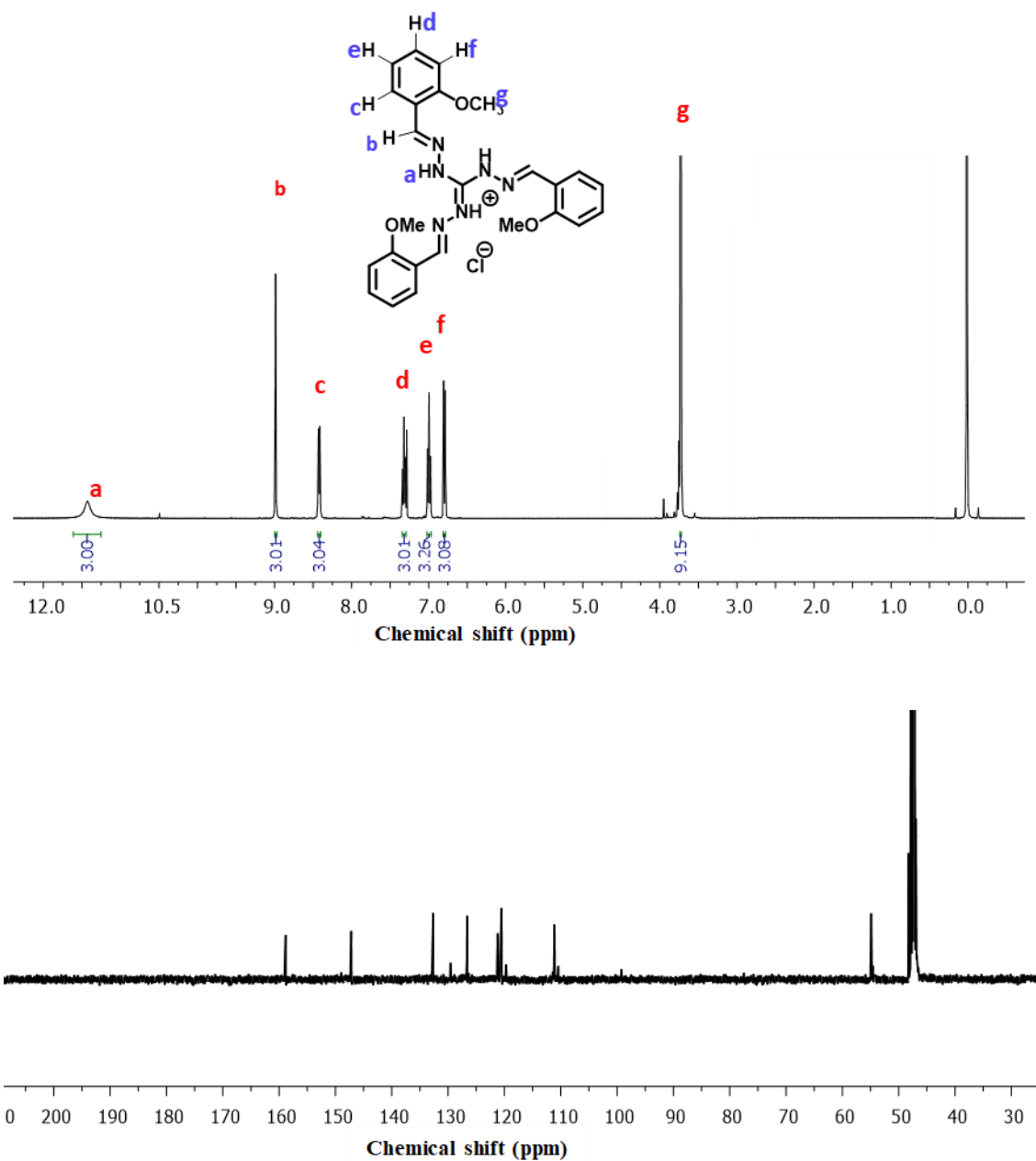
Figure A3.1: ^{1}H and ^{13}C NMR spectra of model compound ATG$_{Cl}$.

PXRD Simulation studies:
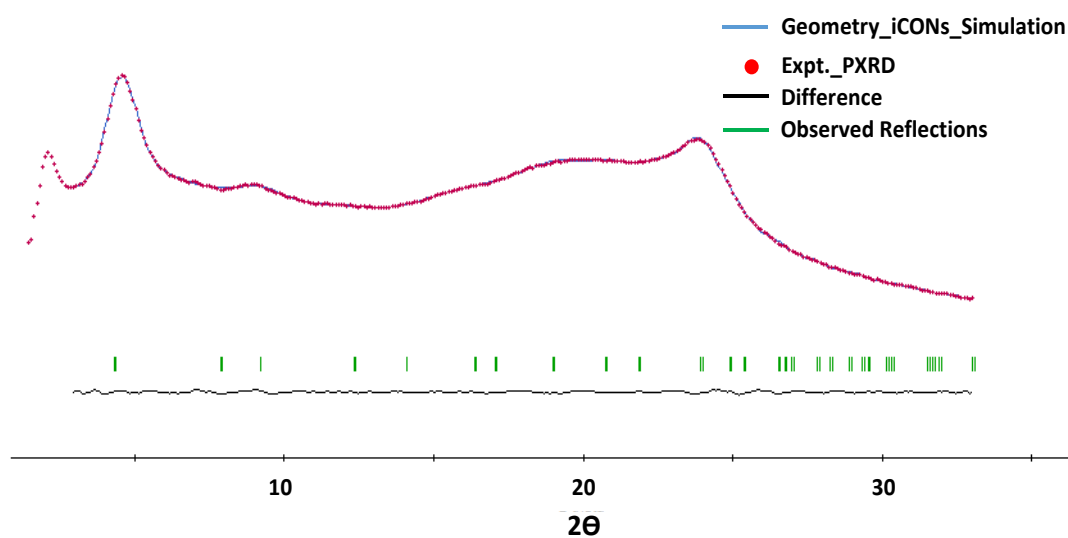
Figure A3.2: Pawley Refinement of DATG$_{Cl}$.
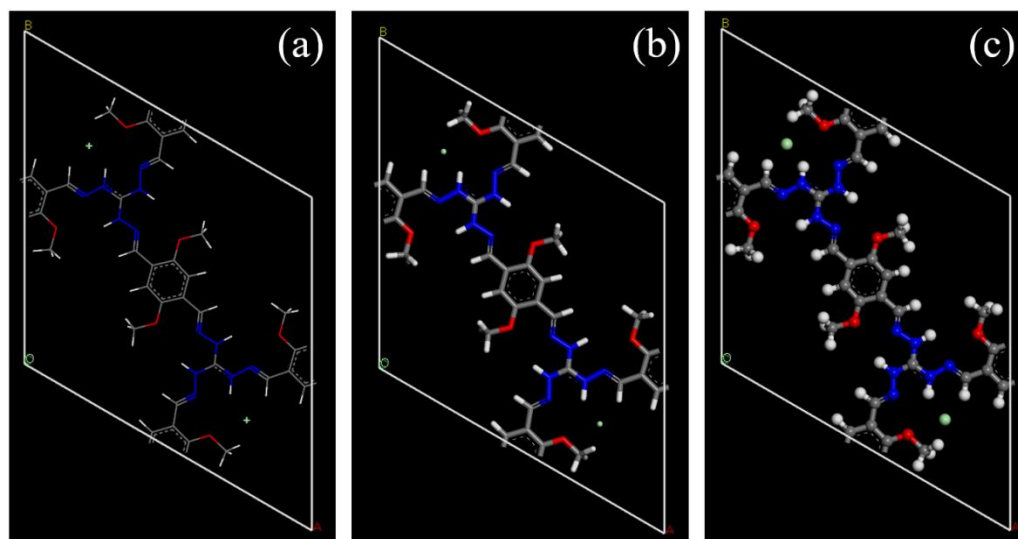
Figure A3.3: Unit cell of DATG$_{Cl}$ in different display style representation. (a) Line, (b) Stick, and (c) Ball and stick.

Figure A3.4: (a) Unit cell; and (b) 2 x 2 super cell of DATG$_{Cl}$-iCONs with a hexagonal sketch connecting central carbon atom of guanidinium moiety present in the center of each corner.
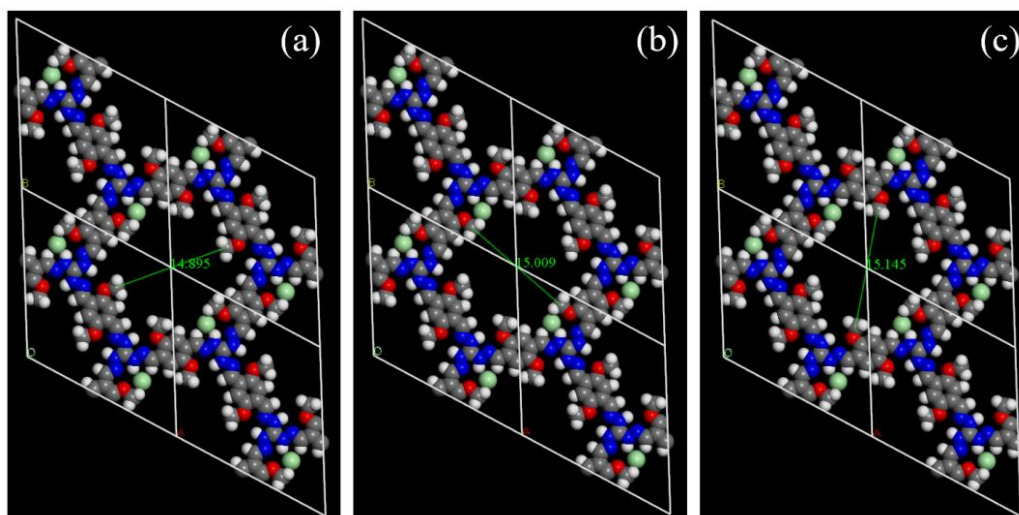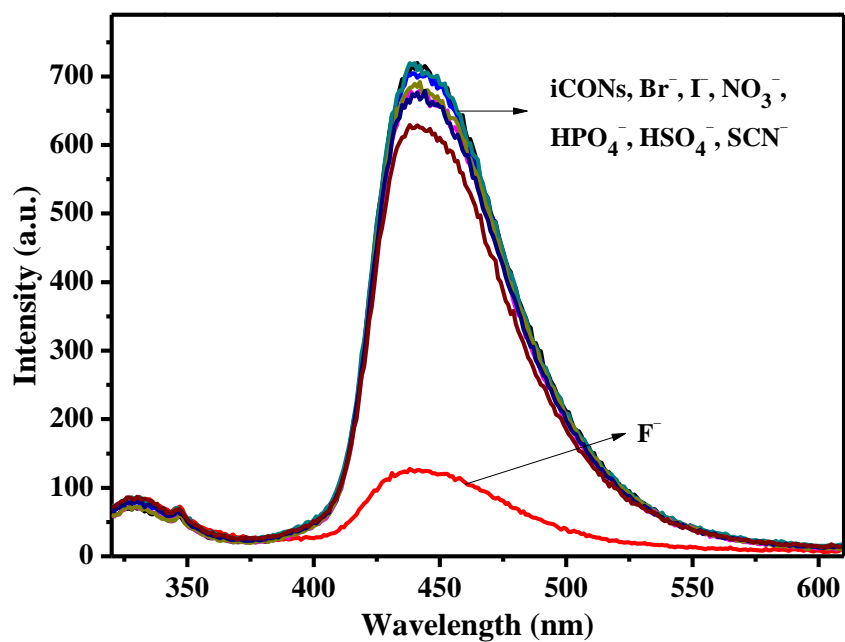

Figure A3.5: (a-c) 2 x 2 super cell of DATG$_{Cl}$-iCONs show the possible pore width (green line) from different angle.
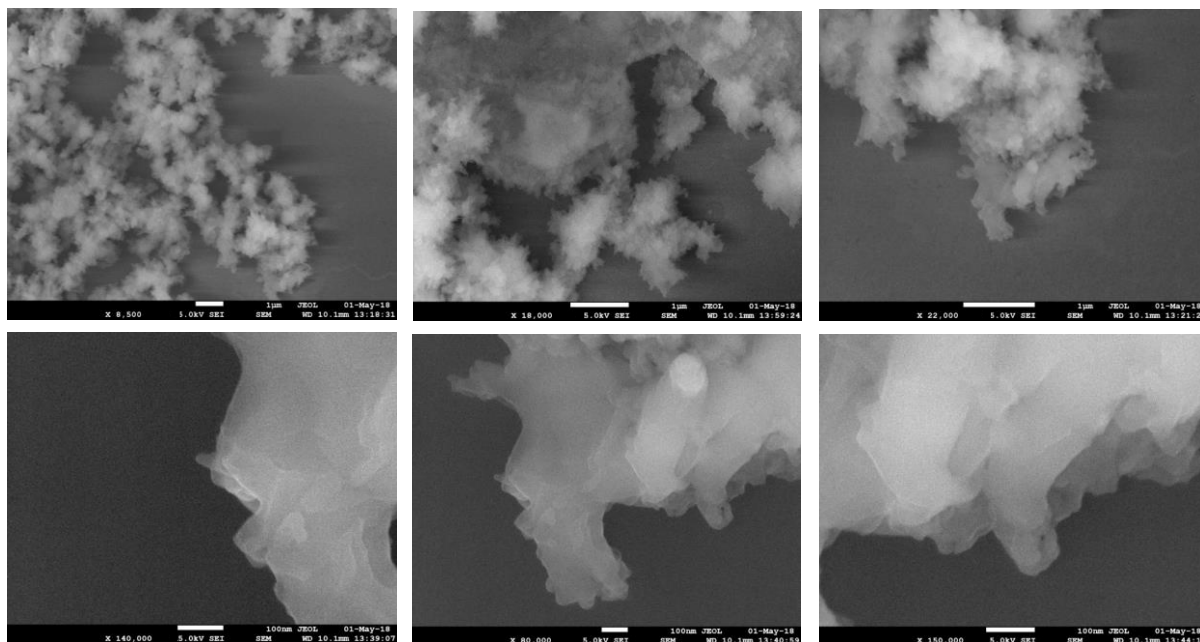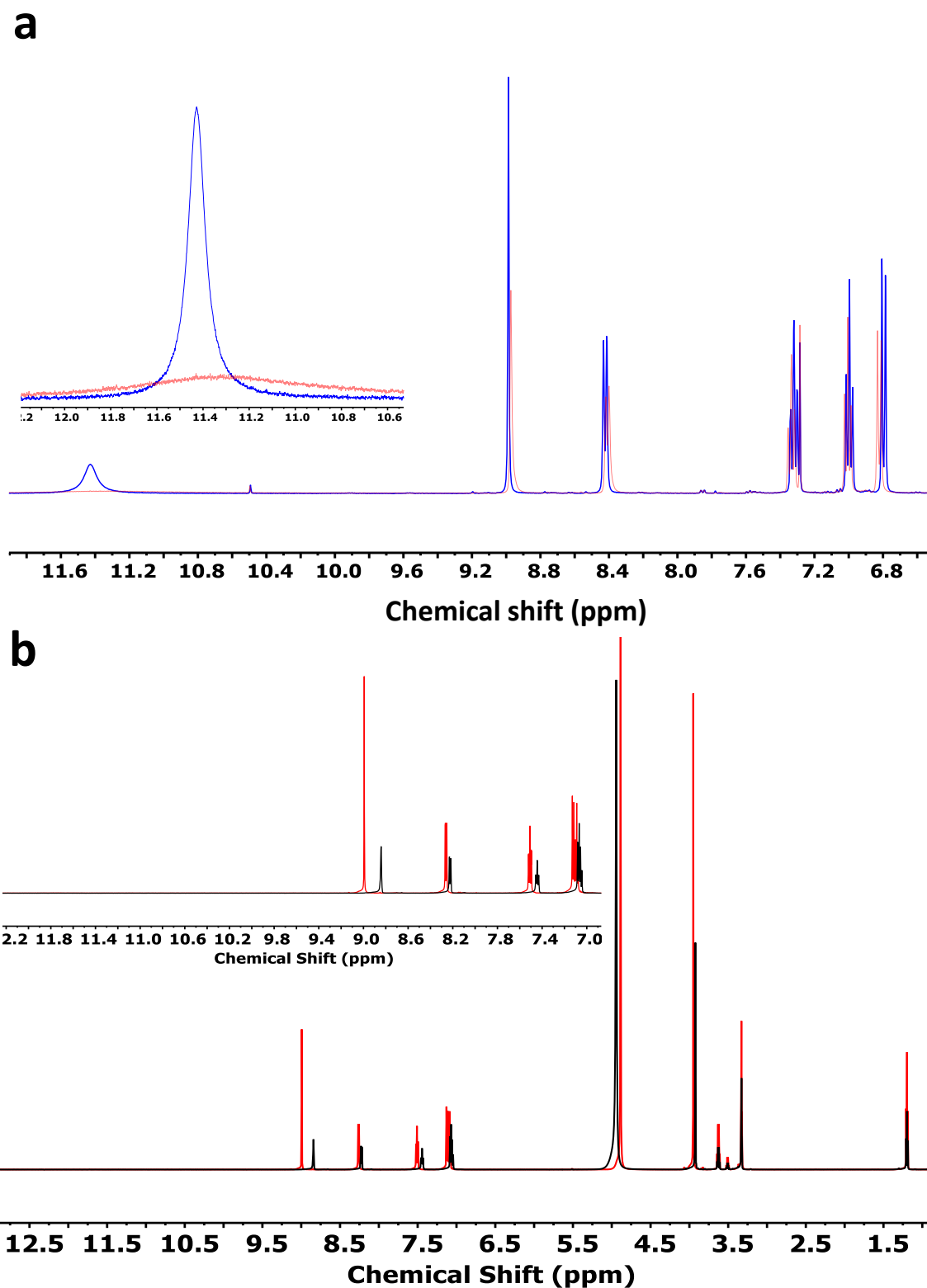
Figure A3.6: SEM images of DATG$_{Cl}$ at different magnifications [scale bar = 1 µm (top row and 100 nm (down row)]
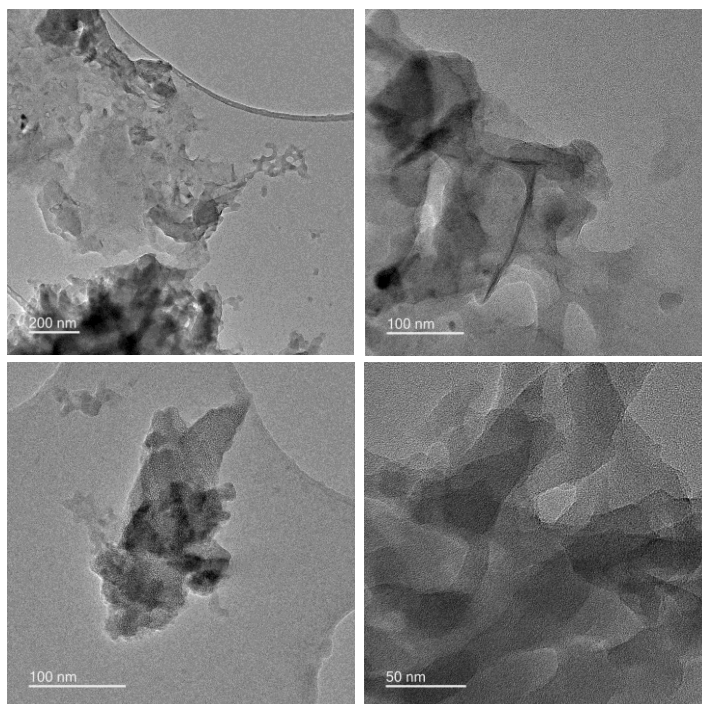
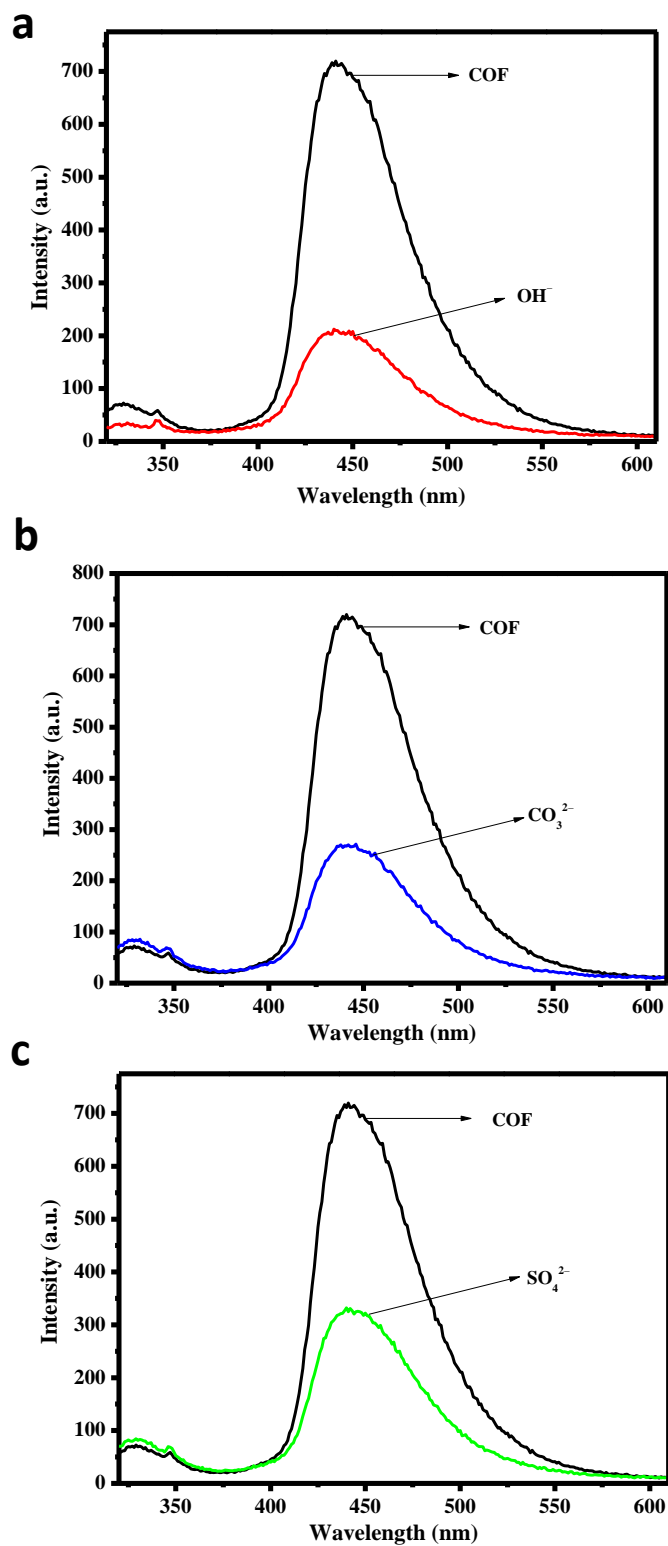

Figure A3.7: TEM images of DATG$_{Cl}$ at different magnifications.

Figure A3.8. Fluorescence spectra of DATG$_{Cl}$-iCONs in MeOH suspension upon addition of 41.5 μM of different anions, λ$_{ex}$ = 337 nm.

a

b

Figure A3.9.(a) ^{1}H NMR spectra of ATG$_{Cl}$ (blue) and ATG$_{Cl}$+ F$^-$ (red) in CDCl$_3$; (b) ^{1}H NMR spectra of ATG$_{Cl}$ (black) and ATG$_{Cl}$+ F$^-$ (red) in D$_4$-methanol

Figure A3.10: Fluorescence spectra of iCONs in MeOH suspension upon addition of 41.5 μM OH⁻, CO_3^{2-} and SO_4^{2-} of different anions, λ_{ex} = 337 nm.

LUMO

LUMO

-4.68 eV

-1.62 eV

3.78 eV

3.35 eV
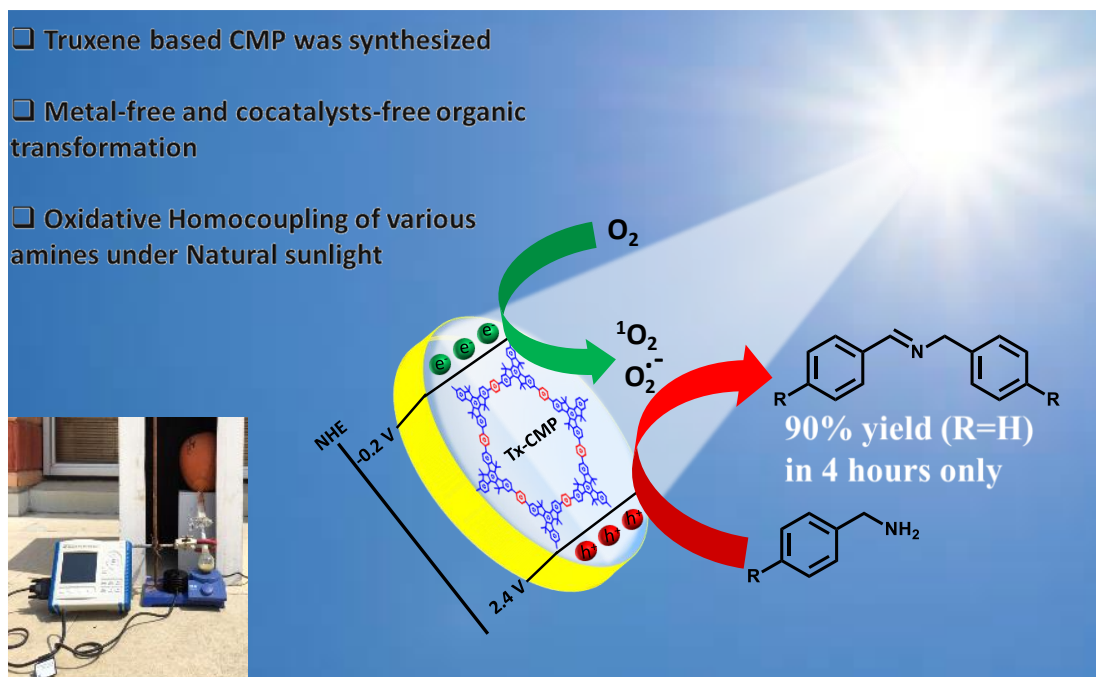
-8.46 eV

-4.97 eV
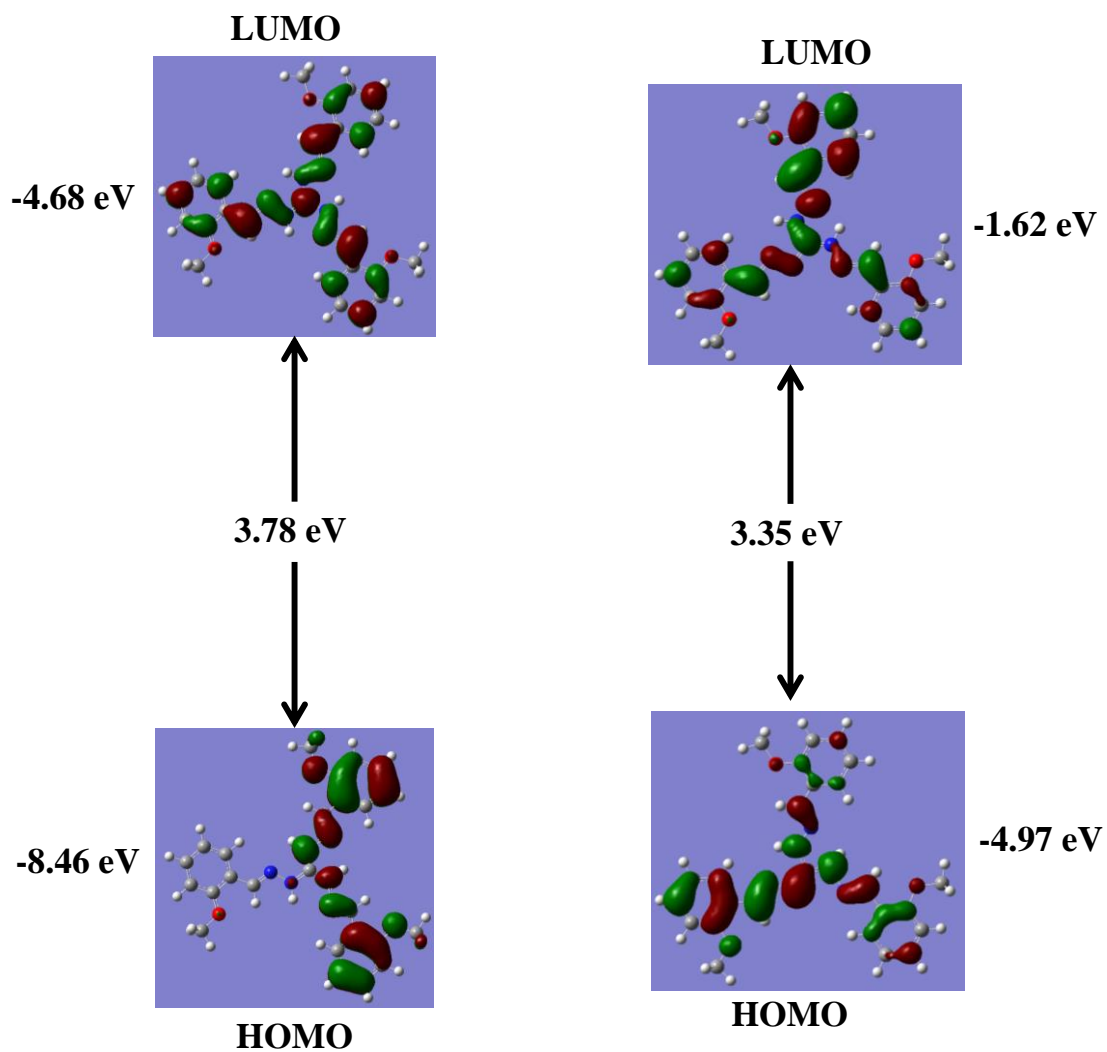
HOMO

HOMO

Figure A3.11: HOMO-LUMO orbitals diagram of protonated ATG$_{Cl}$ (left) and deprotonated ATG$_{Cl}$ (right).

Chapter 4

Natural Sunlight Driven Oxidative Homocoupling of Arylamines by Truxene based Conjugated Microporous Polymer

In this study, we reported the synthesis of novel metal-free Truxene based conjugated microporous polymer (Tx-CMP) and demonstrated heterogeneous photocatalalytic application under direct sunlight for the first time. We employed Tx-CMP for the oxidative homocoupling of arylamines. This model reaction describes an effective greener and sustainable way to harvest natural sunlight effectively for the organic transformations with highest Turnover frequency (TOF) reported under natural sunlight within 4 hours. The higher conversion and selectivity of Tx-CMP has been demonstrated with recyclability at least 5 times without any decline in its catalytic activity under direct sunlight.

4.1 Aim:

Recently, inorganic transition metal complexes[1-8] and organic dyes[9-12] were widely explored as visible light-induced photo-redox homogeneous photocatalyst. Due to their commercial availability, excellent stability and photo-redox properties, these small molecules have shown very promising results in a variety of chemical transformations. However, their intrinsic drawbacks like scarcity, environmental concern, photo-bleaching from the solvolytic attack and post-reaction removal cost, etc., is the huge obstacles for large scale commercial applications. Therefore, metal-free, heterogeneous, visible-light-driven photocatalysts which are recoverable and reusable with high stability are most needed to address the aforementioned concerns. In this respect, the scope of CMPs as metal-free photocatalysts is much wider, because their optoelectronic properties can be easily engineered at the molecular level with the help of rich organic chemistry tools.[13-17]

In addition to the humidity sensing ability of COF-TXDBA (chapter 2), we have also tried to explore the optical properties of COF-TXDBA to find their application in the related areas. Due to wide absorbance in the visible region and small optical band gap (2.3 eV), COF-TXDBA was applied as a photocatalyst for the aerobic homocoupling of benzyl amines. It was observed that COF-TXDBA can oxidize benzylamine to imine under visible light however, the conversion was limited to 32%. Learning from these results and with a motivation to develop an efficient photocatalyst, we tried to develop a porous polymer having truxene moiety as a building block for photocatalytic applications. Further, we have also noticed that nearly all the reports addressing the photocatalytic application use an artificial light source, which requires an expensive setup and high energy source. To address these issues, we thrived to perform the photocatalytic reactions under natural sunlight in the effective sunshine hours, which is a cost-effective way for potential large-scale industrial applications. With a strong motive that the introduction of

Tx molecule in CMP will provide unique photocatalytic properties, we have developed truxene based CMP (Tx-CMP) and employed it as a metal-free sunlight active heterogeneous photocatalyst for the fundamental organic transformation of aryl amines to corresponding imines. The imines also called as Schiff bases are well known for their versatility as intermediates in the synthesis of pharmaceutical or biologically active compounds and fine chemicals.[18] Thus, we believe this work as a major step forward in the field of organo photocatalysis.

4.2 Experimental Section:

4.2.1 Materials and Techniques:

As mentioned in previous chapters, all chemicals and solvents were of analytical grade and used without further purifcation. 1-indanone, 1,4-phenylenediboronic acid, potassium carbonate and Pd(PPh$_3$)$_4$ were purchased from Sigma Aldrich (Bangalore, India). Thin-layer chromatography was performed on aluminium sheets pre-coated with silica gel (Merck, Kiesel gel 60, F254). Column chromatographic separations were performed on silica gel (60–120 mesh). Structural characterisations of the compounds were conducted by ^{1}H NMR and ^{13}C NMR (BrukerBiospin, Switzerland, Avance-iii 400 spectrometer), Infrared spectroscopy (Perkin Elmer Spectrum AX3) and diffuse reflectance (DR) UV-vis spectrophotometer (3000+). NMR spectra were recorded in deuterated chloroform (CDCl$_3$) and deuterated dimethylsulfoxide (DMSO-d$_6$) using tetramethylsilane as the internal standard. N$_2$-physisorption isotherms were recorded on AutosorbiQ$_2$ instrument (Quantachrome) at 77 K. Before measurements, samples were degassed overnight under vacuum at 120 °C. The specific surface area was calculated by the BET Micropore assistant surface area calculations for Tx-CMP. Density functional theory (DFT) method was employed to estimate the pore size distribution for Tx-CMP and Barrett-Joyner-

Halenda (BJH) method for SG-CN. Total pore volume was obtained by the amount of N_2 adsorbed at *p/p₀* ~ 0.9 and 0.95, assuming that adsorption on the external surface was negligible compared to adsorption in pores. The elemental composition of Tx-CMP was estimated by X-ray photoelectron spectroscopy (XPS) with AES module (PHI 5000 Versa Prob II, FEI Inc). Diffuse reflectance UV-Visible (DRUV-Vis) spectra were recorded on a Shimadzu UV-2550 spectrophotometer. Then, the conversion, selectivity, and yield of the reaction products were quantified by gas chromatography (GC-MS Shimadzu GC-2014) equipped with an HP-5 capillary column using calibration curves.
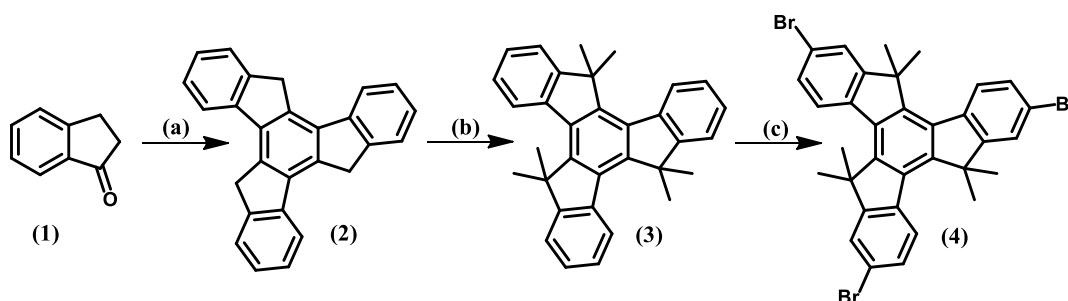
4.2.2 Synthesis:

In Scheme 4.1, the synthetic pathway of the truxene monomer, a well-known electron donor 3D centre, is displayed. Compounds 1-4 were synthesized following reported procedures with minor modification.[19-21] For comparison purpose, mesoporous carbon nitride (SG-CN) was synthesized according to the previous reported procedure.[22] Titanium dioxide, TiO_2 (commercial P25) was used as such.

Synthesis of Truxene (2): Synthesis of truxene (**2**) was done according to the previously reported procedure[19] with minor modifications. 1-indanone (**1**) (13.6g 104 mmol) was dissolved to 60 ml glacial acetic acid in a 100 ml round bottom flask. To this solution, 30 ml of 37% w/w HCl was added slowly and stirred for 16 h at room temperature. After this reaction mixture was poured into ice and the white precipitate was filtered. This white solid was washed with water, acetone, DCM sequentially, and dried to obtain crude Truxene (**2**) which is not soluble in common, deuterated solvents and used for next step as it is.

Synthesis of Hexamethyltruxene (3): To the ice-cold suspension of truxene (2.00 g, 5.84 mmol) in dry THF (150 mL), 'BuOK (13.11 g, 117 mmol) was added with vigorous

stirring under an N_2 atmosphere. To this crimson-colored solution, CH_3I (5.45 mL, 87.6 mmol) was added dropwise and the green reaction mixture was heated at reflux with stirring overnight under an inert atmosphere. After cooling to room temperature, the green suspension was filtered and washed with THF. The solvent was removed from the collected filtrate under vacuum. The remaining solid was purified by column chromatography eluting with a gradient from hexane to EtOAc/hexane to obtain 3 as white crystalline solid. Yield: 69 %. ^1H NMR (CDCl$_3$, 400 MHz) δ ppm: 1.90 (s, 18H), 7.38-7.45 (m, 6H), 7.56 (d, 3H, 8.32 (d, 3H).


Scheme 4.1: Synthetic pathway of monomer 2,7,12-tribromo-5,5,10,10,15,15-hexamethyl -10,15-dihydro-5H-diindeno [1,2-a:1',2'-c] fluorene (4); (a) Acetic acid, HCl, 100 ºC; (b) *t*-BuOK, CH$_3$I, THF, 0 ºC; (c) Br$_2$, CH$_2$Cl$_2$.

Synthesis of 2,7,12-Tribromo-5,5',10,10',15,15'-hexamethyltruxene (4): Synthesis of **4** was done according to the previously reported procedure[21] with minor modifications. To an ice-cold solution of **3** (2 g, 4.69 mmol) in dichloromethane (50 mL), bromine was added (0.95 ml) and the reaction mixture was stirred overnight in dark. After completion of the reaction, the reaction mixture was washed with 5% sodium bicarbonate solution (3 x 50 ml), followed by water (1 x 100 ml) and dried over magnesium sulphate. The organic layer was concentrated under reduced pressure, which afforded a crude solid. Crystallization from DCM/Methanol results in 2.9 g of compound 4. Yield: 90%, ^1H

NMR (CDCl$_3$, 400 MHz) δ ppm: 1.83 (s, 18H), 7.54 (dd, 3H.), 7.65 (d, 3H), 8.10 (d, 3H) (Appendix, Figure A4.1).

Synthesis of Tx-CMP: Scheme 4.2 shows the synthesis of Tx-CMP. In a 100 ml flask compound **(4)** (300 mg, 0.45 mmol), 1,4-phenylenediboronic acid (164 mg, 0.68 mmol), 20 mL DMF, 3.39 mL and 2M K$_2$CO$_3$ solution were taken. This mixture was then degassed by bubbling N$_2$ gas for 20 min. After this, 20 mg of Tetrakis(triphenylphosphine)palladium(0) ([Pd(PPh$_3$)$_4$]) was added to this solution and again degassed for 30 min. This reaction mixture was then heated to 150 ℃ and vigorously stirred. After three days, the reaction medium was cooled to room temperature and the precipitate was filtered, washed with water, acetone, THF and diethyl ether, respectively. Further, the sample was Soxhlet extracted with acetone solution and finally dried at 120 °C in a vacuum oven for structural characterization. Yield 83%.
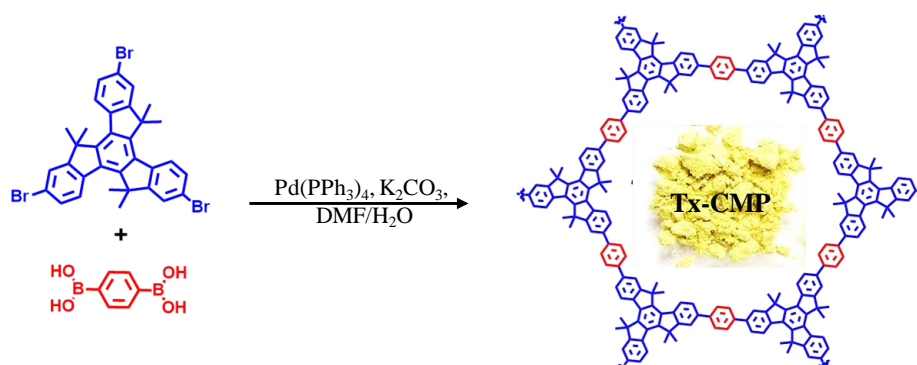
Scheme 4.2: Synthesis route and idealized structure of Tx-CMP.

Synthesis of SG-CN: The mesoporous carbon nitride (SG-CN) was synthesized by following previous literature.[22] Briefly, Cyanamide and tetraethyl orthosilicate (1:6 molar ratio) were dissolved in a 0.01 M HCl (4 g) and ethanol (4 g). The pH of the mixture was adjusted at 2. Further, the mixture was stirred for 30 min and the solvent was removed through the rotary evaporation system and aged at 80 ℃ for 24 h. Then, the obtained solid was calcined at 550 ℃ under inert atmosphere with a ramping rate of 2 ℃/min for 4 h to

obtain the carbon nitride-silica composite. The silica was leached out by treating the composite with 4 M aqueous ammonium bifluoride (NH_4HF_2) solution for 40 h followed by washing with water and ethanol to obtain pure carbon nitride. Further, it was dried in normal oven for overnight at 120 ℃ followed by drying in the vacuum oven at 150 ℃ for 8 h. The obtained carbon nitride was designated as SG-CN.

4.3 Result and Discussion:

### 4.3.1 Structural Characterizations and Thermal Stability:

Solid-state ^{13}C CP/MAS NMR spectroscopy was performed to confirm the formation of Tx-CMP. NMR spectra show signals at 23 and 46 ppm, which are assigned to the methyl groups and tertiary carbon of Tx units, respectively. The signals between 110 and 160 ppm are assigned to the aromatic carbons in the polymer backbone (Figure 4.1a). These signals show the successful formation of Tx based CMP. Thermogravimetric analysis (TGA) measurements showed that the conjugated network remained intact up to ∼400 ℃ (Figure 4.1b).
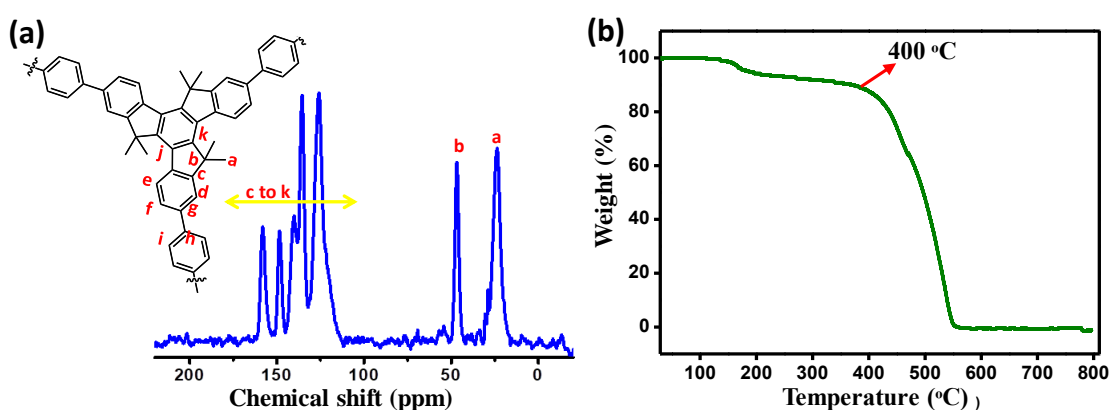
Figure 4.1: (a) Solid-state ^{13}C CP/MAS NMR spectra of Tx-CMP; (b) TGA profile of Tx-CMP.

4.3.2 Porosity Measurement and Photophysical Studies:

The successful establishment of the porous framework of Tx-CMP is clearly verified by the N_2 physisorption analysis (Figure 4.2a). The Type-I isotherm at 77 K displayed a steep nitrogen gas uptake at a low relative pressure (p/p_0 below 0.1) reflecting the presence of micropores, with hysteresis loop indicating also the presence of mesoporosity. The BET specific surface area was found as 1022 m^2/g with average pore volume 0.7 ccg^{-1}. The pore diameter and distribution were obtained by DFT method as shown in the inset of Figure 4.2a, showing a major proportion of micropores with dimensions ranging from 0.7-1.8 nm and also the evidence of mesoporosity.
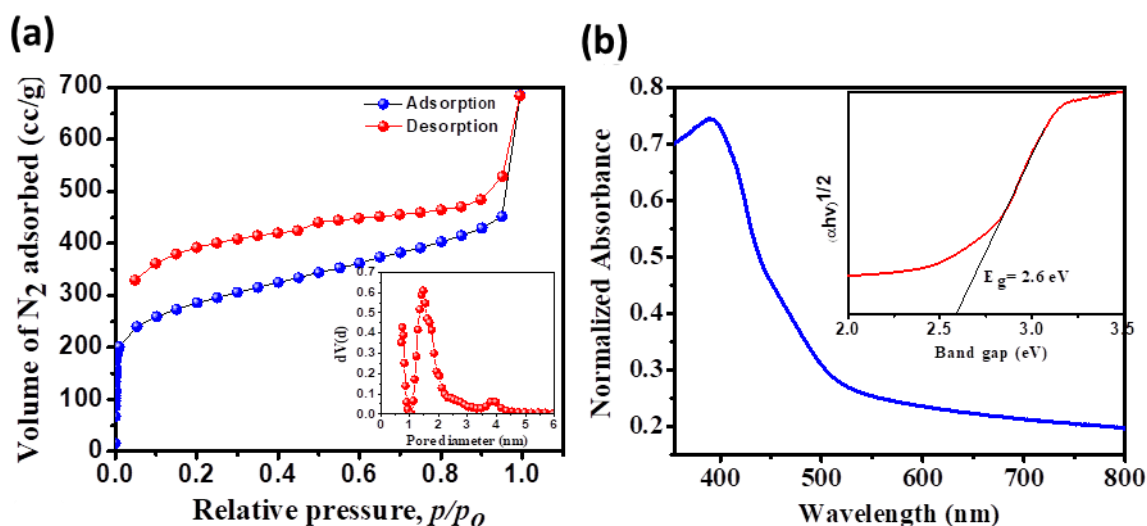

Figure 4.2: (a) N_2-physisorption isotherms and pore size distribution curve (inset); (b) DR UV-Vis spectra and Tauc plot to calculate the optical band gap (inset).

The DR UV-vis spectrum (Figure 4.2b) of Tx-CMP showed a broad absorption band with the absorbance starting around 600 nm with a wide shoulder with a maximum absorbance peak centred around 400 nm. It showed the broad absorption range of the Tx-CMP polymers extends up to visible light region, which is crucial for their activity in the natural sunlight. The characteristic broad shoulder in the spectrum of the microporous polymer could be partially due to the light scattering effect originated from the broad pore

size range in these porous polymers.[23] The optical band gap of Tx-CMP was derived from Tauc plot which shows the bandgap of 2.6 eV (inset of Figure 4.2b).

4.3.3 Morphology and Chemical Composition:

The scanning electron microscope (SEM) images of Tx-CMP showed agglomerated flake type structures (Figure 4.3a). Energy-dispersive X-ray spectroscopy (EDX) experiments

(a)

(b)

No peak at 2.9 keV and 22.9 keV indicates the absence of Palladium
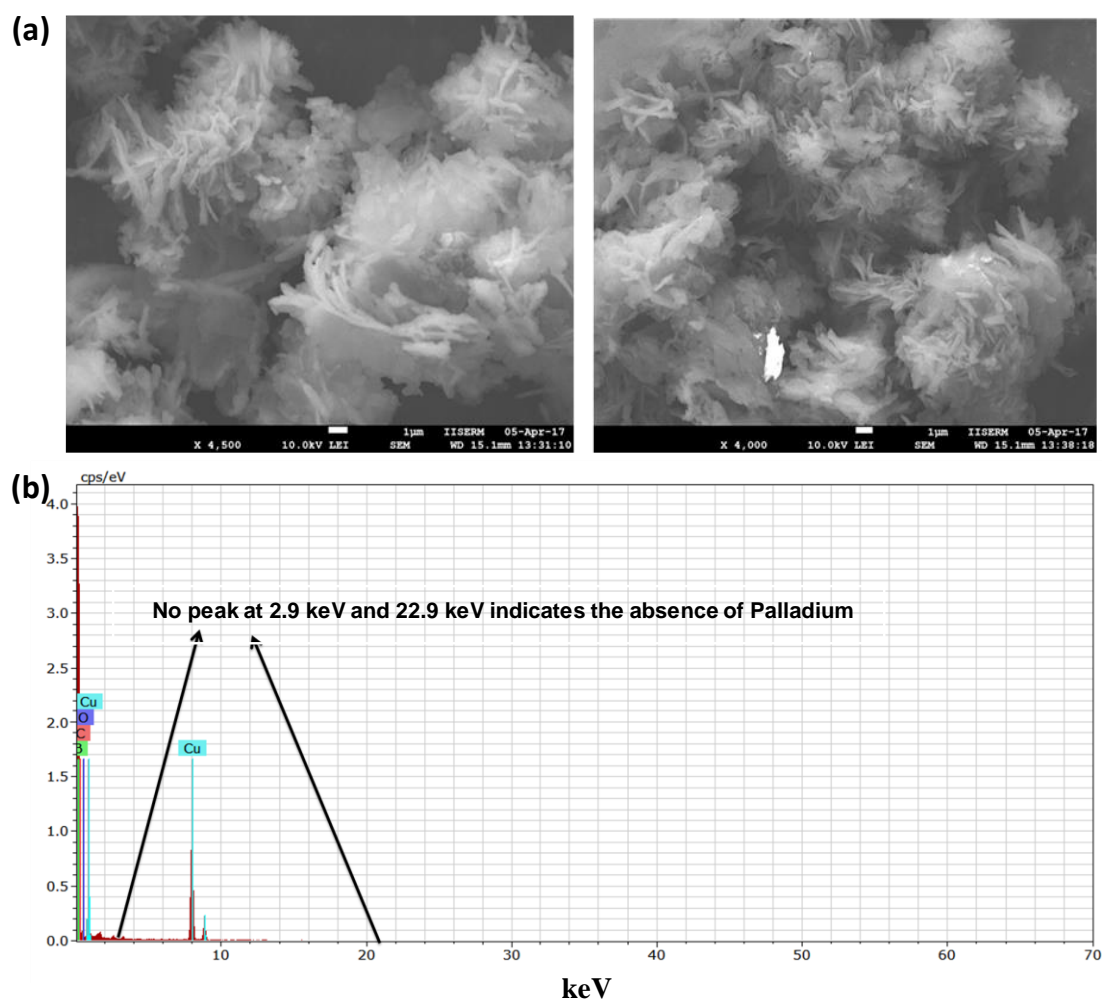
Figure 4.3: (a) Scanning electron microscopic (SEM) images of Tx-CMP at different magnifications. (b) The EDX mapping of Tx-CMP shows (arrows) absence of any traces of Palladium present in the as-prepared Tx-CMP sample.

showed (arrow) the absence of any traces of palladium present in the as-prepared Tx-CMP sample after the Suzuki-coupling reaction (Figure 4.3b). X-ray photoelectron spectroscopy (XPS) survey scan shows that carbon is the major component presents besides trace amount of oxygen and bromine at the dangling ends of the polymeric framework (Figure 4.4a).

4.3.4 Mott−Schottky Electrochemical Measurements:

Mott−Schottky electrochemical measurements were carried to get the information about the conduction band potential. Catalyst ink was prepared by dispersing the catalyst in ethanol, isopropyl alcohol (IPA), nafion and then working electrode was prepared by drop-casting catalyst ink on the glassy carbon electrode (GCE) and left to dry overnight.
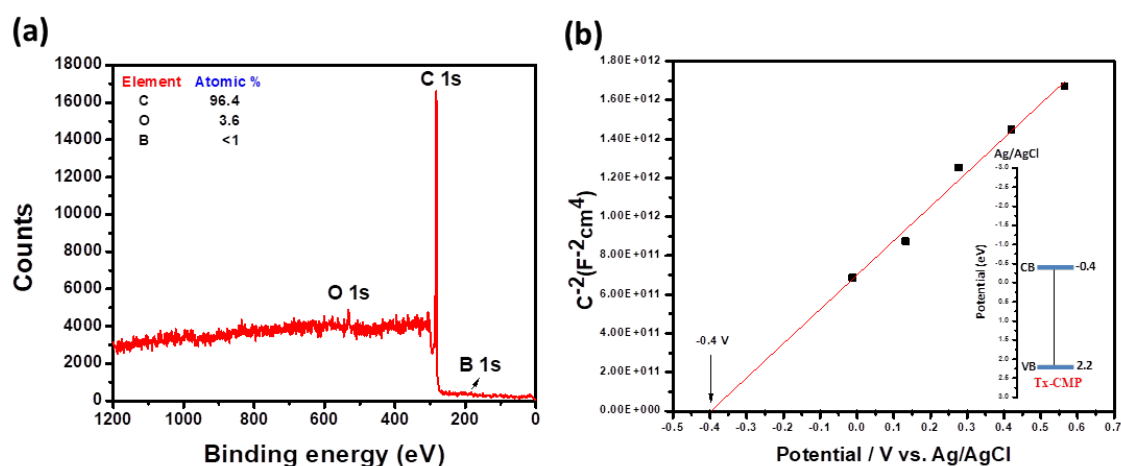

Figure 4.4: (a) XPS survey scan with the elemental composition (inset) of Tx-CMP; (b) Mott−Schottky electrochemical measurement plot of Tx-CMP.

Electrochemical impedance spectra measurements were carried out by standard three-electrode system using platinum wire and Ag/AgCl (3M KCl) as counter and reference electrodes, respectively. The Schottky electrochemical measurements (Figure 4.4b) was conducted in a buffer solution (pH= 7) in the potential range of -0.6 to 1V. Based on

conduction band minimum (CBM) and optical band gap (2.6 eV), the valence band maximum (VBM) was estimated as 2.2 V (vs Ag/AgCl).

4.3.5 Characterization of SG-CN:

The PXRD pattern of SG-CN is shown in Figure 4.5a. The intense peak at *2θ* 27.4° corresponds to (002) plane, due to the interlayer stacking of graphitic carbon nitride layers at a distance of 0.326 nm (JCPDS no.087-1526). The DR UV-vis spectrum is shown in Figure 4.5b. The SG-CN sample showed absorption in the visible region with a steep band at 450 nm arises due to the bandgap transition from nitrogen 2p to carbon 2p orbital. The additional shoulder in the range 450−600 nm is due to the existence of carbon
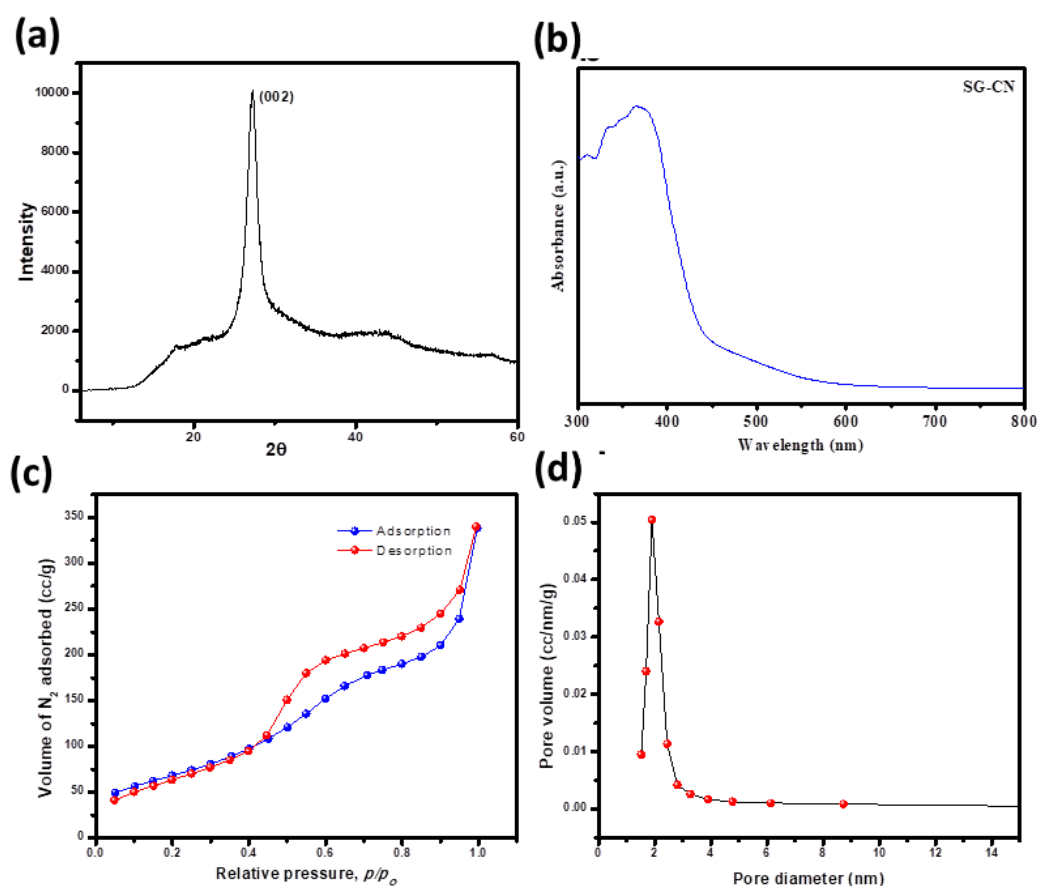

Figure 4.5: Characterization of SG-CN: (a) XRD pattern; (b) DRUV-Vis spectra; (c) N_2-physisorption isotherm and (d) BJH-pore size distribution.

impurities incorporated during the condensation process to synthesize SG-CN. The N_2 physisorption isotherm is shown in Figure 4.5c. The N_2 physisorption isotherm of SG-CN shows type-IV behavior with a hysteresis loop and confirms the mesoporous structure. The BJH pore size distribution is shown in Figure 4.5d. From the BJH pore size distribution, the majority of the pore volume is due to the pores of diameter less than 4 nm.

### 4.3.6 Comparison of TX-CMP with SG-CN and TiO$_2$:

It had been established that the generation of reactive oxygen species (ROS) and the oxidation ability of holes depend on the valence band and conduction band positions of the semiconductors. As shown in Figure 4.6a, the valence band (VB) position is far positive (+2.4 V vs NHE) which indicates that the Tx-CMP is a better oxidant comparable to carbon nitride (+1.4 V). On the other hand, specific surface area (SSA) of a photocatalyst also can play an active role in photocatalytic activity. The SSA and pore volume of the employed photocatalysts, TiO$_2$ (P25) and SG-CN and Tx-CMP had been tabulated in Figure 4.6b.

Catalyst	SSA(m²/g)	Pore (cc/g)
Tx-CMP	1022	0.7
SG-CN	174	0.37
TiO₂(P25)	59.7	0.47
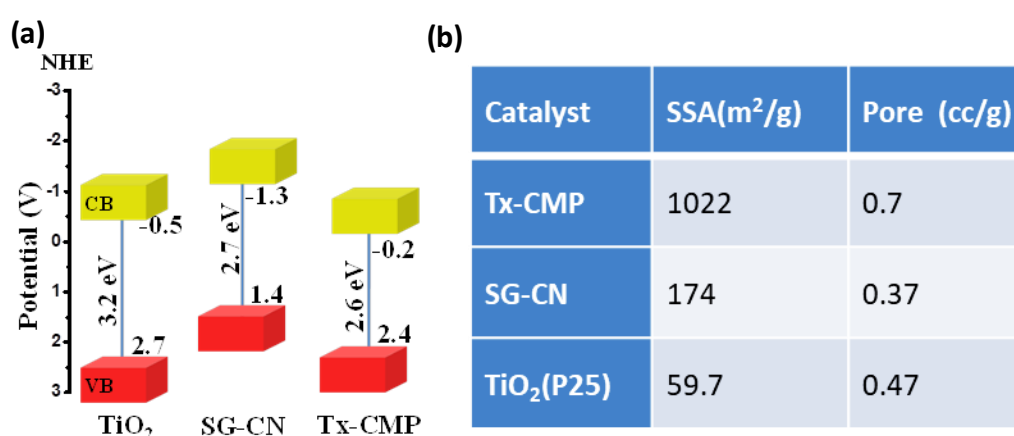
Figure 4.6: (a) Band energy diagram of TiO$_2$, SG-CN and Tx-CMP; (b) N$_2$-Physisorption measurements of TiO$_2$, SG-CN and Tx-CMP.

4.3.7 Photocatalytic Activity of the Catalyst in Natural Sunlight:

The sunlight is largely available, inexpensive, and inexhaustible source of energy which contains approximately 3% of UV, 44% of visible and 53% of NIR. This inspired us to explore the utilization of natural sunlight to drive the chemical reactions rather than other artificial sources of light, which requires a lot of expenditure when large scale industrial applications are concerned. Initially, the natural sunlight-driven oxidative homocoupling of benzylamine (BAN) was taken as a model reaction with Tx-CMP, as a metal-free photocatalyst.
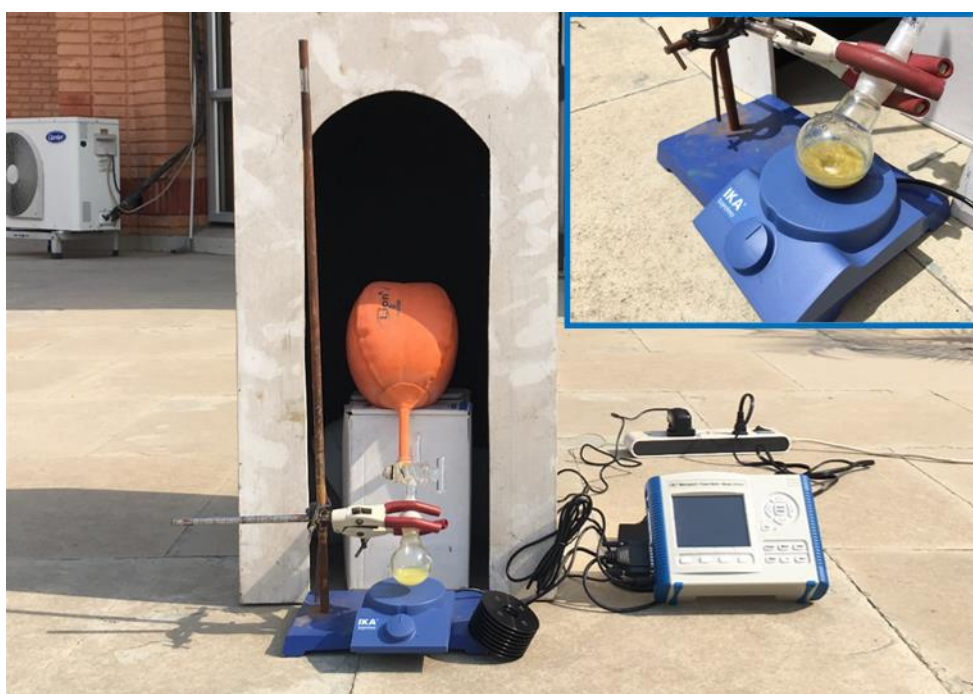
Figure 4.7: The photocatalytic reaction setup for the oxidative homocoupling of arylamines (Inset showing a closer view of the round-bottomed flask kept in sunlight to carry out oxidative homocoupling reactions.)

Due to its high SSA, small optical band gap (2.6 eV) and appropriate band positions, we decided to explore Tx-CMP's photocatalytic activity for photo-oxidation of arylamines in the natural sunlight. Oxidative homocoupling of arylamines to corresponding imines was

carried out by using oxygen as an oxidant and acetonitrile as a solvent in the presence of sunlight, as shown in Figure 4.7.

Table 4.1: Optimization of the conditions for natural sunlight driven oxidative homocoupling of benzylamine.[a]

Entry	Catalyst	Amine conversion (%)[b]	Product selectivity/ yield (%)[b]	TOF[c]
1	No Catalyst	0	-	-
2	No Catalyst, No light	0	-	-
3	Tx-CMP[d]	<1	100/-	-
4	Tx-CMP	>99	91/90	12.4
5	Tx-CMP[e]	>99	89/88	12.4
6	Tx-CMP[f]	77	97/75	9.6

[a]Reaction Conditions: BAN (0.5 mmol), Tx-CMP = 10 mg, Solvent = 5 mL Acetonitrile, Reaction time = 4 h in O_2 atmosphere, under natural sunlight. [b]Calculated by GC-MS. [c]TOF(Turn Over Frequency)= mmoles of benzylamine converted per gram of catalyst per h. [d]Without light, [e]Full-arc experiments(T=35 °C). [f]Under visible light (>420 nm, T=35 °C).

In a general procedure, the oxidative homocoupling of arylamines was performed in a home-made photocatalytic vessel under direct sunlight (Figure 4.7). In a typical reaction, 0.5 mmol of BAN was added to 5 mL of acetonitrile solvent and then 10 mg of Tx-CMP

was added. The reaction mixture was kept for stirring under natural sunlight (In Mohali, India, during May, June and August 2017) and the O_2 atmosphere (1 atm) was maintained during the reaction. The catalyst was separated by microcentrifuge after the reaction for further characterization. The optimization conditions had been shown in Table 4.1. From entries 1-3, it is clear that the photocatalyst and sunlight are indispensable for this reaction. In presence of sunlight (average temp. = 35.2 °C, solar intensity = 80.2 mW/cm^2), >99% conversion was obtained with 90 % yield within 4 h of reaction time (Table 4.1, Entry 4). In order to study the individual effect of UV and Visible light portion of natural sunlight on the catalytic activity, we carried out a reaction with the simulated sunlight under full-arc conditions (T = 35 °C) and under visible light (>420 nm, T = 35 °C) by using 450 W Xe lamp operated at 400 W (Height was adjusted to give the intensity of 80 mW/cm^2) separately which gave 88% and 75% yields respectively (Table 4.1, Entries 5, 6). The reason for the better yield in full-arc over visible light conditions
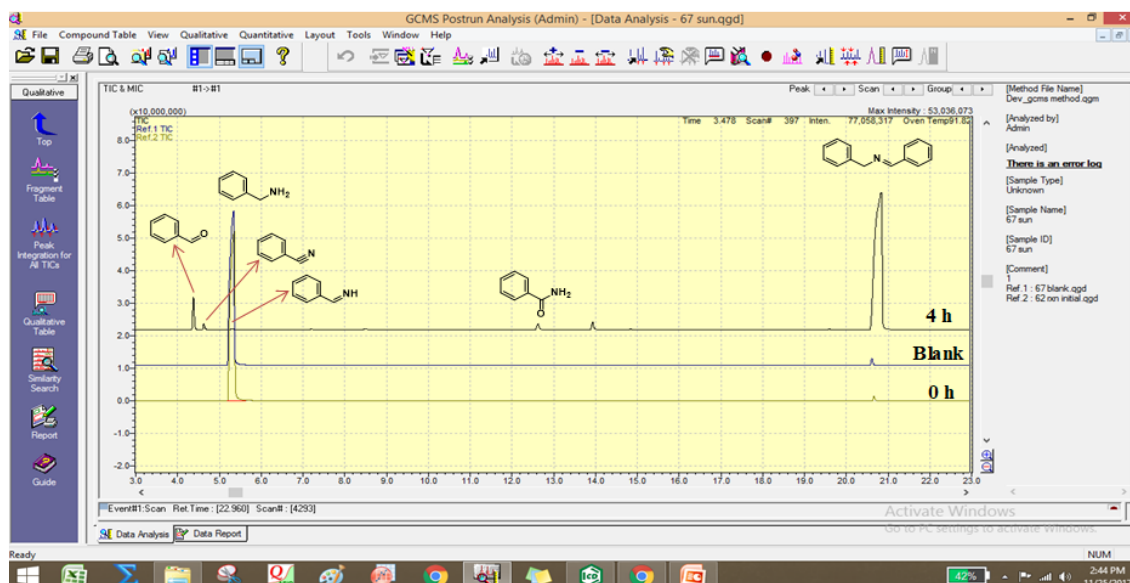
Figure 4.8: GC-MS chromatogram screen shot of reaction mixture at 0 h, 1 h 2 h and 4 h (below).

could be attributed to its absorption in UV region. Moreover, these results also suggested that the Tx-CMP is an efficient natural sunlight active photocatalyst for the oxidative homocoupling of BANs to corresponding imine. The screenshot of GC-MS chromatogram of the reaction mixture at 0 h, after 4 h in dark and sunlight, respectively were provided in Figure 4.8. The average temperature and average solar intensity during these whole studies in natural sunlight had been given in appendix Table A4.1.
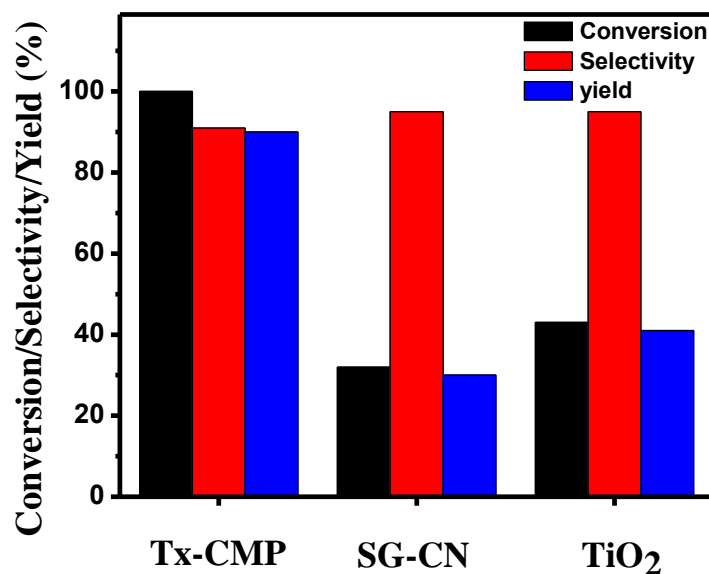

Figure 4.9: Comparison bar diagram of Tx-CMP photocatalytic activity with TiO_2 and SG-CN for Oxidative homocoupling of benzylamine.

Further, the catalytic activity of Tx-CMP was compared with commercially available TiO_2 (P25) and mesoporous carbon nitride (prepared by sol-gel route, SG-CN) for the photooxidation of BAN under natural sunlight. The catalytic activity of these catalysts in sunlight was found to be in the order: Tx-CMP > TiO_2 (P25) > SG-CN, which could be explained on the basis of their band position and surface area parameters as briefed above (Figure 4.9). The better catalytic activity of TiO_2 (P25) over SG-CN is due to its more positive valence band position and formation of the surface complex with BAN which acts as an antenna for visible light absorption.[24] Even though the valence band position of

TiO$_2$(P25) is slightly positive than that of Tx-CMP (Figure 4.6a), the catalytic performance of Tx-CMP is far superior to TiO$_2$ (P25) essentially due to its high SSA and smaller bandgap (Figure 4.6b).

Energy-dispersive X-ray spectroscopy (EDX) experiments showed the absence of any traces of palladium present in the as-prepared Tx-CMP sample after the Suzuki-coupling reaction (Figure 4.3b) which ruled out the possibility of catalytic activity by palladium. From the above experiments, it could be inferred that the SSA and band position stimulated the superior photocatalytic activity of Tx-CMP as compared to TiO$_2$ (P25) and SG-CN in direct sunlight.

4.3.8 Recyclability and Stability of Catalyst:
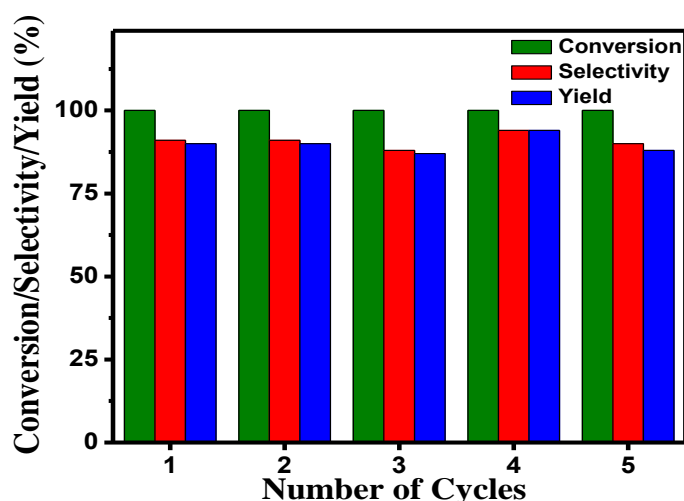
Figure 4.10: Recyclability test of Tx-CMP in Oxidative homocoupling of benzylamine. Reaction Conditions: Substrate (0.5 mmol), Tx-CMP = 10 mg, Solvent = 5 ml.

To study the durability of Tx-CMP in natural sunlight, recyclability tests were conducted for five subsequent cycles. Before using the catalyst for the next cycle, the catalyst was recovered by centrifugation, washed with acetonitrile and dried at 120 °C in a vacuum oven for overnight. As shown in Figure 4.10, the conversion of BAN was >99% in each

cycle with more than 90% yield. Thus, the photocatalytic activity of Tx-CMP remained similar throughout its use in all cycles.
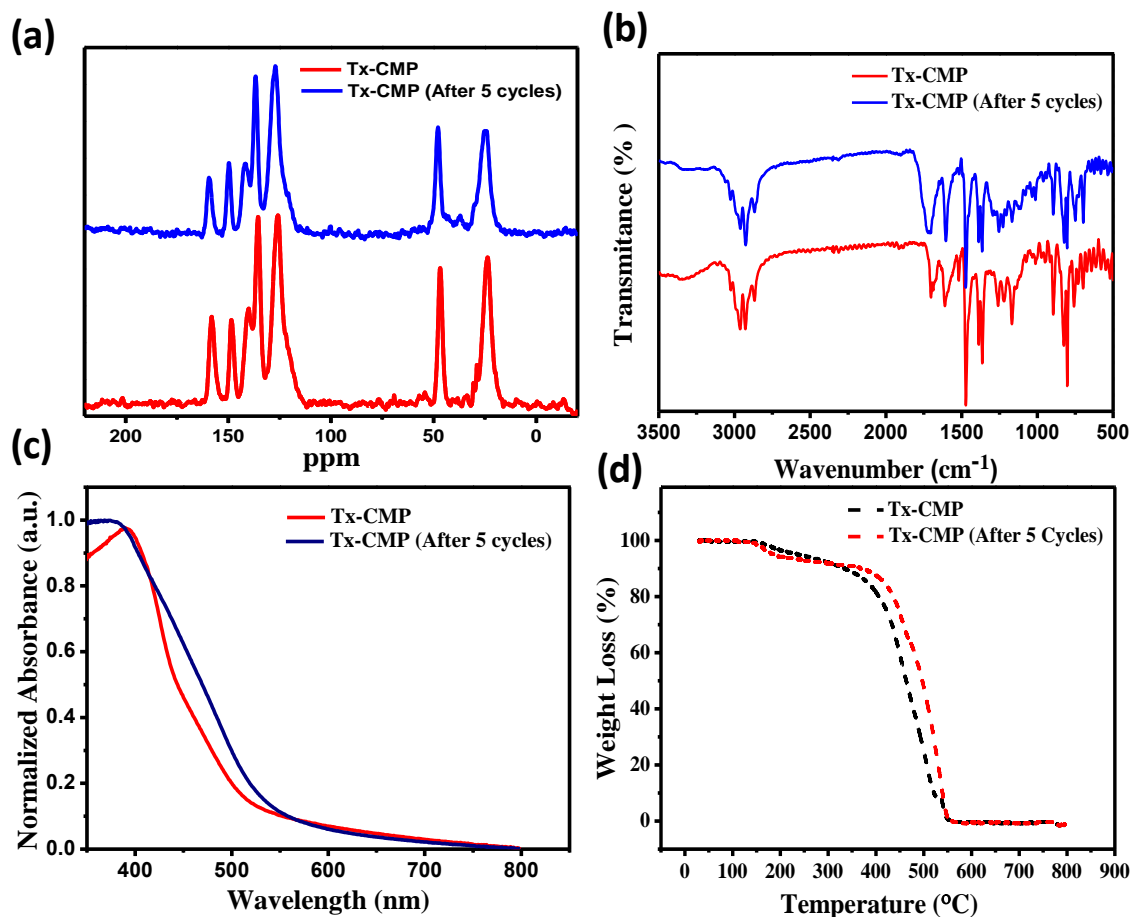

Figure 4.11: (a) Solid-state ^{13}C CP/MAS NMR spectra of Tx-CMP as synthesized (red) and after five cycles of reaction (blue); (b) FTIR spectra of Tx-CMP as-synthesized (red) and after five cycles of reaction (blue); (c) DRUV-Vis spectra of Tx-CMP as-synthesized (red) and after five cycles of reaction (blue); (d) TGA spectra of Tx-CMP as synthesis (red) and after five cycles of reaction (black).

We carried out the Solid-state ^{13}C CP/MAS NMR, FT-IR, DRUV-Vis, TGA and SEM analysis of recovered Tx-CMP after 5th cycle (Figure 4.11a-d and Figure 4.12a). The result shows that Tx-CMP retained similar structural features after being used for 5 consecutive cycles of reaction course. The SSA of Tx-CMP catalyst after 5th cycle was measured to be 904 m^2/g (Figure 4.12b). Only a minor loss in the surface area compared

to that of the fresh one and the retention of the porous structure was observed. This indicated the superior performance and robustness of Tx-CMP as a metal-free photocatalyst for natural sunlight driven oxidative homocoupling of arylamines.

4.4 Mechanistic Studies:

Based on the observation from the above experimental studies and previous reports, a plausible mechanistic pathway for the natural sunlight-driven oxidative homocoupling of arylamines (BAN has been taken as model) was proposed (Scheme 4.3). Generally, this reaction was initiated by the charge carriers, holes and electrons that were generated upon light absorption by Tx-CMP. A similar reaction when carried out under N_2 atmosphere gave only 7% conversion of BAN to imine (Table 4.2, entry 1) which confirmed that the molecular O_2 is essential for this reaction.
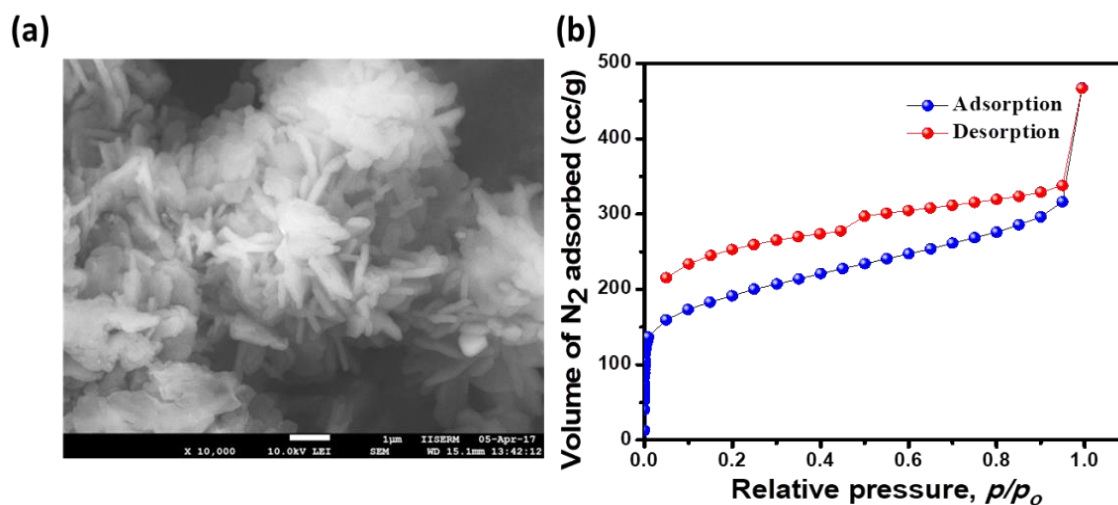
Figure 4.12: (a) Scanning electron microscopic (SEM) images of Tx-CMP at different magnifications after 5th cycles of reaction; (b) N_2-physisorption isotherm of Tx-CMP after recyclability tests for 5th cycles of photocatalytic reaction.
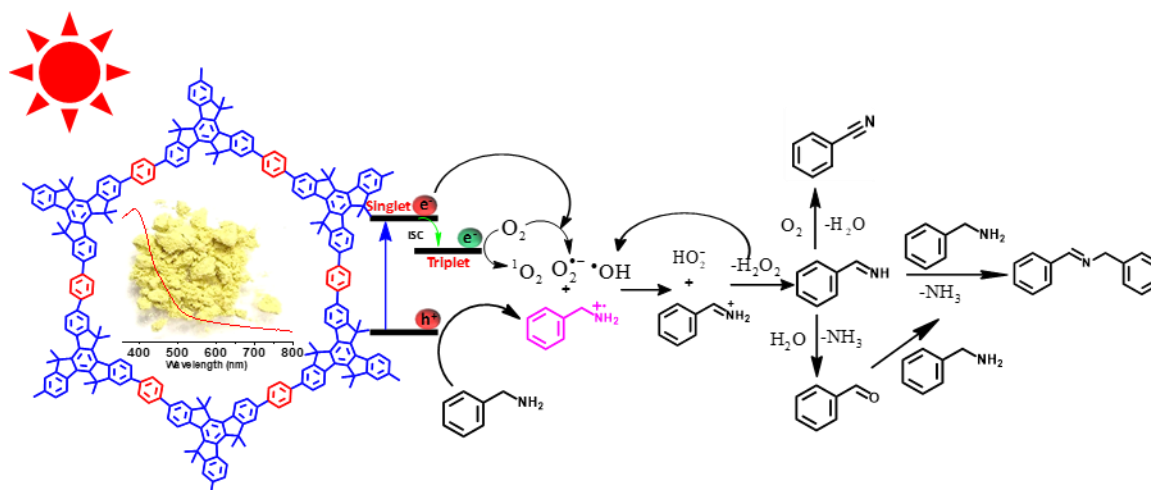
Scheme 4.3: Proposed mechanism for the natural sunlight driven oxidative homocoupling of benzylamine catalyzed by Tx-CMP.

**Table 4.2:** Controlled experiments to predict the mechanism.

Entry	O_2	Additive	Conversion (%)
1[a]	-	-	-
2	+	Hole scavenger	10
3	+	Superoxide scavenger	30
4	+	Singlet oxygen scavenger	77

Reaction Conditions: Substrate (0.5 mmol), Tx-CMP = 10 mg, Solvent = 5 mL Acetonitrile, Reaction time = 4 h under direct sunlight. [a]N_2 atmosphere. KI as hole scavenger. *p*-benzoquinone as superoxide scavenger. NaN_3 as singlet oxygen scavenger.

As reported previously, the molecular oxygen (O_2) is converted into reactive oxygen species (ROS) by electron or energy transfer process (superoxide radical ($O_2^{.-}$) and singlet oxygen ($^1O_2$) species.[25-26] The holes in the valence band of Tx-CMP oxidized the BAN to

benzylamine radical cation.[27] On the formation of benzylamine radical cation, the acidity of benzylic C-H (benzylic hydrogen) adjacent to the amine functional group would increase. The formed ROS would further abstract the benzylic hydrogen from the benzylamine radical cation to form benzyliminium ion. To investigate the influence of benzylamine radical cation, the hole scavenger KI was added and found that the conversion of BAN was decreased drastically to 10% in the presence of KI (Table 4.2, entry 2), which confirmed that the formation of benzylamine radical cation formation step is crucial for this reaction.

To shed more light on mechanistic pathways, the role of ROS in this sunlight driven oxidative homocoupling of BAN was investigated. When *p*-benzoquinone (BQ), a superoxide radical scavenger was added to the reaction mixture, the homocoupling of BAN decreased drastically to 30% in (Table 4.2, entry 3) which indicated the vital role of
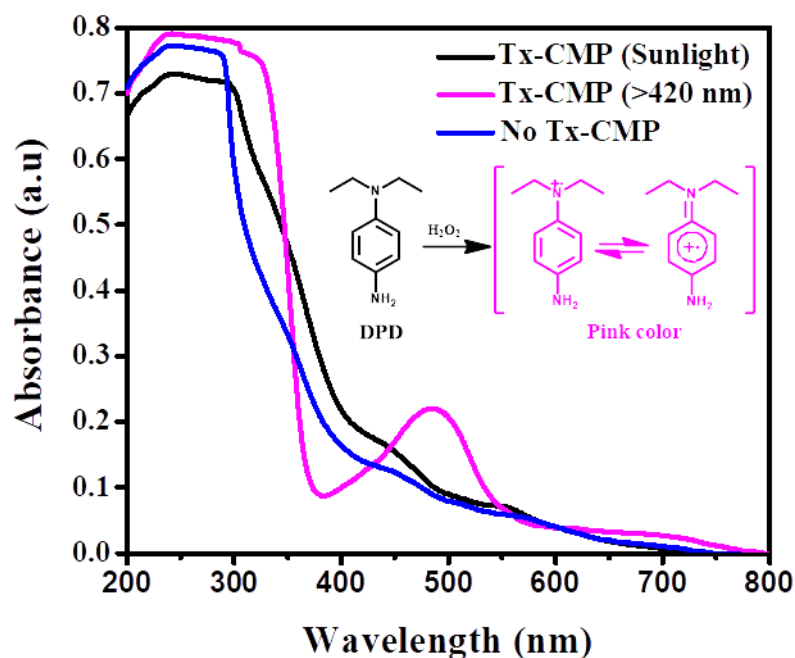
Figure 4.13: UV-Vis absorption spectra of the reaction mixture (Benzylamine) with Tx-CMP in presence of Natural Sunlight and Visible light (450 W Xe lamp (>420 nm)) after adding N,N-diethyl-1,4-phenylenediamine (DPD).

superoxide radicals.[28] The singlet oxygen scavenger sodium azide (NaN$_3$) was also added to the reaction mixture and it was observed that the homocoupling of BAN decreased to 77% (Table 4.2, entry 4) which proved the role of singlet oxygen in this reaction pathway.[26] To note that, the benzyliminium ion further converted into benzylimine with the formation of H$_2$O$_2$ as side product.[29] The H$_2$O$_2$ further dissociated into •OH by the UV light present in the sunlight and helped in the oxidation of BAN to the corresponding imine. The formation of H$_2$O$_2$ and its dissociation into •OH radicals by UV light present in natural sunlight during the reaction has been proved by a controlled experiment by using of *N,N*-diethyl-1,4-phenylenediamine (DPD). Initially, the DPD was added to the reaction mixture (0.5 mmol benzylamine, 5 mL acetonitrile) in the presence of Tx-CMP
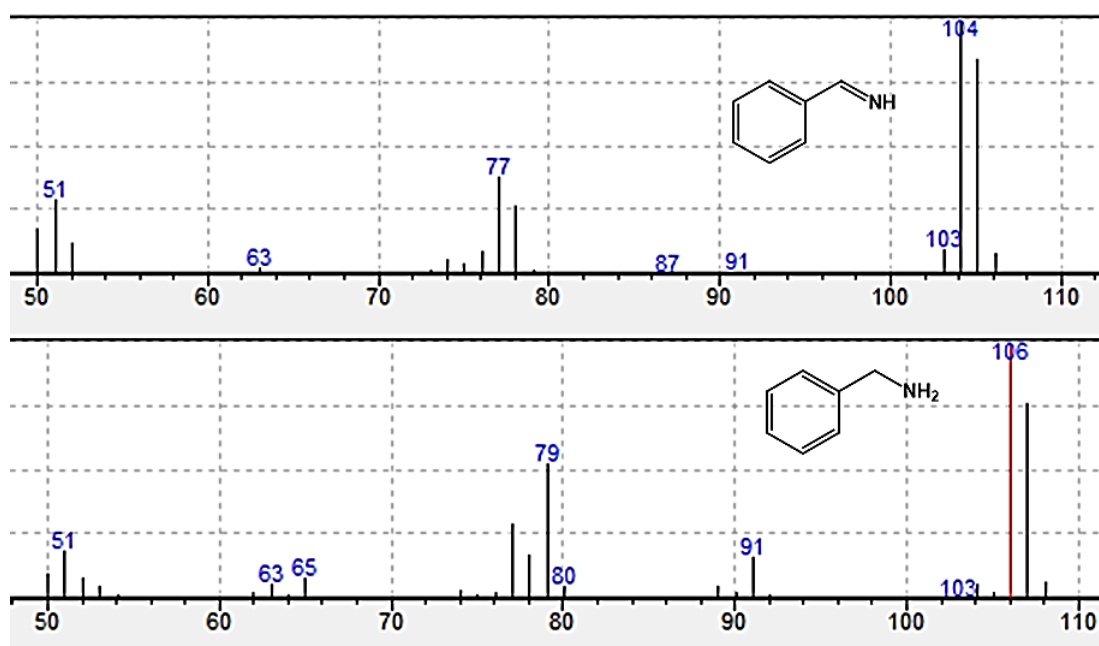
Figure 4.14: Fragmentation spectra of benzylimine and benzylamine.

and kept for magnetic stirring under visible light irradiation (>420 nm). As the reaction proceeds, the formed H$_2$O$_2$ oxidized DPD to DPD radical cation with intense coloration (inset of Figure 4.13). The same reaction was also performed under natural sunlight, which contains 3% of UV. Thus the formed H$_2$O$_2$ immediately dissociated into OH

radicals, which prevented the formation of DPD radical cation. Thus, no characteristic coloration was observed in UV-vis spectrum in Figure 4.13. The same reaction also performed without Tx-CMP under visible light didn't show any characteristic peak in UV-vis spectra. All these observations supported the formation of H_2O_2 and its dissociation to radicals under natural sunlight condition during this reaction.
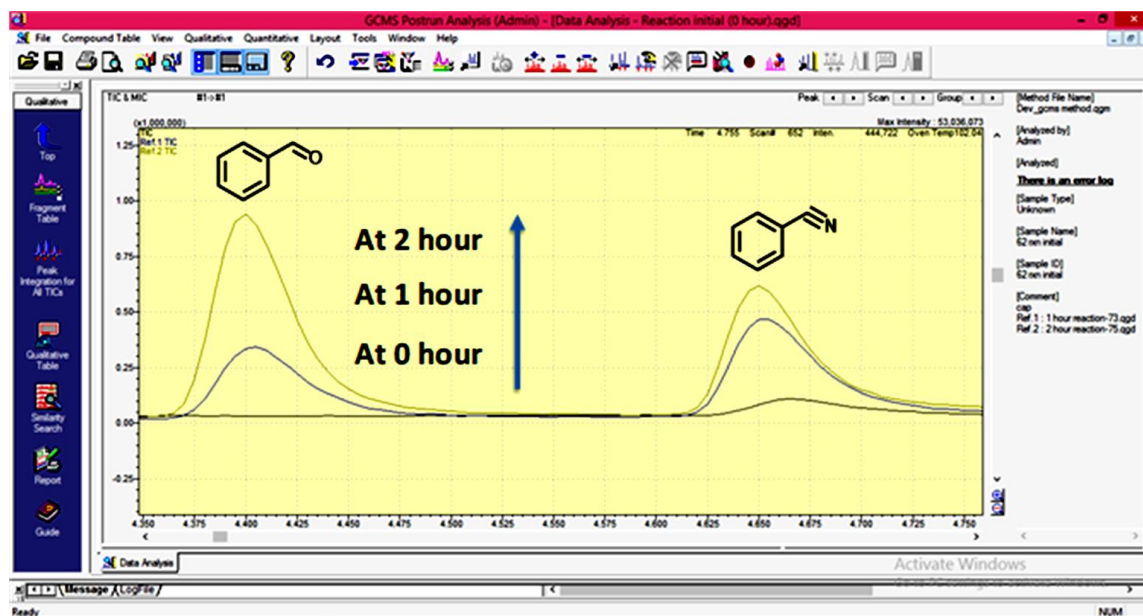
Figure 4.15: GC-MS chromatogram screen shot of reaction mixture at 0 h, 1 h and 2 h.

Further, the benzylimine (detected in GC-MS at retention time of 5.3 min) could react in 3 different ways: 1) Undergo dehydrogenative step to give benzonitrile (detected in GC-MS at 4.6 min retention time).[30] 2) Converts into benzaldehyde (detected in GC-MS at 4.4 min retention time). 3) This further could react with BAN to give the corresponding imine.[31-33]

The formation of benzylimine was confirmed by the fragmentation spectra (Figure 4.14). In order to prove the formation of above intermediates, we monitored the reaction for initial 2 h. We observed that the concentration of benzaldehyde and benzonitrile increased for this time period (Figure 4.15) with consequent decrease in concentration of reactant.
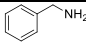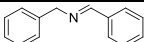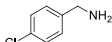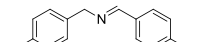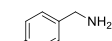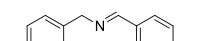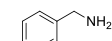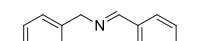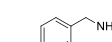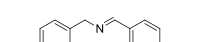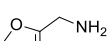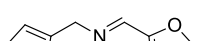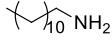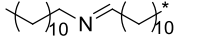
The corresponding increase in the concentration of both (benzaldehyde and benzonitrile) indicated the formation of benzylimine intermediate which could undergo dehydrogenation and hydrolysis, respectively to benzonitrile and benzaldehyde. These additional experiments to understand the mechanism in the natural sunlight as observed earlier in high energy light sources proves the similar mechanistic pathway in the current study.

4.5 Substrate Scope of the Catalyst:

Further, to explore the versatility of Tx-CMP catalyst, various substituted BANs (Table 4.3) were used under the same reaction condition. When BAN is substituted with electron-withdrawing substituents (-Cl & -F), we achieved 77% and 82% conversion with 95% and 92% selectivity, respectively within 4 h of reaction time (Table 4.3, entry 2 and 3). However, the BAN substituted with electron-donating substituents (-CH$_3$ & -OCH$_3$) achieved 96% and 97% conversion with 80% and 81% selectivity, respectively, within 4 h reaction time (Table 4.3, entry 4 and 5).

Besides, the applicability of Tx-CMP for oxidative homocoupling of heterocyclic amine (furfurylamine) was explored resulting in the 98% conversion with 86% selectivity (Table 4.3, entry 6). But the reaction with aliphatic amines (Dodecylamine and n-butylamine) could not give corresponding imine under these experimental conditions (Table 4.3, entry 7 and 8). In this case, only fragmentation products were observed in GC-MS spectrum. This is due to the activation of multiple reactive cen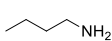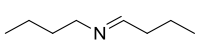ters by reactive oxygen species, which results in unselective auto-oxidation of aliphatic amines.[33] The above experimental results suggested that Tx-CMP is a highly promising photocatalyst which can promote oxidative homocoupling of substituted arylamines and heterocyclic amines to corresponding imines with high conversion and selectivity within 4 h in natural sunlight.

Table 4.3: Photocatalytic activity of the Tx-CMP for selective oxidation of various amines.

Entry	Substrate	Product	Conversion /selectivity (%)	TOF[a]
1			>99/91	12.4
2			77/95	9.6
3			82/92	10.3
4			97/80	12.1
5			96/81	12.0
6			98/86	12.3
7			0/0	-
8			0/0	-

Reaction Conditions: Substrate (0.5 mmol), Tx-CMP = 10 mg, Solvent = 5 mL Acetonitrile, Reaction time = 4 h in O_2 atmosphere, under direct sunlight. [a]TOF = mmoles of amine converted per gram of catalyst per hour.

4.6 Summary:

In summary, this chapter described the design and synthesis of a novel Truxene based conjugated microporous polymer (Tx-CMP) linked through a highly stable C-C bond for the first time. The novel Tx-CMP has high surface area, large pore volume, narrow band gap and extraordinary stability. It serves as a metal-free photocatalyst for the oxidative homocoupling of arylamines with highest TOF number under natural sunlight within 4 hours. This model reaction also describes an effective, greener and sustainable way to

harvest natural sunlight effectively for the organic transformations. Tx-CMP has shown recyclability without any decline in its catalytic activity. This work can open the door for the employment of various conjugated microporous polymers as metal-free heterogeneous photocatalysts for effective harvesting of natural sunlight to drive many organic transformations.

References:

1.   Prier, C. K.; Rankic, D. A.; MacMillan, D. W. C. *Chem. Rev.* **2013**, 113, 5322.

2.   Pham, P. V.; Nagib, D. A.; MacMillan, D. W. C. *Angew. Chem., Int. Ed.* **2011**, 50, 6119.

3.   Nguyen, J. D.; Tucker, J. W.; Konieczynska, M. D.; Stephenson, C. R. J. *J. Am. Chem. Soc.* **2011**, 133, 4160.

4.   Nagib, D. A.; MacMillan, D. W. C. *Nature*. **2011**, 480, 224.

5.   Furst, L.; Narayanam, J. M. R.; Stephenson, C. R. *Angew. Chem., Int. Ed.* **2011**, 50, 9655.

6.   Yoon, T. P.; Ischay M. A.; Du, J. *Nat. Chem.* **2010**, 2, 527.

7.   Tucker, J. W.; Nguyen, J. D.; Narayanam, J. M. R.; Krabbe, S. W.; Stephenson, C. R. J. *Chem. Commun.* **2010**, 46, 4985.

8.   Du, J.; Yoon, T. P. *J. Am. Chem. Soc.* **2009**, 131, 14604.

9.   Marin, M. L.; Santos-Juanes, L.; Arques, A.; Amat, A. M.; Miranda, M. A. *Chem. Rev.* **2012**, 112, 1710.

10.   Neumann, M.; Fuldner, S.; Konig, B.; Zeitler, K. *Angew. Chem., Int. Ed.* **2011**, 50, 951.

11.   Liu, H. J.; Feng, W.; Kee, C. W.; Zhao, Y. J.; Leow, D.; Pan Y. H.; Tan, C. H. *Green Chem.* **2010**, 12, 953.

12.   Romero, N. A.; Nicewicz, D. A. *Chem. Rev.* **2016**, 116, 10075.

13.   Xu, Y. H.; Jin, S. B.; Xu, H.; Nagai, A.; Jiang, D. L. *Chem. Soc. Rev.* **2013**, 42, 8012.

14.   Dawson, R.; Laybourn, A.; Clowes, R.; Khimyak, Y. Z.; Adams, D. J.; Cooper, A. I. *Macromolecules* **2009**, 42, 8809.

15.   Cooper, A. I. *Adv. Mater.* **2009**, 21, 1291.

16.   Jiang, X. J.; Su, F. B.; Trewin, A.; Wood, C. D.; Campbell, N. L.; Niu, H. J.; Dickinson, C.; Ganin, A. Y.; Rosseinsky, M. J.; Khimyak, Y. Z.; Cooper, A. I. *Angew. Chem., Int. Ed.* **2007**, 46, 8574.

17.   Kailasam, K.; Mesch, M. B.; Möhlmann, L.; Baar, M.; Blechert, S.; Schwarze, M.; Schröder, M.; Schomäcker, R.; Senker, J.; Thomas, A. *Energy Technology.* **2016**, 4, 744.

18.   Chen, B.; Wang, L.; Gao, S. *ACS Catal.* **2015**, 5, 5851.

19.   Dehmlow, E. V.; Kelle, T. *Synth. Commun*. **1997**, 27, 2021.

20.   Liu, L; G. Telfer S. *J. Am. Chem. Soc.* **2015,** 137, 3901.

21.   Kim, Y,; Das, S.; Bhattacharya, S.; Hong, S.; Kim, M.G.; Yoon, M.; Natarajan, S.; Kim, K. *Chem. Eur. J.* **2012**, 18, 16642.

22.   Kailasam, K.; Epping, J. D.; Thomas, A.; Losse, S.; Junge, H. *Energy Environ. Sci.* **2011**, 4, 4668.

23.   Wang, Z. J.; Ghasimi, S.; Landfester, K.; Zhang, K. A. I. *J. Mater. Chem. A.* **2014**, 2, 18720.

24.   Lang, X.; Ma, W.; Zhao, Y.; Chen, C.; Ji, H.; Zhao, J. *Chem. Eur. J.* **2012**, 18, 2624.

25.   Wang, Z. J.; Ghasimi, S.; Landfester, K.; Zhang, K. A. I. *Adv. Mater.* **2015**, 27, 6265.

26. Wang, Z. J.; Garth, K.; Ghasimi, S.; Landfester, K.; Zhang, K. A. I. *Chem. Sus. Chem.* **2015**, 8, 3459.

27. Su, F.; Mathew, S. C.; Mohlmann, L.; Antonietti, M.; Wang, X.; Blechert, S. *Angew. Chem., Int. Ed.* **2011**, 50, 657.

28. Yuan, L.; Yang, M.-Q.; Xu, Y.-J. *Nanoscale* **2014**, 6, 6335.

29. Raza, F.; Park, J. H.; Lee, H.-R.; Kim, H.-I.; Jeon, S.-J.; Kim, J.-H. *ACS Catal.* **2016**, 6, 2754.

30. Samanta, S.; Khilari, S.; Pradhan, D.; Srivastava, R. *ACS Sustainable Chem. Eng.* **2017**, 5, 2562.

31. Kang, N.; Park, J. H.; Ko, K. C.; Chun, J.; Kim, E.; Shin, H.-W.; Lee, S. M.; Kim, H. J.; Ahn, T. K.; Lee, J. Y.; Son, S. U. *Angew. Chem. Int. Ed.* **2013**, 52, 6228.

32. Yang, X.-J.; Chen, B.; Li, X.-B.; Zheng, L.-Q.; Wu, L.-Z.; Tung, C.-H. *Chem. Commun.* **2014**, 50, 6664.

33. Lang, X.; Ji, H.; Chen, C.; Ma, W.; Zhao, J. C. *Angew. Chem., Int. Ed.* **2011,** 50, 3934.

Appendix 4:

Table A4.1: The sunlight intensities and temperatures during the photocatalytic study.

S. No.	Date	Temperature (°C)					Average Temperature (°C)	Average Sunlight intensity (mW/cm^2)
		Temperature at each hour (°C)						
1	30/05/2017	11 AM	12 PM	1 PM	2 PM	3 PM	35.2	80.05
		33	34	36	36	37		
2	07/06/2017	1 PM	2 PM	3 PM	4 PM	5 PM	34.2	70.72
		34	34	34	35	34		
3	12/06/2017	12 PM	1 PM	2 PM	3 PM	4 PM	37.6	82.56
		37	37	38	38	38		
4	16/06/2017	1 PM	2 PM	3 PM	4 PM	5 PM	37	81.70
		37	37	37	37	37		
5	23/06/2017	12 AM	1 PM	2 PM	3 PM	4 PM	33.6	77.25
		33	33	34	34	34		
6	25/06/2017	11 AM	12 PM	1 PM	2 PM	3 PM	36.2	80.03
		36	36	36	36	37		
7	26/06/2017	11 AM	12 PM	1 PM	2 PM	3 PM	34.8	78.05
		33	34	35	36	36		
8	14/08/2017	11 AM	12 PM	1 PM	2 PM	3 PM	31.8	65.90
		31	32	32	32	32		

| 9	16/08/2017	11 AM	12 PM	1 PM	2 PM	3 PM	33.6	68.63
		33	34	34	34	33		
10	17/08/2017	11 AM	12 PM	1 PM	2 PM	3 PM	33.6	78.46
		33	33	34	34	34		
11	18/08/2017	11 AM	12 PM	1 PM	2 PM	3 PM	33.6	77.42
		33	33	34	34	34		
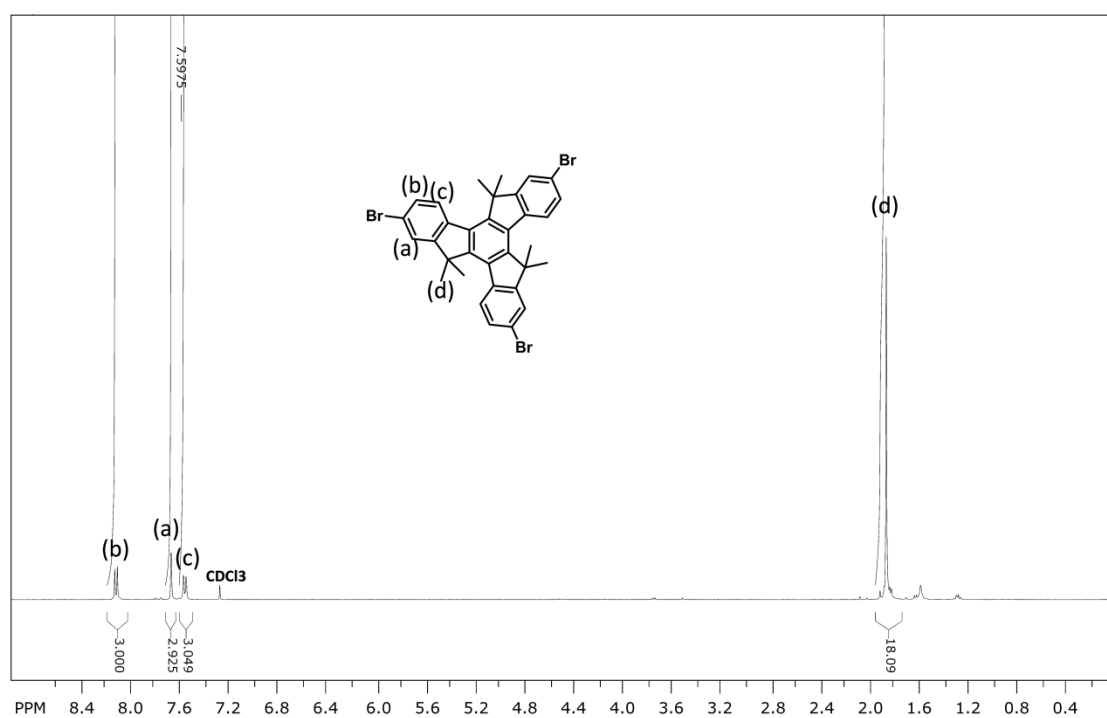
Figure A4.1: ^{1}H NMR of 2,7,12-Tribromo-5,5',10,10',15,15'-hexamethyltruxene.

Chapter 5

Visible-Light Driven Photocatalysis and Band gap Tuning of Truxene based Conjugated Porous Polymers via Donor-Acceptor Combination
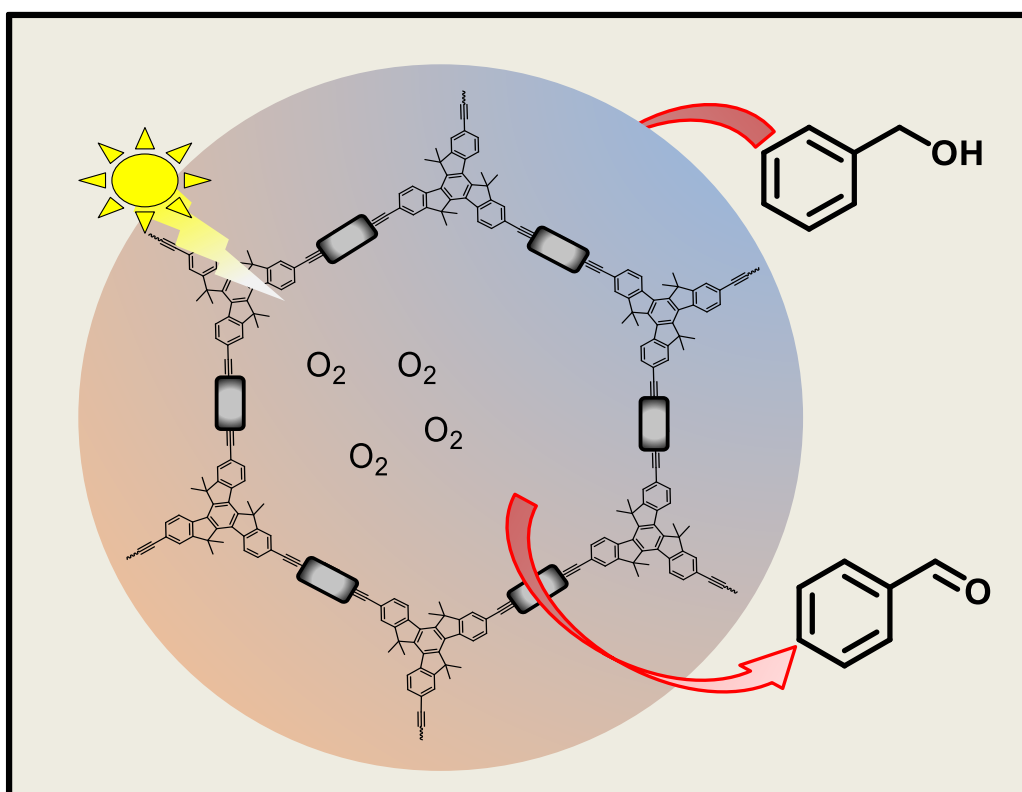
A simple design strategy to develop conjugated porous polymers (CPP) based visible light heterogeneous photocatalyst to perform the desired chemical transformation is demonstrated via tuning of bandgap and band positions using different organic groups. It was observed that by altering the linkers with different electron-accepting capabilities, photocatalytic efficiency can be drastically enhanced. Among the three CPPs, TxOMe-CPP had shown superior photocatalytic activity for the oxidation of benzyl alcohol to benzaldehyde compared to TxBz-CPP and TxBNS-CPP. This strategy could be extended to a wider range of conjugated porous polymeric networks to develop an efficient photocatalyst for specific photocatalytic chemical conversion.

5.1 Aim:

In Chapter 4, the excellent visible-light photocatalytic activity of truxene based microporous polymer (Tx-CMP) has been demonstrated for benzyl amines oxidation to imines with 99% conversion.[1] Apart from the oxidation of benzyl amines, Tx-CMP has also been explored as a heterogeneous visible light photocatalyst for benzyl alcohol to benzaldehyde oxidation. It was observed that Tx-CMP is photocatalytically active for this conversion, but with limited conversion up to the maximum of 28%. In literature, it has been proven that the photocatalytic efficiency of traditional metal-based complexes can be tailored by changing the metal centres or modifying coordinating ligands.[2, 3] Through these changes, redox potential and bandgap of photocatalyst can be tuned to match the activation energies of the specific organic reactions to enhance the photocatalytic performance.[4, 5] Extending these ideas to conjugated porous polymers (CPPs), Zang et al. demonstrated that the connecting site in building blocks to design the CPPs can play a crucial role in changing the bandgap position and accordingly the photocatalytic performance.[6] Further, in their next report, they had shown that the change in chalcogen moieties in the acceptor also have a significant effect on the photocatalytic properties.[7]

Inspired by the above reports, in this chapter, we aim to develop a visible light heterogeneous photocatalyst for the aerobic oxidation of benzyl alcohol to benzaldehyde via tuning of bandgap and band positions of truxene based CPPs. The oxidation of alcohols to aldehydes and ketones has great importance in organic synthesis as well as in industrial chemistry.[8] So far, many metal-based and metal-free catalytic systems have been employed to carry out this conversion.[9-11] In this current study, we developed truxene based metal-free heterogeneous photocatalysts, namely TxBz-CPP, TxOMe-CPP and TxBNS-CPP using 2D linkers with different electron accepting capabilities. These

CPPs were further investigated and compared for their photocatalytic performance to convert benzyl alcohol to benzaldehyde under visible light in aerobic conditions.

5.2 Experimental Section:

5.2.1. Materials and Instruments:

All chemicals and solvents used for synthesis were of analytical grade and used as it is received for synthesis and spectroscopic studies. The synthesized materials were characterized by various spectroscopic techniques as described in Chapter 4, Section 4.2.

5.2.2 Synthesis:

Synthesis of 2,7,12-Tribromo-5,5',10,10',15,15'-hexamethyltruxene (TxMe$_6$Br$_3$) was described in Chapter 4 in detail. Scheme 5.1 represents the synthesis of linkers **2**, **4**, and **7** according to the literature with a slight modification which is given in detail below.[12-13]

5.2.2.1 Synthesis of Linkers:

1,4-bis(trimethylsilylethynyl)benzene (1): 1,4-Diiodobenzene (2 g, 6 mmol) was taken in 60 mL solvent (THF : Triethylamine :: 2 : 1) under the argon atmosphere. To this solution, Pd(PPh$_3$)$_2$Cl$_2$ (0.2450 g, 0.350 mmol) and CuI (0.070 g, 0.350 mmol) were added and stirred for 15 min. To this stirring solution, ethynyltrimethylsilane (0.6 mL, 4.4 mmol) was added by syringe. The temperature was raised to 60˚C slowly with continuous stirring. After 24 h, the reaction mixture was poured into water and product was extracted with DCM. Removal of solvents provided the crude product which was further purified by column chromatography. Targeted product was obtained as light yellow crystalline solid (0.4 g, yield 95 %). ^{1}H NMR (CDCl$_3$, 400 MHz) δ/ppm: 7.41, 0.27.

1,4-Diethynylbenzene (2): To the DCM (10 mL) solution of compound **(1)** (0.400 g, 1.48 mmol), MeOH (10 mL) and K_2CO_3 (1.634 g, 11.8 mmol) were added and stirred for 4 h under inert condition. The reaction was monitored with thin layer chromatography (TLC). After completion of the reaction, solvents were removed under reduced pressure and the remaining solid was dissolved in water. The organic part was extracted with DCM to obtain a colourless solid (0.8 g, 85%). ^{1}H NMR (CDCl$_3$, 400 MHz) δ/ppm: 7.44, 3.17.
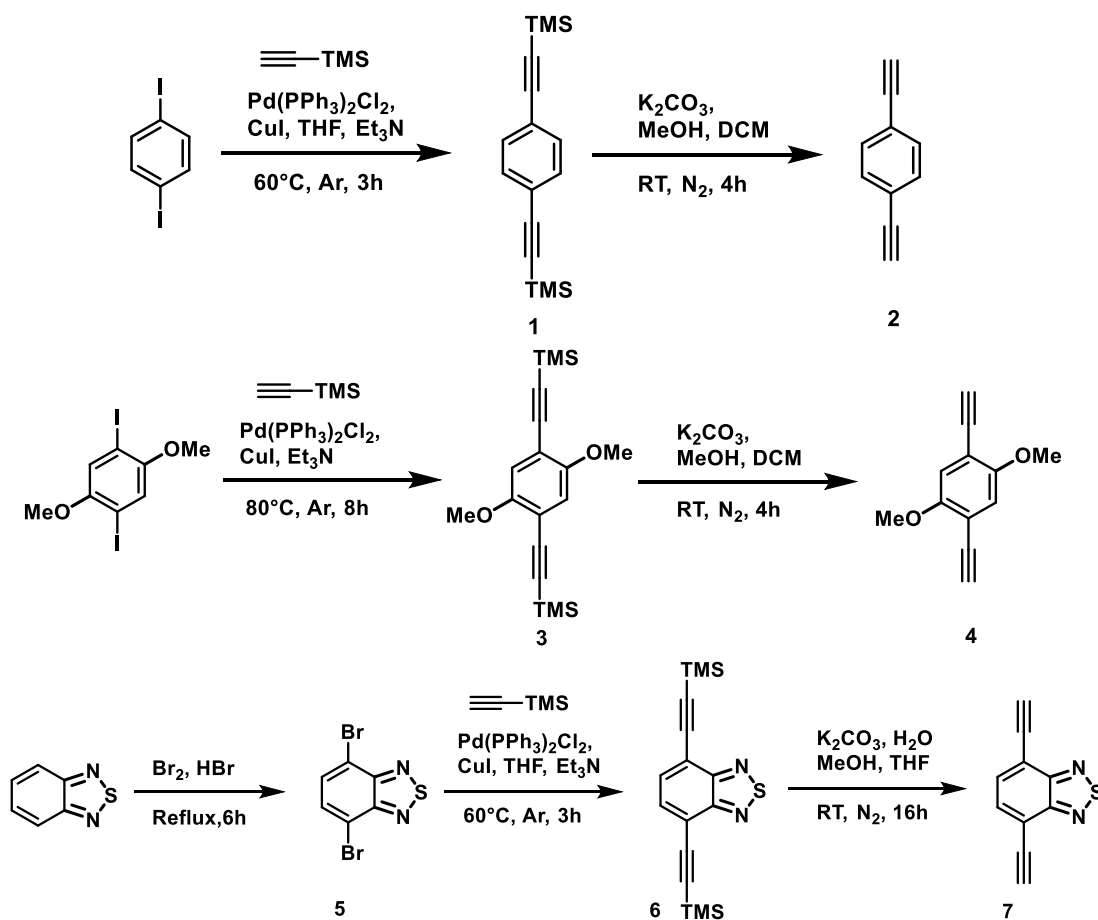
Scheme 5.1: Synthetic scheme of 1,4-Diethynylbenzene (2); 1,4-Diethynyl-2,5-dimethoxy-benzene (4) and 4, 7-Diethynylbenzo[c][1, 2, 5]thiadiazole (7).

(2,5-Dimethoxy-1,4-phenylene)bis(ethyne-2, 1-diyl))bis(trimethylsilane) (3): 1, 4-Diiodo-2,5-dimethoxybenzene (1.0 g, 2.55 mmol), Pd(PPh$_3$)$_4$ (0.57 g, 0.05 mmol), and CuI (0.037 g, 0.1 mmol) were dissolved in 40 mL Et$_3$N under argon environment. The

reaction mixture was purged under Ar flow for 30 min. After purging, trimethylsilylacetylene (7.0 g, 71 mmol) was added with the help of syringe and temperature was slowly raised to 80 °C and stirred for 10 h. After cooling the reaction mixture to room temperature, the insoluble material was collected and washed with DCM to dissolve the product. The organic phase was then washed with water and dried over (MgSO$_4$). The desired product was obtained as a white solid. Yield (14.2 g, 93 %). ^{1}H NMR (CDCl$_3$, 400 MHz) δ/ppm: 0.25, 3.81, 6.89.

1,4-Diethynyl-2,5-dimethoxybenzene (4): Compound (4) was synthesised according to the procedure used for compound (2) using compound (3) (0.240 g, 0.73 mmol), K$_2$CO$_3$ (0.807 g, 5.8 mmol), DCM (10 mL) and MeOH (10 mL). Yield (2.50 g, 98 %). ^{1}H NMR (400 MHz, CDCl$_3$) δ/ppm: 3.37, 3.84, 6.96.

4,7-Dibromobenzothiadiazole (5): Two-necked RB (250 mL) was charged with HBr (75 mL, 28 %) and benzothiadiazole (5.0 g, 37.7 mmol). To this solution, drop wise addition of Br$_2$ (17.6 g, 110.15 mmol) in HBr (50 mL) was completed and the mixture was refluxed for 6 h. After this, the reaction mixture was brought to room temperature, and excess Br$_2$ was removed by adding a saturated solution of NaHSO$_3$. The dark orange precipitate was filtered and washed with water (3 X 50 mL) and further purified by washing with cold Et$_2$O. Yield (10.25 g, 97 %). ^{1}H NMR (400 MHz, CDCl$_3$/[d$_6$] DMSO) δ/ppm: 7.73.

4,7-bis(trimethylsilyl)ethynylbenzo[c][1,2,5]thiadiazole (6): Compound (5) (2 g, 6.8 mmol) was taken in 50 mL solvent (THF : Triethylamine :: 4 : 1) under the argon environment. To this solution Pd(PPh$_3$)$_2$Cl$_2$ (0.19 g, 0.27 mmol) and CuI (0.10 g, 0.27 mmol) were added and kept stirred for 15 min with continues purging of argon gas. To this stirring solution, ethynyltrimethylsilane (3mL, 20 mmol) was added by syringe and

the kept the mixture at RT for 48 h. The precipitate was filtered and dried to obtain the crude product. Yield (1.8 g, 82%). ^{1}H NMR (400 MHz, CDCl$_3$) δ/ppm: 7.70, 0.33.

4,7-Diethynylbenzo[c][1,2,5]thiadiazole (7): 70 mL THF/MeOH (1:1) solution of compound **(6)** (3.22 g, 9.56 mmol) was added with 40 mL of aq. K$_2$CO$_3$ (6.6 g, 48 mmol) and kept in stirring condition for 16 h. The reaction mixture was extracted with H$_2$O and DCM. The crude product was further purified with column chromatography to obtain an orange, light-sensitive solid. Yield (1.12 g, 64%). ^{1}H NMR (400 MHz, CDCl$_3$) δ/ppm: 7.75, 3.67.

5.2.2.2 Synthesis of Conjugated Porous Polymers (CPPs):

General Procedure: The polymer was synthesized via Sonogashira cross-coupling reaction between (TxMe$_6$Br$_3$) and different linkers like **(2)**, **(4)** and **(7)** as shown in Scheme 5.2. In a typical procedure, TxMe$_6$Br$_3$ linker, CuI, and Pd(PPh$_3$)$_4$ were taken in a 50 mL RB flask. Anhydrous DMF (10 mL) and 2M K$_2$CO$_3$ (3 mL) were added to the above mixture. The solution was then deoxygenated by freezing and evacuation (3×3). After this, the reaction mixture was brought to 80 °C slowly and stirred for 3 days under nitrogen environment. After three days, reaction mixture was cooled to RT and centrifuged to collect insoluble material. The obtained solid polymer was washed thoroughly with DMF, Methanol, Acetone, diethyl ether and dried in vacuum oven at 100 °C.

TxBz-CPP: TxBz-CPP was synthesized according to the similar method described above using TxBz-CPP. TxMe$_6$Br$_3$ (48 mg, 0.15 mmol), compound **(2)** (13 mg, 0.1mmol), CuI (1.5 mg, 0.004 mmol) and Pd(PPh$_3$)$_4$ (5 mg, 0.004 mmol), anhydrous DMF (5 mL) and 2M K$_2$CO$_3$ (0.6 mL) were used. Yield 83% (insoluble light yellow polymer).

TxOMe-CPP: TxOMe-CPP was synthesized using TxMe$_6$Br$_3$ (48 mg, 0.07 mmol), compound **4** (18.6 mg, 0.1 mmol), CuI (1.5 mg, 0.004 mmol), and Pd(PPh$_3$)$_4$ (5 mg, 0.004 mmol), anhydrous DMF (5 mL) and 2M K$_2$CO$_3$ (0.6 mL) according to the general procedure described above. Yield 80% (insoluble dark yellow polymer).

**TxBz-CPP**   **TxOMe-CPP**   **TxBNS-CPP**
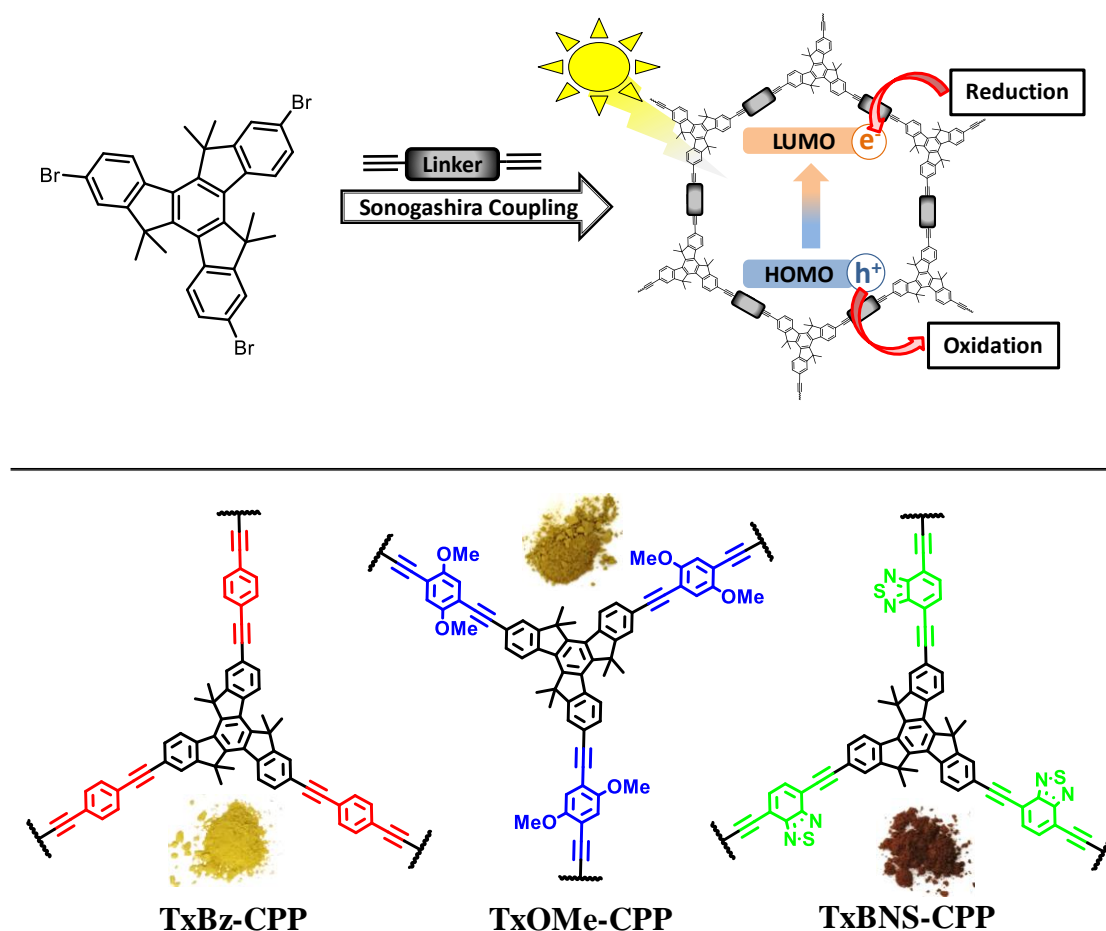
Scheme 5.2: Schematic design of band gap modification in truxene based conjugated microporous poly(benzooxadiazole) networks by altering bi-functional linker by keeping truxene as 3D centre.

TxBNS-CPP: TxBNS-CPP was synthesized using TxMe$_6$Br$_3$ (48 mg, 0.07 mmol), compound (**7**) (20 mg, 0.1mmol), CuI (1.5 mg, 0.004 mmol) and Pd(PPh$_3$)$_4$ (5 mg, 0.004 mmol), anhydrous DMF (5 mL) and 2M K$_2$CO$_3$ (0.6 mL) according to the procedure described above. Yield 72% (insoluble dark red polymer).

5.3 Result and Discussion:

5.3.1 Solid-State NMR:

Constructed from rigid building block, CPPs are insoluble in nearly all the common organic solvents. To get the structural insight of CPPs, solid-state ^{13}C/MAS NMR spectra were recorded (Figure 5.1, Appendix, Figure A5.1). In particular, polymer TxBz-CPP exhibited a signal at 25 ppm for the methyl group and a peak at 48 ppm assigned to the quaternary methylene carbon. An additional broad signal between 80 to 100 ppm was assigned to the sp-carbon atoms arising from the alkyne group. In the aromatic region, a group of signals appearing between 120 to 140 ppm and three signals between 140 to 160 ppm were assigned to the signals arising from the truxene core and benzene carbon atoms from the linker. Polymers TxOMe-CPP and TxBNS-CPP displayed a very similar spectrum like that of polymer TxBz-CPP. The polymer TxOMe-CPP exhibits an additional broad peak between 85 ppm to 100 ppm assigned to the signal for methyl carbon atoms from the methoxy group.
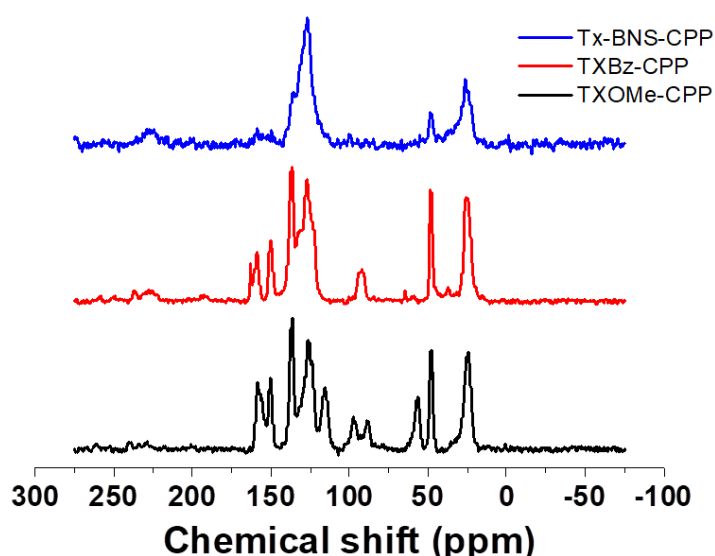
Figure 5.1: Solid-state ^{13}C/MAS NMR spectra of truxene based CPPs.

5.3.2 Thermal Stability and Morphology:

Thermogravimetric test showed that CPPs were stable up to 320 °C under the nitrogen atmosphere (Figure 5.2a-c). To investigate the morphology of CPPs, scanning electron microscopy (SEM) images were taken at different magnifications. The SEM images of all three CPPs exhibited different morphologies at submicron scale (Figure 5.2d-f). TxOMe-CPP exhibited flake-like textures with diameter > 100 nm (Figure 5.2d), whereas, TxBz-CPP showed morphology in which irregular shaped globular particles were fused together (Figure 5.2e). On the other hand, SEM images of TxBNS-CPP showed irregular shaped globular particles arranged to form the sheet-like structures of a few micrometres long (Figure 5.2f). These different morphologies of all these CPPs could be attributed to the different size and shape of the linkers used to connect the truxene molecules, as other conditions were similar during the formation of these CPPs**.**
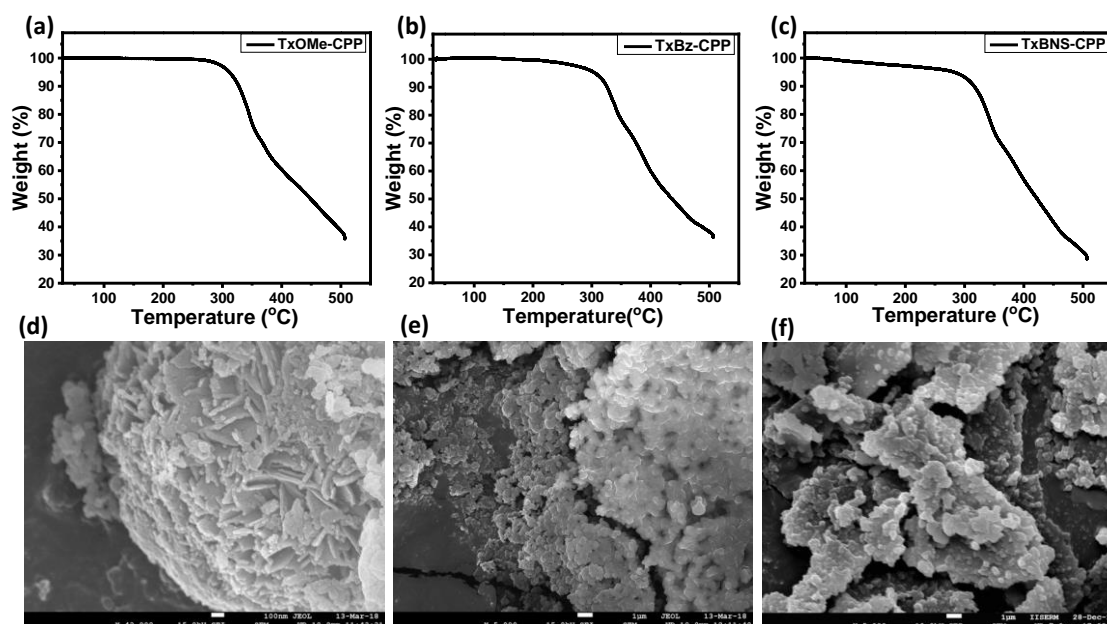
Figure 5.2: (a-c) Thermogravimetric analysis (TGA); (d-f) SEM images of TxOMe-CPP, TxBz-CPP, and TxBNS-CPP, respectively.

5.3.3 UV-vis Spectra and Optical Band Gap:

The Diffuse Reflectance (DR) UV-vis spectra were recorded to explore the optical properties of CPPs (Figure 5.3a). The results showed that TxOMe-CPP and TxBz-CPP have similar absorption profile, where they have a maximum absorbance around 500 nm and broad absorbance feature until 800 nm. Whereas, the absorption range of TxBNS-CPP extended from visible to near-infrared region, indicating a decrease in optical bandgap within the CPP series, which could also be seen in the colour change of CPPs from light yellowish, brownish-yellow to dark red for TxOMe-CPP, TxBz-CPP and TxBNS-CPP, respectively. The bandgap values were calculated through Kubelka–Munk function, with band gaps for respective samples, were provided here: TxOMe-CPP (2.25 eV), TxBz-CPP (2.00 eV) and TxBNS-CPP (1.41 eV) (Figure 5.3b, Appendix, Figure A5.2).
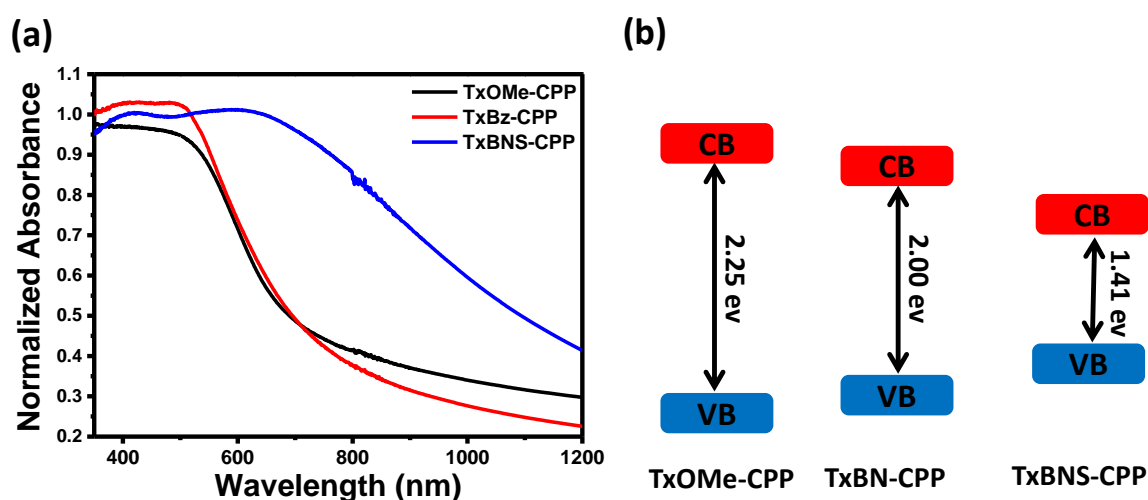

Figure 5.3: (a) DR UV/vis spectra and (b) Optical band gap values of CPP series.

5.3.4 Electron Paramagnetic Resonance (EPR):

Comparison of the electron paramagnetic resonance (EPR) spectra of CPPs reveals that among all CPPs, TxBz-CPP had the lowest signal intensity on light irradiation, whereas, TxOMe-CPP and TxBNS-CPP showed very intense signals when compared to the TxBz-

CPP (Figure 5.4). TxBNS-CPP showed slightly more intense peak as compared to TxOMe-CPP. These results showed that that upon light irradiation more long-lived electron-hole pairs could be generated in TxBNS-CPP and TxOMe-CPP than in TxBz-CPP.[6]
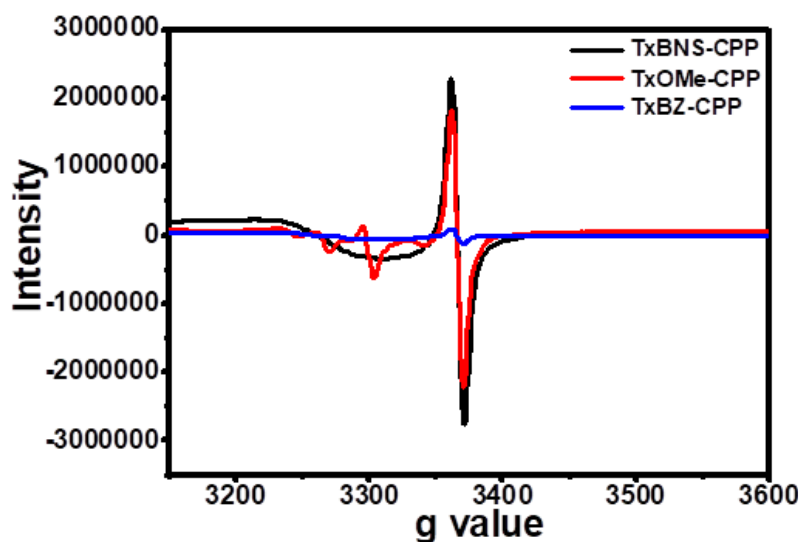
Figure 5.4: Electron paramagnetic resonance (EPR) spectra of TxOMe-CPP, TxBz-CPP and TxBNS-CPP upon light irradiation.

5.3.5 Porosity Studies:
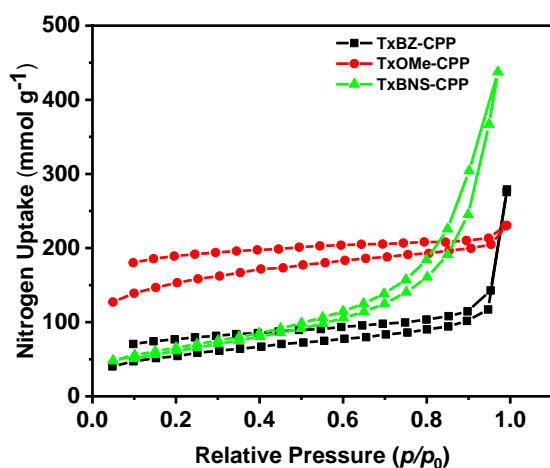
**Figure 5.5:** N_2 adsorption isotherms of truxene based CPPs at 77 K.

The accessible surface areas were determined by Brunauer−Emmett−Teller (BET) for the truxene-based polymers using nitrogen adsorption/desorption isotherms at 77 K. As shown in Figure 5.5, all polymers give rise to a type IV isotherm.[14] The surface areas were 534 m²/g, 191 m²/g and 233 m²/g with pore volumes of 0.357 cm^3/g, 0.432 cm^3/g and 0.401 cm^3/g for TxOMe-CPP, TxBz-CPP and TxBNS-CPP, respectively. (Appendix, Figure A5.3 and Table A5.1)

5.4 Photocatalytic Activity:
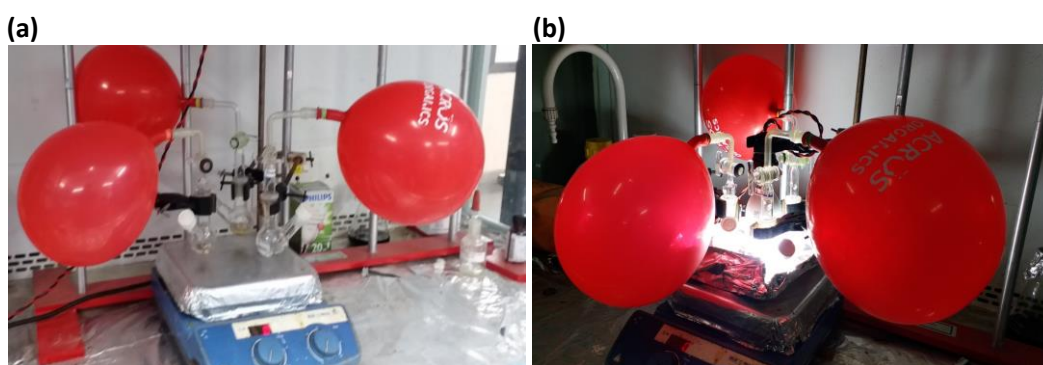
Figure 5.6: Photocatalytic setup for the oxidation of benzyl alcohols to aldehydes using different CPPs.
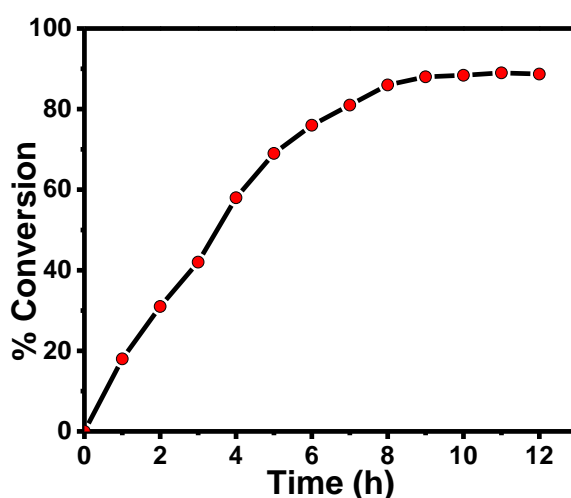
Table 5.1. Photooxidative conversion of benzyl alcohol to benzaldehyde and its derivatives by different CPPs as photocatalysts under visible light irradiation.
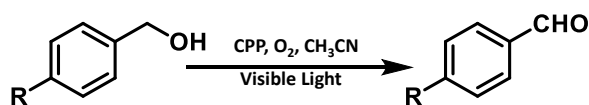
Entry	Polymer	Conversion (%)		
		R = H	**R = F**	**R = OMe**
1	TxBz-CMP	12	7	3
2	TxBNS-CMP	32	18	21

3	TxOMe-CMP	63	58	69

Reaction conditions: 0.1 mmol substrate, 10 mg CPP, 10 ml CH_3CN, CFL (20 W), Reaction time =6 h, 1 bar oxygen and at RT.

The direct and selective oxidation of alcohols to respective aldehydes and ketones has great importance in organic synthesis as well as in industrial chemistry. We investigated and compared the photocatalytic activity of TxBz-CPP, TxOMe-CPP and TxBNS-CPP for alcohol to aldehyde conversion in aerobic conditions, under visible light. First, benzyl alcohol and substituted benzyl alcohol with strong electron-withdrawing substituent (-F) or strong electron-donating (-OCH$_3$) were subjected for the photocatalytic conversion using Tx based CPPs system. To perform the photocatalytic reaction each benzyl alcohol derivative (0.1 mmol) and photocatalyst (10 mg) were taken in acetonitrile (10 mL) in round bottom flask, under O_2 environment using ordinary balloons (Figure 5.6a). This reaction mixture was further irradiated with energy saving CFL bulb (Philips Light 20W) at room temperature (RT) (Figure 5.6b). The conversion was monitored by using Gas chromatography (GC) with standards.

Figure 5.7: Benzyl alcohols to aldehyde conversion with time using TxBNS-CPP as a photocatalyst.

172

As shown in Table 5.1, all the CPPs showed the photocatalytic conversion of benzyl alcohols. However, TxOMe-CMP (entry 3) showed the significantly higher conversions as compared to the other two CPPs (entries 1 and 2) under same reaction conditions. The time dependent studies show that TxOMe-CMP could provide maximum conversion up to (89%) within 9 h of reaction (Figure 5.7, Appendix, Table A5.2).

5.5 Mechanistic Aspects:

Generally, photocatalytic reaction proceed via excess charge carriers, electrons (e^-) and holes (h^+), generated in semiconducting material upon light irradiation. These charge carriers act as the oxidative and reductive centre for photocatalytic reactions. In the excited state, photocatalyst can transfer either electron or energy to the molecular (O_2) present in the reaction medium resulting in the generation of superoxide radical ($O_2^{\bullet-}$) and singlet oxygen ($^1O_2$), which are responsible for the oxidation reaction in most of these

Table 5.2: Controlled experiments to predict the mechanism.
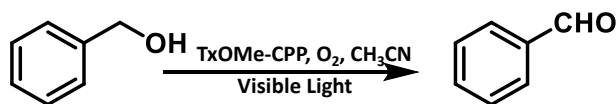
Entry	Catalyst	Oxygen (O_2)	Light	Additive	Conversion (%)
1.	-	+	+	-	<1
2.	+	+	-	-	n.d.
3.	+	-	+	-	<3
4	+	+	+	$CuCl_2$	29
5.	+	+	+	Ammonium oxalate	36

6.	+	+	+	Benzoquinone	11
7.	+	+	+	Sodium azide	65
8.	+	+	+	*tert*-butyl alcohol	86
9.	+	+	+	Catalase	88

Reaction conditions: 0.1 mmol substrate, 10 mg TxOMe-CPP, 10 ml CH_3CN, CFL (20 W), Reaction time = 6 h, 1 bar oxygen and at RT.

cases.[6, 7] To check the necessity of photocatalyst (TxOMe-CPP) or O_2 environment or light for the photocatalysis, three controlled reactions were performed. The negligible conversion in the absence of catalyst or light showed that indispensability of both to precede the photocatalytic reaction (entry 1 and 2, Table 5.2). Further, replacing the O_2
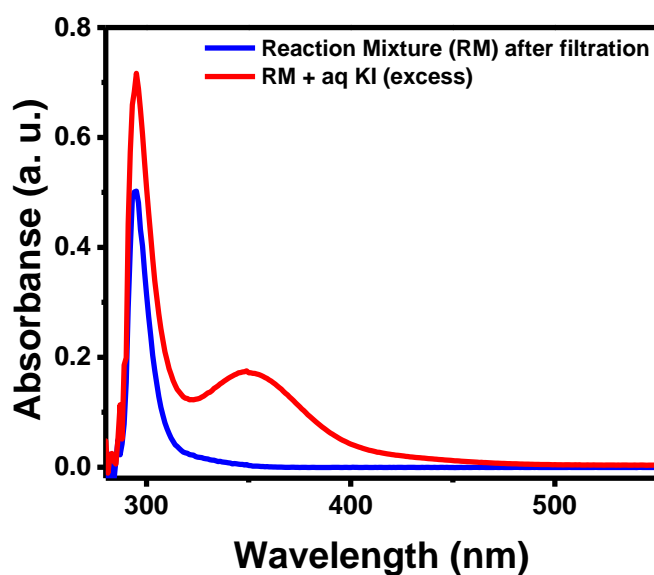
Figure 5.8: UV-vis absorption spectra of reaction mixture after removal of TxOMe-CPP and after addition of aq. saturated KI to this mixture.

environment with N_2 reduced the conversion down to 3%. This showed that the molecular O_2 was a crucial component (entry 3, Table 5.2) for the photocatalytic oxidation process.

Further, to unveil the mechanistic aspects of the photocatalytic oxidation reaction, a series of control experiments were performed. On addition of $CuCl_2$ and ammonium oxalate as electron and hole scavenger, respectively, the conversion drops to 29% and 36% proving the active role of photogenerated electron and hole pair in the reaction (entry 4, 5, Table 5.2).[15] The role of reactive oxygen species (ROS) was confirmed by using benzoquinone (BQ) and sodium azide (NaN_3) as superoxide scavenger ($^{\bullet}O_2^{-}$) and singlet oxygen ($^1O_2$) scavenger respectively.[16, 7] It was observed that conversion was reduced to 11 % and 65% in the presence of benzoquinone and NaN_3 respectively (entry 6, 7, Table 5.2). These results indicated that benzaldehyde generation was a combined action of both the ROS,
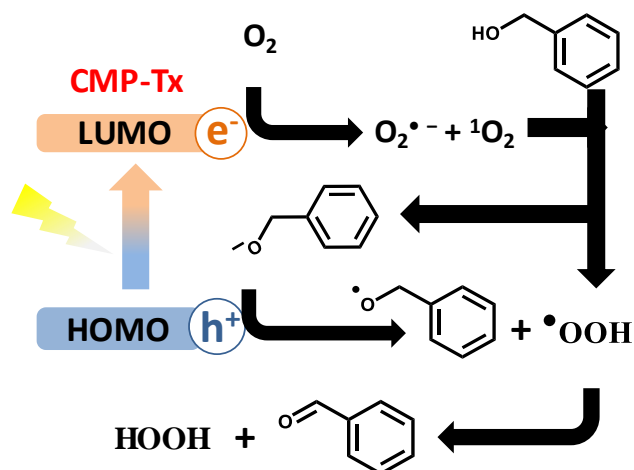

Scheme 5.3: Proposed mechanism for the photocatalytic oxidation of alcohols to respective aldehydes by TxOMe-CPP.

however, energy transfer process was dominated by electron transfer process which makes $O_2^{\bullet-}$ a major intermediate for reaction to proceed. The possible role of the hydroxyl radical ($\bullet$OH), a strong non-selective oxidant, was checked by adding *tert*-butyl alcohol as

an •OH scavenger, which shows negligible effect in the photocatalytic process (entry 8 in Table 5.2).[15] On the basis of controlled experiments and previous reports, a plausible mechanistic pathway was shown in Scheme 5.3. As shown in Scheme 3, activated molecular oxygen ($•O_2-$ and $^1O_2$) extracts one proton from benzyl alcohol and produce its anionic form and •OOH species. The benzyl anion was further oxidized by the photogenerated hole into its corresponding radical, which again oxidized by •OOH species to produce the benzaldehyde and H_2O_2. The formation of H_2O_2 was confirmed by UV/vis absorption spectra of I_3^- in aqueous KI solution (Figure 5.8).[17] Further, as H_2O_2 itself a known potential oxidant, its interference in photocatalytic oxidation reaction was checked in the presence of catalase as an H_2O_2 scavenger. The quantitative conversion of 88% clearly indicated that H_2O_2 is just a by-product of the reaction and didn't take part in the oxidation process (entry 8, Table 5.2).

5.6 Recyclability and Stability Test:

The recyclability of the photocatalyst was confirmed by using TxOMe-CPP for eight consecutive cycles. After each reaction, the catalyst was filtered followed by washing with acetonitrile and finally dried in a vacuum oven for 2 h at 90 °C. TxOMe-CPP retained excellent conversion, ~86 %, at least up to eight cycles (Figure 5.9a). Further, no
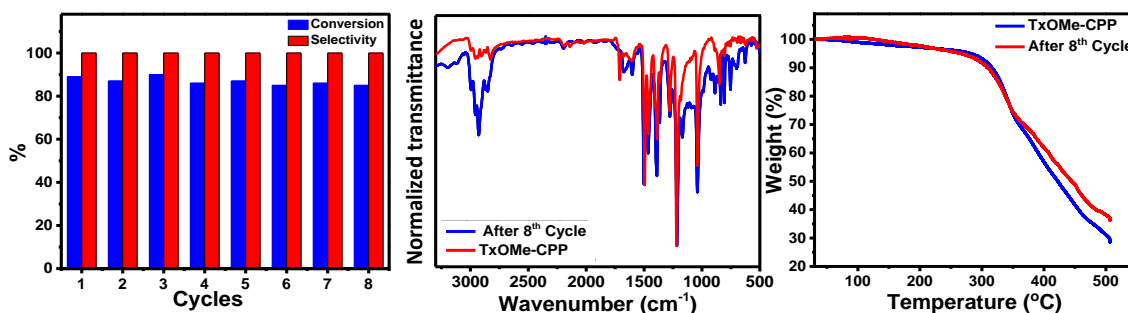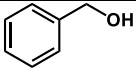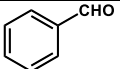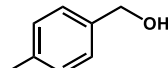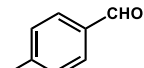

Figure 5.9: (a) Recyclability test of TxOMe-CPP for the oxidation of benzyl alcohol; (b, c) IR spectrum and TGA profile of TxOMe-CPP and after eight cycles of catalysis.
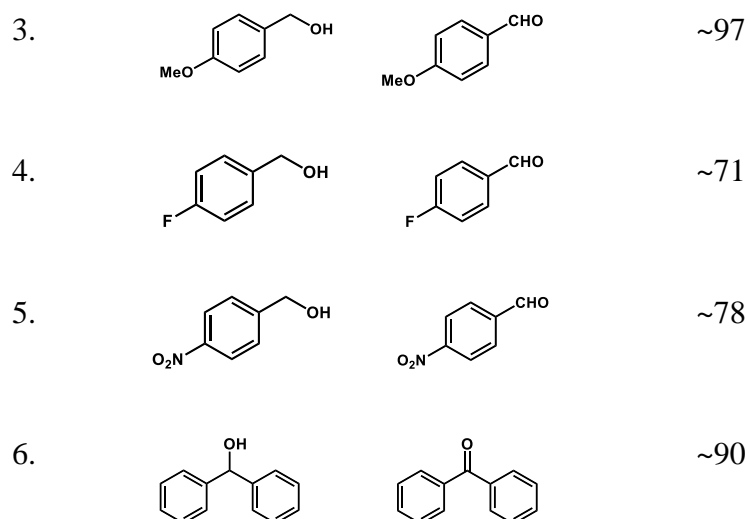
apparent change observed in the FT-IR spectrum and TGA profile and DRUV-vis absorption sepctra of TxOMe-CPP after eight cycles (Figure 5.9b-c). These results indicate the excellent stability and recyclability of the TxOMe-CPP at least up to eight cycles.

5.7 Substrate Scope of the Catalyst:

To further explore the versatility of the TxOMe-CPP catalyst, various substituted benzyl alcohols (Table 5.3) were subject for the photocatalytic conversion under the same reaction conditions. We achieved a very high isolated yield up to ~92% and ~97% of benzyl alcohols substituted with electron-donating groups, $-CH_3$ and $-OCH_3$, respectively, within 9 h of reaction time (entries 2 and 3, Table 5.3). However, benzyl alcohols substituted with electron-withdrawing groups, $-F$ and $-NO_2$ provide a moderate yield up to ~71% and ~78% respectively, under similar reaction conditions (entries 4 and 5, Table 5.3). Further, the oxidation of secondary alcohol also provides an excellent conversion up to ~90% (entries 6, Table 5.3). These experiments suggest that TxOMe-CPP acts as a very promising visible-light photocatalyst for the oxidation of benzyl alcohol and its derivatives within 9 h of reaction time.

Table 5.3. Scope of the TxOMe-CPP for the selective oxidation of alcohols as a photocatalyst.

Sr. No.	Reactant	Product	% Isolated yield
1.			~89
2.			~92

3.	[4-MeO-benzyl alcohol structure]	[4-MeO-benzaldehyde structure]	~97
4.	[4-F-benzyl alcohol structure]	[4-F-benzaldehyde structure]	~71
5.	[4-nitro-benzyl alcohol structure]	[4-nitro-benzaldehyde structure]	~78
6.	[diphenylmethanol structure]	[benzophenone structure]	~90

Reaction conditions: 0.5 mmol substrate, 50 mg CMP, 50 ml CH_3CN, CFL (20 W), Reaction time = 9 h, 1 bar oxygen and at RT. Isolated product was characterised by ^{1}H and ^{13}C NMR in $CDCl_3$ as solvent (Appendix, A5.4-A5.9).

5.8 Summary:

In summary, this chapter demonstrated a simple design strategy to develop a visible light heterogeneous photocatalyst based on truxene molecule for the aerobic oxidation benzylalchohol to benzaldehyde via tuning of the band gap and band positions using different organic groups. It was observed that just by altering the linkers with different electron-accepting capabilities, photocatalytic efficiency can be enhanced. Among the CPPs, TxOMe-CPP had shown superior photocatalytic activity for the oxidation of benzylalcohol to benzaldehyde compared to TxBz-CPP and TxBNS-CPP. This strategy could be extended to a wider range of conjugated porous polymeric networks to develop an efficient photocatalyst for specific photocatalytic chemical conversion.

References:

1. Battula V. R.; Singh H.; Kumar S.; Bala I.; Pal S. K.; Kailasam K. *ACS Catal.* **2018**, 8, 6751.

2. Nguyen J. D.; D'Amato E. M.; Narayanam J. M. R., Stephenson C. R. J. *Nat. Chem.* **2012**, 4, 854.

3. Gao X. H.; Bin Wu H. B.; Zheng L. X.; Zhong Y. J.; Hu Y.; Lou X. W. *Angew. Chem. Int. Ed.* **2014**, 53, 5917.

4. Yang W. L.; Zhang L.; Hu Y.; Zhong Y. J.; Wu H. B.; Lou X. W. *Angew. Chem. Int. Ed.* **2012**, 51, 11501.

5. Yang J. H; Wang D. G.; Han H. X.; Li C. *Acc. Chem. Res.* **2013**, 46, 1900.

6. Wang Z. J.; Ghasimi S.; Landfester K.; Zhang K. A. I. *Adv. Mater.* **2015**, 27, 6265.

7. Wang Z. J.; Garth K.; Ghasimi S.; Landfester K.; Zhang K. A. I. *ChemSusChem* **2015**, 8, 3459.

8. Kochi, J.; Sheldon, R. Metal Catalyzed Oxidations of Organic Compounds; *Academic Press: New York* **1981**.

9. Lang, X.; Ma, W.; Chen, C.; Ji, H.; Zhao, J. *Acc. Chem. Res.* **2014**, 47, 355.

10. Tsukamoto, D.; Shiraishi, Y.; Sugano, Y.; Ichikawa, S.; Tanaka, S.; Hirai, T. *J. Am. Chem. Soc.* **2012**, 134, 6309.

11. Chen, Y.-Z.; Wang, Z. U.; Wang, H.; Lu, J.; Yu, S.-H.; Jiang, H.-L. *J. Am. Chem. Soc.* **2017**, 139, 2035.

12. Olavarria-Contreras I. J.; Perrin M. L.; Chen Z.; Klyatskaya S.; Ruben M.; Zant H. S. J. *J. Am. Chem. Soc.* **2016**, 138, 27, 8465.

13. Zhao Y. L.; Liu L.; Zhang W.; Sue C.H.; Li Q.; Miljanic´ O. S.;. Yaghi O. M.; Stoddart J. F. *Chem. Eur. J.* **2009**, 15, 13356.

14. Sing, K. S. W.; Everett, D. H.; Haul, R. A. W.; Moscou, L.; Pierotti, R. A.; Rouquerol, J.; Siemieniewska, T. *Pure Appl. Chem.* **1985**, 57, 603.
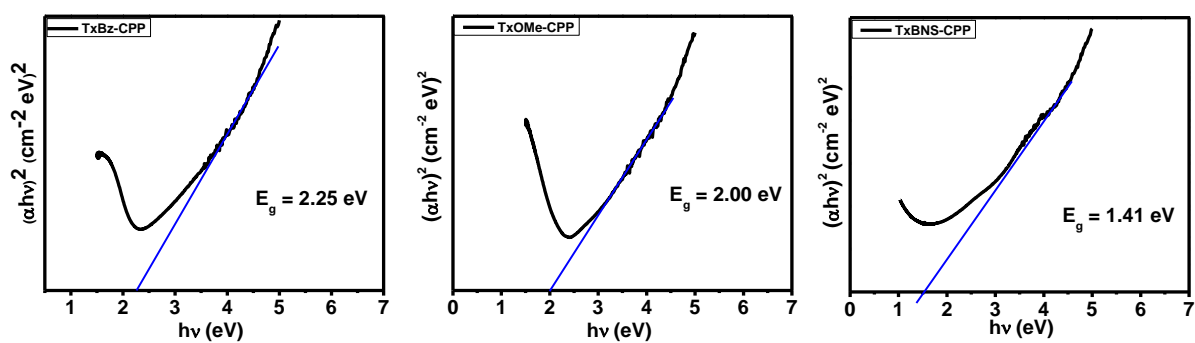
15. Ghosh, S.; Kouamé, N. A.; Ramos, L.; Remita, S.; Dazzi, A.; Deniset-Besseau, A.; Beaunier, P.; Goubard, F.; Aubert, P.-H.; Remita, H. *Nat. Mater.* **2015**, 14, 505.

16. Yuan, L.; Yang, M.-Q.; Xu, Y.-J. *Nanoscale* **2014**, 6, 6335.

17. Zou, Q.; Zhang, L.; Yan, X.; Wang, A.; Ma, G.; Li, J.; Möhwald, H.; Mann, S. *Angew. Chem.,* **2014**, 126, 2398.
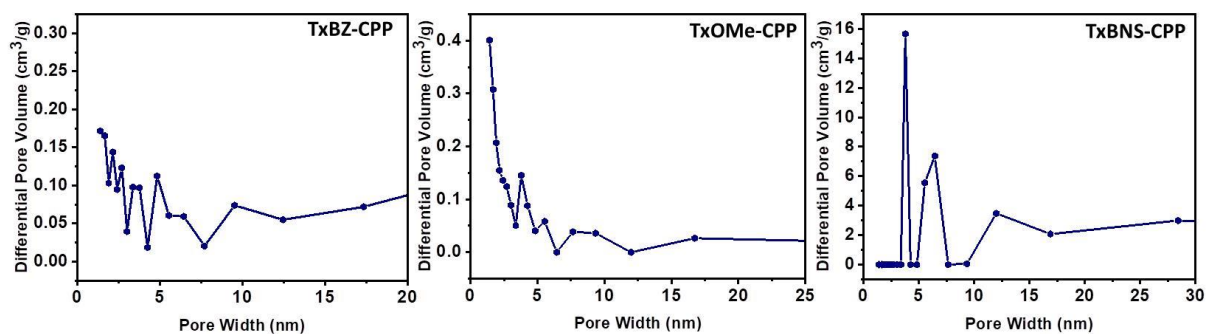
Appendix 5:
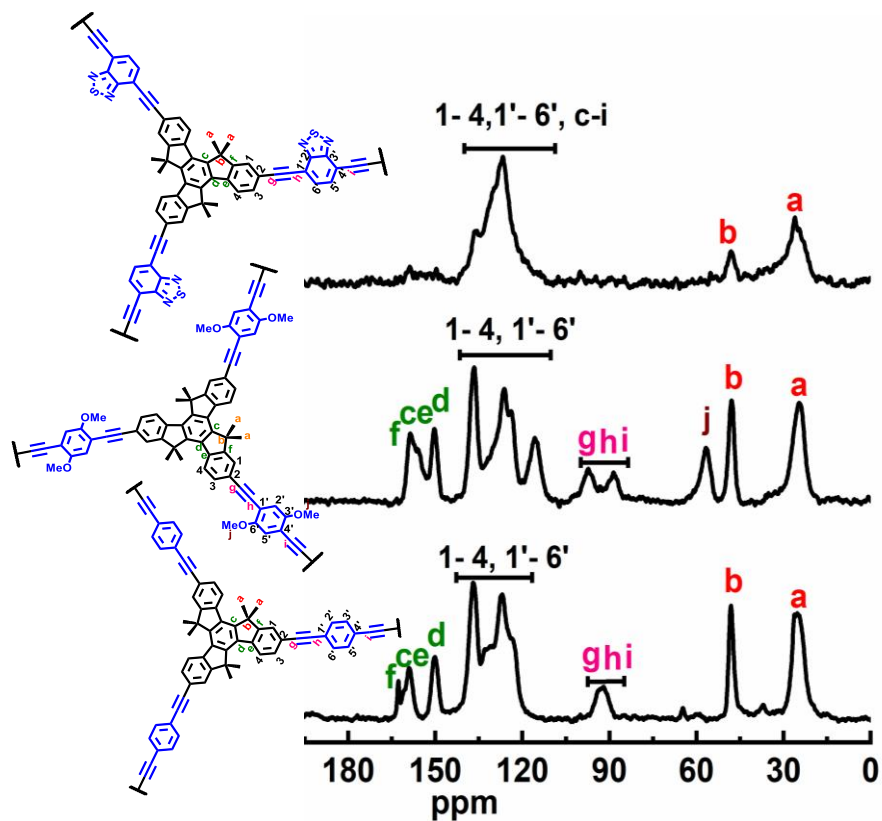
Figure A5.1: Solid-state ^{13}C/MAS NMR spectra of truxene based CPPs.

.

Figure A5.2: Band gap values of TxOMe-CPP, TxBz-CPP and TxBNS-CPP calculated from Kubelka–Munk function.

Figure A5.3: Pore size distribution curve of truxene based CPPs at 77 K calculated by BJH method.

Table A5.1: BET surface area and the pore volume of TxOMe-CPP, TxBz-CPP and TxBNS-CPP measured at 77 K.

Polymer	S_{BET} ($m^2\ g^{-1}$)	Pore Volume ($cm^3\ g^{-1}$)
TxOMe-CPP	533 m²/g	0.357 cc/g
TxBz-CPP	190 m²/g	0.432 cc/g
TxBNS-CPP	223 m²/g	0.401 cc/g

Table A5.2: Benzyl alcohol to aldehyde conversion with time using TxBNS-CPP as a photocatalyst.

S.N.	Time in Hours	% Conversion
1.	1	18
2.	2	31
3.	3	42

4.	4	58
5.	5	69
6.	6	76
7.	7	81
8.	8	86
9.	9	88
10.	10	88.7
11.	11	89.1
12.	12	89.1
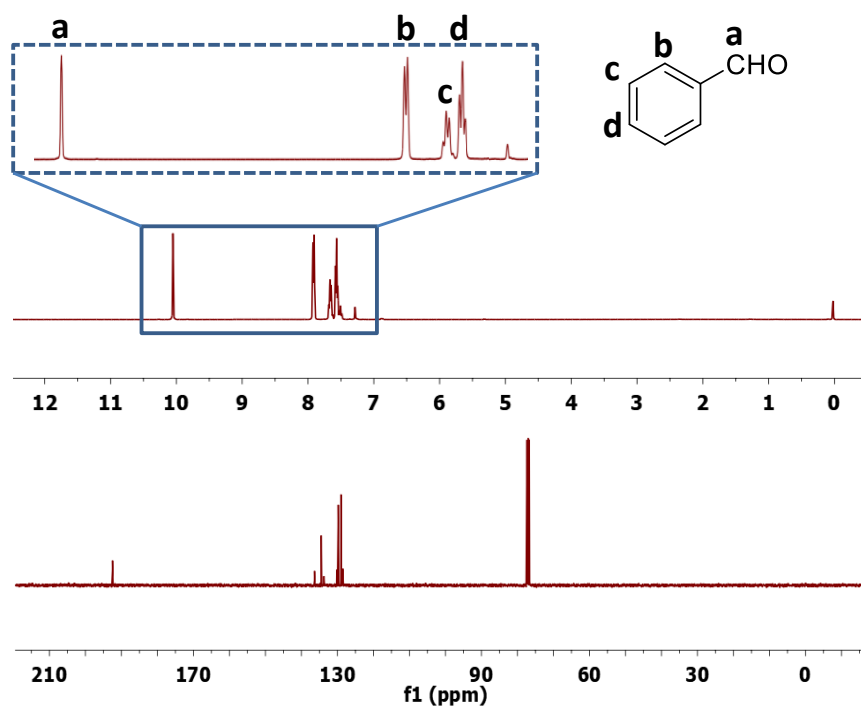
Figure A5.4: ^{1}H (top) and ^{13}C NMR (bottom) of isolated product of the photocatalytic conversion of phenylmethanol using TxOMe-CPP as photocatalyst.
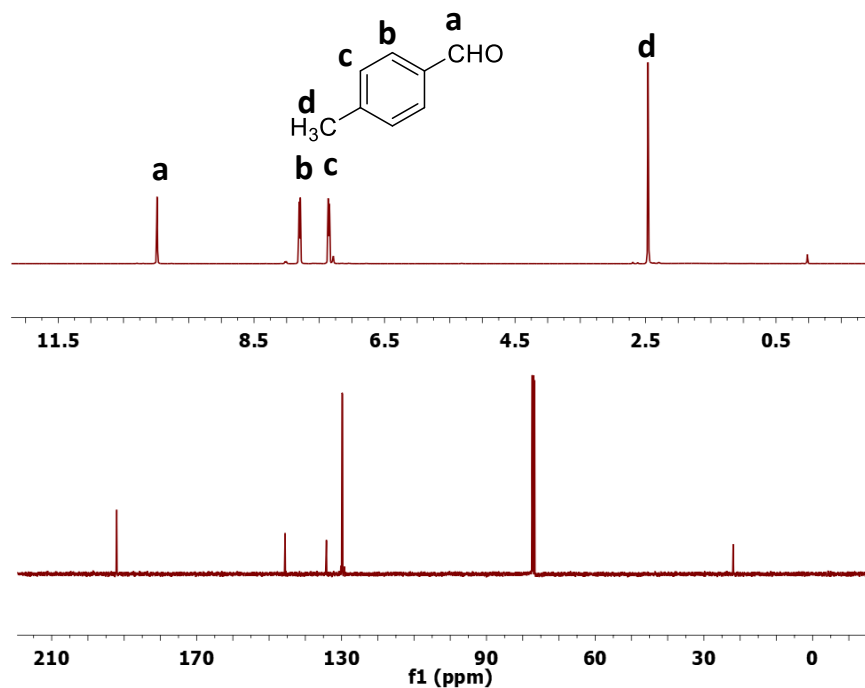
Figure A5.5: ^{1}H (top) and ^{13}C NMR (bottom) of the isolated product of the photocatalytic conversion of *p*-tolylmethanol using TxOMe-CPP as photocatalyst.
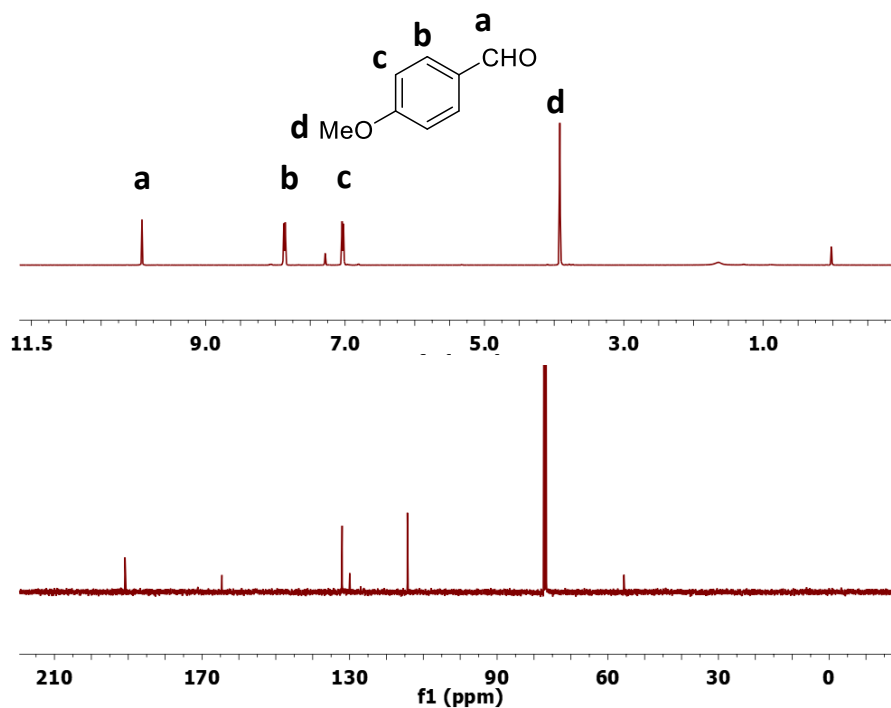
Figure A5.6: ^{1}H (top) and ^{13}C NMR (bottom) of isolated product of the photocatalytic conversion of (4-methoxyphenyl)methanol using TxOMe-CPP as photocatalyst.

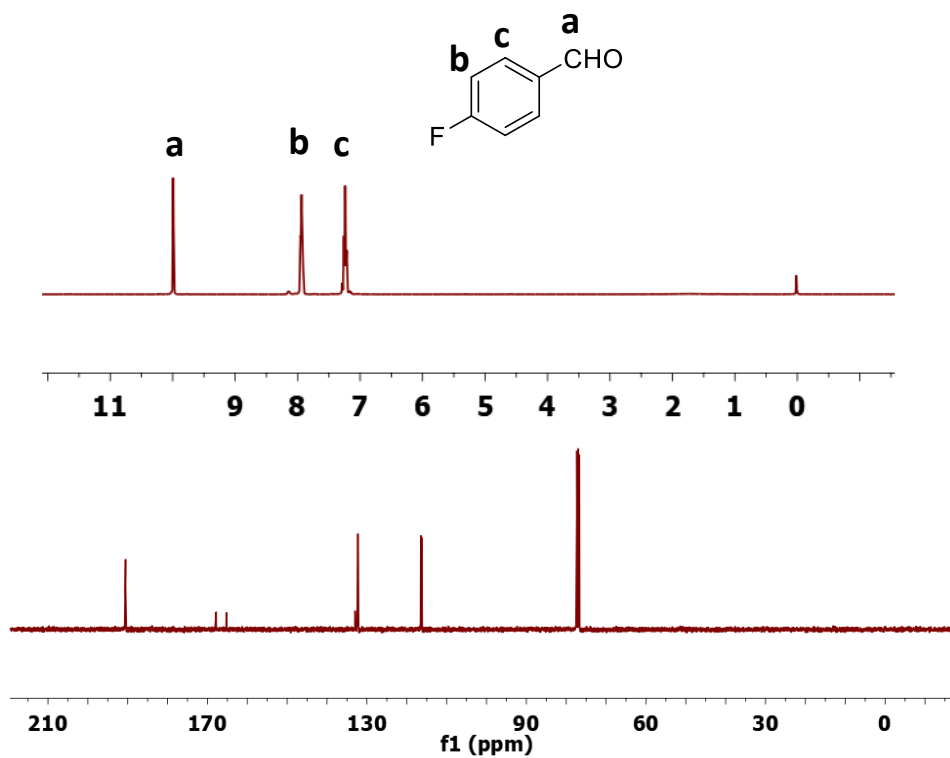**Figure A5.7:** ^{1}H (top) and ^{13}C NMR (bottom) of the isolated product of the photocatalytic conversion of (4-fluorophenyl)methanol using TxOMe-CPP as photocatalyst.

Figure A5.8: ^{1}H (top) and ^{13}C NMR (bottom) of the isolated product of the photocatalytic conversion of (4-nitrophenyl)methanol using TxOMe-CPP as photocatalyst.
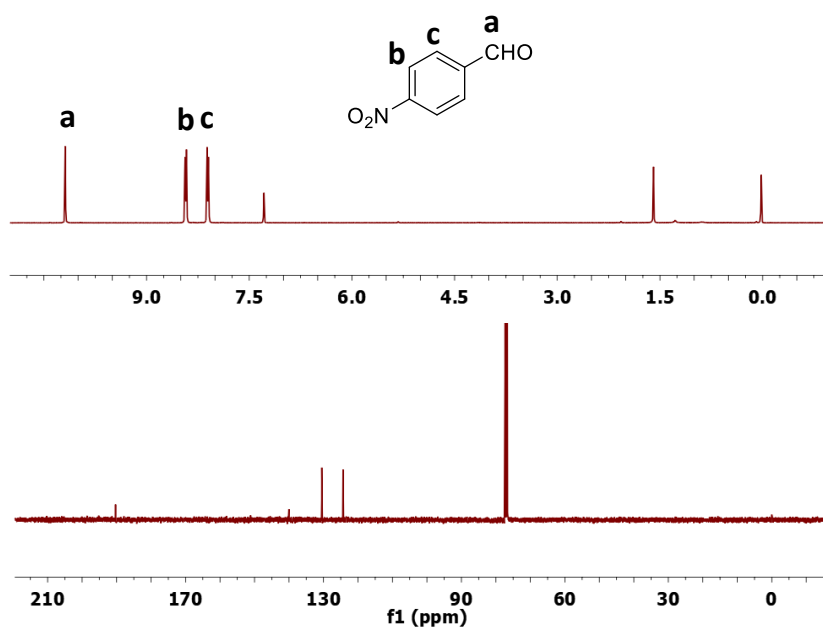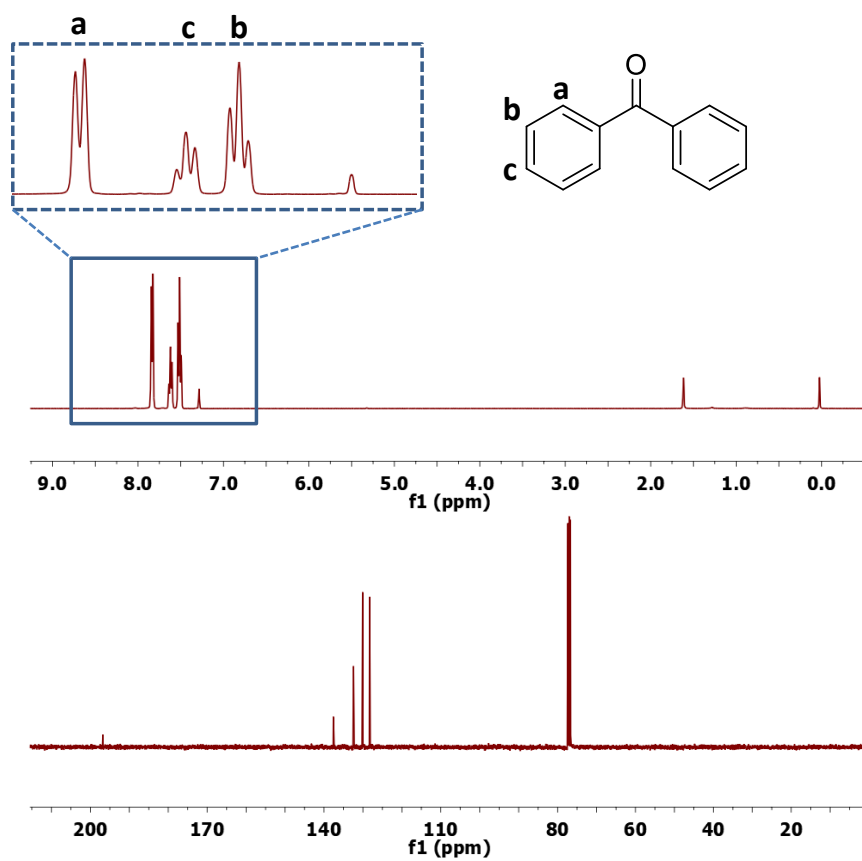
Figure A5.9: ¹H (top) and ¹³C NMR (bottom) of isolated product of the photocatalytic conversion of benzophenone using TxOMe-CPP as photocatalyst.

Chapter 6

Conclusions

In summary, the research of this thesis work mainly focuses to explore the sensing and photocatalytic applications of newly designed crystalline and amorphous porous organic frameworks. Porous organic polymers (POPs) with well-defined pores and the very high surface area received great attention in recent years. Being purely organic materials, POPs can be easily designed using rich organic synthetic tools and can be processed from molded monolith to thin films, which is nearly impossible in the case of other inorganic/hybrid porous structures. Decorated with these many advantages, POPs have strengthened their way to various applications such as adsorption, separation, catalysis, proton conduction, solar cells, drug delivery, etc. Among all POPs, covalent organic frameworks (COFs) devised through the reticular chemistry approach are very interesting porous materials due to their crystalline structures and open voids. Further, conjugated microporous polymers (CMPs) are widely explored amorphous POPs because of their synthetic simplicity and low bandgap. This thesis work described four examples of strategic design and synthesis of new COFs and CMPs for sensing and visible light photocatalytic applications.

To design the COFs, Truxene was employed as a building block to successfully synthesize novel covalent organic frameworks (COFs). The condensation reaction between truxene and 1,4-phenylenediboronic acid (DBA) results in a crystalline COF with boron ester linkages (COF-TxDBA) and a surface area of 1526 m^2 g^1, as confirmed by powder X-ray diffraction (PXRD) and Brunauer–Emmett–Teller (BET) surface area measurements. This was the first study where nanochannels generated by periodic COF planar layers were shown to ease the interactions of the boron ester linkages with the

water molecules for efficient humidity sensing. The COF-TXDBA based % RH sensor exhibited a change of 3 orders of magnitude in impedance in the 11–98% RH range, with the response and recovery times of 37 s and 42 s, respectively. The response transients measured by switching sensor back and forth in 4 loops of % RH range displays excellent reversibility of the sensor with a deviation of 2.3% in the switching process. These features unfold the additional role that the COFs can play in emerging applications. Further, exfoliation of 2D COFs into covalent organic nanosheets (CONs) not only help to reduce fluorescence turn-off phenomena but also provide well-exposed active sites for fast response and recovery for various applications. Working in the same direction, we have demonstrated a new approach of bottom-up construction of highly fluorescent self-exfoliable covalent organic nanosheets (CONs) via condensing a fluorophore with an ionic linker. This unique design not only provides an opportunity to tune the photophysical properties of CONs via choosing an appropriate fluorophore but also promotes exfoliation because of intrinsic ionic repulsions between the layers. The highly fluorescent self-exfoliable ionic CONs was constructed by condensing triaminoguanidinium chloride (TG$_{Cl}$), an intrinsic ionic linker, with a fluorophore 2, 5-dimethoxyterephthalaldehyde (DA). These fluorescent iCONs have shown selectively sensing ability towards fluoride ions down to ppb level via fluorescence turn-off mechanism. A closer look at the quenching mechanism via NMR, zeta potential measurement, lifetime measurement and DFT calculations reveal unique proton triggered fluorescence switching behavior of newly synthesized ionic CONs. These results provide a fundamental approach to develop a photo-luminescent artificial molecular switch based on 2D organic nanosheets.

In addition to the development of electrochemical and chemosensors based on crystalline POPs, we have also synthesized series of amorphous conjugated POPs to use them as

photocatalyst. We had successfully designed a novel Truxene based conjugated microporous polymer (Tx-CMP) linked through a highly stable C-C bond. The novel Tx-CMP has a high surface area, large pore volume, narrow bandgap, and extraordinary stability. It serves as a metal-free photocatalyst for the oxidative homocoupling of amines with optimal conversion under natural sunlight within 4 h. This model reaction also describes an effective, greener and sustainable way to harvest natural sunlight effectively for the organic transformations. The higher conversion and selectivity of Tx-CMP has been demonstrated with recyclability for at least 5 times without any decline in its catalytic activity under direct sunlight. We have also demonstrated a simple design strategy to develop a visible light heterogeneous photocatalyst for desired chemical transformation. A series of conjugated porous polymers (CPP) with different bandgap and band positions were synthesized using three linkers with different electron-accepting properties keeping truxene as 3D center. It was observed that just by altering the linkers with different electron-accepting capabilities, photocatalytic efficiency for the photocatalytic oxidation of benzylachohol by CPP enhanced drastically up to 89%. Among three CPPs, TxOMe-CPP had shown superior photocatalytic activity for the oxidation of benzylalcohol to benzaldehyde compared to TxBz-CPP and TxBNS-CPP. This strategy could be extended to a wider range of conjugated porous polymeric networks to develop an efficient photocatalyst for specific photocatalytic chemical conversion.

We believe that the research work of this thesis will work as a catalyst for the acceleration of the research field of POPs to explore them for various applications.

List of publications

1. **Singh, H.;** Devi, M.; Jena, N.; Iqbal, M. M.; Nailwal, Y.; Sarkar, A. D.; Pal, S. K. *ACS Appl. Mater. Interfaces* **2020**, 12, 13248.

2. Battula, V. R.; **Singh, H.**; Kumar, S.; Bala, I.; Pal, S. K.; Kailasam, K. *ACS Catal.* **2018**, 8, 6751.

3. Bala, I.; Ming, L.; Yadav R. A. K.; De, J.; Dubey, D. K.; Kumar, S.; **Singh, H.**; Jou, J. H.; Kailasam, K.; Pal, S. K. *ChemistrySelect* **2018**, 3, 7771.

4. Bala, I.; Gupta, S. P.; Kumar, S.; **Singh, H.**; De, J.; Sharma, N.; Kailasam, K.; Pal, S. K. *Soft Matter* **2018**, 14, 6342.

5. **Singh, H.**; Tomer, V. K.; Jena, N.; Bala, I.; Sharma, N.; Nepak, D.; Sarkar, A. D.; Kailasam, K.; Pal, S. K. *J. Mater. Chem. A* **2017**, 5, 21820.

6. Bala, I.; **Singh, H.**; Battula, V. R.; Gupta, S. P.; De, J.; Kumar, S.; Kailasam, K.; Pal, S. K. *Chem. Eur. J.* **2017**, 23, 14718.

Book Chapter

Singh H., Kumar S., Pal S.K. (2016) Discotic Liquid Crystalline Polymers: Structure and Chemistry. In: Thakur V., Kessler M. (eds) Liquid Crystalline Polymers. Springer, Cham pp 583-615.

Conferences

1. Poster presentation entitled "Natural sunlight driven oxidative homocoupling of amines by a truxene-based conjugated microporous polymer" at International Conferences on Frontiers in Chemical Sciences held at IIT-Guwahati, 2018.

2. Participated in National Conference on Liquid Crystal (NCLC) held in October 2017 at Indian Institute of Science Education and Research Mohali (IISERM), S.A.S. Nagar Mohali, India 2017.

3. Participated in "Inside Raman 2015" workshop organized by Renishaw Metrology Systems in December, 2015 at the Indian Institute of Science Education and Research Mohali (IISERM), S.A.S. Nagar Mohali, India, 2015.

VITA

Harpreet Singh

Harpreet Singh was born and raised in Hanumangarh Jn., a small district of Rajasthan, where he did his schooling. In 2006, he joined IISER Pune as BS-MS student based on his IIT-JEE rank. He was awarded INSPIRE Scholarship by Department of Science and Technology, Govt. of India from 2006 to 2011. In his MS thesis, he worked on Banana and Star shaped Liquid Crystalline Oligo-(Phenylenevinylene)s under the supervision of Prof. Manickam Jayakannan. He graduated in 2011, receiving Integrated BS-MS dual degree with major in chemistry. He had qualified CSIR-NET in 2012 while he was teaching to 12th class students. In 2013, he joined Dr. R. Vaidyanathan*'s* group to work on a research project entitled "Development of porous coordination polymers or metal-organic frameworks for capture and separation of CH_4 and CO_2" in house project of IISER Pune. In 2014, he moved to the IISER Mohali to join Ph.D. program and began working under the guidance of Dr. Santanu Kumar Pal. His research interest includes the design and synthesis of porous organic polymers for sensing and visible light photocatalytic applications. During his Ph.D. program he attended national and international conferences and presented his work. He has authored and co-authored eight publications and one book chapter in reputed peer-reviewed international journals.